

**Mechanical and Tribological Properties of AA6061-2SiCp-xGr
Hybrid Nanocomposites Fabricated Through Ultrasonically
Assisted Stir Casting Method**

*Submitted in partial fulfillment of the requirements
for the award of degree of*

**DOCTOR OF PHILOSOPHY
in
Mechanical Engineering**

by

A PRASAD REDDY

(Roll. No. 714014)

under the supervision of

Dr. P. Vamsi Krishna

Associate Professor

Department of Mechanical Engineering

&

Dr. R. Narasimha Rao

Professor

Department of Mechanical Engineering



**DEPARTMENT OF MECHANICAL ENGINEERING
NATIONAL INSTITUTE OF TECHNOLOGY
WARANGAL - 506 004, TELANGANA, INDIA.
NOVEMBER-2019**

**Mechanical and Tribological Properties of AA6061-2SiCp-xGr
Hybrid Nanocomposites Fabricated Through Ultrasonically
Assisted Stir Casting Method**

*Submitted in partial fulfillment of the requirements
for the award of degree of*

**DOCTOR OF PHILOSOPHY
in
Mechanical Engineering**

by

A PRASAD REDDY
(Roll. No. 714014)

under the supervision of

Dr. P. Vamsi Krishna
Associate Professor
Dept. of Mechanical Engineering

Dr. R. Narasimha Rao
Professor
Dept. of Mechanical Engineering



**DEPARTMENT OF MECHANICAL ENGINEERING
NATIONAL INSTITUTE OF TECHNOLOGY
WARANGAL-506 004, TELANGANA, INDIA.
NOVEMBER-2019**



NATIONAL INSTITUTE OF TECHNOLOGY, WARANGAL – 506004

Mechanical Engineering Department

Approval Sheet

This Thesis entitled "**Mechanical and Tribological Properties of AA6061-2SiCp-xGr Hybrid Nanocomposites Fabricated Through Ultrasonically Assisted Stir Casting Method**" by **Mr. A. Prasad Reddy (Reg. No. 714014)** is approved for the degree of Doctor of Philosophy.

Examiner

Prof. APURBBA KUMAR SHARMA

Supervisor

Dr. P. VAMSI KRISHNA

Co-Supervisor

Prof. R. NARASIMHA RAO

Chairman

Prof. N. SELVARAJ

Date: 13th November 2019



NATIONAL INSTITUTE OF TECHNOLOGY

WARANGAL – 506 004, Telangana State, INDIA

CERTIFICATE

This is to certify that the work presented in the thesis entitled "**Mechanical and Tribological Properties of AA6061-2SiCp-xGr Hybrid Nanocomposites Fabricated Through Ultrasonically Assisted Stir Casting Method**" which is being submitted by **Mr. A Prasad Reddy (Roll No. 714014)**, is a bonafide work submitted to National Institute of Technology, Warangal in partial fulfillment of the requirement for the award of the degree of **Doctor of Philosophy in Mechanical Engineering**.

To the best of our knowledge, the work incorporated in the thesis has not been submitted to any other university or institute for the award of any other degree or diploma.

Dr. P. Vamsi Krishna
Supervisor
Associate Professor
Department of Mechanical Engineering
National Institute of Technology
Warangal-506 004, Telangana, India.

Dr. R. Narasimha Rao
Co-Supervisor
Professor
Department of Mechanical Engineering
National Institute of Technology
Warangal-506 004, Telangana, India.

Prof. N. Selvaraj
Chairman-DSC
Head of the Department
Department of Mechanical Engineering
National Institute of Technology
Warangal-506 004, Telangana, India.



NATIONAL INSTITUTE OF TECHNOLOGY WARANGAL – 506 004, Telangana State, INDIA

Declaration

This is to certify that the work presented in the thesis entitled "**Mechanical and Tribological Properties of AA6061-2SiCp-xGr Hybrid Nanaocomposites Fabricated Through Ultrasonically Assisted Stir Casting Method**" is a bonafide work done by me under the supervision of **Dr. P. Vamsi Krishna**, Associate Professor, Department of Mechanical Engineering, NIT Warangal, India and Co-supervision of **Dr. R. Narasimha Rao**, Professor, Department of Mechanical Engineering, NIT Warangal, India and was not submitted elsewhere for the award of any degree.

I declare that this written submission represents my ideas in my own words and where others' ideas or words have been included, i have adequately cited and referenced the original sources. I also declare that i have not misrepresented or fabricated or falsified any idea / data / fact / source in my submission. I understand that any violation of the above will be a cause for disciplinary action by the Institute and can also evoke penal action from the sources which have thus not been properly cited or from whom proper permission has not been taken when needed.

.....
(Signature)

.....
(Name of the student)

.....
(Roll No.)

Date:

Dedicated

To

Family

ABSTRACT

World wide the global requirement is increasing for new generation of materials to satisfy advanced engineering applications. The usage of metal matrix nanocomposites (MMNCs) has been substantially increased in many sectors due to its stiffness, strength to weight ratio, mechanical and tribological properties. Ceramic nano-reinforcement particles are added to improve the mechanical and tribological properties of the aluminium and its alloys. The aluminium metal matrix nanocomposites (AA-MMNCs) have been used in various applications. The nano-sized ceramic particles reinforced AA-MMNCs are observed to be better mechanical and tribological properties due to the strengthening effect of nanoparticles. The strength of these AA-MMNCs is proportional to the weight percentage of nano-reinforcement and particle size. The recent reports reveal that the wear properties of AA-MMNCs containing more than one nano-reinforcement (i.e. hybrid nanocomposites) are observed to be beneficial compared to single nanoparticle reinforced composites.

The present study investigate the mechanical and tribological behaviour of AA6061 aluminium alloy, AA6061-x wt. % SiCp ($x = 0.5, 1, 1.5, \text{ and } 2$) (denoted as 0.5NC, 1NC, 1.5NC, and 2NC) nanocomposites and AA6061-2wt. % SiCp-y wt. % graphite ($y = 0.5, 1, 1.5, 2 \text{ and } 3$) (denoted as 0.5HNC, 1HNC, 1.5HNC, 2HNC, and 3HNC) hybrid nanocomposites. The nanocomposites are fabricated through ultrasonic assisted stir casting process. The results have proven that microstructures are greatly refined with the addition of SiCp and graphite nano-reinforcement particles. The density, yield strength, tensile strength and microhardness of the nanocomposites increased with increase of wt. % of SiCp nano-reinforcements in the matrix. In case of hybrid nanocomposites the density, tensile strength, and microhardness decreased with increase of graphite nano-reinforcements in the matrix. Strength of nanocomposites is affected due to the strengthening effect of SiCp and graphite nano-reinforcement particles. Enhancement of yield strength of nanocomposites and hybrid nanocomposites is predicted using various strengthening mechanisms such as Orowan strengthening effect, thermal dislocation mismatch effect, load bearing effect, Hall-Petch effect, and porosity effect. The Orowan strengthening effect and thermal dislocation mismatch effect is found to play a significant role in the nanocomposites. The predicted yield strength values using Ramakrishnan's model, Zhang and Chen model, modified Clyne model, Mirza and Chen model are compared with the experimental results.

The dry sliding wear behaviour of AA6061 aluminium alloy, nanocomposites, and hybrid nanocomposites on EN31 steel counter face at an applied load of 5-20 N, sliding distance of 1000-3000 m, and sliding velocity of 0.5-2 m/s is studied. The wear response in terms of volumetric wear rate, wear coefficients, and coefficient of friction is analyzed and compared with each other. The wear rate is low with increasing the wt. % of SiCp nano-reinforcements in the AA6061 aluminium alloy matrix. It is noticed that the wear coefficients of nanocomposites decreased with increase of SiCp nano-reinforcements in the matrix at all conditions. The microhardness of the SiCp reinforced AA6061 aluminium alloy based nanocomposite materials dominated the wear coefficients. Experimental results also confirm the increase of coefficient of friction for nanocomposites with rise of SiCp nano-reinforcement particles.

The effect on tribological properties is found to be better with the addition of graphite as a secondary reinforcement in the nanocomposites. The wear rate is decreased with increasing the graphite nano-reinforcements up to 2 wt. % and then increased. It can be seen that the wear coefficients of hybrid nanocomposites decreased with the increase of graphite nano-reinforcements in the matrix. The experimental results also confirm the increase of coefficient of friction for 3HNC hybrid nanocomposite with more than 2 wt. % of graphite addition in the matrix.

The two body abrasive wear experiments of AA6061 aluminium alloy, 2NC nanocomposite, and 2HNC hybrid nanocomposite are conducted with pin-on-disc equipment at an applied load of 5-20 N, sliding distance of 60-180 m, sliding velocity of 0.5-2 m/s, and grit size of 50-150 μm . The wear response in terms of volumetric wear rate, wear coefficients, and coefficient of friction is analyzed and compared with each other. The volumetric abrasive wear rate reduced for 2NC nanocomposite and 2HNC hybrid nanocomposite. The wear coefficients decreased with increase of applied normal loads, sliding distances and sliding velocities. The wear coefficients increased with increase of abrasive grit particle size. The volumetric wear rate is lower for least size abrasive grit paper and higher for coarse sized grit paper.

Overall results showing the improvement in tribological properties of hybrid nanocomposites by reducing the wear and friction.

ACKNOWLEDGEMENT

I would like to express my special appreciation and thanks to my supervisors **Dr. P. Vamsi Krishna**, Associate Professor, Department of Mechanical Engineering and **Dr. R. Narasimha Rao**, Professor, Department of Mechanical Engineering, NIT, Warangal for suggesting the topic of my thesis and their ready and able guidance throughout the course of my work.

I express my sincere thanks to Director NIT Warangal **Prof. N. V. Ramana Rao** for providing all academic and administrative help during the course of my work.

I like to extend my sincere thanks to **Prof. N. Selvaraj**, Chairman (Doctoral Scrutiny Committee), Head of the Mechanical Engineering Department and to the members of DSC, **Prof. A. Venu Gopal**, Department of Mechanical Engineering, **Prof. N. Narasaiah**, Department of Metallurgical and Materials Engineering, and **Dr. B. Satish Ben**, Associate Professor, Department of Mechanical Engineering, for all the support bestowed on me by suggesting and verifying the research work.

I am thankful to all the staff members of the Department of Mechanical Engineering and to all my well-wishers for their inspiration and help.

Non-teaching staff of the Mechanical Engineering Department have been instrumental in making arrangements during DSC meetings, and their help is acknowledged. Finally, i am extremely thankful to my friends and well-wishers who helped me directly and indirectly during my entire course.

This work is also the outcome of the blessing guidance and support of my father **Mr. A. Madhava Reddy**, my mother **Mrs. A. Saraswathi** and my brother **Mr. A. Bhaskar Reddy**. This work could have been a distant dream if i did not get the moral encouragement and help from my wife **Mrs. A. Puspha Latha** and my son **A. Abhinav**. This thesis is the outcome of the sincere prayers and dedicated support of my family.

I would like to thank my senior research scholar **Dr. Vishnumurthy Nallapati** for giving his valuable inputs and suggestions whenever required. Finally I wish to acknowledge the support given to me by all the **Ph.D.** and **M.Tech** Scholars specially for their cooperation during the course of my work.

(A Prasad Reddy)

List of Contents

<i>Abstract</i>	<i>i</i>
<i>Acknowledgement</i>	<i>iii</i>
<i>List of Contents</i>	<i>iv</i>
<i>List of Tables</i>	<i>ix</i>
<i>Table of Figures</i>	<i>xi</i>
<i>List of Abbreviations and Symbols</i>	<i>xix</i>

Chapter-1 Introduction **1-19**

1.1	Introduction	1
1.2	Aluminium	1
1.3	Aluminium Alloys	2
1.3.1	Casting aluminium alloys	2
1.3.2	Wrought aluminium alloys	3
1.4	Applications of Aluminium Alloys	4
1.5	Metal Matrix Composites (MMCs)	5
1.6	Reinforcements	6
1.7	Aluminium Metal Matrix Nanocomposites (AA-MMNCS)	6
1.7.1	Fabrication Techniques	7
1.7.2	Advantages of AA-MMNCS	14
1.7.3	Applications of AA-MMNCS	15
1.7.4	Mechanical Properties	15
1.7.5	Tribological Properties	16
1.8	Organization of the Thesis	18

Chapter-2 Literature Review **20-48**

2.1	Introduction	20
2.2	Mechanical Properties of AA-MMNCs	20
2.2.1	Effect of Type of Nano-reinforcements on Yield Strength and Ultimate Tensile Strength	21
2.2.2	Effect of Reinforcement Particle Size and Volume Fraction on Yield Strength and Ultimate Tensile Strength	26
2.2.3	Hardness of AA-MMNCs	30
2.2.4	Effect of Morphology and Fabrication Process on Strength Properties	31
2.3	Strengthening Mechanisms	36
2.4	Yield Strength Prediction Models	39
2.5	Tribological Properties of AA-MMNCs	40
2.6	Abrasive Wear Characteristics of AA-MMNCs	44
2.7	Motivation for the Present Work	46
2.8	Identified Gaps in the Literature	46
2.9	Objective of the Research Work	47
2.10	Complete Work Plan Flow Chart	47

Chapter-3 Experimentation **49-68**

3.1	Introduction	49
3.2	Materials Selection	49
3.3	Fabrication of Composites	51
3.4	Density Measurement	54
3.4.1	Experimental Density	54
3.4.2	Theoretical Density	55
3.5	Characterization	57

3.5.1	Specimen Preparation	57
3.5.2	X-Ray Diffraction Analysis (XRD)	57
3.5.3	Optical Microscopy	59
3.5.4	Scanning Electron Microscopy	59
3.5.5	Transmission Electron Microscopy	60
3.6	Mechanical Properties	61
3.6.1	Tensile Test	61
3.6.2	Hardness Test	63
3.7	Wear Test	64
3.7.1	Dry Sliding Wear Test on EN31 Steel	64
3.7.2	Two Body Abrasive Wear Test	66
3.8	Summary	68

Chapter-4 Characterization 69-81

4.1	Introduction	69
4.2	Density	69
4.3	XRD Analysis	71
4.4	Optical Microstructure	73
4.5	Transmission Electron Microscopy	76
4.6	Scanning Electron Microscopy	78
4.7	Summary	81

Chapter-5 Mechanical Properties 82-108

5.1	Introduction	82
5.2	Microhardness	82
5.3	Tensile Properties	84
5.4	Fractography	88

5.5	Yield Strength Prediction	91
5.5.1	Nanocomposites	91
5.5.2	Hybrid Nanocomposites	101
5.6	Summary	107

Chapter-6 Tribological Properties 109-189

6.1	Introduction	109
6.2	Tribological Properties of AA6061/SiCp Nanocomposites	109
6.2.1	Volumetric Wear Rate	109
6.2.2	Wear Coefficients	118
6.2.3	Coefficient of Friction	120
6.2.4	Worn Surfaces of Pin Specimens	123
6.2.5	EDX Analysis	128
6.2.6	Wear Debris	130
6.2.7	Wear Mechanism	131
6.3	Tribological Properties of Hybrid Nanocomposites	131
6.3.1	Volumetric Wear Rate	131
6.3.2	Wear Coefficients	141
6.3.3	Coefficient of Friction of Pin Materials	143
6.3.4	Worn Surfaces of Pin Specimens	146
6.3.5	EDX Analysis	152
6.3.6	Wear Debris of Pin Materials	155
6.3.7	Wear Mechanism	157
6.4	Two Body Abrasive Wear of Nanocomposites	158
6.4.1	Volumetric Wear Rate	158
6.4.2	Wear Coefficients	172
6.4.3	Worn Surface Analysis	174

6.4.4	Wear debris	181
6.4.5	Coefficient of friction	184
6.4.6	Wear Mechanism	186
6.5	Summary	188
Chapter-7 Conclusions and Future Scope		190-193
7.1	Conclusions	190
7.2	Other Observations	192
7.3	Future Scope for this Research Work	193
Miscellaneous		
References		194
List of Publications		212
Bio-Data		213

LIST of TABLES

Table	Title	Page
1.1	List of casting aluminium alloys	2
1.2	Wrought aluminium alloy designation system	3
1.3	The various treatments of AA6061 aluminium alloy	5
1.4	Aluminium based nanocomposites used in automobile sector	15
2.1	Research reported in literature on properties of different nano ceramic reinforcements	22
2.2	Mechanical properties of SiCp reinforced aluminium based nanocomposites	24
2.3	Mechanical properties of dual phase particles reinforced aluminium based hybrid nanocomposites	25
2.4	Mechanical properties of SiCp reinforced aluminium based nanocomposites as a function of volume fractions	28
2.5	Microhardness of the SiCp reinforced aluminium based nanocomposites as a function of volume fractions	31
2.6	List of various strengthening mechanism equations	36
2.7	List of various yield strength prediction model equations	39
3.1	Details of AA6061 aluminium alloy, β -SiCp and graphite nano-reinforcements particles	51
3.2	Specifications of TEM (FEI make: Model G2S Twin)	61
3.3	Specifications of UTM (Universal Testing Machine)	63
3.4	Specification of the pin on disc machine	64
3.5	Tribological test process parameters used in experiments	65
3.6	Tribological test process parameters used in two body abrasive wear test	67
5.1	Average grain size of nanoparticle reinforced AA6061 nanocomposites	93
5.2	Yield strength of hybrid nanocomposites are predicted using these parameters	104
5.3	Yield strength contribution from various strengthening mechanisms	104
5.4	Predicted and experimental yield strengths of hybrid nanocomposites	106

6.1	Volumetric wear rate of different materials obtained at 0.5 m/s sliding velocity	110
6.2	Volumetric wear rate of different materials obtained at 1 m/s sliding velocity	110
6.3	Volumetric wear rate of different materials obtained at 1.5 m/s sliding velocity	111
6.4	Volumetric wear rate of different materials obtained at 2 m/s sliding velocity	111
6.5	Volumetric wear rate of different materials obtained at 0.5 m/s	132
6.6	Volumetric wear rate of different materials obtained at 1 m/s sliding velocity	133
6.7	Volumetric wear rate of different materials obtained at 1.5 m/s sliding velocity	133
6.8	Volumetric wear rate of different materials obtained at 2 m/s sliding velocity	134

Table of FIGURES

Figure	Title	Page
1.1	The nomenclature line diagram of wrought aluminium alloys	3
1.2	(a) electrical conductors, (b) wheel rim, (c) garden frame, (d) radiators, (e) engine blocks, (f) hub caps, (g) oxygen gas cylinder, (h) bicycle frame, and (i) tweeter speaker	4
1.3	Stir casting design setup	7
1.4	Schematic diagram of powder metallurgy process	8
1.5	Schematic diagram of mechanical ball milling	9
1.6	Line diagram of friction stir process	9
1.7	Schematic illustration of ARB process with three cycles	10
1.8	Illustration spark plasma sintering process [11]	11
1.9	Compo casting setup [12]	12
1.10	Schematic line diagram of ultrasonically assisted casting setup [13]	13
1.11	(a) Initial ultrasonication process (b) nucleation starts (c) acoustic streaming (d) schematic view of vapor gas nuclei [14]	13
1.12	Line diagram of sliding friction	16
1.13	(a) schematic view of abrasive wear (b) two body abrasive wear (c) three body abrasive wear	18
1.14	Schematic view of adhesive wear mechanism	18
2.1	Predicted yield strength as a function of reinforcement particle size for different volume fractions in Al_2O_3 reinforced magnesium nanocomposites tested at 20 °C [57]	29
2.2	Predicted yield strength as a function of volume fraction of reinforcement particles for various sizes of Al_2O_3 reinforced Mg based nanocomposites tested at 20 °C [57]	29
2.3	SEM backscattered electron images of AA6063/SiCp nanocomposites (a) spark plasma sintering followed by hot extrusion, and (b) die pressing followed by hot extrusion [44]	32
2.4	The FESEM micrographs of extruded samples A356/SiCp/Cr (a) lower magnification, and (b) higher magnification [44]	32
2.5	The FESEM micrographs of extruded samples A356/SiCp/Cu (a) lower magnification, and (b) higher magnification [44]	33
2.6	The FESEM micrographs of extruded samples A356/SiCp/Ti (a)	33

	lower magnification, and (b) higher magnification [44]	
2.7	The SEM micrographs of extruded samples Al2014/SiCp (a) higher magnification, and (b) lower magnification [40]	34
2.8	Optical images of the Al/SiCp nanocomposites (a) Aluminium, (b) 1 vol. % of SiCp, (c) 3 vol. % of SiCp, (d) 5 vol. % SiCp, (e) 7 vol. % of SiCp, and (f) 9 vol. % of SiCp [33]	34
2.9	SEM micrographs of the nanocomposites (a) 1 wt. %, and (b) 2 wt. % [50]	35
2.10	SEM micrographs of the Al/SiCp nanocomposites (a) 2wt. %, (b) 4wt. %, and (c) 8 wt. % [68]	35
2.11	The flow chart that represents entire research work	48
3.1	The optical emission spectrometer setup	50
3.2	The photographic images of (a) AA6061 aluminium alloy (b) β -SiCp and (c) graphite	50
3.3	Schematic diagram of ultrasonically assisted stir casting setup	51
3.4	Ultrasonically assisted stir casting setup	53
3.5	Images of (a) electro mechanical stirrer (b) SS 304 stirrer rod coated with zirconia (ZrO_2) (c) mild steel die (d) graphite crucible and (e) stainless steel crucible	53
3.6	Photograph snapshot of (a) nanocomposite samples and (b) hybrid nanocomposite samples	54
3.7	High precision digital electronic weighing balance	55
3.8	XRD equipment (Model PANalytical)	58
3.9	Schematic description of Bragg's Law	58
3.10	Optical microscopy (Quasmo make model: QX-4RT)	59
3.11	Scanning electron microscopy equipment	60
3.12	Transmission electron microscopy equipment at Hyderabad Central University	60
3.13	Electro-mechanical universal testing machine (Blue Star WDW-100S) at NIT Warangal	62
3.14	Tensile test sample dimensions according to ASTM E8/E8M standards	62
3.15	Nanocomposite samples as per ASTM E8 standards	62

3.16	Micro Vicker's hardness tester (Make: Shimadzu, Model: HMV-G20ST)	63
3.17	(a) snapshot of dry sliding wear testing of sample (b) top view of dry sliding wear testing of sample	65
3.18	(a) snapshot of dry sliding wear testing of sample before (b) snapshot of top view of dry sliding wear after test	66
3.19	(a) Snapshot of two body abrasive wear testing of sample (b) Top view of abrasive wear testing of sample	67
3.20	(a) snapshot of two body abrasive wear testing of sample before (b) top view of after two body abrasive wear test	68
4.1	Theoretical, experimental density and porosity of the AA6061 aluminium alloy, 0.5NC, 1NC, 1.5NC and 2NC nanocomposites	70
4.2	Density of AA6061 aluminium alloy, 0.5HNC, 1HNC, 1.5HNC, 2HNC and 3HNC hybrid nanocomposites	70
4.3	XRD analysis of SiCp, AA6061 aluminium alloy and its nanocomposites	71
4.4	XRD of pure AA6061 aluminium alloy, 2NC nanocomposite, and 0.5HNC, 1HNC, 1.5HNC, 2HNC and 3HNC hybrid nanocomposites	72
4.5	Optical micrographs of (a) AA6061 aluminium alloy, (b) 0.5NC, (c) 1NC, (d) 1.5NC, and (e) 2NC	73
4.6	Average grain size (a) AA6061 aluminium alloy, (b) 0.5NC, (c) 1NC, (d) 1.5NC, and (e) 2NC	74
4.7	Optical images of various materials (a) AA6061 aluminium alloy, (b) 0.5HNC, (c) 1HNC, (d) 1.5HNC, (e) 2HNC, and (f) 3HNC	75
4.8	Average grain size (a) AA6061 aluminium alloy, (b) 0.5HNC, (c) 1HNC, (d) 1.5HNC, (e) 2HNC, and (f) 3HNC	76
4.9	(a) SiCp nanoparticles, (b) SiCp nanoparticle, (c) SAD pattern of SiCp particles, (d) graphite particles, (e) graphite particle and (f) SAD pattern of graphite particles	76
4.10	(a) TEM image of SiCp, (b) distribution of various sizes of SiCp nanoparticles, (c) TEM image of graphite and (d) distribution of various sizes of Gr nanoparticles	77
4.11	Morphology of different abrasive grit papers (a) 50 μm (b) 100 μm (c) 150 μm	78
4.12	SEM micrographs (a) AA6061 aluminium alloy, (b) 0.5NC, (c) 1NC, (d) 1NC and (e) 2NC	79
4.13	SEM micrographs (a) 2NC, (b) 0.5HNC, (c) 1HNC, (d) 1.5HNC, (e) 2HNC, and (f) 3HNC	80

5.1	Microhardness of AA6061 aluminium alloy and its nanocomposites	83
5.2	Microhardness of AA6061 aluminium alloy and its hybrid nano-composites	83
5.3	Stress-strain curves of AA6061 aluminium alloy and its nanocomposites	85
5.4	Mechanical properties of AA6061alloy and its composites	85
5.5	Stress-strain curves of AA6061 aluminium alloy and its hybrid nanocomposites	86
5.6	Mechanical properties of AA6061 aluminium alloy and its hybrid nanocomposites	87
5.7	SEM micrographs of fractured surfaces of materials (a) AA6061 aluminium alloy, (b) 0.5NC, (c) 1NC, (d) 1.5NC, and (e) 2NC	88
5.8	SEM micrographs of fractured surfaces of materials (a) AA6061 aluminium alloy, (b) 0.5HNC, (c) 1HNC, (d) 1.5HNC, (e) 2HNC, and (f) 3HNC	89
5.9	Grain size of AA6061 aluminium alloy based nanocomposites as a function of nano particle size and its volume fraction	94
5.10	Predicted yield strength as a function of volume fraction of reinforcement particles for various particles sizes in nano-SiCp particulate-reinforced AA6061alloy nanocomposites tested at 20 °C	96
5.11	Predicted yield strength as a function of reinforcement particle size for a volume fraction of 0.02 in nano-SiCp particulate-reinforced AA6061 aluminium alloy nanocomposites tested at 20 °C	96
5.12	Factors as a function of reinforcement particle size for a volume fraction of 0.02 in nano-SiCp particulate-reinforced AA6061alloy nanocomposites tested at 20°C (a) Different improvement factors (b) Orowan strengthening improvement factor between 2.5 nm and 0.6 nm	97
5.13	Relative contribution of factors as a function of reinforcement particle size for a volume fraction of 0.02 in nano-SiCp particulate-reinforced AA6061alloy nanocomposites tested at 20 °C	99
5.14	Orowan and dislocation mismatch improvement factors as a function of volume fraction of reinforcement particles with sizes of ($d_p = 10$, 50, and 1000 nm) in AA6061/SiCp nanocomposites tested at 20 °C	99
5.15	The yield strength of various models compared with the experimental data in AA6061/SiCp nanocomposites tested at 20 °C	100
5.16	The yield strength of various models compared with the experimental data in Hybrid nanocomposites tested at 20 °C	107

6.1	Wear rate of AA6061 aluminium alloy, 0.5NC, 1NC, 1.5NC, and 2NC nanocomposites as a function of applied normal load (a) 1000 m (b) 2000 m and (c) 3000 m	113
6.2	Wear rate of AA6061 aluminium alloy, 0.5NC, 1NC, 1.5NC, and 2NC nanocomposites as a function of sliding distance (a) 5 N (b) 10 N and (c) 15 N and (d) 20 N	114
6.3	Wear rate of AA6061 aluminium alloy, 0.5NC, 1NC, 1.5NC, and 2NC nanocomposites as a function of sliding velocity (a) 5 N (b) 10 N and (c) 15 N and (d) 20 N	117
6.4	Wear coefficient of AA6061 aluminium alloy, 0.5NC, 1NC, 1.5NC, and 2NC nanocomposites as a function of (a) applied normal load, (b) material, (c) sliding distance, and (d) sliding velocity	119
6.5	Coefficient of friction of AA6061 aluminium alloy, 0.5NC, 1NC, 1.5NC and 2NC nanocomposites (a) applied normal load, (b) sliding velocity, and (c) sliding distance	121
6.6	Coefficient of friction of AA6061 aluminium alloy based materials at 20N normal loads, 2 m/s sliding distance and 1000 m sliding distance (a) time and (b) materials	122
6.7	SEM images of worn surfaces of different materials at 5 N applied normal load, 0.5 m/s sliding velocity, and 1000 m sliding distance (a) AA6061 aluminium alloy, (b) 0.5NC, (c) 1NC, (d) 1.5NC and (e) 2NC	123
6.8	SEM images of worn surfaces of different materials at 5 N applied normal load, 2 m/s sliding velocity, and 1000 m sliding distance (a) AA6061 aluminium alloy (b) 0.5NC, (c) 1NC, (d) 1.5NC and (e) 2NC	124
6.9	SEM images of worn surfaces of different materials at 20 N applied normal load, 0.5 m/s sliding velocity, and 1000 m sliding distance (a) AA6061 aluminium alloy (b) 0.5NC, (c) 1NC, (d) 1.5NC and (e) 2NC	125
6.10	SEM images of worn surfaces at 20 N applied normal load, 2 m/s sliding velocity and 3000 m sliding distance (a) AA6061 aluminium alloy, (b) 0.5NC, (c) 1NC, (d) 1.5NC and (e) 2NC	126
6.11	EDX of wear surfaces of AA6061/SiCp nanocomposites at applied normal loads 20 N at 2 m/s sliding speed (a) 0.5NC, (b) 1NC, (c) 1.5NC, and (d) 2NC	129
6.12	Schematic view of wear generation model including wear debris of AA6061 aluminium alloy and 2NC nanocomposite	130
6.13	Wear mechanisms of the nanocomposites are drawn at various conditions and with approximate boundaries in the present study	131
6.14	Wear rate of AA6061 aluminium alloy, nanocomposite, and hybrid	135

	nanocomposites as a function of applied normal load (a) V_{LD_L} condition and (b) V_{HD_H} condition	
6.15	Volumetric wear rate of AA6061 aluminium alloy, 2NC nanocomposite, 0.5HNC, 1HNC, 1.5HNC, 2HNC, and 3HNC hybrid nanocomposites (a) $L_L V_L$ condition and (b) $L_H V_H$ condition	137
6.16	Volumetric wear rate of AA6061 aluminium alloy, 2NC nanocomposite, 0.5HNC, 1HNC, 1.5HNC, 2HNC, and 3HNC hybrid nanocomposites (a) L_LD_L condition and (b) $L_H D_H$ condition	139
6.17	Wear coefficient of AA6061 aluminium alloy, 2NC nanocomposite and 2HNC hybrid nanocomposite as a function of (a) applied normal load (b) materials (c) sliding distance and (d) sliding velocity	141
6.18	Friction coefficient (FC) values of Al6061 alloy based composite materials (a) FC verses load at V_{LD_L} , (b) FC verses load at V_{HD_H} , (c) FC verses sliding velocity at L_LD_L , (d) FC verses sliding velocity at $L_H D_H$, (e) FC verses sliding distance at V_{LL} , and (f) FC verses sliding distance at V_{HL}	144
6.19	Friction coefficient of AA6061 aluminium alloy based materials (a) $L_LD_L V_L$ condition, and (b) $L_H D_H V_H$ condition	145
6.20	SEM micrographs of worn surfaces at $L_LD_L V_L$ condition (a) AA6061 aluminium alloy, (b) 2NC, (c) 0.5HNC, (d) 1HNC, (e) 1.5HNC, (f) 2HNC, and (g) 3HNC	147
6.21	SEM images of worn surfaces at $L_H D_H V_H$ condition (a) AA6061 aluminium alloy, (b) 2NC, (c) 0.5HNC, (d) 1HNC, (e) 1.5HNC, (f) 2HNC, and (g) 3HNC	148
6.22	SEM images of worn surfaces at $L_H D_L V_L$ condition (a) AA6061 aluminium alloy, (b) 2NC, (c) 0.5HNC, (d) 1HNC, (e) 1.5HNC, (f) 2HNC, and (g) 3HNC	149
6.23	SEM images of worn surfaces at $L_H D_H V_H$ condition (a) AA6061 aluminium alloy, (b) 2NC, (c) 0.5HNC, (d) 1HNC, (e) 1.5HNC, (f) 2HNC, and (g) 3HNC	150
6.24	EDAX analysis of 2HNC hybrid nanocomposite worn surface at $L_LD_L V_L$	153
6.25	EDAX analysis of 2HNC hybrid nanocomposite worn surface at $L_H D_H V_H$	154
6.26	Schematic view of wear generation model including wear debris of AA6061 aluminium alloy, 2NC nanocomposite and 2HNC hybrid nanocomposite	156
6.27	EDAX analysis of wear debris of 2HNC hybrid nanocomposite	156
6.28	Wear mechanism of the 2HNC hybrid nanocomposite is drawn at various conditions and with approximate boundaries in the present	157

	study	
6.29	Wear rate of AA6061 aluminium alloy, 2NC nanocomposite and 2HNC hybrid nanocomposite as a function of applied normal load (a) 60 m, (b) 120 m, and (c) 180 m	159
6.30	Wear rate of AA6061 aluminium alloy, 2NC nanocomposite and 2HNC hybrid nanocomposite as a function of grit size (a) 5 N, (b) 10 N, (c) 15 N, and (d) 20 N	162
6.31	Wear rate of AA6061 aluminium alloy, 2NC nanocomposite and 2HNC hybrid nanocomposite as a function of abrasive grit size (a) 5 N, (b) 10 N, (c) 15 N, and (d) 20 N	165
6.32	Wear rate of AA6061 aluminium alloy, 2NC nanocomposite and 2HNC hybrid nanocomposite as a function of sliding velocity (a) 5 N, (b) 10 N, (c) 15 N, and (d) 20 N	169
6.33	Wear coefficient of AA6061 aluminium alloy, 2NC nanocomposite and 2HNC hybrid nanocomposite as a function of (a) applied normal load, (b) abrasive grit size, (c) sliding distance and (d) sliding velocity	173
6.34	Worn surface of pin materials tested on abrasive grit papers at 5 N applied normal load (a) AA6061 alloy at grit size of 50 μm , (b) AA6061 alloy at grit size of 100 μm , (c) AA6061 alloy at grit size of 150 μm , (d) 2NC at grit size of 50 μm , (e) 2NC at grit size of 100 μm , (f) 2NC at grit size of 150 μm , (g) 2HNC at grit size of 50 μm , (h) 2HNC at grit size of 100 μm , and (i) 2HNC at grit size of 150 μm	175
6.35	Worn surface of pin materials tested on abrasive grit papers at 20 N applied normal load (a) AA6061 alloy at grit size of 50 μm , (b) AA6061 alloy at grit size of 100 μm , (c) AA6061 alloy at grit size of 150 μm , (d) 2NC at grit size of 50 μm , (e) 2NC at grit size of 100 μm , (f) 2NC at grit size of 150 μm , (g) 2HNC at grit size of 50 μm , (h) 2HNC at grit size of 100 μm , and (i) 2HNC at grit size of 150 μm	176
6.36	Worn surface of abrasive grit papers tested at 5 N applied normal load. AA6061 alloy tested on (a) 50 μm size grit paper, (b) 100 μm size grit paper, and (c) 150 μm size grit paper. 2NC nanocomposite tested on (d) 50 μm size grit paper, (e) 100 μm size grit paper, and (f) 150 μm size grit paper. 2HNC hybrid nanocomposite tested on (g) 50 μm size grit paper, (h) 100 μm size grit paper, and (i) 150 μm size grit paper	179
6.37	Worn surface of abrasive grit papers tested at 20 N applied normal load. AA6061 alloy tested on (a) 50 μm size grit paper, (b) 100 μm size grit paper, and (c) 150 μm size grit paper. 2NC nanocomposite tested on (d) 50 μm size grit paper, (e) 100 μm size grit paper, and (f) 150 μm size grit paper. 2HNC hybrid nanocomposite tested on (g) 50 μm size grit paper, (h) 100 μm size grit paper, and (i) 150 μm	180

	size grit paper	
6.38	SEM micrographs of various wear debris collected after abrasion process. AA6061 alloy tested at 5 N (a) 50 μm size grit paper, (b) 100 μm size grit paper, and (c) 150 μm size grit paper. 2NC nanocomposite tested at 5 N (d) 50 μm size grit paper, (e) 100 μm size grit paper, and (f) 150 μm size grit paper. 2HNC hybrid nanocomposite tested at 5 N (g) 50 μm size grit paper, (h) 100 μm size grit paper, and (i) 150 μm size grit paper	182
6.39	SEM micrographs of various wear debris collected after abrasion process. AA6061 alloy tested at 20 N (a) 50 μm size grit paper, (b) 100 μm size grit paper, and (c) 150 μm size grit paper. 2NC nanocomposite tested at 20 N (d) 50 μm size grit paper, (e) 100 μm size grit paper, and (f) 150 μm size grit paper. 2HNC hybrid nanocomposite tested at 20 N (g) 50 μm size grit paper, (h) 100 μm size grit paper, and (i) 150 μm size grit paper	183
6.40	Coefficient of friction of AA6061 aluminium alloy, 2NC nanocomposite and 2HNC hybrid nanocomposite tested abrasive grit paper (a) applied normal load, (b) abrasive grit size, (c) sliding velocity and (d) sliding distance	185
6.41	Coefficient of friction of AA6061 aluminium alloy, 2NC nanocomposite and 2HNC hybrid nanocomposite tested abrasive grit papers of sizes 150 μm , 100 μm , and 50 μm as a function of sliding duration	186
6.42	Two body abrasive wear mechanism of the 2HNC hybrid nanocomposite is drawn at various conditions and with approximate boundaries in the present study	187
6.43	The mechanism of abrasive grit particle removal on 150 μm abrasive grit paper is drawn at various conditions and with approximate boundaries in the present study tested on 2HNC hybrid nanocomposites	187

LIST OF ABBREVIATIONS AND SYMBOLS

<i>Symbol</i>		<i>Description</i>
%	:	Percentage
wt. %	:	weight percent
μ	:	Microns
μm	:	micrometers
$^{\circ}\text{C}$:	Degrees centigrade
ρ	:	Density
Δv	:	Volume loss
Δw	:	Weight loss
<	:	Less than
>	:	Greater than
\pm	:	Plus or minus
=	:	Equals to
+	:	Plus/added to
-	:	Minus
\times	:	Multiplication / multiplied to
/	:	Division/divided by
&	:	And
\emptyset	:	diameter
2D	:	Two dimensional
3D	:	Three dimensional
A_{probe}	:	Cross sectional area of the probe
ASTM	:	American Society for Testing Materials
Al	:	Aluminium
AA	:	Aluminium Association
Al_2O_3	:	Aluminium oxide
MMC	:	Metal Matrix Composite
CMC	:	Ceramic Matrix Composite
PMC	:	Polymer Matrix Composite

AA-MMNC	:	Aluminium Metal Matrix Nanocomposite
AA-HMNC	:	Aluminium Hybrid Metal Matrix Nanocomposite
MMNC	:	Metal Matrix Nanocomposite
HMNC	:	Hybrid Metal Matrix Nanocomposite
YS	:	Yield Strength
UTS	:	Ultimate Tensile Strength
XRD	:	X Ray Diffraction
COF	:	Coefficient of Friction
mm	:	Millimeters
cm	:	Centimetres
m	:	Meters
km	:	Kilometer
N	:	Newton
MPa	:	Mega Pascal
s	:	Second
L	:	Load
SD	:	Sliding Distance
SV	:	Sliding Velocity
Si	:	Silicon
SiC	:	Silicon Carbide
SiCp	:	Silicon Carbide Particulate
SiCw	:	Silicon Carbide Whisker
Ti	:	Titanium
TiC	:	Titanium Carbide
Vol.	:	Volume
Vs	:	Versus
Mg	:	Magnesium
SS	:	Stainless Steel
K	:	Wear Coefficient of the Material
H ₂ O	:	Water
CH ₂ O	:	methanol

HCl	:	Hydrochloric Acid
HF	:	Hydrofluoric Acid
HNO ₃	:	Nitric Acid
HV	:	Vickers Hardness
Ltd.	:	Limited
F	:	Force
F.C.C	:	Face Centred Cubic
Fe	:	Iron
g	:	Grams
GPa	:	Giga Pascal
Gr	:	Graphite
Cr	:	Chromium
Cu	:	Copper
C	:	Carbon
B ₄ C	:	Boron Carbide
cc	:	Cubic centimetre
Mn	:	Manganese
Li	:	Lithium
Ta	:	Tantalum
Mo	:	Molybdenum
Zn	:	Zinc
Ni	:	Nickel
Zr	:	Zirconium
T4	:	T4 Heat Treated
T6	:	T6 Heat Treated
CNT	:	Carbon Nanotubes
TiO ₂	:	Titanium Dioxide
WC	:	Tungsten Carbide
WO ₃	:	Tungsten trioxide
BN	:	Boron nitride
O	:	Oxygen

Si_3N_4	:	Silicon Nitride
TiB_2	:	Titanium Diboride
SiO_2	:	Silica
AlN	:	Aluminium Nitride
TiC	:	Titanium Carbide
ARB	:	Accumulative Roll Bonding
I	:	Ultrasonic Intensity
f	:	Frequency
c	:	Speed of sound
A_u	:	Amplitude
P_e	:	Ultrasound Pressure
P	:	Output Power
C_m	:	Speed of Ultrasound
ρ_m	:	Density of molten metal
Al/SiCp	:	Aluminium reinforced with silicon carbide
Al/SiCp/Gr	:	Aluminium reinforced with silicon carbide and graphite
β	:	Constant equal to 1.25
b_m	:	Burgers vector of matrix
G_m	:	Shear modulus
ρ^{CTE}	:	Dislocation density
α_m	:	Thermal expansion coefficient of matrix
α_p	:	Thermal expansion coefficient of particle
d_p	:	Size of reinforcement particles
d_c	:	Average grain size of composite
d_m	:	Average grain size of matrix
n	:	Empirical constant
P	:	Porosity percent
$d_{\text{grain size}}$:	Average grain size
k	:	Hall-Petch equation slope
V_f	:	Volume fraction of reinforcement particles

A	:	Constant is (equal to 12)
ΔT	:	Temperature change from stress free homologous to room temperature
$\Delta\sigma$:	Enhancement of yield strength
σ_{ync}	:	Yield strength of the nanocomposite
σ_m	:	Yield strength of the matrix
τ	:	Average inter-particle spacing
α	:	Proportional constant
f_p	:	Degradation factor
M	:	Mass of specimen
NC	:	Nanocomposite
HNC	:	Hybrid Nanocomposite
V	:	Volume of specimen
M	:	mass
v	:	Volume fraction
θ	:	Scattering angle
d_{hkl}	:	Distance between planes
t	:	Positive integer
λ	:	wavelength
SEM	:	Scanning Electron Microscopy
TEM	:	Transmission Electron Microscopy
UTM	:	Universal testing machine
H	:	Hardness
W_l	:	Volumetric wear rate
EN31	:	Excellent high carbon steel
SAD	:	Selected Area Diffraction
f	:	contribution factor
K	:	Dimensionless wear coefficient
L_L	:	Lower load
L_H	:	Higher load
D_L	:	Lower sliding distance

D _H	:	Higher sliding distance
V _L	:	Lower sliding distance
V _H	:	Higher sliding distance
GR	:	Grooves
G	:	Graphite thin film
D	:	Delaminating layer
EDX	:	Energy dispersive X-ray
B	:	Adhesive wear mechanism
A	:	Abrasive wear mechanism
F	:	Abrasive grit paper fractured
BG	:	blunting
DR	:	debris
P	:	Particle pickup
JCPDS	:	Joint Committee on Powder Diffraction Standards
PF	:	Abrasive grit paper fracture
CR	:	Chips removal
GF	:	Abrasive grit particle fracture
LS	:	Longer scratches
SS	:	Smaller scratches
CS	:	Circular scratches
SA	:	Severe abrasive wear mechanism
$Q_{v/l}$:	Volume loss per unit sliding distance
rpm	:	rotations per minute
GNF	:	Graphite nanofiber
Vol. %	:	volume fraction percent

Chapter 1

Introduction

1.1 Introduction

Worldwide there is an increase of demand for light weight and high strength materials to minimize the greenhouse emissions by reducing the total weight of the elements in the assembly unit. In this regard, researchers are investigating new materials such as Nanomaterials, Nanocomposites, and Hybrid nanocomposites. The hybrid metal matrix nanocomposite materials are using rather than base alloys, and its composites. The hybrid metal matrix nanocomposites are better due to its extreme properties such as high strength to weight ratio, low density, excellent wear resistance, and high corrosion resistance. The demand is increasing day by day for the hybrid metal matrix nanocomposites in automobile sectors, aircrafts, aerospace, marine, building structures, and sporting goods. Aluminium-based hybrid metal matrix nanocomposites are developed mostly for performance optimization by considering low production cost in different applications because these are easier to fabricate than titanium and magnesium.

1.2 Aluminium

Aluminium is the third most abundant element in the Earth's crust after oxygen and silicon. Aluminium is represented with symbol Al. Aluminium atomic number is 13, atomic weight is 27 and belongs to XIII group elements in the periodic table. Aluminium crystal system is face centred cubic structure (FCC). It is extracted from bauxite ore.

It is silvery white in colour, nonmagnetic, and ductile material. The density of the commercially available pure aluminium is 2.7 g/cc and the melting point is 660C. It is pure soft metal with yield strength of 15 MPa and ultimate tensile strength of 90 MPa. Yield strength of aluminium alloys vary in between 100 MPa to 600 MPa. It has high corrosion resistance due to the formation of thin oxide layer on the surface. It has high thermal conductivity and good electrical properties. It has many applications such as foils in the packaging industry, leak proof drink containers, and for electrical purposes as they are highly conductive.

1.3 Aluminium Alloys

Aluminium based alloys are mostly used materials in various industrial applications. The major alloying elements are copper (Cu), silicon (Si), magnesium (Mg), manganese (Mn), lithium (Li), zinc (Zn), iron (Fe) etc. Some other elements such as titanium (Ti), tantalum (Ta), molybdenum (Mo), chromium (Cr), nickel (Ni), vanadium (V), and zirconium (Zr) are added in minor quantity for grain refinement. They can be classified into two categories i.e., casting alloys and wrought alloys.

1.3.1 Casting Aluminium Alloys

The casting aluminium alloys are developed by the Aluminum Association (AA) of United States of America. Each casting alloy is designated by four digit number with a decimal point separating the 3rd and 4th digits. The various casting aluminium alloys are listed in the Table 1.1.

Table 1.1: List of casting aluminium alloys

Alloy Composition	Alloy Designation
Pure Al (99.0% minimum) with impurities	1xx.x
Al-(4% to 4.6%) Cu	2xx.x
Al-(5% to 17%) Si, with addition of Cu and/ or Mg	3xx.x
Al-(5% to 12%) Si	4xx.x
Al-(4% to 10%) Mg	5xx.x
Al-(6.2% to 7.5%) Zn	7xx.x
Al-Sn	8xx.x
Al with addition of other elements	9xx.x

1.3.2 Wrought Aluminium Alloys

The major alloying elements like copper (Cu), silicon (Si), zinc (Zn), iron (Fe), lithium (Li) magnesium (Mg) and manganese (Mn) can be added to the pure aluminium to improve the mechanical, tribological, thermal and electrical properties etc. The aluminium wrought alloys are designated based on major alloying elements and is presented in Table 1.2. The nomenclature line diagram is shown in figure. 1.1 [1]. The 1st digit represents the alloy group. The 2nd digit represents the modifications to alloy or impurity limit. The last two digits specify the aluminium alloy or indicates the aluminium purity.

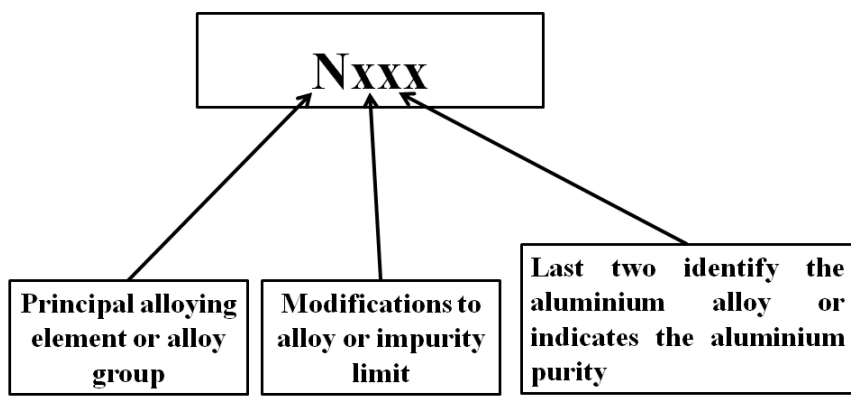


Figure 1.1: The nomenclature line diagram of wrought aluminium alloys

Table 1.2: Wrought aluminium alloy designation system

Major alloying elements	Designation	Nomenclature
99% Al with minimum impurities	1xxx	Al
Cu	2xxx	Al-(2% to 6%) Cu
Mn	3xxx	Al-(1% to 1.2%) Mn
Si	4xxx	Al-(1% to 6%) Si
Mg	5xxx	Al-(0.5% to 5%) Mg
Mg and Si	6xxx	Al-(0.5% to 1.2%) Mg-(0.4% to 1.4%) Si
Zn	7xxx	Al-(1% to 9%) Zn
Fe or Li	8xxx	Al-(0.7% to 8.6%) Fe, Al-(2.45%) Li

1.4 Applications of Aluminium Alloys

The aluminium alloys have excellent properties that made them to use in different applications such as automobile industry, food preparation, packaging, architecture, electrical transmission elements, energy generation, marine industry, defence structures, ladders, high pressure gas cylinders, road barriers, furniture, lithographic printing plates, sports, radiators and engine blocks. The various applications of aluminium alloys are presented in figure 1.2 [2-6].



Figure 1.2: (a) electrical conductors, (b) wheel rim, (c) garden frame, (d) radiators, (e) engine blocks, (f) hub caps, (g) oxygen gas cylinder, (h) bicycle frame, and (i) tweeter speaker

1.5 Metal Matrix Composites (MMCs)

The composite materials can be categorized into various types based on the type of matrix or type of reinforcements. Major portion of metal based matrix composites are known as metal matrix composites (MMCs), higher volume fraction of ceramic based matrix composites are ceramic matrix composites (CMCs) and higher fraction of polymer based matrix composites are polymer matrix composites (PMCs). In case of metal matrix composites the metallic elements and its alloys are used as a matrix and the chemically stable or non reactive ceramic elements are used as reinforcements. The light metals which has high corrosion resistance and creep resistance are mostly useful as matrix for the fabrication of MMCs. The pure metals and its alloys such as Al, Mg, and Ti are the matrix materials used in various structural and defence applications since last two decades.

Table 1.3: The various treatments of AA6061 aluminium alloy

Name of the Process	Treatment Conditions
Annealing	413 °C for 2 to 3 hours, cooling at 10 °C to 260 °C per hour and air cooling
Cold Working	O, T4, and T6 temper condition
Hot Working	260 °C to 372 °C
Forging	233 °C to 483 °C
Welding	Excellent weldability characteristics For thinner sections gas tungsten arc welding Thick sections gas metal arc welding For good properties 4043 alloy filler wire can be used
Forming	Formed and worked in the annealed condition Easily can be perform stamping, bending, spinning, and deep drawing
Machinability	Good machinability in T4 and T6 temper condition and also can be machined in annealed temper
Heat Treatment	533 °C for 1 hour followed by quenching in water 160 °C for 18 hours in air cooling 177 °C for 8 hours in air cooling

Incorporation of hard ceramic particles to the metal matrix can enhance the strength properties of the MMCs. AA6061 aluminium alloy has received considerable attention for last three decades due to its major advantages such as heat-treatable, good weldability, brazability,

solderability, workability and machinability. The various treatments are shown in Table 1.3. Fabrication and heat treatment of AA6061 aluminium alloy after casting process is to be done for better properties. It is used in marine fittings, bicycle frames, camera lenses, drive shafts, electrical fittings, electrical connectors, rail coaches, brake components, valves, truck frames, ship building, couplings, tubes, structural elements in tower applications and motor boats.

1.6 Reinforcements

The second phase reinforcing elements in the matrix such as silicon carbide (SiCp), alumina (Al_2O_3), boron carbide (B₄C), carbon nanotubes (CNTs), graphite, titanium dioxide (TiO_2), tungsten carbide (WC), silicon nitride (Si_3N_4), titanium diboride (TiB₂), silica (SiO₂), aluminium nitride (AlN) and titanium carbide (TiC) of micron and nano-sized particles are considered to improve the properties of the matrix materials. Among all the ceramic reinforcement particles, the silicon carbide has good wear resistance, corrosive resistance, high strength, superior chemical inertness, high stiffness, higher hardness, high melting point and is economic [6]. The motive of hard ceramic reinforcement in the MMCs is to improve the corrosion resistance, yield and ultimate tensile strength, stiffness, tribological properties, and to moderate the temperature resistance.

1.7 Aluminium Metal Matrix Nanocomposites (AA-MMNCs)

It is evident from the literature that large sized ceramic particle reinforced composites exhibited less strength, fracture toughness, and lower ductility. However, the properties of the composites depend on the size, type of reinforcement particles, and fabrication process. Researchers have reported that strength, wear resistance, stiffness, thermal resistance, and damping capacity of aluminium metal matrix nanocomposites (AA-MMNCs) were improved without affecting the ductility when the size of the reinforcement is at nano-scale. There are different production processes to synthesize ceramic particulate reinforced aluminium metal matrix nanocomposites (AA-MMNCs). These methods are classified into three categories liquid state methods, solid-state methods, and vapour deposition. Researchers fabricated aluminium based metal matrix nanocomposites using different methods such as powder metallurgy, mechanical milling and friction stir welding, accumulative roll bonding (ARB), spark plasma sintering, stir casting, squeeze casting, and ultrasonic dispersion process. In the

literature, significant work has been carried out using stir casting method and powder metallurgy technique.

1.7.1 Fabrication Techniques

1.7.1.1 Stir Casting

The stir casting technique is implemented in the year 1968 for fabrication of MMCs [7]. Stir casting process is a liquid state technique used for fabrication of composite materials, in which the reinforcement particles are mixed with a molten metal matrix by means of mechanical stirring. Then the liquid composite material is cast by conventional casting methods and metal forming techniques. Ray et al. [7] produced Al/Al₂O₃ nanocomposites through stir casting method and proved that the maximum upto vol. % ≤ 30 of hard particles can be reinforced in the molten slurry. The mechanical properties of the MMCs depend on the processing temperature, stirring speed, stirrer blade angles and stirring time. The line diagram of stir casting setup is shown in figure 1.3. It is a mass production process with low fabrication cost and used to produce complex shapes. Major disadvantage of this process is low wettability between the matrix material and reinforcements, non-uniform dispersion of reinforcements in the matrix, chance of formation of clusters, and porosity.

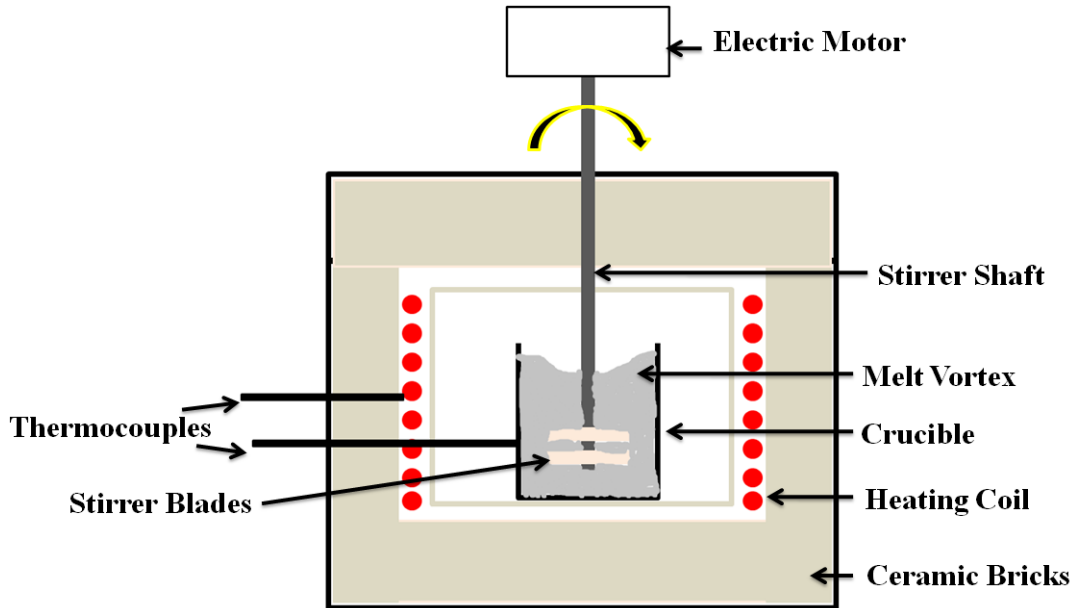


Figure 1.3: Stir casting design setup

1.7.1.2 Powder Metallurgy Technique

Powder metallurgy is a material processing technique in which particulate materials are consolidated to semi finished and finished products. The schematic view of powder metallurgy process is shown in figure 1.4 [8]. Powder metallurgy technique is introduced to overcome formation of clusters, grain boundary strengthening, and wettability during processing of metal matrix nanocomposites. The stages in this technique are mixing, blending, and degassing the solidified product in a vacuum and hot isostatic pressing. The process temperature is lower than other techniques and inter phase kinetics can be controlled through powder metallurgy route. Powder metallurgy technique shows near net shape and uniform dispersion of nano-reinforcement particles in aluminium matrix. Powder metallurgy route is suitable for parts that are required to be manufactured from a single or multiple materials in powder form and minimizes the machining, scrap losses are suitable for high volume production of components.

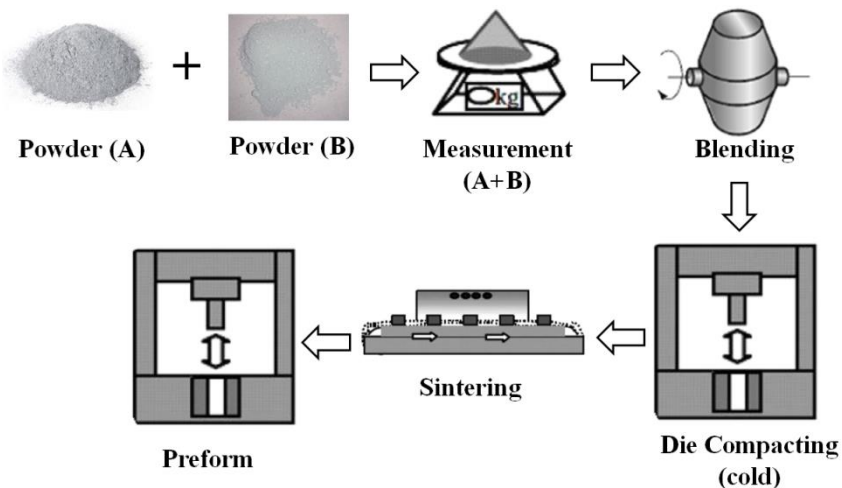


Figure 1.4: Schematic diagram of powder metallurgy process

1.7.1.3 Mechanical Milling

Mechanical milling is a powder processing techniques which involve deformation, breaking the powder particles and welding several times. The schematic view of mechanical ball milling is shown in figure 1.5 [9]. In this method, the powder particles are trapped between the colliding balls and an inner surface of the vial. It is used to synthesize composites by introducing ceramic reinforcements into metal alloys. It increases the strength, wear resistance, creep resistance, and microhardness of the composites. Mechanical alloying is

extensively employed to obtain extended solid solutions, amorphous structures, nanocrystalline solids, metastable phases, and immiscible components. Sintering temperature is reduced because of the introduction of bulk and surface energies to powder particles during the milling process. Mechanical alloying process is not suitable for mass production and maintenance is difficult. It is time taking process to obtain required properties of composites.

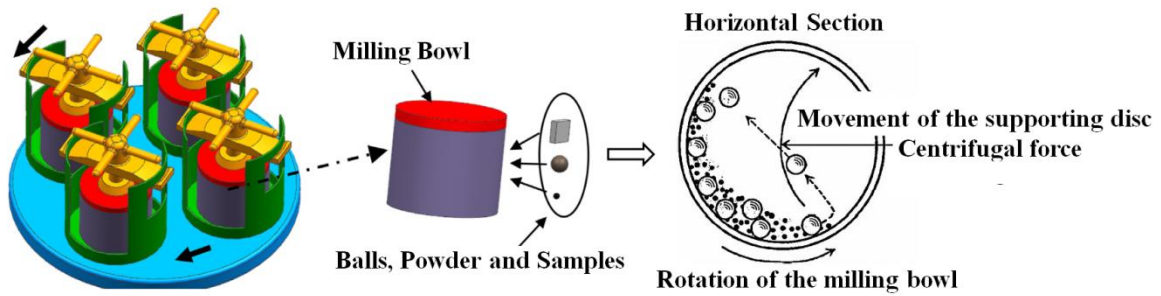


Figure 1.5: Schematic diagram of mechanical ball milling

1.7.1.4 Friction Stir Processing

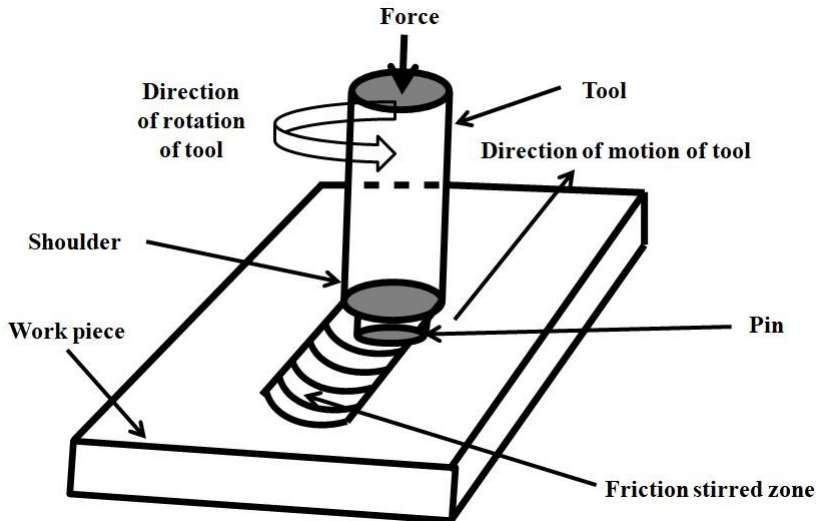


Figure 1.6: Line diagram of friction stir process

Friction stir processing is a solid-state technique. It develops the significant grain refinement, homogeneous particles distribution, and plastic deformation of the base material under stirring of a tool. This technique is familiar and used for the surface modification of a base material. The material surface properties can be easily changed by introducing the ceramic particles, metal oxides, intermetallics, and compounds. The line diagram of friction stir process is shown in figure 1.6. Friction stir processing technique is only useful in

improving the strength of the surface and joints. The properties of the surface of the composites depend on speed of the pin, force on the tool, and geometry of the pin. This process provides higher hardness on the surface and improved creep resistance.

1.7.1.5 Accumulative roll bonding (ARB)

Accumulative roll bonding (ARB) is a mechanical processing technique which is used to improve mechanical properties of the matrix material. The ARB schematic illustration is shown in figure 1.7 [10]. Reduced porosity, uniform particle distribution, and improvement in bond strength between reinforcement particles and the base aluminium matrix are the benefits of this technique. The increase of number of ARB cycles increases the uniform particle distribution and bond strength of matrix and reinforcements.

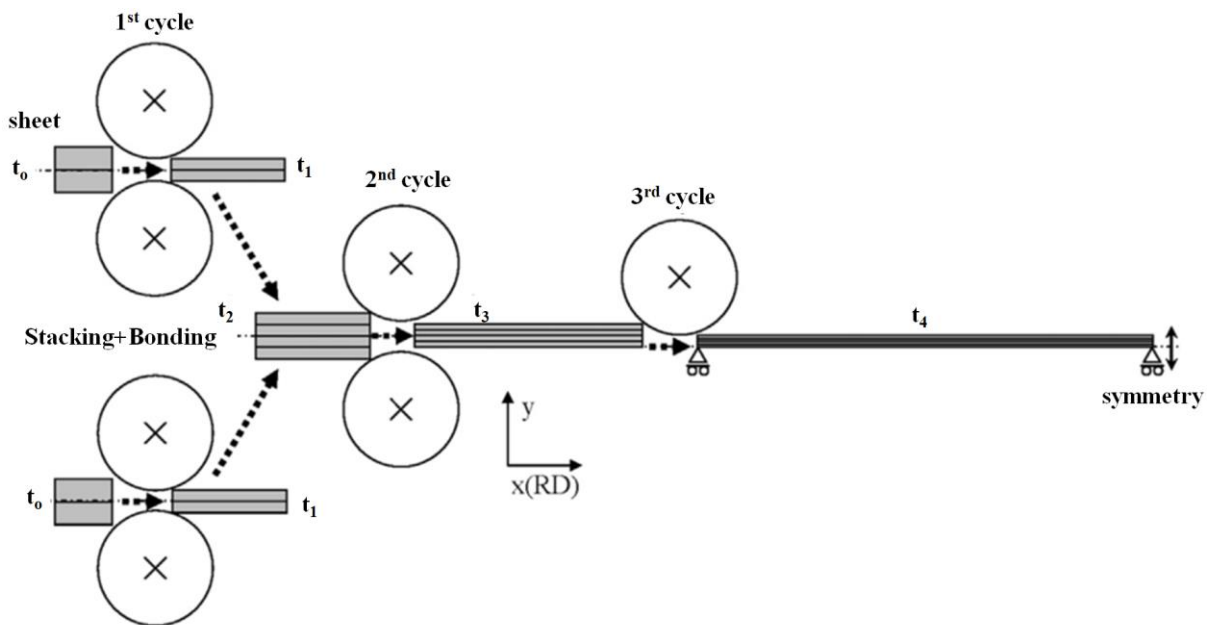


Figure 1.7: Schematic illustration of ARB process with three cycles

1.7.1.6 Spark Plasma Sintering

Spark plasma sintering is a high speed powder consolidation sintering process capable of processing conductive and non conductive materials. The basic theory of spark plasma sintering process is based on the electrical spark discharge phenomenon where low voltage pulse current momentarily generates spark plasma in fine local areas between the particles at high energy. Spark plasma sintering is a new method in which the sintering completes in few minutes. Illustration of spark plasma sintering process is shown in figure 1.8 [11]. In this

process, high sintering rates are possible due to internal heating of the sample. The higher densification occurs at lower sintering temperature and which minimizes the temperature by 250 °C as compared to conventional sintering and material processing time becomes 5 to 25 min. The relatively low temperatures combined with fast processing times ensure tight control over grain growth and microstructure. No coarsening and grain refinement were allowed to occur in spark plasma sintering process and high relative densities can be reached in very short period of time. The considerable grain growth cannot be reached by conventional sintering process. Nano-sized powder can be easily sintered without considering grain growth through spark plasma sintering compared to the conventional sintering process. The nanocomposites produced by spark plasma sintering exhibits good mechanical properties.

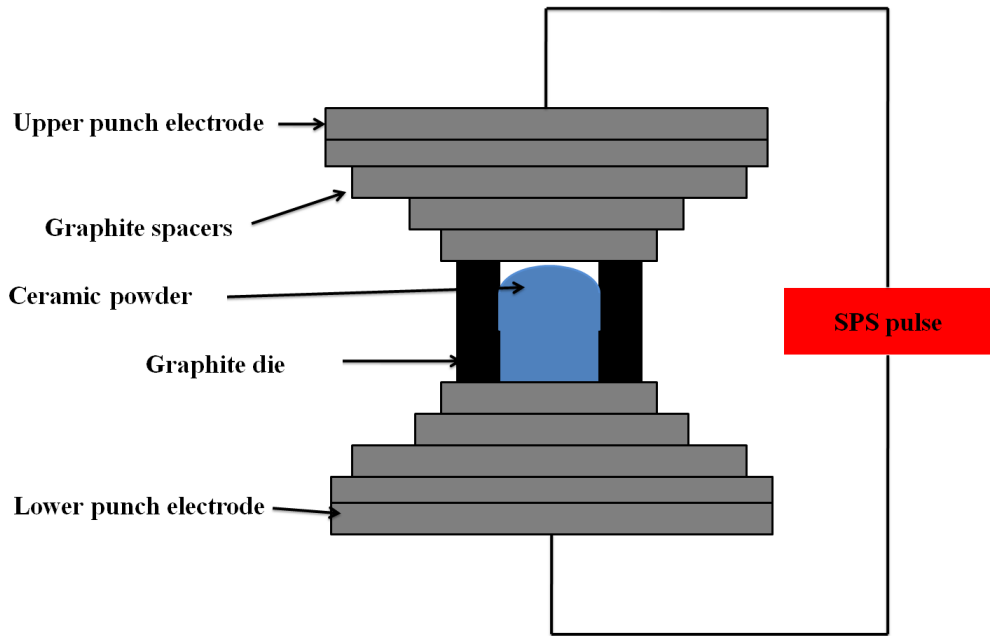


Figure 1.8: Illustration spark plasma sintering process [11]

1.7.1.7 Compo Casting

Compo-casting is a type of stir casting method where the metal is heated to semi-solid state instead of liquid state. The hard reinforcement particles are incorporated in the semisolid metallic slurry using mechanical stirrer. The hard particles are mixed uniformly in the matrix with weak agglomeration. The operating process temperature is low during the process compared to the liquid state technique. The compo casting setup is shown in figure 1.9 [12]. The method exhibited good wettability to the liquid molten slurry which is an

advantage of using this process but the formation of clusters can not be controlled. In the liquid metallurgy route, the ceramic nanoparticles uniform distribution is difficult because of their high surface area, low wettability, and the chance of formation of clusters.

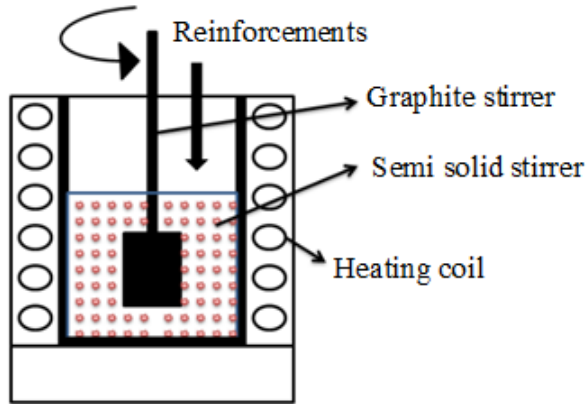


Figure 1.9: Compo casting setup [12]

1.7.1.8 Ultrasonic Assisted Stir Casting Method

For homogeneous distribution of nano-sized reinforcement particles in the matrix and good wettability with the matrix through the liquid state processing techniques, researchers have introduced the ultrasonic assisted casting method. The schematic line diagram of ultrasonically assisted stir casting setup is shown in figure 1.10 [13]. The ultrasonication process and nucleation growth is presented in figure 1.11 [14]. In this technique, the ultrasonic energy produces the nonlinear effects into the molten metal such as cavitation and acoustic streaming. In ultrasonic cavitation process, small size transient zones are created in the molten melt. These small size zones reach high pressures and temperatures with high heating and cooling rates. During this process, shock force incorporates with local high temperatures and disintegrates the clusters and cleans the surface of the nano-reinforcement particles. In the ultrasonic cavitation-assisted process, the dissolved gases can be removed, molten metal purifies, and grain size reduces and improves the wettability in between the matrix and the reinforcement particles [15].

The nano-sized reinforcement particles distribution in the metal matrix and grain refinement is depended on the ultrasonic intensity. Researchers implemented a relationship between the ultrasonic intensity and the process parameters. The relationship is as follows [16]:

$$I = \frac{\rho c (2\pi f A)^2}{2} \quad (1.1)$$

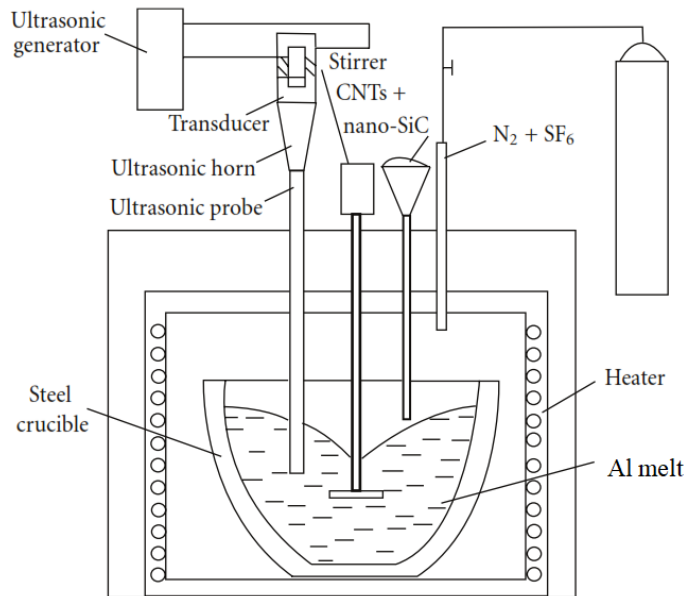


Figure 1.10: Schematic line diagram of ultrasonically assisted casting setup [13]

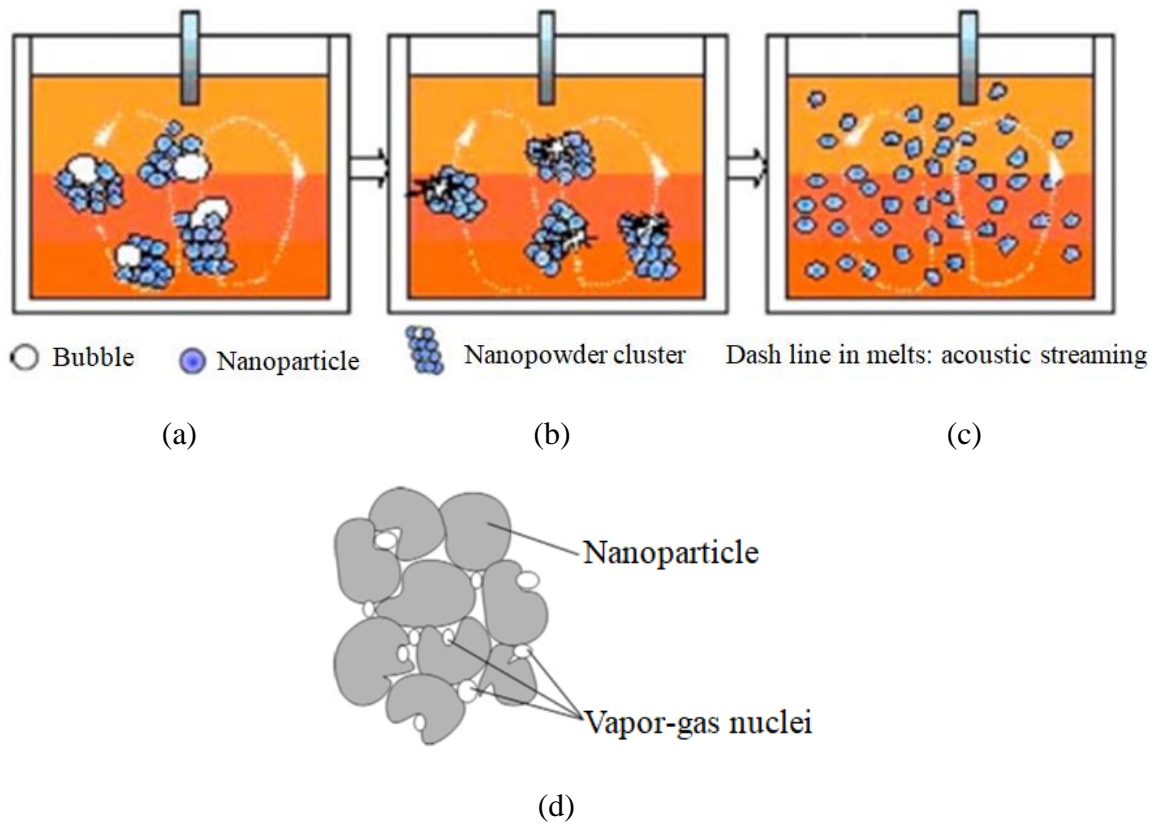


Figure 1.11: (a) Initial ultrasonication process (b) nucleation starts (c) acoustic streaming (d) schematic view of vapor gas nuclei [14]

where density of the molten metal is ρ (g/cc), 'c' is speed of sound in the molten metal (m/s), 'f' is frequency (kHz), 'A' is amplitude (μm) and 'I' is ultrasonic intensity (kW/cm^2).

The cavitation phenomenon in the molten metal leads to acoustic streaming effect which carries and distributes the wetted nano-sized reinforcement particles into the molten metal. The ultrasonic sound pressure (P_e) in the molten metal is given by the equation [16].

$$P_e = \left(\frac{2P\rho_m C_m}{A_{probe}} \right)^2 \quad (1.2)$$

where ' ρ_m ' is density of molten metal (g/cc), 'P' is output power of ultrasound generator (kW), ' C_m ' is speed of ultrasound in molten metal (m/s) and ' A_{probe} ' is area of probe (cm^2).

The value of ' P_e ' is estimated value (MPa), it should be larger than the threshold value required for ultrasonic streaming [17].

1.7.2 Advantages of AA-MMNCs

It was noticed that AA-MMNCs offered excellent properties compared to monolithic materials such as ferrous, aluminium and titanium alloys. Advantages of AA-MMNCs were observed when compared to unreinforced matrix material:

- High strength to weight ratio
- Improvement of stiffness and damping capacity
- Enhancement of wear and abrasion resistance properties
- Controlled thermal expansion coefficient
- Good heat or thermal management properties
- Better performance of electrical applications
- Mass control (in reciprocatory motion applications)
- Controlled ductility

The above mentioned properties and their enhancements depend on the type of reinforcing particles, size of reinforcement particles, volume or weight fraction of reinforcement particles, interaction with the matrix material, fabrication process, and heat or surface treatments if any. The property of an element can be tailored based on the nature of working condition and its application.

1.7.3 Applications of AA-MMNCs

Last two decades, AA-MMNCs have been utilized for structural and functional applications in aerospace, automobile, defense and also in sports and recreation. In the automobile sector such as Honda, Chysler, Nissan, Toyota and General motors, etc used SiCp, Gr and Al_2O_3 reinforced aluminium nanocomposites as shown in Table 1.4. In the automotive sector, the aluminium based nanocomposites elements have been used like pistons, pulleys, bearing surfaces, cv joints, cam shafts, tappets, rockers, brake components, suspension elements, engine blocks, cylinder liners, gears and valves, etc [2-9].

Table 1.4: Aluminium based nanocomposites used in automobile sector [2-9]

Composite	Company	Applications
Al/SiCp	Toyota, Martin Marietta, Zollner, Lanxide	Pistons
Al/SiCp/Gr	UWM (University of Wisconsin Milwaukee), Associated Engineering, Inc,	
Al/SiCp	Toyota,	Piston rings
Al/SiCp	Lotus Elise, Chrysler Prowler, General Motors EV1, Volkswagen Lupo 3L, Toyota RAV4-EV	Disc brakes and brake calipers
Al/SiCp/Gr	UWM	
Al/SiCp	GKN, Duralcan	Propeller shaft
Al/SiCp	General Motors	Drive shaft, rear brake, drum for EV1, engine cradle
Al/SiCp	Alcoa Innometalx	Multichip electronic module
Al/SiCp	Nissan	Connecting rod
Al/SiCp	Honda	Engine blocks

1.7.4 Mechanical Properties

Mechanical properties of composite materials are influenced by reinforcement phases and its particle sizes in the matrix. The metal matrix composite material properties such as

elasticity, yield strength, ultimate tensile strength, ductility and microhardness are usually part of material specifications and are obtained by tensile testing and microhardness testing.

1.7.5 Tribological Properties

Tribology is as a science and technology that deals where two surfaces are interacting in a relative motion. It is the basic concept which is considered in the design of various engineering applications in tribological systems. The tribological concept includes the investigation of the principles of lubrication, wear and friction in various applications. The concept is new, segregated science and complex phenomena. Tribology is very critical in various applications such as biomedical, wind turbines, green tribology, bearings, gears, cams, brakes, seals, clutches, wheels, micro and nanoelectromechanical systems, and space tribology where there are harsh environment conditions of outer space. In tribological systems the material loss would be a function of many conditions such as metallurgical properties, physical and chemical properties, surface roughness, surface asperity, and geometry of the elements. The importance of material and economic losses made the importance of investigations on the wear in tribological systems important.

1.7.5.1 Dry Sliding Friction

If two flat solid or liquid surfaces are placed in contact with each other and then one of the surfaces is moved relative to the other, then this movement is resisted. This resistance to movement is known as friction. The line diagram of sliding friction is presented in figure 1.12.

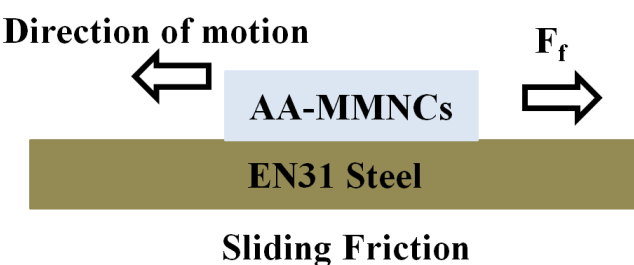


Figure 1.12: Line diagram of sliding friction

1.7.5.2 Wear

Wear is defined as the material removal from the surface or gradual removal or degradation of material over the surface of an element due to mechanical action of the two mating parts. The wear is classified based on the type of wear mechanism i.e., abrasive wear, erosive wear, adhesive wear, corrosion wear, oxidation wear, surface fatigue and fretting wear. The wear mechanisms are depended on various external factors and input parameters. Since four decades many researchers reported the wear mechanisms obtained from the metal matrix composites during dry sliding and abrasive wear test. The material removal rate is very high in case of abrasive wear due to presence of hard particles in between mating surfaces than the dry sliding wear.

Dry sliding wear and abrasive wear of AA-MMNCs was broadly studied since four decades and also special attention has been given on dry sliding wear and abrasive wear of nanoparticles reinforced AA-MMNCs. The input parameters, counter surface material, counter surface characteristics, type of matrix, weight percentage, size and type of nano-reinforcements was investigated and proven that these parameters contribute to the results in a positive or negative way based on the test conditions. The nanoparticles reinforced AA-MMNCs had revealed the better results due to the contribution of nanoparticle in isotropic manner. In case of abrasive wear mechanism, the material is removed due to the application of normal load on hard material during sliding on soft material surface. There are different modes of abrasive wear based on hard asperities in between mating parts such as two body abrasive wear and three body abrasive wear. The schematic view of abrasive wear, two body abrasive wear and three body abrasive wear mechanism is presented in figure 1.13 [2]. In adhesive wear mechanism, during dry sliding the soft material gets severe plastic deformation and induced wear debris sticking on hard surface of mating parts. In between two mating solid surfaces under high external normal load induces the frictional heat and debonding of atoms takes place. Subsequently, the debonded material detached from the soft material surface. The detaching from the soft material and sticking on to the hard material surface is known as adhesive wear mechanism. The schematic view of adhesive wear mechanism is presented in figure 1.14 [2].

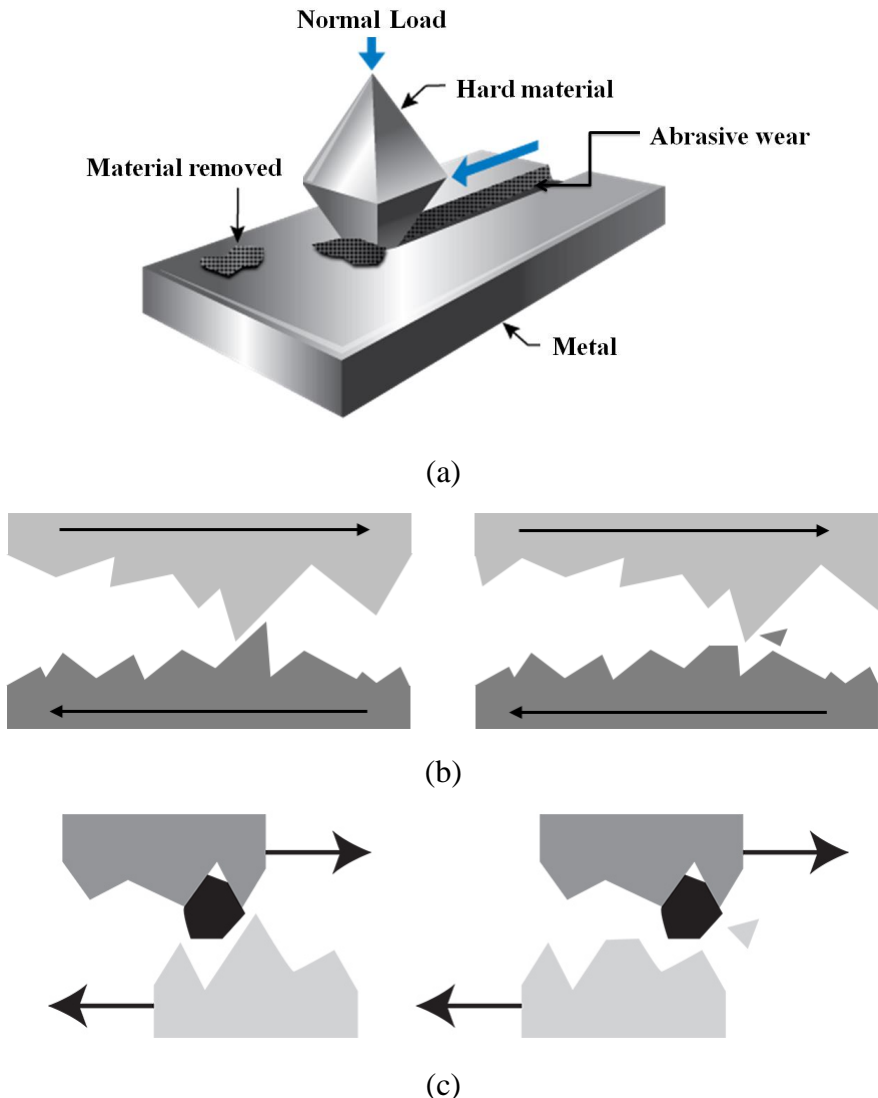


Figure 1.13: (a) schematic view of abrasive wear (b) two body abrasive wear (c) three body abrasive wear

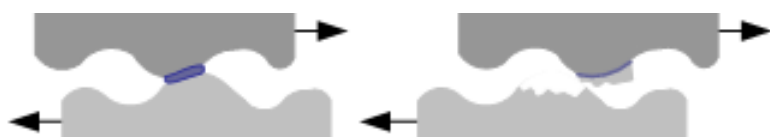


Figure 1.14: Schematic view of adhesive wear mechanism

1.8 Organization of the Thesis

CHAPTER-1: This chapter presents an introduction to pure aluminium, aluminium alloys, aluminium based composites and fabrication methods in general. In this chapter the different types of wear mechanisms are explained briefly.

CHAPTER-2: This chapter provides a comprehensive review of literature on aluminium based nanocomposites and hybrid nanocomposites. This chapter briefly outlines the research work carried out by various researchers; filtered the gaps from the literature and problem formulation was presented.

CHAPTER-3: A complete details about materials and experimental procedure used for fabrication process and testing of aluminium based nanocomposites and hybrid nanocomposites are described. The ASTM standards are used for testing properties and are also mentioned in detail.

CHAPTER-4: This chapter demonstrates the phase analysis, microstructural evaluation of nano-reinforcements, nanocomposites and emery papers.

CHAPTER-5: This chapter provides mechanical properties of AA6061/SiCp nanocomposites and AA6061/SiCp/Graphite hybrid nanocomposites. It describes predicted yield strength of AA6061/SiCp nanocomposites and AA6061/SiCp/Graphite hybrid nanocomposites using various strengthening mechanisms. Reported the predicted yield strength of nanocomposites using various yield strength prediction models and compared to experimental results. The fractography surfaces of AA6061/SiCp nanocomposites and AA6061/SiCp/Graphite hybrid nanocomposites were reported.

CHAPTER-6: This chapter reports the complete dry sliding wear behaviour of AA6061/SiCp nanocomposites and AA6061/SiCp/Graphite hybrid nanocomposites. The two body abrasive wear behaviour of AA6061 aluminium alloy, AA6061/2SiCp nanocomposite and AA6061/2 SiCp/2Graphite hybrid nanocomposite was reported. The wear rate, wear coefficients at various wear parameters, worn surface of pin, abrasive grit paper and wear debris was discussed.

CHAPTER-7: Presents summary of the results and suggestions for future work on dual nanoparticle reinforced aluminium based nanocomposites.

Chapter 2

Literature Review

2.1 Introduction

In this chapter, a brief discussion on the research work carried out on the aluminium based metal matrix nanocomposites (AA-MMNCs) is presented. The review consists of mechanical, tribological, and metallurgical properties of nanocomposites. The review also includes the strengthening mechanisms, yield strength prediction models and the influence of the single and dual phase reinforcement particles and its size on the properties. It includes the effect of single phase particles reinforced AA-MMNCs on tribological properties. The literature consist the influence of primary phase particles and secondary phase solid lubricant particles on dry sliding wear and abrasive wear characteristics of aluminium based hybrid metal matrix nanocomposites (AA-HMMNCs).

2.2 Mechanical Properties of AA-MMNCs

As per the application prudent, mechanical properties of AA-MMNCs and AA-HMMNCs have a great significance. Basically crystal structure and physical properties of the reinforcements control the mechanical properties of the nanocomposites. The properties of the nanocomposites can be tailored by varying the type of reinforcements and processing routes. Research reports also specified that the mechanical properties of nanocomposites depends on type of nano-reinforcement particles, size, shape, volume fraction of nanoparticles and fabrication process.

2.2.1 Effect of Type of Nano-Reinforcements on Yield Strength and Ultimate Tensile Strength

Researchers have been developing the composites based on the cost, availability, and properties of the reinforcement particles. Reinforcement particles in the matrix improve the strength of the composites due to its good interface bonding and its superior properties. The interface bonding plays a key role in the AA-MMNCs. The structure of ceramic particles, physical properties, and its thermal properties control the mechanical properties of the AA-MMNCs. There are different types of reinforcement particles with different properties. The ceramic reinforcements such as, silica (SiO_2) [18], titanium dioxide (TiO_2) [17], alumina (Al_2O_3) [19], titanium carbide (TiC) [20], boron carbide (B_4C) [21], graphite [22], carbon nanotubes (CNT) [23], silicon carbide (SiCp) [24], aluminium nitride (AlN) [25], silicon nitride (Si_3N_4) [26], titanium nitride (TiN) [27], boron nitride (BN) [28], titanium diboride (TiB_2) [29], tungsten trioxide (WO_3) [30], and tungsten carbide (WC) [31] are few particulates studied by various researchers, but silicon carbide was mostly used as primary reinforcement for fabrication of AA-MMNCs. Various properties of the nano ceramic reinforcements are presented in Table 2.1.

The mechanical properties of the nanocomposites were improved due to the formation of phases in matrix and uniform distribution of second phase particles in the matrix. Among them, SiCp reinforced aluminium composites hold the promise for future growth due to their tailored properties, low cost, higher strength to weight ratio, good forming characteristics, higher hardness, and mass production capability [32]. Particularly in automobile sector, the SiCp reinforced aluminium composite elements have been used like pistons, cylinder liners, connecting rod, gears, valves, pulleys, propeller shaft, engine cradle, bearing surfaces etc [2-8]. Li et al. [33] fabricated Al/SiCp nanocomposites through ultrasonic assisted stir casting technique. It is observed that the grain size of Al/SiCp nanocomposites reduced with the addition of SiCp nanoparticles. The yield strength and ultimate tensile strength improved with the addition of SiCp particles in the matrix. Yao et al. [34] synthesized AA6063/5 vol. % SiCp nanocomposites through powder metallurgy route by combining: (i) spark plasma sintering followed by hot extrusion, and (ii) die pressing followed by hot extrusion. The mechanical properties such as yield strength and ultimate tensile strength improved with the addition of SiCp particles.

Table 2.1: Research reported in literature on properties of different nano ceramic reinforcements [18-31]

Reinforcement / 50 nm	Density (g/cc)	Fracture Toughness (MPa.m ^{1/2})	Structure	Hardness (Kg/mm ²)	Melting Point (°C)	Coefficient of Thermal Expansion (°C ⁻¹)	Thermal Conductivity (W/m. K)
Al ₂ O ₃	3.96	4.5	Trigonal	2100	2072	8.4×10^{-6}	35
AlN	3.26	2.6	Hexagonal	1100	2200	4.6×10^{-6}	320
B ₄ C	2.52	3	Hexagonal	2800	2763	5×10^{-6}	35
BN	2.29	2.6	Hexagonal	205	2973	7.2×10^{-6}	1700
Carbon nanotubes	1.6	2.7	Cylindrical	2600	2800	2×10^{-5}	3500
SiO ₂	2.4	0.62	Tetragonal	800	2230	0.65×10^{-6}	1.3
Graphene	2	2.8	Hexagonal	-	4627	-6×10^{-6}	5300
Si ₃ N ₄	3.2	6.1	Trigonal	1580	1900	3.3×10^{-6}	30
TiC	4.93	-	Cubic	2470	3160	7×10^{-6}	5.64
TiN	5.2	-	Cubic	2100	2930	9.35×10^{-6}	19.2
TiB ₂	4.52	6.2	Hexagonal	1800	3230	6.4×10^{-6}	25
WC	15.6	-	Hexagonal	2100	2870	1×10^{-6}	110
WO ₃	7.16	-	Monoclinic	720	1473	-	-
SiCp	3.2	4	Cubic	2500	2730	5.12×10^{-6}	120
Graphite	2.26	2.2	Hexagonal	1700	4027	4.06×10^{-6}	398

The mechanical properties of SiCp reinforced aluminium based nanocomposites investigated by various researchers are presented in Table 2.2. The improvement in mechanical properties is attributed to the presence of second phase particles and increase in dislocation density of the matrix [35]. It is interpreted from the literature that single reinforced nanocomposite has shown good properties, but there are few limitations. Multi phase hard particles reinforced hybrid nanocomposites have shown better improvement in interfacial bonding and mechanical properties. Boostani et al. [36] investigated the mechanical properties of A356/SiCp/Graphene hybrid nanocomposites. Graphene encapsulated SiCp nanoparticles reinforced hybrid nanocomposites exhibited better mechanical properties. Zhang et al. [37] fabricated Al/x wt. % SiCp ($x = 0.25$ and 0.5)/y wt. % CNTs ($y = 0.25$ and 0.5) hybrid nanocomposites through powder metallurgy followed by spark plasma sintering method. The mechanical properties of the hybrid nanocomposites had improved with increase of reinforcement particles content in the matrix. It is attributed to the pinning effect of CNTs which delay the pulling out and peeling of CNTs to further. Sanjay et al. [38] synthesized the Al/0.5%SiCp/x% Ti ($x = 3$ and 5) hybrid nanocomposites through microwave sintering process. The strength properties of the hybrid nanocomposites had improved with fixing 0.5% SiCp as primary reinforcement and by varying the Ti phase in the matrix. The addition of Ti/SiCp second phase particles in the matrix resulted in good strength.

Li et al. [39] produced Al-Cu/SiCp/Mg₂Si hybrid nanocomposites through powder metallurgy technique. The mechanical properties were improved with the addition of SiCp/Mg₂Si reinforcements in the matrix. Zhang et al. [40] fabricated bimodal sized AA2014/(40 nm) 1 vol. % SiCp/ (15 μ m) 4vol% SiCp composites through semi-solid stirring method. The yield strength and ultimate tensile strength of bimodal sized SiCp/Al2014 composites were significantly enhanced. Senelet al. [41] fabricated Al/SiCp/Graphene hybrid nanocomposites through powder metallurgy route. The yield strength and ultimate tensile strength of the hybrid nanocomposites had increased with the increase of graphene nanoparticles in the matrix. The dual phase particles reinforced hybrid nanocomposites were investigated by various researchers [42]. The mechanical properties of hybrid nanocomposites were improved due to the dual phase particles strengthening effect, which are presented in Table 2.3.

Table 2.2: Mechanical properties of SiCp reinforced aluminium based nanocomposites

Composition	Fabrication Method	Yield Strength (MPa)	Ultimate Tensile Strength (MPa)	Elongation (%)
AA6063/5vol. %SiCp [34]	Spark Plasma Sintering followed by Hot Extrusion	392	496	7.1
AA6063/5vol. %SiCp [34]	Hot Compaction followed by Hot Extrusion	449	526	3.5
AA7075/2% SiCp [43]	Stir Casting	80±8	139±10	2.2±0.5
AA7075/2% SiCp [43]	Friction Stir Process	312±5	402±9	21±1.4
A356/2%Cr/3%SiCp [44]	Stir Casting	101±5	175±10	5.3±0.8
A356/2%Cu/3%SiCp [44]	Stir Casting	99±7	168±8	6.7±0.6
A356/2%Ti/3%SiCp [44]	Stir Casting	131±11	228±17	8.5±0.5
Al/1vol % SiCp [45]	Powder Metallurgy followed by Hot Extrusion	--	205±18	17±3
Al/10vol% SiCp [45]	Powder Metallurgy followed by Hot Extrusion	--	405±15	4±1
A356/1wt%SiCp [32]	Stir Casting	137	173	5.38
Al/Mg/SiCp [46]	Friction Stir Process	119.8	290.1	--
AA5083/1wt%SiCp [47]	Powder Metallurgy, Cold Isostatic Pressing followed by Sintering	117	255	11
AA5083/3wt%SiCp [47]	Powder Metallurgy, Cold Isostatic Pressing followed by Sintering	158	335	8.76
AA5083/5wt%SiCp [47]	Powder Metallurgy, Cold Isostatic Pressing followed by Sintering	194	352	4.5
Al/0.3vol%SiCp [48]	Powder Metallurgy, Microwave Sintering and followed by Hot Extrusion	117±2	130±3	11.9±1.3
Al/0.5vol%SiCp [48]	Powder Metallurgy, Microwave Sintering and followed by Hot Extrusion	125±3	144±7	9.8±0.8
Al/1.0vol%SiCp [48]	Powder Metallurgy, Microwave Sintering and followed by Hot Extrusion	140±5	160±9	8.6±0.6
Al/1.5vol%SiCp [48]	Powder Metallurgy, Microwave Sintering and followed by Hot Extrusion	158±9	178±6	7.3±0.9
A356/2wt%SiCp [49]	Ultrasonic Treatment followed by Squeeze Casting	144	259	5.3

Table 2.3: Mechanical properties of dual phase particles reinforced aluminium based hybrid nanocomposites

Composition	Fabrication Method	Yield Strength (MPa)	Ultimate Tensile Strength (MPa)	Elongation (%)
Al356/SiCp/Graphene [35]	Ultrasonic Assisted Stir Casting Method	225	365	8.3
Al/0.25SiCp/0.25CNTs [37]	Powder Metallurgy followed by Sintering	--	162±1	27.3±1.8
Al/0.5SiCp/0.5CNTs [37]		185	247±2	20.7±2.5
Al/0.75SiCp/0.75CNTs [37]		--	160±2	21.3±1.4
Al/0.5% SiCp/3% Ti [38]	Powder Metallurgy followed by Microwave Sintering	111.4±27.1	142.9±25.3	12.3±0.8
Al/0.5% SiCp/5% Ti [38]		150.9±15.3	183.9±18.2	10.6±0.2
Al2014/SiCp/SiCp [40]	Semi Solid Stirring technique	358±14	585±20	9.9±1
Al-Cu/SiCp/Mg ₂ Si [50]	Stir Casting	210	325	6.3

2.2.2 Effect of Reinforcement Particle Size and Volume Fraction on Yield Strength and Ultimate Tensile Strength

In various research articles it is identified that the size of the reinforcement particles in the matrix was influencing the mechanical properties. Wu et al. [51] evaluated the compressive strength of the AA7075 alloy reinforced with B₄C particles of 56.9 μm , 4.2 μm , and 2 μm sizes. The 2 μm size of B₄C reinforced composites exhibited maximum yield stress compared to 56.9 and 4.2 μm size B₄C reinforced composites processed through powder metallurgy route without effecting ductility. Balci et al. [52] fabricated TiB₂ reinforced aluminium composites with particle sizes 40 μm and 320 nm through mechanical alloying followed by cold pressing and pressure less sintering process. The aluminium composites reinforced with TiB₂ of size 320 nm particles revealed higher strength compared to micron-sized TiB₂ reinforced composites. Harichandran et al. [53] fabricated the aluminium composites by reinforcing micron and nano-sized B₄C particles in the matrix through ultrasonic assisted stir casting technique. Boron carbide (B₄C) reinforced aluminium nanocomposites revealed better yield and ultimate tensile strength without affecting ductility compared to the micron-sized B₄C reinforced aluminium composites. Wang et al. [54] prepared composites of Al-Cu alloy reinforced with 4.7 μm and 77 μm size SiCp particles through mechanical mixing. The 4.7 μm sized SiCp particles reinforced Al-Cu alloy composites resulted in better yield strength and ultimate tensile strength than the 77 μm sized SiCp particles reinforced Al-Cu alloy composites. The smaller and bigger sized SiCp particles reinforced Al-Cu alloy based composites fracture surface resulted in ductile fracture of the matrix. But smaller sized SiCp particles reinforced Al-Cu alloy composites exhibited better ductile properties than the micron-sized reinforced composites.

Sun et al. [55] fabricated composites of aluminium reinforced with different sizes (4.7 μm , 16.7 μm , 39.1 μm , and 70.7 μm) of SiCp particles through the mechanical alloying technique followed by hot extrusion. The yield strength and ultimate tensile strength of the composites increased with decrease in the size of the reinforcing particles. The ductility decreased but it is better than higher sized particles reinforced aluminium composites. EI-Kady et al. [56] fabricated composites of aluminium reinforcement of various sizes (10 μm , 40 μm , and 70 nm) of SiCp particles through powder metallurgy route. The compressive strength and hardness of the composites increased with increase in the SiCp reinforcement

content in the matrix. As the size of the SiCp reinforcement particles decreases, the compressive strength of composites increased. The micron-sized reinforced metal matrix composites possess good strength, but ductility reduced. Micron-sized particles have a lower surface area-to-volume ratio and act as micro-crack initiators in the matrix, which leads to significant decrement in the ductility of the composites.

Many investigations proved that ceramic nano-sized particles reinforced metal matrix composites attained good strength with a similar ductility equivalent to that of the metal matrix [54]. The influence on the ductility is less because the nanoparticles have large surface area to volume ratio and it leads to less crack initiation as compared to micron sized reinforced composites. Researchers have confirmed that the strength depends on the aspect ratio of the particle. The strength of the composites increased as the size of the particle decreases from micron size to nano-size in the matrix. This may be due to very fine particles that act as a barrier to the dislocation movement. These obstacles are more in case of nano-reinforced composites when compared to same weight percentage of the micron size reinforced composites [56]. The predicted yield strength of the Mg based nanocomposites decreased with increase of reinforcement particle size as presented in figure 2.1 [57]. The predicted yield strength of the Mg based nanocomposites increased with increase of volume fraction of reinforcement particles in the matrix as shown in figure 2.2 [57]. The mechanical properties of SiCp reinforced aluminium based nanocomposites as a function of volume fraction are presented in Table 2.4.

Amouri et al. [58] fabricated A356/x wt. % SiCp ($x = 0.5$ and 1.5) nanocomposites through stir casting method and applied T6 heat treatment on a part of casted specimens. Reports revealed that the dendrite size decreased with addition of SiCp nano-reinforcement particles to the A356 alloy matrix. The SiCp nano-reinforcement particles act as nucleation sites during solidification period. It is identified that the strength of A356/SiCp nanocomposites increased with rise of volume fraction of SiCp particles. Qiang et al. [33] produced Al/x vol. % SiCp ($x = 1, 3, 5, 7$, and 9) nanocomposites through ultrasonically assisted stir casting method. It reveals that the mechanical properties of the Al/SiCp nanocomposites improved with increase of SiCp nano-reinforcement particles in the matrix. The grain refinement is observed due to the addition of SiCp nanoparticles and with increase of volume fraction of SiCp nanoparticles in the Al matrix.

Table 2.4: Mechanical properties of SiCp reinforced aluminium based nanocomposites as a function of volume fractions

Composition	Fabrication Method	Yield Strength (MPa)	Ultimate Tensile Strength (MPa)	Elongation (%)	Microhardness (HV)
Al/1vol % SiCp [45]	Powder Metallurgy followed by Hot Extrusion	--	205±18	17±3	--
Al/10vol% SiCp [45]		--	405±15	4±1	--
AA5083/1wt%SiCp [47]	Powder Metallurgy, Cold Isostatic Pressing followed by Sintering	117	255	11	115
AA5083/3wt%SiCp [47]		158	335	8.76	152
AA5083/5wt%SiCp [47]		194	352	4.5	165
Al/0.3vol%SiCp [59]	Powder Metallurgy, Microwave Sintering and followed by Hot Extrusion	117±2	130±3	11.9±1.3	49±6
Al/0.5vol%SiCp [59]		125±3	144±7	9.8±0.8	56±3
Al/1.0vol%SiCp [59]		140±5	160±9	8.6±0.6	73±4
Al/1.5vol%SiCp [59]		158±9	178±6	7.3±0.9	82±4
A356/0.5wt%SiCp [57]	Stir Casting	239	305	0.65	--
A356/1.5wt%SiCp [57]		366	403	0.38	--
Al/1vol%SiCp [33]	Ultrasonic Assisted Stir Casting	51.6±0.5	83.2±2.8	3.62±0.21	28.2±0.7
Al/3vol%SiCp [33]		63.3±2.6	130.5±4.5	3.5±0.43	36.4±1.1
Al/5vol%SiCp [33]		76.4±3.4	138.7±3.8	3.1±0.36	40.6±2.0
Al/7vol%SiCp [33]		101.9±3.0	169.3±3.1	2.86±0.23	42.9±2.3
Al/9vol%SiCp [33]		103.1±2.7	170.0±6.5	1.8±0.21	43.8±2.6
AA6063/1vol.%SiCp [34]	Ultrasonic Assisted Stir Casting	296±10	445±16	10.0±1.4	--
AA6063/5vol.%SiCp [34]		343±16	496±3.1	4.4±0.3	--
AA6063/10vol.%SiCp [34]		545±13	603±18	2.3±0.7	--

The enhancement in yield strength and ultimate tensile strength of the Al/SiCp nanocomposites are attributed due to the pinning effect of SiCp nanoparticles at the grain boundaries and dislocation climbing. Yao et al. [34] synthesized AA6063/x vol. % SiCp ($x = 1, 5, \text{ and } 10$) nanocomposites through ultrasonic assisted stir casting technique. The mechanical properties of the Al/SiCp nanocomposites increased and grain size decreased with rise of SiCp particles in the matrix.

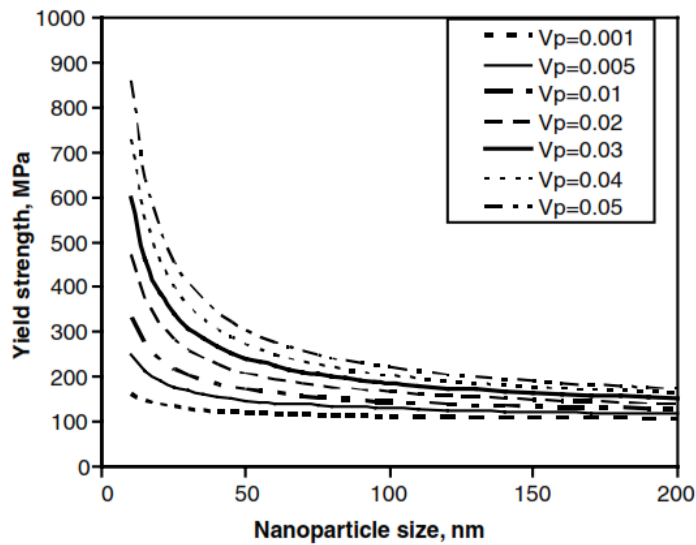


Figure 2.1: Predicted yield strength as a function of reinforcement particle size for different volume fractions in Al_2O_3 reinforced magnesium nanocomposites tested at 20°C [57]

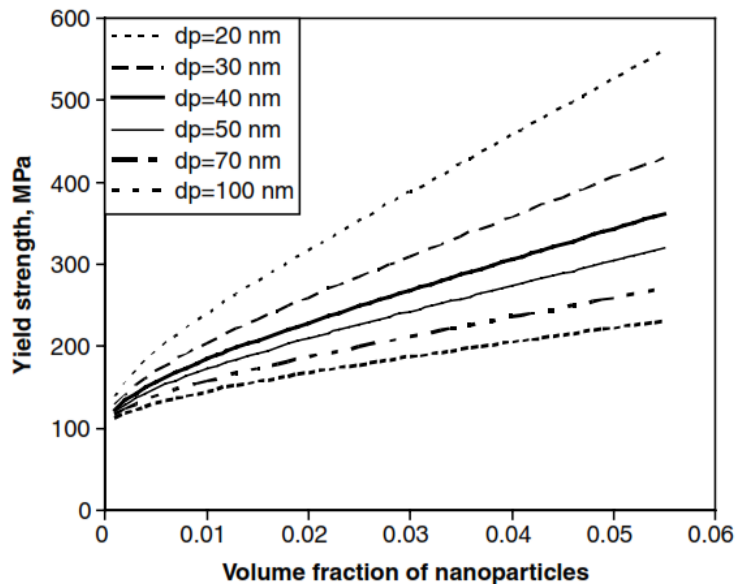


Figure 2.2: Predicted yield strength as a function of volume fraction of reinforcement particles for various sizes of Al_2O_3 reinforced Mg based nanocomposites tested at 20°C [57]

This would be attributed to the increase of dislocation density in the matrix with rise of SiCp nanoparticles in the matrix. As the increase in content of SiCp nanoparticles leads to a stronger inhibiting effect on grain growth, reduction in inter particle distance in the matrix, which resulted in good mechanical properties.

2.2.3 Hardness of AA-MMNCs

The resistance offered by the material to form localized indentation is called as hardness. The volume fraction of reinforcement nanoparticles in the matrix influences the hardness of nanocomposites [58, 60]. Some of the researchers explained the importance of hard ceramic particles in the preparation of metal matrix nanocomposites and also tells hardness increases as the weight percentage of the reinforcement content increases [61]. Some reports found that the size of the reinforced particles decreased simultaneously increasing the hardness of the composite because of high surface to volume ratio [62]. Volume or weight fraction of reinforcement increases and particle size decreases relatively the hardness value increases; this was proved by researchers [63]. The microhardness of the SiCp reinforced aluminium nanocomposites are presented in Table 2.5.

Hardness of the nanocomposites not only depends on the size of reinforcement particles but also depends up on the hardness of particles, crystal structure of the composites and good interfacial bonding between the reinforcement particles and the matrix. Ali et al. [64] produced the AA6061/SiCp composites through compo-casting technique by varying the size of particles and volume fraction. It is observed that with the addition of SiCp particles there is an increase in the hardness of AA6061 aluminium alloy and it decreases with increase of size of SiCp particles. Kollo et al. [45] fabricated SiCp reinforced aluminium composites through high-energy milling followed by hot consolidation by varying SiCp particle size. The composites reinforced with nanoparticles are between two and three times harder than the materials made with micron-scale particles reinforced composites. Dehnavi et al. [65] produced Al413/SiCp nanocomposites through continuous and discontinuous ultrasonic treatments. In the report, it was found that the hardness of the nanocomposites increased with increase in the reinforcement volume fraction. It is also evident that ultrasonic treatment significantly improved the hardness of the nanocomposite specimens in comparison with the stirred specimens of equal volume fraction.

Table 2.5: Microhardness of the SiCp reinforced aluminium based nanocomposites as a function of volume fractions

Composition	Fabrication Method	Microhardness (HV)
AA5083/1wt%SiCp [47]	Powder Metallurgy, Cold Isostatic Pressing followed by Sintering	115
AA5083/3wt%SiCp [47]		152
AA5083/5wt%SiCp [47]		165
Al/0.3vol%SiCp [49]	Powder Metallurgy, Microwave Sintering and followed by Hot Extrusion	49±6
Al/0.5vol%SiCp [49]		56±3
Al/1.0vol%SiCp [49]		73±4
Al/1.5vol%SiCp [49]		82±4
Al/1vol%SiCp [33]	Ultrasonic Assisted Stir Casting	28.2±0.7
Al/3vol%SiCp [33]		36.4±1.1
Al/5vol%SiCp [33]		40.6±2.0
Al/7vol%SiCp [33]		42.9±2.3
Al/9vol%SiCp [33]		43.8±2.6
AA7075/2% SiCp [43]	Stir Casting	88.5±2.3
AA7075/2% SiCp [43]	Friction Stir Process	121±1.3
A356/2%Cr/3%SiCp [44]	Stir Casting	110±5
A356/2%Cu/3%SiCp [44]		103±11
A356/2%Ti/3%SiCp [44]		147±14

2.2.4 Effect of Morphology and Fabrication Process on Strength Properties

The fabrication techniques such as stir casting, squeeze casting, mechanical alloying and followed by hot compaction, powder metallurgy route, spark plasma sintering, laser deposition, spray deposition, ultrasonic assisted stir casting technique and friction stir processing were investigated [46, 41, 66, 67]. The nano-reinforcement particles dispersion is complicated through stir casting method. The reduction of agglomeration through powder metallurgy technique is difficult. Homogeneous dispersion of nano-reinforcement particles in the matrix is costly and lengthy process. Researchers fabricated AA-MMNCs through various processes since two decades. The grain refinement and uniform dispersion of nano-reinforcement particles executed better mechanical properties. Yao et al. [34] synthesized AA6063/5vol. % SiCp nanocomposites through powder metallurgy route. The SEM

micrographs shown in figure 2.3 [44], reveals that the particles were distributed uniformly in the matrix both through plasma sintering, die pressing followed by hot extrusion process. The mechanical properties were improved but through die pressing followed by hot extrusion process better results were achieved than spark plasma sintering followed by hot extrusion method. Mousavian et al. [44] fabricated A356/SiCp nanocomposites through powder metallurgy route. The SiCp particles are mixed with Cr, Cu, and Ti particles separately to improve SiCp particle incorporation and which are mechanically ball milled. The SEM micrographs shown in figures 2.4, 2.5, and 2.6 [44] reveals that the SiCp nanoparticles are mixed uniformly in the matrix. The Ti mixed SiCp particles executed better mechanical properties than Cu and Cr mixed SiCp reinforced nanocomposites.

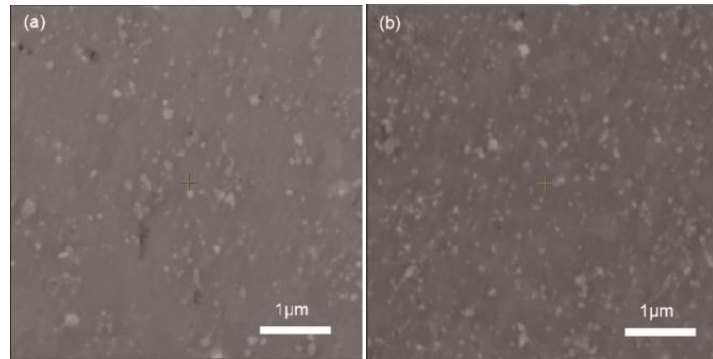


Figure 2.3: SEM backscattered electron images of AA6063/SiCp nanocomposites (a) spark plasma sintering followed by hot extrusion, and (b) die pressing followed by hot extrusion [44]

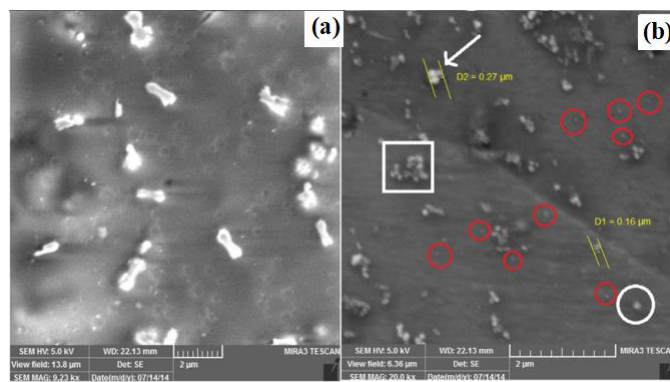


Figure 2.4: The FESEM micrographs of extruded samples A356/SiCp/Cr (a) lower magnification, and (b) higher magnification [44]

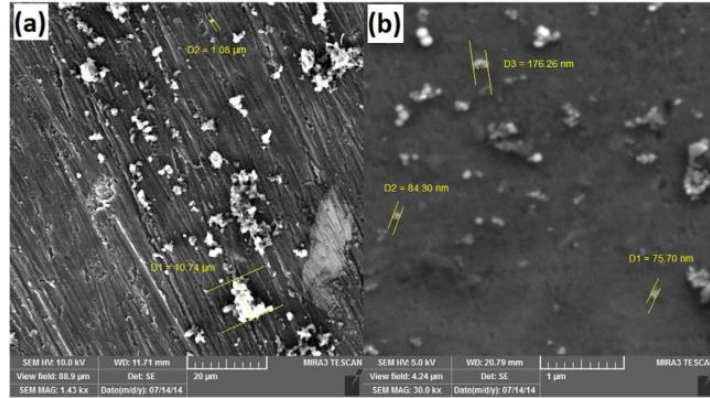


Figure 2.5: The FESEM micrographs of extruded samples A356/SiCp/Cu (a) lower magnification, and (b) higher magnification [44]

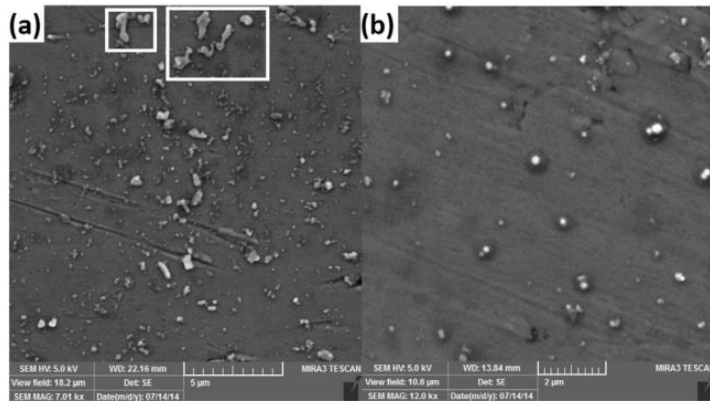


Figure 2.6: The FESEM micrographs of extruded samples A356/SiCp/Ti (a) lower magnification, and (b) higher magnification [44]

The hot extruded specimens reveal that the fragmentation of SiCp platelets in the microstructure, which lead to complete change in the microstructures. Zhang et al. [40] produced the SiCp bimodal sized particles reinforced Al2014 nanocomposites through semi solid stirring technique. The morphology of Al2014/SiCp nanocomposites exhibited better dispersion of reinforcement particles in the matrix with good interfacial bonding which is shown in figure 2.7 [40]. The results reveal good mechanical properties with better dispersion. Qiang et al. [33] fabricated Al/SiCp nanocomposites through ultrasonic vibration technique. The increase of SiCp nanoparticles in the matrix grain size reduced with this technique and the mechanical properties were improved. The microstructure of Al/SiCp nanocomposites with increase of SiCp nanoparticles in the matrix is shown in figure 2.8 [33]. Jianyu et al. [50] produced Al-Cu/SiCp nanocomposites through stir casting technique. The

SiCp nanoparticles were distributed uniformly with formation of nanoparticle clusters in the matrix is shown in figure 2.9 [50].

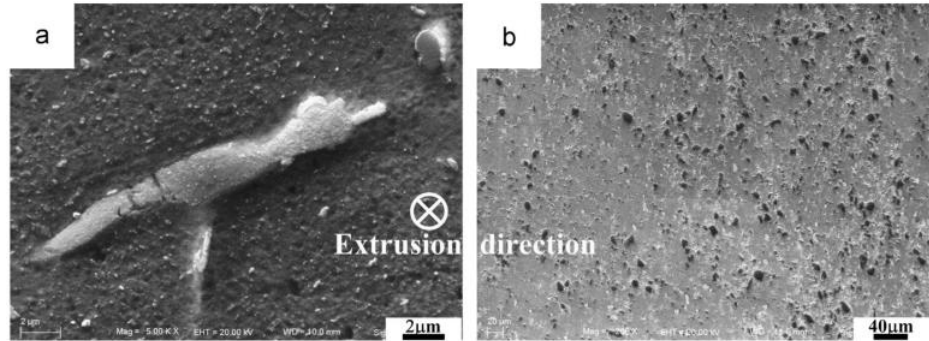


Figure 2.7: The SEM micrographs of extruded samples Al2014/SiCp (a) higher magnification, and (b) lower magnification [40]

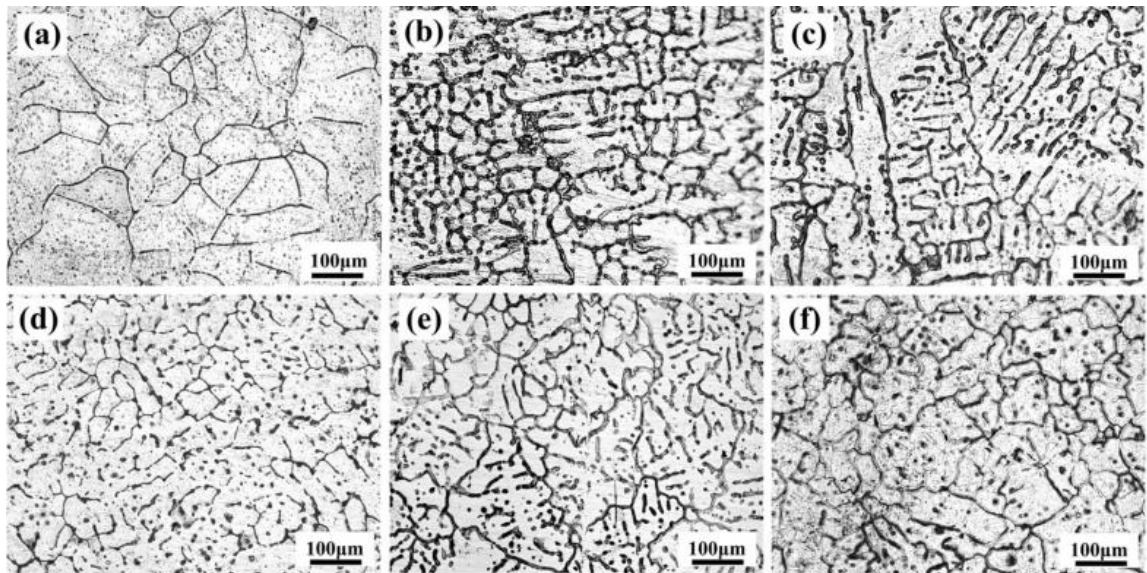


Figure 2.8: Optical images of the Al/SiCp nanocomposites (a) Aluminium, (b) 1 vol. % of SiCp, (c) 3 vol. % of SiCp, (d) 5 vol. % SiCp, (e) 7 vol. % of SiCp, and (f) 9 vol. % of SiCp [33]

Later many modifications have been done by the researchers in various liquid state metallurgical methods. The ultrasonic-assisted stir casting method is introduced for better wettability and dispersion of hard nanoparticles in the aluminium alloy matrix [16]. Lü et al. [68] synthesized the Al/SiCp nanocomposites through ultrasonic vibration followed by squeeze casting technique. The SEM micrographs of Al/SiCp nanocomposites are shown in figure 2.10 [68]. The mechanical properties of the Al/SiCp nanocomposites were improved

with ultrasonic vibration and with the addition of SiCp nano-reinforcement particles in the matrix.

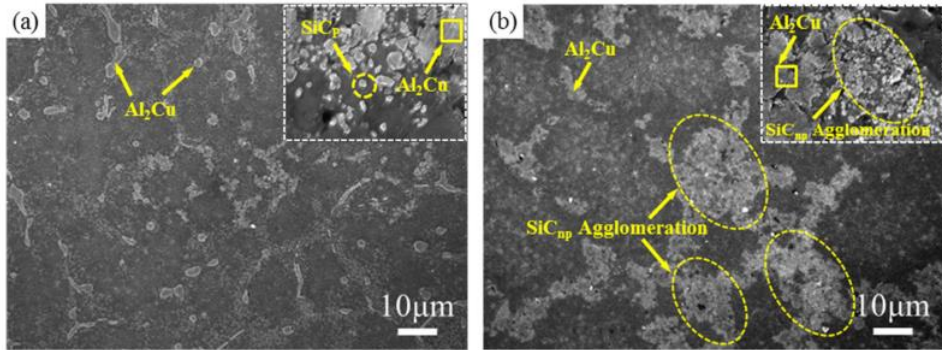


Figure 2.9: SEM micrographs of Al-Cu/SiCp nanocomposites (a) 1 wt. %, and (b) 2 wt. % [50]

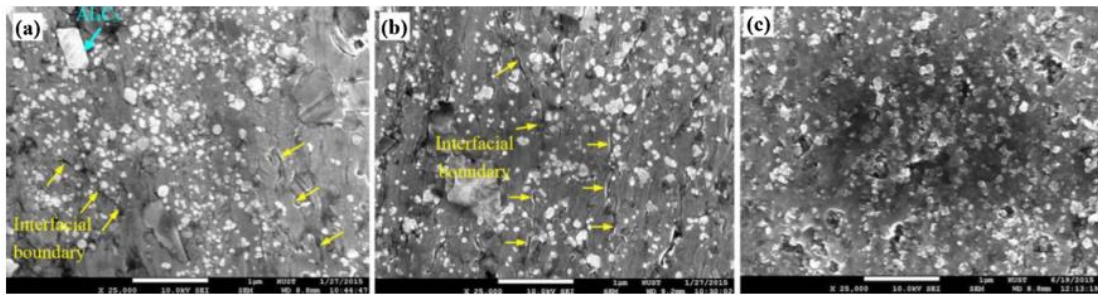


Figure 2.10: SEM micrographs of the Al/SiCp nanocomposites (a) 2 wt. %, (b) 4 wt. %, and (c) 8 wt. % [68]

Yong et al. [69] fabricated A356/SiCp nanocomposites through ultrasonic assisted casting method. The results revealed that SiCp nano-reinforcement particles (2 wt. %) were well dispersed by reducing the formation of SiCp nanoparticle clusters in the A356 alloy matrix by strong cavitation and acoustic streaming effects in molten metal. Srivastava et al. [70] produced Al6061- y wt. % (50 nm) Al_2O_3 ($y = 1, 2$, and 3) nanocomposites by ultrasonic assisted stir casting process. The application of ultrasonic intensity resulted in better dispersion of Al_2O_3 nanoparticles in the matrix up to 2 wt. %. The addition of above 2 wt. % led to poor distribution, clusters of Al_2O_3 nanoparticles and microcracks were induced in the Al6061 alloy matrix. The viscosity of molten melt increased with the rise of Al_2O_3 nanoparticles in the matrix which reduces the efficiency of ultrasonic treatment. Therefore, the reduction in efficiency of ultrasonic treatment would be resulting in more nanoparticle clustering. Several investigations have proven that the ceramic nanoparticles were distributed

uniformly in the alloy matrix through ultrasonic-assisted casting process. Better dispersion of hard nanoparticles in the molten metal would be depending on various process parameters such as processing time, processing temperature, ultrasonic pressure, weight percent of nanoparticles and ultrasonic intensity.

2.3 Strengthening Mechanisms

The yield strength of composites is influenced by the type of reinforcement particles, size of reinforcement particles and volume fraction of reinforcement particles. During plastic flow of material due to the application of external loads which is very difficult to predict either all of these above mentioned mechanisms are acting simultaneously [71]. The increment in yield strength of AA-MMNCs is mainly due to the contribution of four strengthening mechanisms i.e., Dislocation mismatch effect [72], Orowan strengthening effect [73], Hall-Petch effect [16], Load bearing effect [74]. The strengthening mechanism equations are presented in Table 2.6. Nano-sized reinforcements in the metal matrix composites provide a large interfacial area in between the reinforcement and alloy matrix which contributes to significant enhancement in mechanical properties. The thermal stresses are induced because of thermal expansion coefficient mismatch between the matrix and nano reinforcement particles during cooling of molten metal from the initial fabrication conditions. The induced thermal stresses near the interface around the nano-reinforcements are sufficient for plastic strain in the matrix [75].

Table 2.6: List of various strengthening mechanism equations

(i)	$\Delta\sigma_y(nc) = k \frac{1}{\sqrt{d_{grainsize}}} [74]$, where $d_{grainsize} = \frac{4\alpha d_p}{3V_f}$ (Zener empirical relationship) [74] $\Delta\sigma_{HP} = k \left[\frac{1}{\sqrt{d_c}} - \frac{1}{\sqrt{d_m}} \right]$ (grain refinement)[16]
(ii)	$\Delta\sigma_{Orowan} = \frac{0.13G_m b_m}{\tau} \ln \left[\frac{d_p}{2b_m} \right]$, where $\tau = d_p \left[\left(\frac{1}{2V_f} \right)^{\frac{1}{2}} - 1 \right]$ [73]
(iii)	$\Delta\sigma_{CTE} = \beta G_m b_m [\rho^{CTE}]^{\frac{1}{2}}$, where $\rho^{CTE} = \frac{A(\alpha_m - \alpha_p)\Delta TV_f}{b_m d_p (1 - V_f)}$ [72]
(iv)	$\Delta\sigma_{load} = 0.5V_f \sigma_m$ [74]
(v)	$\Delta\sigma_{porosity} = e^{-nP}$, where $n = 1.943$, equiaxed reinforcement particles, $P = \text{porosity}$ [74]

where ' $\Delta\sigma_{y(nc)}$ ' is enhancement of yield strength of the composite, 'k' is Hall-Petch equation slope, ' $d_{grain\ size}$ ' is the grain size, ' α ' is the proportional constant, ' d_p ' is the reinforcement particle size, ' V_f ' is the volume fraction of reinforcement particles, ' d_m ' is the average grain size of AA6061 aluminium alloy matrix, ' d_c ' is the average grain size of nanocomposites, ' $\Delta\sigma_{HP}$ ' is the enhancement of yield strength of the composite due to grain refinement, ' $\Delta\sigma_{Orowan}$ ' is the yield strength improvement, ' G_m ' is the shear modulus of matrix material, ' b_m ' is burgers vector of matrix, ' τ ' is the average inter-particle spacing, 'A' is a constant is equal to be 12; ' $\alpha_m - \alpha_p$ ' is the difference of thermal expansion coefficient matrix and reinforcement particles, and ' ΔT ' is the temperature change from the stress free homologous temperature to the room temperature, ' β ' is a constant equal to 1.25, ' ρ^{CTE} ' is dislocation density, ' $\Delta\sigma_{CTE}$ ' is the enhancement of yield strength due to dislocation mismatch.

Due to the application of external loads the dislocations bow out between two particles. Yielding occurs when the bowed-out dislocation becomes semi-circular in shape. The formation of the Orowan loops makes the dislocation motion more and more difficult which results in large work hardening. The Orowan strengthening mechanism is significant if the reinforcement particle size is between 1 nm and 1 μm . In this mechanism, the nano-reinforcement particles are proven to be sheared or by-passed by dislocations [76]. Hall-Petch developed a relationship between yield strength and grain size. According to the Hall-Petch strengthening effect, the yield strength of the composites improved with decreasing the grain size. Later, Zener developed a relationship between the grain size as a function of volume fraction and reinforcement particle size. Sanaty et al. [77] developed a linear relationship between grain size as a function of reinforcement particle size and volume fraction extracted from graph based on the literature data for magnesium based nanocomposites.

The load bearing mechanism explains that there is a strong bond between the matrix and reinforcement nanoparticles. Then the nanoparticles would carry a percentage of loads depending on the weight percentage of reinforcements in the matrix. It gives rise to transfer load between the matrix and reinforcement. The porosity of the metal matrix nanocomposites plays the major role on the yield strength. The porosity of the nanocomposites increases with increase in volume fraction of the nano-sized reinforcement particles in the matrix and reduces the yield strength [74]. The porosity of nanocomposites will interrupt load balance between the nano-reinforcement particles and matrix material that results in stress

concentration, crack initiations and crack propagation. This is leading to a reduction in the yield strength properties. It is important to consider the effect of porosity in the prediction of yield strength for the metal matrix nanocomposites.

Park et al. [78] predicted the enhancement of yield strength for Al/CNT nanocomposites using various strengthening mechanisms. It was proved that the load bearing and thermal dislocation mismatch strengthening effect is more significant on yield strength compared to other mechanisms. Sree Manu et al. [79] predicted the enhancement of yield strength for Al-Si/Al₂O₃ nanocomposites using strengthening mechanisms. It was identified that the Orowan effect is exhibited better than the other mechanisms. Srivastava et al. [16] predicted the enhancement of yield strength for Al6061/Al₂O₃ nanocomposites. It was observed that the dislocation mismatch effect and Orowan strengthening effect is more significant than the Hall-Petch effect. Deng et al. [75] predicted the enhancement of yield strength for Mg/Al₂O₃ and Ti/Y₂O₃ nanocomposites. The Orowan strengthening mechanisms is very effective when the reinforcement particle size is less than 100 nm. In many investigations when the particle size is above 1 μ m, particles reinforced composites revealed that the Orowan strengthening effect is almost negligible.

Xin Zhang et al. [80] predicted the enhancement of yield strength for Al/SiCp/CNTs hybrid nanocomposites. The enhancement of yield strength through Hall-Petch strengthening mechanism and load bearing effect has shown higher values which are more significant. Bhadauria et al. [81] predicted the enhancement of yield strength for Al/GNPs nanocomposites. The load transfer strengthening effect executed highest contribution towards enhancing the yield strength of the Al/GNPs nanocomposites. The thermal dislocation mismatch and grain refinement showed lesser enhancement of yield strength than the load bearing effect because the interfacial bonding area is larger which resulted in higher sharing of bearing loads. Amirkhanlou et al. [82] predicted the enhancement of yield strength for Al-Si-Mg-Cu/Mg₂Si/TiB₂ hybrid nanocomposites. The dislocation mismatch and Orowan strengthening mechanism exhibited significant effect to enhance the yield strength in the hybrid nanocomposite. The prediction values of yield strength contribution from dislocation mismatch, Orowan, load bearing, and Hall-Petch effect are 65.5 MPa, 38.3 MPa, 6.7 MPa, and 1.4 MPa respectively. Fan et al. [83] predicted the yield strength of the Al/WO₃/WAl₁₂ hybrid nanocomposites. The Orowan strengthening mechanisms is more significant.

2.4 Yield Strength Prediction Models

Researchers investigated in several ways to develop the yield strength prediction models for MMCs from last two decades. There are various models developed and proposed for MMNCs. Different prediction models are described for studying the enhancement of yield strength of nanocomposites which are presented in Table 2.7. In order to take into account that the various strengthening mechanisms effects are simultaneously present, the rules of addition of strengthening effects was first developed. However, the summation model, in some cases, may over-predict the yield strength of the MMCs. An analytical compounding model to compute the yield strength of MMNCs, taking into account both the additive and synergetic effects, was developed by Ramakrishnan by integrating a modified shear log model and an enhanced dislocation density model [84]. Zhang and Chen implemented yield strength prediction model by integrating the Ramakrishnan model as to take into account the of Orowan effect, considered to be particularly important in the case of MMNCs [85].

Table 2.7: List of various yield strength prediction model equations

(i)	Ramakrishnan's model[84]	$\sigma_{ync} = (\sigma_m) \left(1 + \frac{\Delta\sigma_{load}}{\sigma_m}\right) \left(1 + \frac{\Delta\sigma_{\Delta CTE}}{\sigma_m}\right)$
(ii)	Zhang and Chen model[85]	$\sigma_{ync} = (\sigma_m) \left(1 + \frac{\Delta\sigma_{load}}{\sigma_m}\right) \left(1 + \frac{\Delta\sigma_{\Delta CTE}}{\sigma_m}\right) \left(1 + \frac{\Delta\sigma_{Orowan}}{\sigma_m}\right)$
(iii)	Mirza and Chen model[74]	$\sigma_{ync} = (\sigma_m) \left(1 + \frac{\Delta\sigma_{load}}{\sigma_m} - P\right) \left(1 + \frac{\Delta\sigma_{\Delta CTE}}{\sigma_m}\right) \left(1 + \frac{\Delta\sigma_{Orowan}}{\sigma_m}\right) \left(1 + \frac{\Delta\sigma_{HP}}{\sigma_m}\right) (e^{-nP})$
(iv)	Modified Clyne model[72]	$\sigma_{ync} = \sigma_m + \Delta\sigma_{HP} + \Delta\sigma_{load} + \sqrt{\Delta\sigma_{Orowan}^2 + \Delta\sigma_{\Delta CTE}^2}$
(v)	Quadratic summation model [70]	$\sigma_{ync} = \sigma_m + \sqrt{\Delta\sigma_{HP}^2 + \Delta\sigma_{Orowan}^2 + \Delta\sigma_{\Delta CTE}^2 + \Delta\sigma_{load}^2}$
(vi)	Compounding model[70]	$\sigma_{ync} = (\sigma_m) \left(1 + \frac{\Delta\sigma_{HP}}{\sigma_m}\right) \left(1 + \frac{\Delta\sigma_{load}}{\sigma_m}\right) \left(1 + \frac{\Delta\sigma_{\Delta CTE}}{\sigma_m}\right) \left(1 + \frac{\Delta\sigma_{Orowan}}{\sigma_m}\right)$

Mirza and Chen developed a model to predict the yield strength of MMNCs including load bearing effect, thermal dislocation mismatch effect, Orowan effect, Hall-Petch effect and porosity effect [74]. Sanaty et al. [77] suggested the quadratic summation model for prediction of yield strength of MMCs. This model is proposed for micron size particles reinforced composites. In several reports specify that the nanocomposite properties

significantly improved and the assumptions for micron size particles reinforced composites cannot be applied to nanocomposites. This model assumes that the total enhancement of yield strength is proportional to the sum of the squares of each strengthening effect under square root. Orowan and thermal mismatch effect played a major role in the incremental of yield strength of hybrid nanocomposites. Hall-Petch and load bearing effect is negligible compared to other strengthening mechanisms. Orowan and thermal mismatch strengthening mechanisms have direct influence on yield strength of MMNCs. So that it is required to take the sum of squares of Orowan and thermal mismatch effect under square root. Considering these two strengthening mechanisms under square root is known as Modified clyne model [77]. Summation of contribution of each strengthening mechanism is known as arithmetic summation model. According to this model the various strengthening effect acts and independently contribute the yield strength of the hybrid nanocomposites [86]. According to compounding model the enhancement of yield strength due nano-reinforcements is multiplied to σ_{ync} [86].

Zhang et al. [85] predicted the yield strength of Mg/Al₂O₃ and Ti/Y₂O₃ nanocomposites by integrating the Orowan strengthening effect to Ramakrishnan model. The Zhang and Chen proposed model resulted in good agreement with the experimental data collected from literature. Khandelwal et al. [86] fabricated the Al6061/Al₂O₃ nanocomposites through ultrasonically assisted stir casting technique. The yield strength properties were predicted using various models above mentioned. The experimental values of various Al6061/Al₂O₃ nanocomposites are compared to theoretical values of yield strength. The quadratic summation technique and modified Clyne model are close to the experimental values up to 2wt. % Al₂O₃. Xiao et al. [87] predicted the yield strength of TiB₂ reinforced magnesium nanocomposites using various prediction models. The experimental results reveal good agreement with Zhang and Chen model. Many reports noted that the predicted yield strength is very much dependent on the size of the reinforcement particle, thermal property of reinforcement particles and volume fraction reinforcement particles in the matrix [80].

2.5 Tribological Properties of AA-MMNCs

In recent trends, the ceramic particles reinforced aluminium based composites have been used in various fields such as aerospace, structural, automobile and defence applications [88]. It has been identified that the sliding characteristics of materials are of notable

importance in tribological systems. The dry sliding wear behaviour of AA-MMNCs by reinforcing variety of fibre, whisker and particulate type of reinforcements and varying volume fraction with respect to type of aluminium alloy was studied extensively. It is noticed that the hard particles reinforced AA-MMNCs executed good strength and better tribological properties than the unreinforced aluminium and its alloys [89]. Sannino et al. [90] investigated and reported on the tribological parameters affecting the dry sliding wear behaviour of aluminium composites. The parameters such as applied normal load, sliding velocity, sliding distance, temperature and environment, the counterpart and its surface finish. The wear properties varied with respect to above parameters in the applied environment.

Aiguo et al. [91] reported that the wear rate increased linearly as a function of sliding distance in steady state condition and also wear mechanisms changed with increase of sliding velocity. The tribological properties of composites are dependent on various parameters such as reinforcement particle size (micro or nano), reinforcement content, and reinforcement phase in the base material and type of fabrication process [92]. AA-MMNCs have been used in various tribological systems such as cylinder liners, bearing surfaces, brake components and propeller shaft. In this wide variety of applications, the tribological properties are very important. The wear rate of sensitive parts in above applications has been improved by reinforcing SiCp particles in the aluminium matrix [93]. Zou et al. [94] noticed that the wear rate of SiCp particles reinforced Al-Si-Cu based composites was lower than that of Al-Si-Cu matrix. Depth of penetration into the subsurface and plastic flow of pin material is decreased by reinforcing SiCp particle in the base material. Researchers [95] examined the wear properties of AA5252/SiCp composites with varying reinforcement particle size. Tribological properties of AA5252-SiCp nanocomposites were good compared to the micron-sized SiCp particles reinforced AA5252-SiCp composites. Micron size particles reinforced AA5252-SiCp composite has higher wear resistance when applied normal loads were minimal. The nanoparticles reinforced AA5252-SiCp composites revealed superior wear resistance at higher applied normal loads.

Mazahery et al. [64] studied the tribological properties of AA6061/SiCp composites with varying average reinforcement particle size and its content. The hardness of material and applied normal load on pin had significant influence on tribological properties during dry sliding of Al6061/SiCp composites. Manivannan et al. [96] examined the tribological properties of Al6061/SiCp nanocomposites. The reports revealed that the wear rate of

nanocomposite is lower than the Al6061 alloy. Shirazi et al. [97] reported the wear properties of Al6061/SiCp nanocomposites. The study revealed that the rise of SiCp content in the Al6061 alloy material improved the hardness and reduced the wear loss. Better tribological properties were observed for SiCp nanoparticles reinforced aluminium based nanocomposites due to the presence of primary phase SiCp nanoparticles and rise of dislocations in the base material [98]. The SiCp nanoparticles act as barriers to the dislocations movement under applied external loads on the matrix. Many experiments proved that the incorporation of SiCp nano-reinforcement particles in the aluminium based alloy increases the frictional heat between the contact surfaces. Reason for damage of automobile and machine parts are due to the heavy friction and wear. An appropriate solid lubricant is added for reducing the coefficient of friction and improving the wear behaviour of the SiCp reinforced aluminium based composite materials during dry sliding [99].

Researchers conducted experiments to examine the wear properties of aluminium based composites by introducing SiCp as primary reinforcement and a solid lubricant as secondary reinforcement in the matrix material at various tribo parameters [100, 101]. These works were focused to understand the combined effects of hard and soft type of reinforcements in the wear behaviour on the matrix material. It was revealed that the addition of solid lubricant as secondary reinforcement found to have beneficial effect especially in terms of wear properties. Addition of solid lubricant as secondary reinforcement in the matrix is for better wear properties and reduction in coefficient of friction of the Al/SiCp nanocomposites. Carvalho et al. [102] examined the wear behaviour of Al-Si/CNTs/SiCp hybrid nanocomposites at dry condition on reciprocating pin-on-plate. The wear rate was reduced by reinforcing CNTs as primary reinforcements and SiCp as secondary reinforcements in the Al-Si matrix. Babu et al. [103] noticed the minimal wear loss and friction coefficient for A356-10vol%Al₂O₃-10vol% GNF hybrid nanocomposites. Results shown enhancement in wear resistance and reduction in friction coefficient for more than 15 vol. % of GNF (graphite nanofiber) and Al₂O₃ fiber reinforced composites. This could be due to the presence of GNFs and Al₄C₃ agglomerations within the matrix. The graphite particles are the most extensively used solid lubricant in the aluminium based matrix due to its low cost and yield better tribological properties with SiCp, Al₂O₃ and B₄C particles. Aruri et al. [104] described that there was decrease in wear rate of Al6061-SiCp-Al₂O₃ and Al6061/SiCp/graphite hybrid composites. Reduction in wear rate was due to the incorporation

of various ceramic reinforcements (i.e., SiCp, Al_2O_3 , and graphite). SiCp reinforcement particles bear the external applied load and graphite act as a solid lubricant in the Al6061-SiCp-graphite hybrid nanocomposites. Ravindran et al. [105] investigated the tribological properties of Al2024-5wt. % SiCp-5wt. % (graphite) hybrid composites. Hardness and wear resistance of hybrid composites improved due to the increase of SiCp and graphite nano-reinforcement particles in the base material. Significant wear resistance was observed for Al2024-5 wt. %SiCp-5 wt. % (graphite) based hybrid nanocomposites.

Chen et al. [106] examined tribological properties of Al2014-5vol. % (graphite) composite. The graphite reinforced Al2014 alloy based composite revealed minimum wear loss and friction coefficient than that of base material. Ames et al. [107] studied the wear properties of A356-20%SiCp-3% (graphite) hybrid composite. Results revealed that higher wear resistance with the introduction of SiCp and graphite particles was seen. Improvement in wear resistance was attributed to the load bearing effect of SiCp reinforcement particles and its abrasive nature. Mostafapour et al. [108] examined the Al5083-graphite- Al_2O_3 hybrid nanocomposites. The nanocomposite with graphite of 75% hybrid ratio resulted in reduced wear rate and friction coefficient. Suresha et al. [109] prepared the LM25 aluminium alloy/SiCp/graphite hybrid composite. The wear rate of hybrid composites was reduced than LM25-SiCp composites. Singh et al. [110] specified that the friction coefficient reduced by reinforcing 6 wt. % graphite in Al/10 wt. % SiCp composites. An increase in mechanical properties of Al/10SiCp/6 (graphite) hybrid composite was due to the addition of SiCp and graphite reinforcements in the matrix. Basavarajappa et al. [111] produced Al2219/15SiCp composite and Al2219/15SiCp/3(graphite) hybrid composites. Graphite reinforced hybrid composite revealed lower degree of subsurface deformation than the non-graphite reinforced composite and the deformation was increased with increasing the sliding velocities.

The incorporation of solid lubricant as secondary reinforcements in the Al-SiCp hybrid nanocomposites improved the tribological properties. There is a scope for Al/SiCp/graphite hybrid nanocomposites in various tribological systems such as automobile industry and aircraft applications including engine block, engine valves, pistons and cylinders due to their good sliding characteristics [112]. Utilization of Al/SiCp/graphite hybrid nanocomposite elements in an automobile assembly unit led to reduce the usage of oil and service cost. From the literature it is observed that the hybrid nanocomposites are better choice compared to nanocomposites. However, the secondary reinforcement used in previous

studies is in micro level or hybrid nanocomposites were fabricated by other than ultrasonic assisted process. Due to various applications and better properties of hybrid nanocomposites, in depth study of its tribological properties is necessary.

2.6 Abrasive Wear Characteristics of AA-MMNCs

The abrasive wear behaviour of materials depends up on several parameters such as applied normal load, abrasive grit particle size, the orientation of abrasive grit particles, reinforcement particle size, type and volume fraction of reinforcements, and the fracture toughness of the pin material, environmental conditions, and hardness [88]. Tung et al. [113] investigated the abrasive wear behaviour of contact surfaces of cylinder bore and piston ring system which results in the abrasive wear is dominant wear mechanism. The abrasive wear mechanism affected the efficiency of combustion process. It was noticed that the abrasive wear was found to be severe than the dry sliding wear characteristics. It is attributed due to the presence of hard ceramic asperities in between mating parts and this can lead to inefficiency of the wear of critical parts in the various tribological systems.

Rohatagi et al. [114] mentioned that the abrasive wear resistance of Al-2.5 wt. % of SiO_2 composites is three times better than the pure aluminium. Singh et al. [115] reported that the BS LM6-10wt. % of Al_2SiO_5 composite wear rate increased with increase in abrasive paper grit size and normal load on pin material. Canakci et al. [116] worked on B4C reinforced Al 2024 composites and revealed that the abrasive wear resistance improved compared to the base alloy. Wang et al. [117] examined the abrasive wear resistance of the Al_2O_3 -reinforced aluminium composite and observed six times improvement than the base material. Alpas et al. [118] worked on SiCp reinforced Al2024 composite and reported that the abrasive wear resistance increased with the increase of sliding distance. Axen et al. [119] indicated that the abrasive wear resistance of Al_2O_3 reinforced aluminium composites improved at fine abrasive grit paper and low normal loads. Another report showed that the abrasion wear resistance of Al6061-20% SiCp composites improved with the decrease of abrasive grit particle size. Sahin et al. [120] reported that the abrasive grit particle size is more significant parameters in two-body abrasion wear. The wear rate increases with the increase of abrasive grit particle size and applied normal load but decreases with the increase of SiCp reinforcement particles in the matrix.

Wilson et al. [121] reported on transition of wear behaviour of Al6061-20 vol. % SiCp composite in the case of two body abrasion tests. In this case the state of abrasive wear changed when the size of abrasive grit was reduced as finer grits promotes low stress abrasion i.e. the chipping and reinforcement removal to more plastic smearing of the base material. Turenne et al. [122] proved that the wear resistance increases with decreased abrasive grit particle size when tested on Al6061-20%SiCp composites. Ma et al. [123] conducted various experiments on the abrasive wear of Al6061 and its SiCp, SiCw reinforced composites on P400 and P600 abrasive grit papers. It was noticed that the wear rate of composite with SiCw reinforcement was higher compared to SiCp reinforced composites. This was due to greater tendency of agglomeration of ceramic in former composite.

Gurcan et al. [124] reported on abrasive wear behaviour of saffil and SiCp reinforced Al6061 composites over P400 grit paper. It was identified that the wear resistance increased for saffil and SiCp reinforced hybrid composites when compared to SiCp reinforced composites. Hamblin et al. [125] specified in his reports that the two body abrasive wear behaviour depends on the abrasive grit particles. In reports it reveals that the wear rates increased linearly with speed, with partial decrease in friction due to lubrication effect caused by fine wear particles. It is attributed due to greater fragmentation and fracturing of ceramic reinforcements in the composites. Das et al. [126] investigated the abrasive wear characteristics of Al-Si/SiCp composites. The results reveal that the better abrasive wear properties for high volume fraction reinforced composites were obtained.

Recent research reports have proven that the wear resistance of multi-phase particle-reinforced aluminium hybrid nanocomposites was higher compared to base alloy and single-phase particles reinforced nanocomposites. The synergistic effect of two-phase nano-reinforcements on two-body abrasive wear behaviour was examined. The dual-phase SiCp and graphite nanoparticles reinforced aluminium hybrid nanocomposites have several applications such as the fabrication of disc brakes, brake callipers, and pistons in the automobile industry. The addition of graphite particles as a secondary reinforcement to the SiCp reinforced aluminium nanocomposites is favourable in the generation of tribo-layer, subsurface plastic deformation and machinability. During sliding action, the graphite prevents sticking or welding to the abrasive or hard surface by forming tribo-layer. This inspection is needed to examine the abrasion wear behaviour of aluminium based hybrid nanocomposites.

2.7 Motivation for the Present Work

Demand for high performance aluminium metal matrix nanocomposite materials is (AA-MMNCs) increasing day by day due to the government regulations in various countries to minimize the power loss, green house emissions, and fuel consumption. The AA-MMNCs have been developed according to the demand in various sectors such as automobile, aircrafts, aerospace and marine applications. In many applications the mechanical and tribological properties are very important. The mechanical properties of AA-MMNCs basically depend on the type of fabrication technique, type of reinforcement, size of reinforcement, dispersion of reinforcements and solidification process. The researchers implemented ultrasonic assisted stir casting technique for removing the gasses, grain refinement and for better particle distribution in the molten composition. Hence, the grain refinement, good wettability and particle dispersion would be improving the mechanical properties of AA-MMNCs.

In various applications, there exist situations where two mating elements are in sliding contact with each other. There are possibilities of elements failure in an assembly unit due to worn out of material during dry sliding that lead to huge economic losses. Hence it was specified that, an investigation is required in studying the dry sliding wear behaviour and abrasive wear behaviour of aluminium based hybrid nanocomposites. Due to the various applications and better properties of hybrid nanocomposites, in depth study of its tribological properties is necessary.

2.8 Identified Gaps in the Literature

After comprehensive study of the existing literature, a number of gaps have been identified in fabrication of HMMNCs:

- It is observed that SiCp/graphite aluminium composites are synthesized using different routes, such as stir-casting, squeeze casting, powder metallurgy route, etc. Better nanoparticles distribution was not found through these fabrication techniques.
- Literature survey further indicates that more studies will be required to exploit beneficial effect of dual phase nanoparticles of SiCp and graphite in AA6061 aluminium alloy.

- Limited studies have been reported on yield strength prediction of aluminium nanocomposites by considering various strengthening mechanisms including porosity and Hall-Petch effect.
- In the Hall-Petch and Zener relationship, the proportional limit is not found in the literature for AA6061 aluminium alloy nanocomposites.
- But no systematic attempt has been made on the influence of the hybridization of both primary phase SiCp particles and secondary phase graphite particles in dry sliding wear and abrasive wear characteristics of hybrid nanocomposites.

2.9 Objective of the Research Work

The following objectives of the present research were adopted:

- To study the microstructure, phase formation, mechanical and tribological properties of AA6061 aluminium alloy, 0.5NC, 1NC, 1.5NC, and 2NC nanocomposites with varying SiCp (50 nm) ($x = 0, 0.5, 1, 1.5$, and 2) reinforcement in the matrix fabricated through ultrasonic assisted stir casting technique.
- Finding proportionality constant (α) in the modified Zener and Hall-Petch empirical relationship for the AA6061 nanocomposites based on grain size and volume fraction. Prediction of yield strength and yield strength improvement factors using various strengthening mechanisms by varying the reinforcement particle size and its volume fraction.
- To study the microstructure, phase formation, mechanical and tribological properties of 0.5HNC, 1HNC, 1.5HNC, 2HNC, and 3HNC hybrid nanocomposites fabricated through ultrasonically assisted stir casting technique.
- Prediction of yield strength of AA6061-2SiCp-x (Graphite) ($<1 \mu\text{m}$) hybrid nanocomposites using various strengthening mechanisms and prediction models.
- To study the two body abrasive wear behaviour of AA6061 aluminium alloy, 2NC nanocomposite and 2HNC hybrid nanocomposite.

2.10 Complete Work Plan Flow Chart

The overall work plan of the present research is presented in the figure 2.11. The figure reveals the selection of alloy matrix material, nano-reinforcements, fabrication

technique, testing method, characterization of materials, and tribological properties of nanocomposites and hybrid nanocomposites.

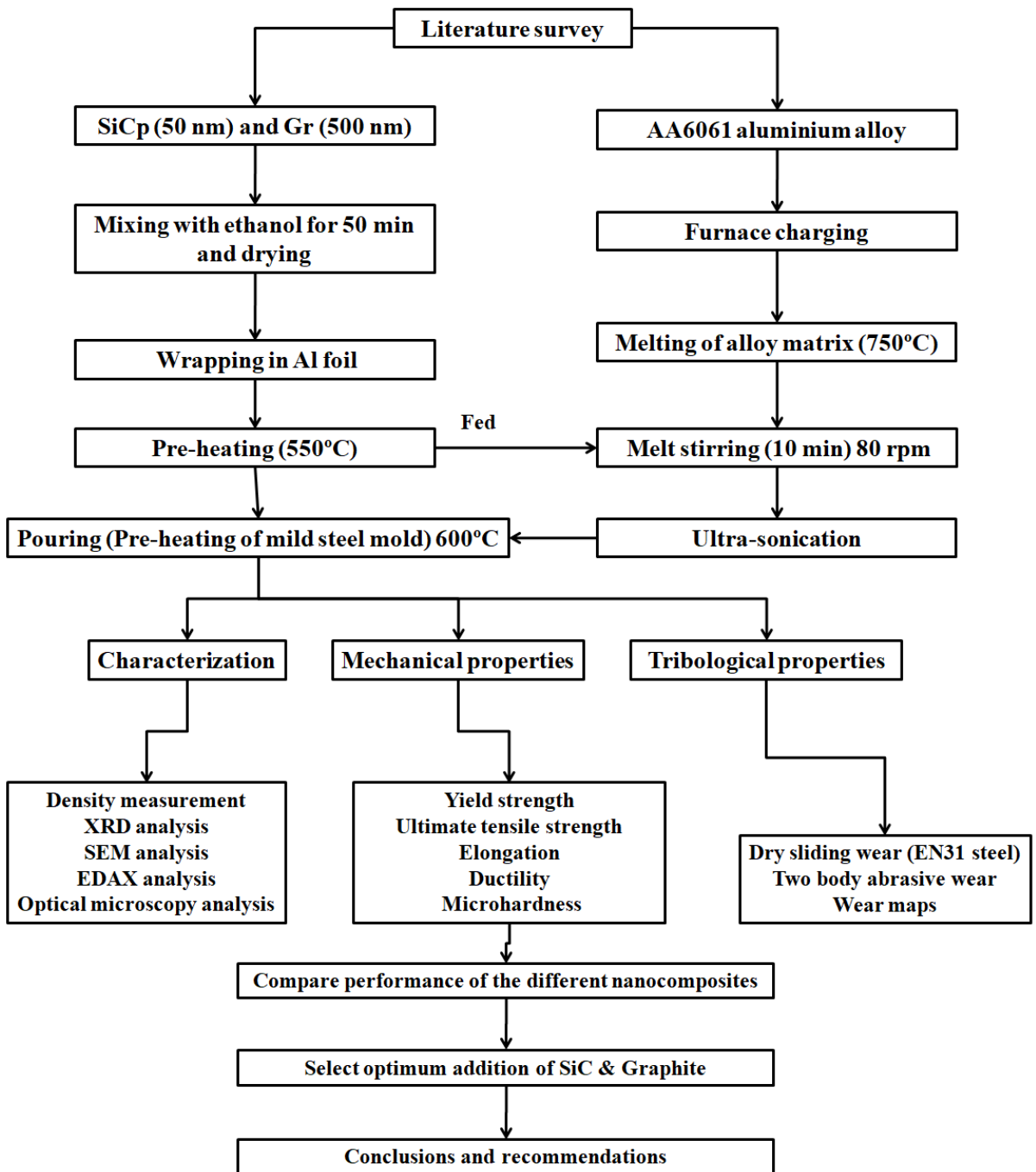


Figure 2.11: The flow chart for the present research work

Chapter 3

Experimentation

3.1 Introduction

In this chapter, the author would present a detail discussion on the selection of materials, AA6061 aluminium alloy, AA6061-x wt. % SiCp ($x = 0.5, 1, 1.5$, and 2) nanocomposites and AA6061-2wt. % SiCp-y wt. % graphite ($y = 0.5, 1, 1.5, 2$ and 3) hybrid nanocomposites fabrication. Basic procedure for measurement of density, material characterization, mechanical properties evaluation, steady state dry sliding wear and two body abrasive wear of materials are reported.

3.2 Materials Selection

In the present study, AA6061 aluminium alloy, an alloy from (Al-Mg-Si) 6xxx series having magnesium and silicon as major alloying elements was chosen as matrix material. A commercial ingot of an AA6061 aluminium alloy was supplied by Bharat Aerospace Metals, India in the T6 condition with a nominal composition of Mg-0.93, Si-0.52, Fe-0.25, Cu-0.18, Mn-0.14, Zn-0.09, Cr-0.07, Ni-0.03, Ti-0.01, and Al (Balance). The elemental chemical analysis of AA6061 aluminium alloy was done using Optical Emission Spectrometer; BAIRD-DV6 is shown in figure 3.1. The spectrometer is equipped with specimen mounting block, system to disperse the excitation radiation, detectors to measure the intensity of the emitted radiation, dedicated computer for converting signals into format for data processing

and a computer with Baird application software. The nano beta phase silicon carbide (SiCp) and nano graphite (graphite) particulate type reinforcements were chosen for the fabrication of MMNCs and HMMNCs. The beta phase silicon carbide nanoparticles with an average particle size of 50 nm with 99% purity were supplied by US Research Nanomaterials, Inc., USA. The morphology of silicon carbide was cubic and it was fabricated by Plasma Chemical Vapor Deposition method. Graphite particles of average particle size 500 nm was supplied by Mknano, M K Impex Corp., Canada. The details of AA6061 aluminium alloy, β -SiCp and graphite reinforcements is shown in Table 3.1. Figure 3.2 (a), (b) and (c) shows the photographic images of AA6061 aluminium alloy, β -SiCp and graphite respectively.



Figure 3.1: The optical emission spectrometer setup

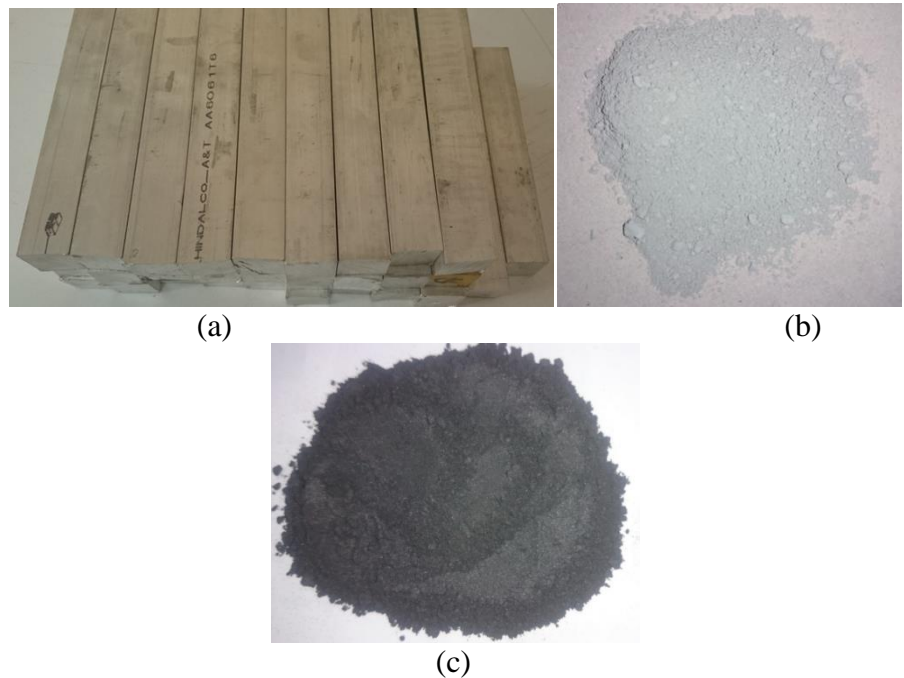


Figure 3.2: The photographic images of (a) AA6061 aluminium alloy (b) β -SiCp and (c) graphite

Table 3.1: Details of AA6061 aluminium alloy, β -SiCp and graphite nano-reinforcements particles [78, 101, 127]

Material/Properties	Hardness (GPa)	Average particle size (nm)	Density (g/cm ³)	Melting Point (°C)
AA6061 aluminium alloy		-	2.7	650
β -SiCp	24.5-28	50	3.218	2730
Graphite	0.25	500	2.266	3730

3.3 Fabrication of Composites

The AA6061/ x wt. % SiCp (x = 0, 0.5, 1, 1.5, and 2) nanocomposites (named as 0.5NC, 1NC, 1.5NC, 2NC) were fabricated using an ultrasonically assisted stir casting technique under protective argon atmosphere. The schematic diagram of ultrasonically assisted stir casting setup is shown in figure 3.3.

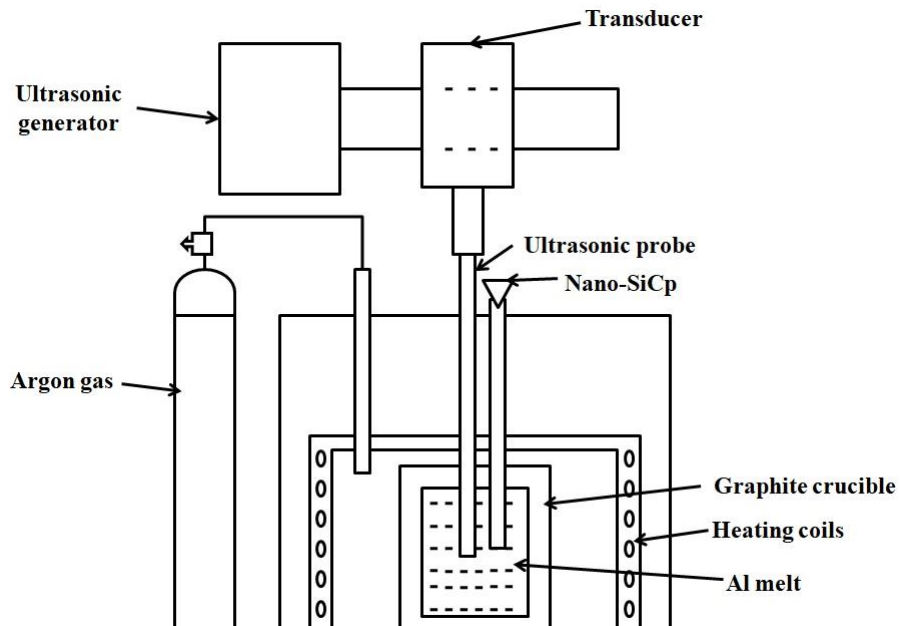


Figure 3.3: Schematic diagram of ultrasonically assisted stir casting setup

The experimental setup shown in figure 3.4 consists of electrical resistance heating furnace, thermocouples, ultrasonic unit, air compressor for cooling the ultrasonic generator, furnace control unit, and argon supply unit. Firstly, the matrix AA6061 aluminium alloy

ingots of 800 g were melted at 750 °C temperature in a 150 mm height by 70 mm diameter graphite crucible by resistance heating furnace. In case of nanocomposites fabrication, SiCp nano-reinforcement particles were folded in an aluminium foil and preheated to 550 °C in a muffle furnace. The preheated wrapped aluminium foil was fed into the inner base of the graphite crucible with the assistance of a plunger. Then the molten metal was mechanically stirred using stirrer at 80 rpm. The constant rotational speed was maintained for 10 min to achieve complete mixing. Ultrasonic horn of 20 mm diameter made up of Ti-10Al-4V alloy coated with zirconia (ZrO_2) was used to transmit ultrasonic waves at 20 kHz frequency with maximum power of 2.4 kW. Later, the ultrasonic probe was dipped to a depth of 40 mm from the top surface of the molten slurry. Subsequently, the mixture of the molten slurry was processed with ultrasound energy wave for 25 min to break the clustered nano-reinforcement particles. After sonication, the graphite crucible was instantly removed from the resistance heating furnace, and the slurry of molten metal was then poured into a mild steel mould. The mould was preheated to 550 °C formerly being filled with the slurry of molten aluminium.

In case of hybrid nanocomposites fabrication the primary reinforcement 2wt. % of SiCp was fixed. Because, the better properties were exhibited by 2 wt. % of SiCp reinforced AA6061 aluminium alloy based nanocomposites compared to lower content of SiCp nanocomposites. It is revealed that the net effect on properties is less with addition of 0.5 wt. % of SiCp to 1.5 wt. % of SiCp reinforced AA6061 aluminium alloy based nanocomposites. The SEM micrographs are the proof that the more SiCp nanoparticles clusters will found as mentioned in chapter 5. The addition of above 2 wt. % of nanoparticles leads to poor distribution, clusters of nanoparticles and microcracks were induced in the base alloy proved by various researchers and specified in their reports [16]. AA6061/2wt. % SiCp/y wt. % graphite ($y = 0.5, 1, 1.5, 2$ and 3) hybrid nanocomposites (named as 0.5HNC, 1HNC, 1.5HNC, 2HNC and 3HNC) were fabricated using an ultrasonically assisted stir casting technique under protective argon atmosphere.

In case of hybrid nanocomposites fabrication, commercially available pure AA6061 aluminium alloy ingot of 500 g was melted at 750 °C in a steel crucible of inside diameter 70 mm, thickness 8 mm and length 120 mm. The SiCp and graphite nano-reinforcement particles were folded in an aluminium foil and preheated to 550 °C in a muffle furnace. Upon reaching 780 °C, nano-sized SiCp and graphite particles enclosed with aluminium foil and

preheated up to 550 °C, were fed into the AA6061 aluminium alloy melt. Mechanical stirrer was used to mix the nano-sized SiCp and graphite particles into the AA6061 aluminium alloy melt for about 10 min. The ultrasonic probe was preheated to 780 °C and inserted into the AA6061 aluminium alloy melt to a depth of about 25 mm for 25 min. The ultrasonic processed molten composition was poured into a mild steel mould, which was preheated to 550 °C. After solidification, the cast ones were removed from the die.

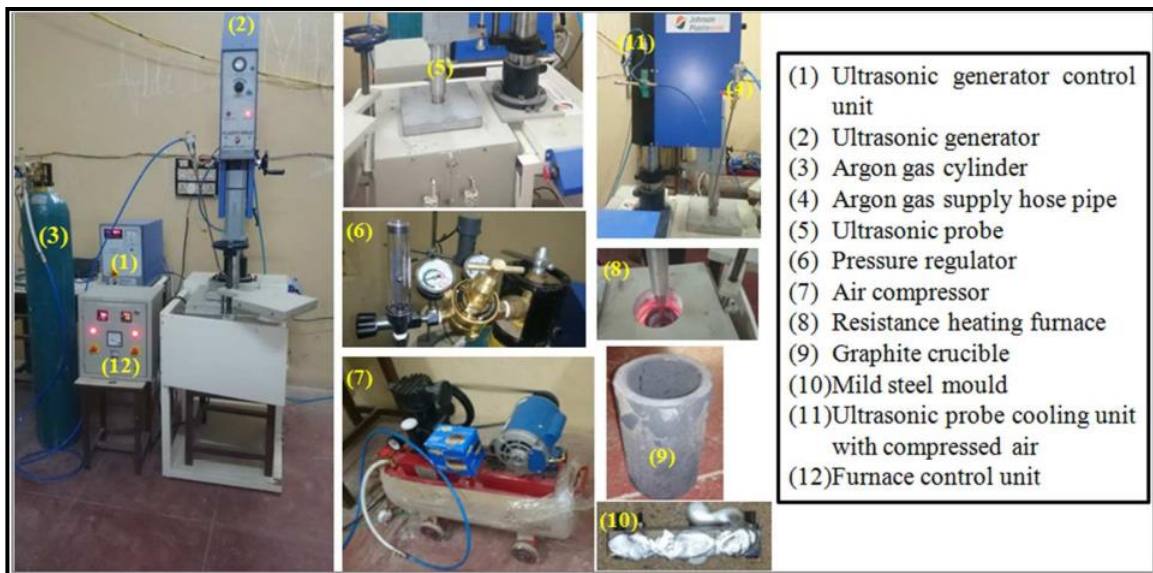


Figure 3.4: Ultrasonically assisted stir casting setup

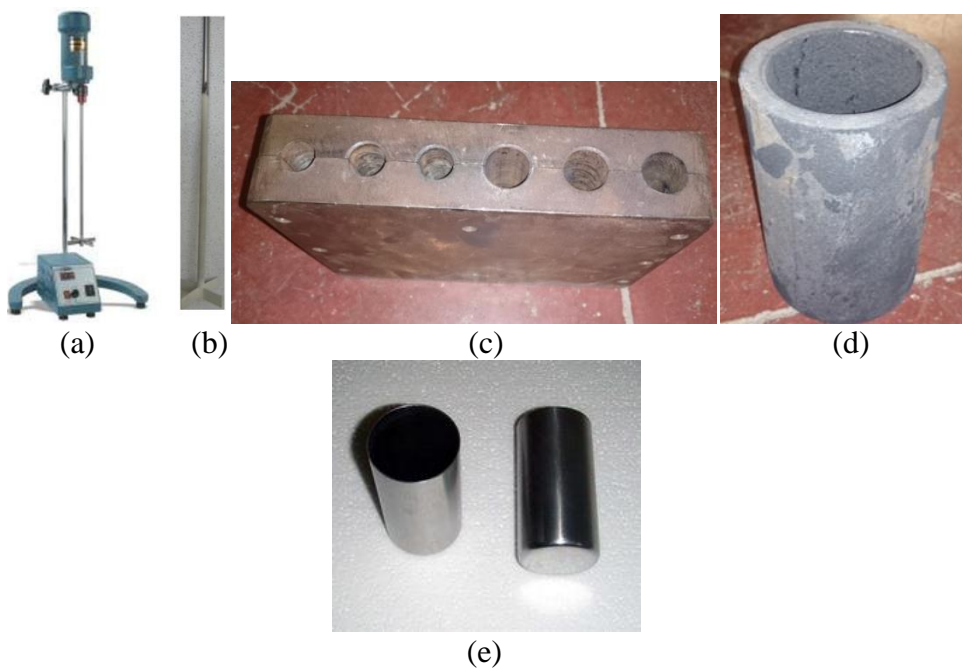


Figure 3.5: Images of (a) electro mechanical stirrer (b) SS 304 stirrer rod coated with zirconia (ZrO_2) (c) mild steel die (d) graphite crucible and (e) stainless steel crucible

Figure 3.5 (a), (b), (c), (d) and (e) depicts the photographic images of the various elements used in the fabrication of nanocomposites. Figure 3.5 (a) represents the electro mechanical stirrer attached with variable speed motor; figure 3.5 (b) shows the SS304 stirrer rod used to create stirring action which was coated with zircon (ZrO_2), figure 3.5 (c) indicates the mild steel mould used for pouring molten slurry and left for solidification, figure 3.5 (d) shows the graphite crucible and figure 3.5 (e) indicates the stainless steel crucible. The fabricated nanocomposites and hybrid nanocomposites specimens are shown in figure 3.6.



Figure 3.6: Photograph snapshot of (a) nanocomposite samples and (b) hybrid nanocomposite samples

3.4 Density Measurement

3.4.1 Experimental Density

The density of the AA6061 aluminium alloy, 0.5NC, 1NC, 1.5NC, and 2NC nanocomposites and 0.5HNC, 1HNC, 1.5HNC, 2HNC and 3HNC hybrid nanocomposites was measured using Archimedes principle. It is easy method for measuring volume of a given specimens. The density of the AA6061 aluminium alloy, nanocomposites and hybrid nanocomposites specimens was examined using a high precision digital electronic weighing balance with an accuracy of 0.0001g is shown in figure 3.7. Ten vertical measurements were made on each specimen. Mass of the specimen was measured on balance with five decimal point accuracy.

Procedure for measuring density

- Mass of the specimen was measured in air (M_{sa}) in grams

- Then the sample is submerged completely in water and the mass is measured (M_{sw}) in grams

- The water displaced ($V = M_{sa} - M_{sw}$) in grams. When ($\rho_w = 1 \frac{g}{cm^3}$)

$$\rho_{sm} = \frac{M_{sa}}{M_{sa} - M_{sw}} \quad (3.1)$$

- By using the equation 3.1, the density of specimen was calculated.
- The densities measured for all combination of AA6061 aluminium alloy, MMNCs and HMMNCs. Each experiment is conducted ten times and the average of ten results is considered.



Figure 3.7: High precision digital electronic weighing balance

3.4.2 Theoretical Density

Theoretical density of the 0.5NC, 1NC, 1.5NC, and 2NC nanocomposites and 0.5HNC, 1HNC, 1.5HNC, 2HNC and 3HNC hybrid nanocomposites was calculated using rule of mixtures [16]. Nanocomposite materials consist of two phases i.e., matrix material and nano-reinforcements. The volume of nanocomposite material is equal to the sum of volume of SiCp nano-reinforcements and the volume of the AA6061 aluminium alloy matrix. The volume of nano-reinforcements and AA6061 aluminium alloy matrix can be calculated from weight equations 3.2, 3.3, and 3.4. The total volume of the nanocomposite is given in equation 3.5.

$$V_{SiC} = \frac{M_{SiC}}{\rho_{SiC}} \quad (3.2)$$

$$V_{Gr} = \frac{M_{Gr}}{\rho_{Gr}} \quad (3.3)$$

$$V_{AA6061} = \frac{M_{AA6061}}{\rho_{AA6061}} \quad (3.4)$$

$$V_{nc} = V_{AA6061} + V_{SiC} \quad (3.5)$$

Where, V_{nc} is volume of nanocomposite, V_{AA6061} is volume of AA6061 aluminium alloy matrix and V_{SiC} is volume of SiCp nano-reinforcements.

The volume fraction of SiCp nano-reinforcements and AA6061 aluminium alloy matrix can be defined as:

$$\nu_{SiC} = \frac{V_{SiC}}{V_{nc}} \quad (3.6)$$

$$\nu_{AA6061} = \frac{V_{AA6061}}{V_{nc}} \quad (3.7)$$

$$\nu_{nc} = \frac{V_{SiC}}{V_{nc}} + \frac{V_{AA6061}}{V_{nc}} = 1 \quad (3.8)$$

The sum of volume fraction of SiCp nano-reinforcements and AA6061 aluminium alloy matrix is equal to one.

The theoretical density of the nanocomposites can be written as equation 3.9 [16]:

$$\rho_{nc} = \rho_{SiC} \nu_{SiC} + \rho_{AA6061} \nu_{AA6061} \quad (3.9)$$

In case of hybrid nanocomposites total volume of the hybrid nanocomposite is given in equation 3.10.

$$V_{hnc} = V_{AA6061} + V_{SiC} + V_{Gr} \quad (3.10)$$

Where, V_{hnc} is volume of hybrid nanocomposite, V_{AA6061} is volume of AA6061 aluminium alloy matrix, V_{SiC} is volume of SiCp nano-reinforcements and V_{Gr} is volume of graphite nano-reinforcements. The volume fraction of SiCp, graphite nano-reinforcements and AA6061 aluminium alloy matrix can be defined as:

$$v_{SiC} = \frac{V_{SiC}}{V_{hnc}} \quad (3.11)$$

$$v_{graphite} = \frac{V_{graphite}}{V_{hnc}} \quad (3.12)$$

$$v_{AA6061} = \frac{V_{AA6061}}{V_{hnc}} \quad (3.13)$$

$$v_{hnc} = \frac{V_{SiC}}{V_{hnc}} + \frac{V_{AA6061}}{V_{hnc}} + \frac{V_{graphite}}{V_{hnc}} = 1 \quad (3.14)$$

The theoretical density of the hybrid nanocomposites can be written as equation 3.15 [16]:

$$\rho_{hnc} = \rho_{SiC} v_{SiC} + \rho_{AA6061} v_{AA6061} + \rho_{graphite} v_{graphite} \quad (3.15)$$

3.5 Characterization

AA6061 aluminium alloy based MMNCs and HMMNCs are fabricated and further analyzed for microhardness, phase analysis, and the study of microstructure through optical microscopy and scanning electron microscopy, volumetric wear rate and coefficient of friction measurement.

3.5.1 Specimen Preparation

The specimen preparation includes cutting, mechanical grinding, coarse polishing, fine polishing and etching. The specimens were polished by using different silicon carbide abrasive papers of grades 200, 400, 600, 800, 1000, and 1200, respectively, and followed by cloth polishing. For microstructural features, the polished specimens were etched with 25 ml methanol (CH_2O), 25 ml hydrochloric acid (HCl), 25 ml nitric acid (HNO_3) and one drop of hydrofluoric acid (HF) for 40 seconds. After they were cleaned with water and dried with acetone, etch-polish-etch procedures were used to attain real microstructure.

3.5.2 X-Ray Diffraction Analysis (XRD)

To identify the phases formation in the prepared AA6061 aluminium alloy, AA6061- x wt. % SiCp ($x = 0.5, 1, 1.5$, and 2) nanocomposites and AA6061-2wt. % SiCp- y wt. % graphite ($y = 0.5, 1, 1.5, 2$ and 3) hybrid nanocomposites X-ray Diffraction (XRD) technique

was used. The technique was used to measure the average spacing between layers or rows of atoms, orientation of a single crystal or grain, crystal structure of an unknown material, impurities, size, shape, internal stress of small crystalline regions and phases of the fabricated specimens. In this technique, an incident beam of X-rays to interfere with one another as they leave the crystal. The phenomenon is called X-ray diffraction. The XRD setup is shown in figure 3.8.



Figure 3.8: XRD equipment (Model PANalytical)

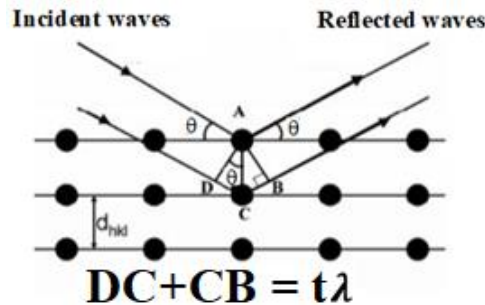


Figure 3.9: Schematic description of Bragg's Law [163]

The Bragg's law stated and followed the interference of these waves is given below [163]:

$$t\lambda = 2d_{hkl} \sin \theta \quad (3.16)$$

where t is order of reflection, λ is the wavelength and d_{hkl} is the lattice spacing. The schematic description of Bragg's Law is shown in figure 3.9. By varying the incidence angle of the incoming X-ray beam by ' θ ' and scattering angle by ' 2θ ' the scattered intensity is

measured as a function of the latter. The XRD setup is used where the sample remains in a fixed position while both X-ray source and detector rotate by ‘θ’, clockwise and anticlockwise, respectively. These precise movements were performed by a goniometer which is a main part of the diffractometer.

3.5.3 Optical Microscopy

The microstructure of the fabricated materials through ultrasonically assisted stir casting technique was analyzed through optical microscope. The major role of optical microscope in microstructure study was the analysis of grain size and reinforced particles in the AA6061 aluminium alloy matrix. The study of MMNCs and HMMNCs microstructures was carried out using optical microscopy to determine the primary characteristics of the samples. For study of microstructure, the specimens were observed using a (Make: Quasmo-Model: QX-4RT) optical microscope shown in figure 3.10. The magnification of optical microscopy is 4X, 10X, 20X, 40X, and 100X. The mechanical stage is 4"double layer than can move in a range 105x105 mm.

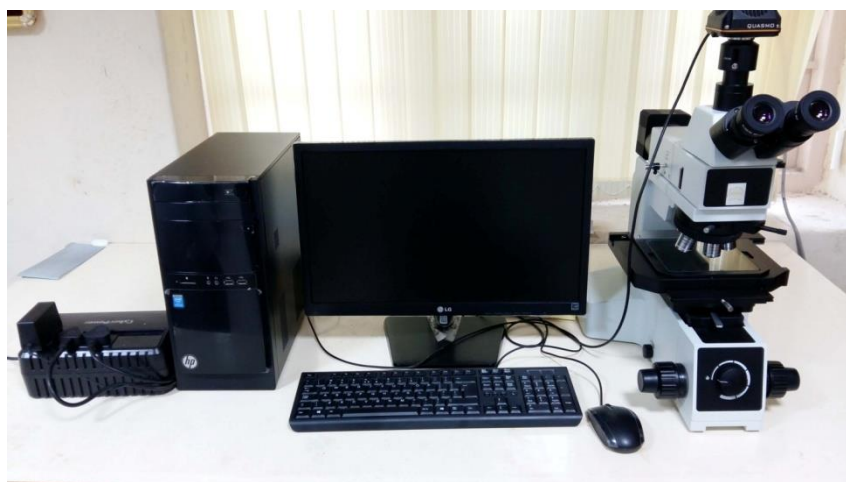


Figure 3.10: Optical microscopy (Quasmo make model: QX-4RT)

3.5.4 Scanning Electron Microscopy

The scanning electron microscope (SEM) is a microscope that uses electrons rather than light to form an image. The scanning electron microscope (SEM) is used to examine the topography, morphology, composition and crystallographic information. The basic principle of SEM is the electron beam produced from the tungsten filament is focused with magnetic

lenses and hits the specimen. The electron beam collides with top surface electrons from the specimen. Many signals are generated by the interaction of the electron beam with the specimen. Each of these signals are sensitive to a different aspect of the specimen and gives a variety of information about the specimen by detecting the signals which will emit. The SEM setup [TESCAN make, Model: Vega LMU 3] used in this study is shown in figure 3.11. Resolution of the SEM is of the order of 3.0 nm at high vacuum mode and 3.5 nm at low vacuum mode. The magnification of SEM can go up to 1.5x to 100000x which depends on the chamber.

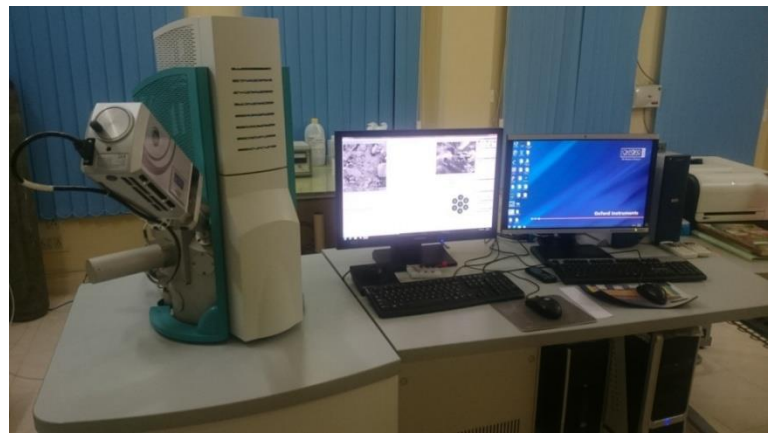


Figure 3.11: Scanning electron microscopy equipment

3.5.5 Transmission Electron Microscopy



Figure 3.12: Transmission electron microscopy equipment at Hyderabad Central University

Transmission Electron Microscopy (TEM) is an instrument used to view thin samples for examining the morphology, crystallographic information, average particle size and composition of specimens. TEM is the most powerful microscope that can go up to 1 nanometer magnification. TEM operates on the basic principle, electron beam passes through a thin-section of material and gets scattered. The electromagnetic lenses focus on the scattered electrons and thus converts into an image. The TEM setup [FEI make, Model: Tecnai G2S Twin] used in this study for nanoparticle size analysis (Central University of Hyderabad, India) is shown in figure 3.12. The specifications of the TEM are presented in Table 3.2.

Table 3.2: Specifications of TEM (FEI make: Model G2S Twin)

Type	TWIN	S-TWIN
TEM point resolution (nm)	0.27	0.24
TEM line resolution (nm)	0.144	0.144
Minimum focus step (nm)	2	1.8
TEM magnification range	25x-700 kx	25 x-1030 kx
Camera length (mm)	52-6,000	30-4,500
Maximum diffraction angle	$\pm 10^\circ$	$\pm 13^\circ$
STEM resolution (nm)	1.0	1.0
STEM magnification range	100 x-5 Mx	100 x-5 Mx
EDS solid angle (srad)	0.13	0.13

3.6 Mechanical Properties

3.6.1 Tensile Test

The tensile test of AA6061 aluminium alloy, MMNCs and HMMNCs was conducted as per American Society for Testing and Materials (ASTM E8/E8M) standards [70]. In this test, the stress versus strain diagram, yield strength and ultimate tensile strength were obtained. Tensile test of AA6061 aluminium alloy, MMNCs and HMMNCs was conducted at room temperature (25 °C) with a strain rate of $10^{-3}/s$ using computerized electromechanical tensile testing machine shown in figure 3.13. The dimensions of samples prepared as per ASTM E8/E8M standards is shown in figure 3.14. The prepared nanocomposites specimens

as per ASTM E8/E8M are shown in figure 3.15. This UTM was used to conduct simple tension, compression and 3-point bending test. The results were recorded accurately with a break point. The stress at maximum is referred to as the ultimate tensile strength. Tensile experiments were repeated for the same composition for five times to get accurate results on each composite sample and subsequently each of them was averaged. The specifications of UTM are presented in Table 3.3.



Figure 3.13: Electro-mechanical universal testing machine (Blue Star WDW-100S) at NIT Warangal

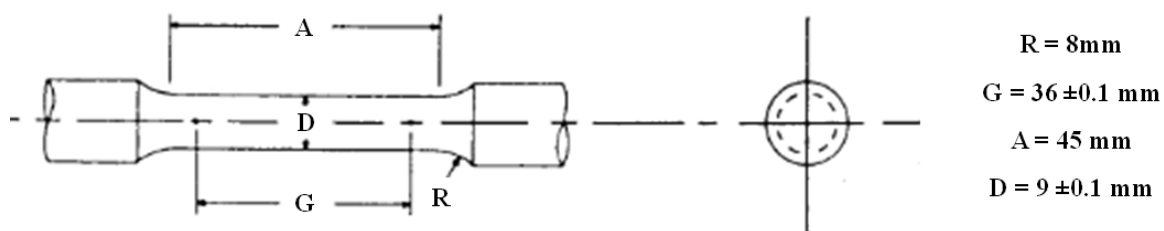


Figure 3.14: Tensile test sample dimensions according to ASTM E8/E8M standards



Figure 3.15: Nanocomposite samples as per ASTM E8 standards

Table 3.3: Specifications of UTM (Universal Testing Machine)

Make	M/s. Jin Ahn Testing, China
Model	WDW-100S
Maximum load	$\pm 100\text{kN}$ (Celtron USA)
Temperature	-100 °C to 300 °C (chamber) 300 °C to 1000 °C (3-zone split furnace)
Available extensometers (50% maximum strain)	25 mm, Resolution = 0.1 μm 12.5 mm, Resolution = 0.1 μm
Daylight	1400 mm
Speed range	0.0005 mm/min to 500 mm/min
Tests that can be performed	Simple tension/compression, 3-point bending

3.6.2 Hardness Test



Figure 3.16: Micro Vicker's hardness tester (Make: Shimadzu, Model: HMV-G20ST)

The microhardness of the materials indicates the mechanical properties of the specimens. When the surface properties concerned its importance to wear and friction processes, then measurement of microhardness of the material is a quick method to get mechanical property. The basic principle of microhardness test is forcing an indenter into the material surface and measuring the dimensions of the indentation. The microhardness of AA6061 aluminium alloy, MMNCs and HMMNCs materials was measured using vickers microhardness tester [Make: Shimadzu, Model: HMV-G20ST] shown in figure 3.16. The indenter with a square based pyramidal diamond shape of face angles 136°, 250 gf test load,

and 10 s dwell time were used for microhardness study. The vicker microhardness experiments were conducted according to ASTM: E384-08 standard [16]. Six readings were taken and the average value was considered. The magnification can vary from 800x to 1000x with objective lense of 10x, 40/50x, 80/100x along with 10x eyepiece. The test load can vary from 10 gf to 2000 gf with dwell time of 5 to 99 sec, with loading speed of 15 to 70 $\mu\text{m/sec}$.

3.7 Wear Test

3.7.1 Dry Sliding Wear Test on EN31 Steel

Wear tests were conducted as per G 99-05 ASTM standards (pin diameter of 8 mm and length of 25 mm) using pin-on-disc setup of Magnum Model-TE-165 [95]. The specifications of pin on disc machine is presented in Table 3.4. The wear test process parameters used in experiments is shown in Table 3.5. Snapshot of dry sliding wear test of sample is shown in figures 3.17 and 3.18. Based on the mass loss and volumetric wear rate observed in the trial experiments with AA6061 aluminium alloy and its nanocomposites parametric ranges were fixed.

Table 3.4: Specification of the pin on disc machine

Pin dimensions	3 to 12 mm diameter and 10 to 50 mm length
Disc dimensions	160 mm diameter and 12 mm thickness
Wear track radius	8 mm to 120 mm diameter
Disc rotating speeds	100 rpm to 1000 rpm
Sliding speed range	0.5 m/s to 26 m/s
Normal load	200 N (maximum)
Frictional force	0 to 200 N (digital read out)
Wear height loss measurement	LVDT of 1.0 μm least count
Input power	230 V, 5 A, I Phase, 50 Hz

$$\Delta V_l = \frac{M_i - M_f}{\rho} \quad (3.17)$$

$$W_l = \frac{\Delta V_l}{SD} \quad (3.18)$$

$$K = \frac{\Delta V_l \times H_m}{SD \times L} \quad (3.19)$$

where ‘ ΔV_l ’ volume loss; $(M_i - M_f)$ change in mass (mm^3); ‘ ρ ’ density of pin specimen (10^{-6} g/mm^3); ‘SD’ is sliding distance of pin (m), ‘ W_l ’ volume metric wear rate (mm^3/m), ‘K’ is wear coefficient of pin material, ‘ H_m ’ is hardness of pin material in (N/mm^2) and ‘L’ is normal load on pin material (N).



Figure 3.17: (a) snapshot of dry sliding wear test of sample (b) top view of dry sliding wear test of sample

Table 3.5: Tribological test process parameters used in experiments

Tribological parameters (Units)	Experimental Conditions
Normal load (N)	5, 10, 15, 20
Sliding velocity (m/s)	0.5, 1, 1.5, 2
Sliding distance (m)	1000, 2000, 3000
Materials	AA6061 aluminium alloy, 0.5NC, 1NC, 1.5NC, 2NC, 0.5HNC, 1HNC, 1.5HNC, 2HNC, 3HNC
Temperature (°C)	25±2
Humidity (%)	67±2
Surface roughness, Ra (μm)	0.21
Repeated test for each sample	3

The disc was made up of EN31 steel of diameter 165 mm by 8 mm thick. The pin samples were cleaned with acetone before performing the wear tests. After performing the

wear test, wear rates and wear coefficients were calculated from equations 3.17, 3.18 and 3.19. All the tests were repeated for three times and average value was taken individually.



Figure 3.18: (a) snapshot of dry sliding wear test of sample before (b) snapshot of top view of dry sliding wear after test

3.7.2 Two Body Abrasive Wear Test

Two body abrasion wear tests were conducted as per ASTM D6037 standard using pin-on-disc machine [Magnum make model (TE-165), Bangalore, India] [88]. The two body abrasive wear process parameters used in experiments is shown in Table 3.6. The two body abrasion wear test was conducted with silicon carbide coated emery papers [CUMI make, Muragappa Group, India] at applied normal loads of 5-20 N, sliding distance of 60-180 m and sliding velocity of 0.5-2 m/s. The abrasive grit papers were sized ($\Phi 50$ mm, 12 mm thickness) to fix on EN31 steel wheel to act as a medium for abrasion.

The samples were cleaned with acetone before performing the abrasion wear experiments. After performing the two body abrasion test, wear rate was calculated from equations 3.17 and 3.18. Every experiment was repeated for four times and average values were taken. To identify the feasible wear mechanism during abrasion test, the worn surfaces

of pin specimens and various sizes of abrasive grits were examined. The samples were cleaned with acetone after two body abrasive wear tests. The weight of the sample was measured before and after abrasion wear test and noted the corresponding weight loss of the sample. Figure 3.19 denotes the two body abrasive wear testing of a nanocomposite specimen. After performing the two body abrasion test, weight loss, volume loss, volumetric wear rates and wear coefficients were calculated using the equations 3.17, 3.18, and 3.19 respectively. Figure 3.20 shows the snapshot of two body abrasive wear testing of sample before and after.



Figure 3.19: (a) Snapshot of two body abrasive wear testing of sample (b) Top view of abrasive wear testing of sample

Table 3.6: Tribological test process parameters used in two body abrasive wear test

Tribological parameters (Units)	Experimental Conditions
Normal load (N)	5, 10, 15, 20
Sliding velocity (m/s)	0.5, 1, 1.5, 2
Sliding distance (m)	60, 120, 180
Abrasive grit particle size (μm)	50, 100, 150
Materials	AA6061 aluminium alloy, 2NC and 2HNC
Temperature ($^{\circ}\text{C}$)	25 \pm 2
Humidity (%)	67 \pm 2
Surface roughness, Ra (μm)	0.21
Repeated test for each sample	4



Figure 3.20: (a) snapshot of two body abrasive wear testing of sample before (b) top view of after two body abrasive wear test

3.8 Summary

The AA6061 aluminium alloy reinforced with SiCp and graphite nano particles were fabricated using the ultrasonically assisted stir casting technique. The fabricated nanocomposites and hybrid nanocomposite specimens were prepared for characterization, mechanical and tribological tests according to ASTM standards. The morphology, topography, phases, abrasive grit papers, worn surfaces, fractography of tensile samples and chemical composition of the various nanocomposites and hybrid nanocomposites were analyzed using optical microscope, SEM and XRD. The mechanical properties of nanocomposites and hybrid nanocomposites were measured using tensile testing machine and Vickers microhardness tester. The wear tests were conducted on a pin on disc setup against the counter body material. The two body abrasive wear test was conducted on a pin with abrasive grit paper fixed on steel EN31. The worn surfaces of pin material and worn surfaces of grit papers were examined using SEM.

Chapter 4

Characterization

4.1 Introduction

In this chapter, the author would present the characterization of ultrasonically assisted stir casted samples. The density, porosity, average grain size of the AA6061 aluminium alloy, nanocomposites and hybrid nanocomposites are presented. Further, the morphology, phase analysis of nanocomposites and hybrid nanocomposites, TEM analysis on topography of SiCp and graphite particles is studied in detail.

4.2 Density

The theoretical, experimental density and porosity of the AA6061 aluminium alloy, 0.5NC, 1NC, 1.5NC and 2NC nanocomposites are shown in figure 4.1. Density of AA6061 aluminium alloy, 0.5NC, 1NC, 1.5NC and 2NC nanocomposites is found to be 2.685 g/cm³, 2.691 g/cm³, 2.695 g/cm³, 2.7 g/cm³ and 2.709 g/cm³ respectively from experimental data. The obtained experimental density of the nanocomposites is observed to be less than the theoretical density. This is due to the presence of voids and pores in the nanocomposites. Density of 0.5NC, 1NC, 1.5NC, and 2NC nanocomposites is increased by 0.2%, 0.37%, 0.6%, and 0.9% respectively compared to AA6061 aluminium alloy. The density of the nanocomposites improved with increasing weight percent of nano SiCp in the AA6061 aluminium alloy matrix, because the density of the SiCp is greater than the base alloy matrix. During ultrasonic cavitation process, the SiCp reinforcement clusters disintegrate into

nanoparticles and distribute in the matrix. The porosity of the nanocomposites increased with increasing weight percentage of SiCp nano-reinforcements.

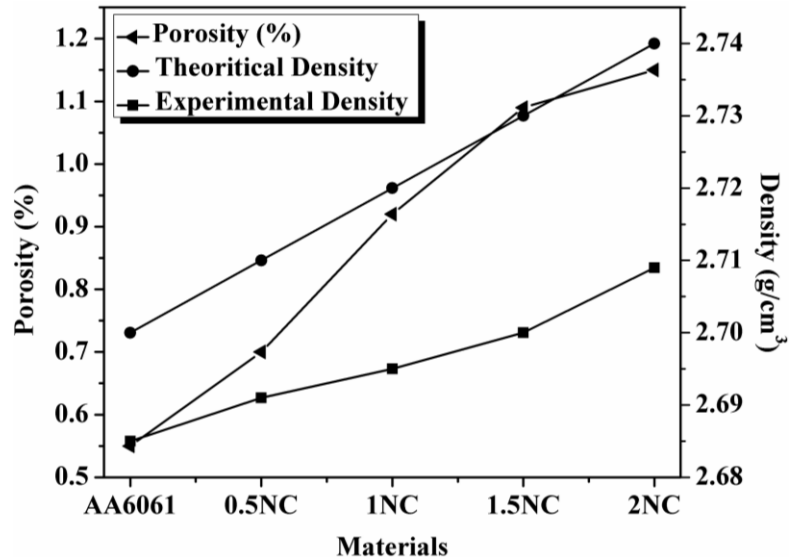


Figure 4.1: Theoretical, experimental density and porosity of the AA6061 aluminium alloy, 0.5NC, 1NC, 1.5NC and 2NC nanocomposites

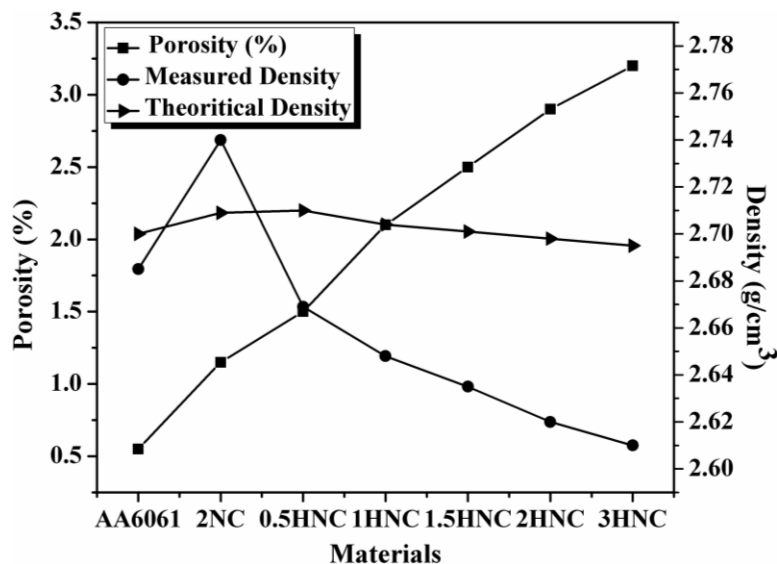


Figure 4.2: Density of AA6061 aluminium alloy, 0.5HNC, 1HNC, 1.5HNC, 2HNC and 3HNC hybrid nanocomposites

Figure 4.2 represents the theoretical, experimental density and porosity of the AA6061 aluminium alloy, 0.5HNC, 1HNC, 1.5HNC, 2HNC and 3HNC hybrid nanocomposites. Density of AA6061 aluminium alloy, 0.5HNC, 1HNC, 1.5HNC, 2HNC and

3HNC hybrid nanocomposites is found to be 2.685 g/cm^3 , 2.657 g/cm^3 , 2.648 g/cm^3 , 2.603 g/cm^3 , 2.594 g/cm^3 , and 2.569 g/cm^3 respectively from experimental data. Density of 0.5HNC, 1HNC, 1.5HNC, 2HNC and 3HNC hybrid nanocomposites is decreased by 1%, 1.4%, 3.1%, 3.4%, and 4.3% respectively compared to AA6061 aluminium alloy. It is noticed that the density of hybrid nanocomposites reduced due to the presence of lower density of graphite powder compared to the nanocomposite and base material. The porosity of hybrid nanocomposites increased with increase of graphite nano-reinforcements in the AA6061 aluminium alloy matrix. This would be attributed to the rise in contact surface area of graphite nanoparticles with air and more quantity of air occupy some space in the molten metal during ultrasonic operation. Similarly, the rise in porosity of nanocomposites reported with increase of weight percent in the matrix [127].

4.3 XRD Analysis

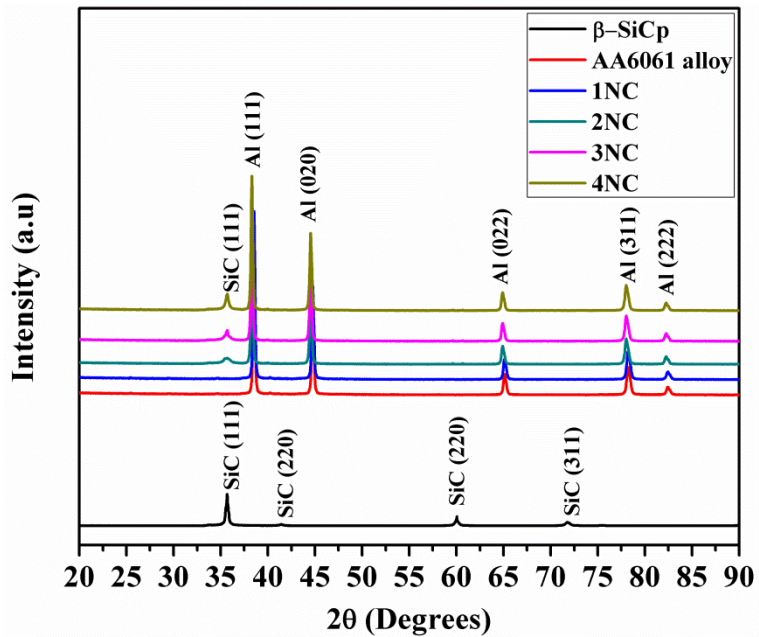


Figure 4.3: XRD analysis of SiCp, AA6061 aluminium alloy and its nanocomposites

The properties of nanocomposites are influence by the nature of the reinforcing material used. XRD studies have been used for identification of phases in the nanocomposites. The phases of nanocomposites are recognize through JCPDs software. In XRD pattern, ‘ 2θ ’ peaks have been observed ranging from 20° to 90° . XRD analysis of the nanocomposites is presented in figure 4.3. XRD spectrum confirms the presence of strong diffraction peaks at ‘ 2θ ’ values of 38.43° for (111), 44.56° for (020), 64.94° for (022), 78.3°

for (311), and 82.14° for (222) planes belongs to aluminium (JCPDS Card No.89-4037). The strong diffraction peaks at '2θ' values of 35.68° for (111), 41.44° for (200), 60.1° for (220), 71.8° for (311), and 82.14° for (222) planes belongs to SiCp (JCPDS Card No.74-2307). It is observed that high-intensity peaks pertain to aluminium and small intensity peaks pertain to SiCp reinforcement particles in the AA6061 nanocomposites.

XRD analysis of AA6061 aluminium alloy, SiCp, graphite, 2NC nanocomposite, 0.5HNC, 1HNC, 1.5HNC, 2HNC and 3HNC hybrid nanocomposites is presented in figure 4.4. XRD spectrum confirms the presence of strong diffraction peaks at '2θ' values of 38.43° for (111), 44.56° for (020), 64.94° for (022), 78.3° for (311), and 82.14° for (222) planes belongs to aluminium (JCPDS Card No.89-4037). The strong diffraction peaks at '2θ' values of 35.68° for (111), 41.44° for (200), 60.1° for (220), 71.8° for (311), and 82.14° for (222) planes belongs to SiCp (JCPDS Card No.74-2307). The strong diffraction peaks at '2θ' values of 26.48° for (111), 44.38° for (101), 54.57° for (004) and 72.71° for (110) planes belongs to C (JCPDS Card No.75-1621). The XRD pattern for 1.5HNC, 2HNC and 3HNC hybrid nanocomposites at different intensity of peaks are exhibited at C (002), SiCp (111), Al (111), Al (020), Al (022), Al (311), and Al (222). The intensity of peak is lower for graphite and SiCp due to lower content in the matrix. The intensity of peaks of graphite doesn't appear in the 0.5HNC and 1HNC hybrid nanocomposite due to its lower content in the matrix.

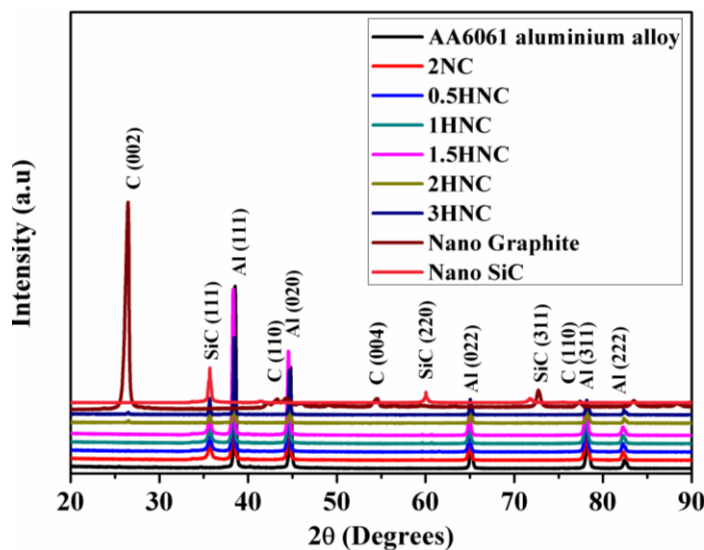


Figure 4.4: XRD of pure AA6061 aluminium alloy, 2NC nanocomposite, and 0.5HNC, 1HNC, 1.5HNC, 2HNC and 3HNC hybrid nanocomposites

4.4 Optical Microstructure

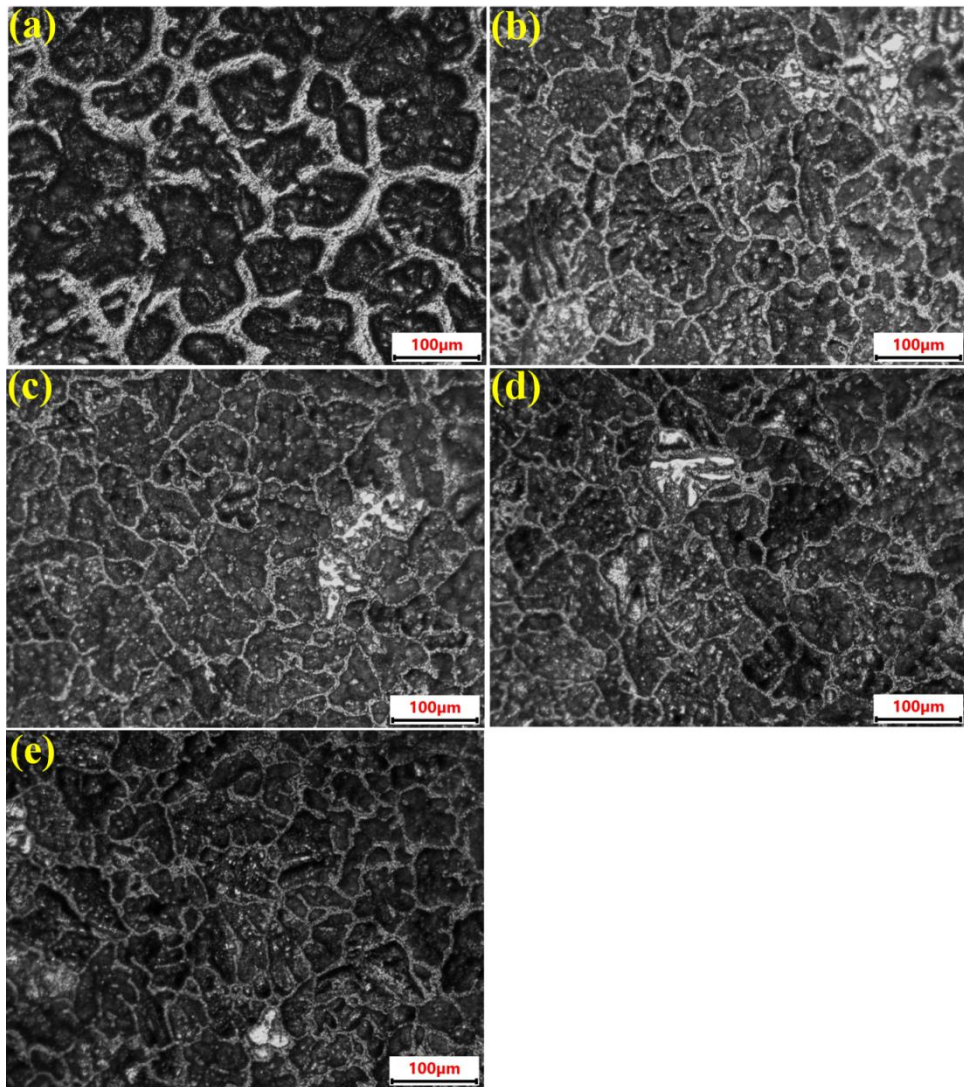


Figure 4.5: Optical micrographs of (a) AA6061 aluminium alloy, (b) 0.5NC, (c) 1NC, (d) 1.5NC, and (e) 2NC

Figure 4.5 shows the optical micrographs of various materials processed through ultrasonically assisted stir casting i.e., AA6061 aluminium alloy, 0.5NC, 1NC, 1.5NC and 2NC nanocomposites. The grain refinement is observed in the microstructure by increasing SiCp content in the AA6061 aluminium alloy matrix. The optical micrographs reveal the variation of grain size of nanocomposites compared to AA6061 aluminium alloy. The variation of average size of grains is represented in figure 4.6. Five samples were considered for calculating the variation in grain size. The average grain size of different materials is 120 μm for AA6061 aluminium alloy, 75 μm for 0.5NC, 69 μm for 1NC, 55 μm for 1.5NC and

27 μm for 2NC. The microstructure of different nanocomposites reveals that the average grain size is reduced with increasing SiCp nano-reinforcements in the AA6061 aluminium alloy. The reduction of average grain size compared to base alloy is 38%, 43%, 54% and 78% for 0.5NC, 1NC, 1.5NC and 2NC respectively. This would be attributed to the increase of SiCp nano-reinforcements in molten metal, which act as heterogeneous nucleation sites and increase the rate of nucleation. Grain refinement occurs mainly based on the reinforcement particle size, wt. % of nanoparticles and ultrasonic cavitation effect [127].

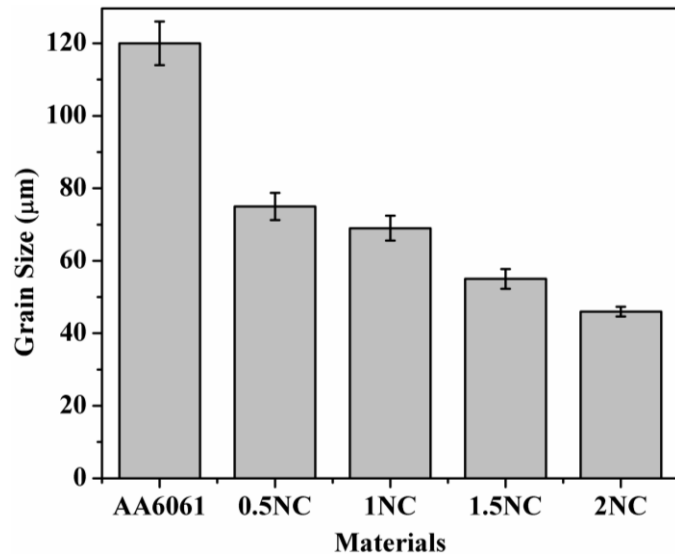


Figure 4.6: Average grain size (a) AA6061 aluminium alloy, (b) 0.5NC, (c) 1NC, (d) 1.5NC, and (e) 2NC

Figure 4.7 shows the optical micrographs of various materials processed through ultrasonically assisted stir casting i.e., AA6061 aluminium alloy, 0.5HNC, 1HNC, 1.5HNC, 2HNC and 3HNC hybrid nanocomposites. The grain refinement is observed in the microstructure by keeping SiCp as constant with increasing graphite content in the AA6061 aluminium alloy matrix. The optical micrographs reveal the variation of grain size of hybrid nanocomposites compared to AA6061 aluminium alloy.

The variation of average size of grains is represented in figure 4.8. The average grain size of different materials is 120 μm for AA6061 aluminium alloy, 42 μm for 0.5HNC, 35 μm for 1HNC, 25 μm for 1.5HNC, 20 μm for 2HNC and 15 μm for 3HNC respectively. The microstructure of different hybrid nanocomposites reveals that the average grain size is reduced with increase in the graphite nano-reinforcements in the AA6061 aluminium alloy.

The reduction of average grain size compared to base alloy is 65%, 71%, 79%, 83% and 88% for 0.5HNC, 1HNC, 1.5HNC, 2HNC and 3HNC respectively. This would be attributed to the increase of graphite nano-reinforcements in molten metal, which act as heterogeneous nucleation sites and increase the rate of nucleation.

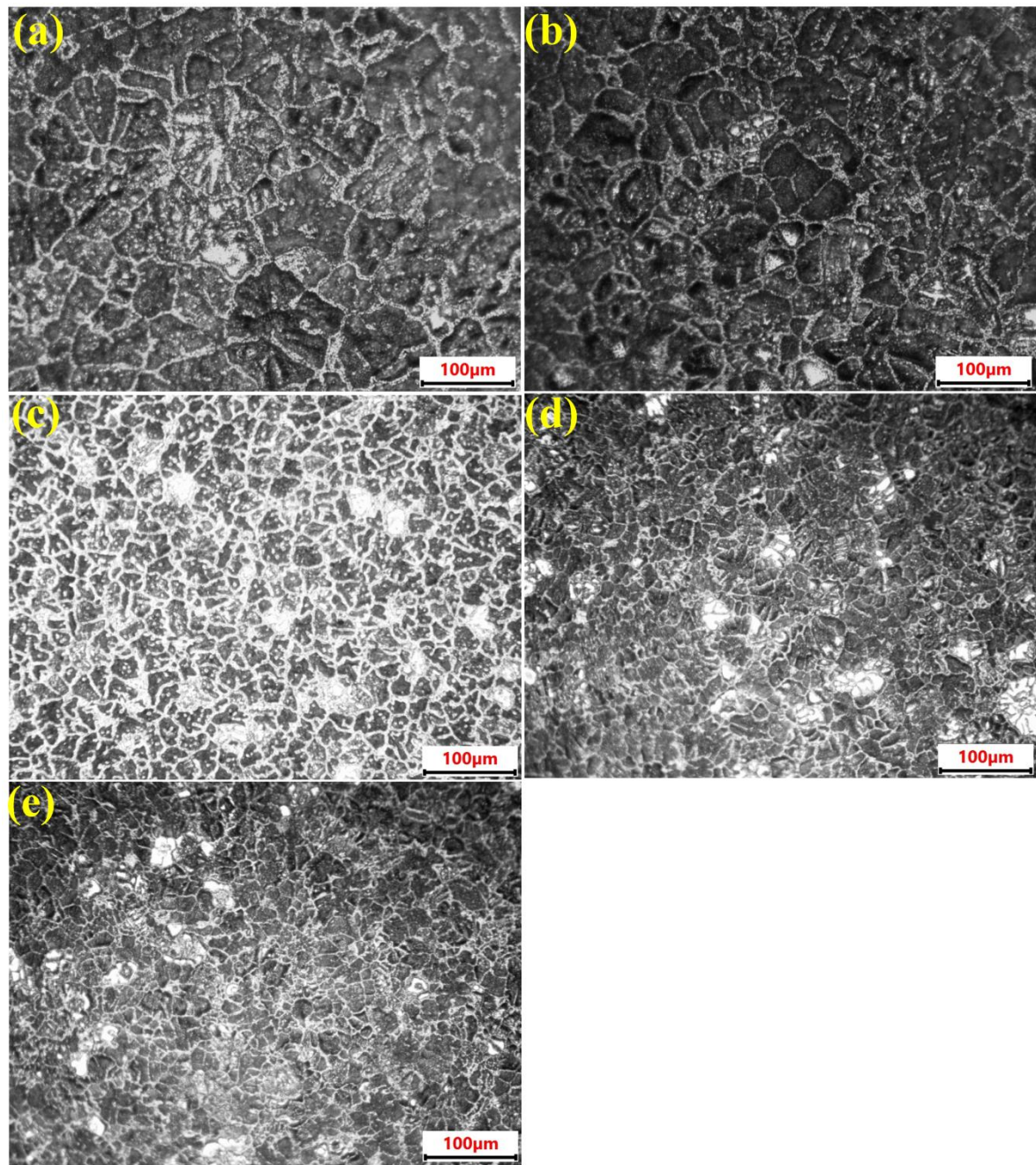


Figure 4.7: Optical images of various materials (a) 0.5HNC, (b) 1HNC, (c) 1.5HNC, (d) 2HNC, and (e) 3HNC

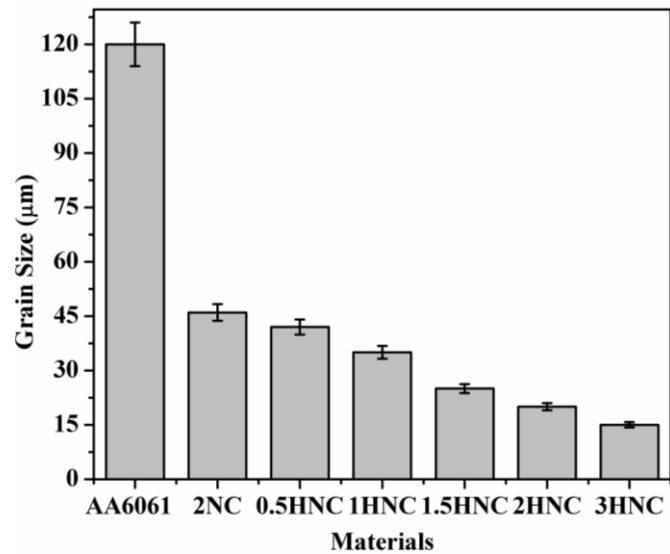


Figure 4.8: Average grain size (a) AA6061 aluminium alloy, (b) 0.5HNC, (c) 1HNC, (d) 1.5HNC, (e) 2HNC, and (f) 3HNC

4.5 Transmission Electron Microscopy

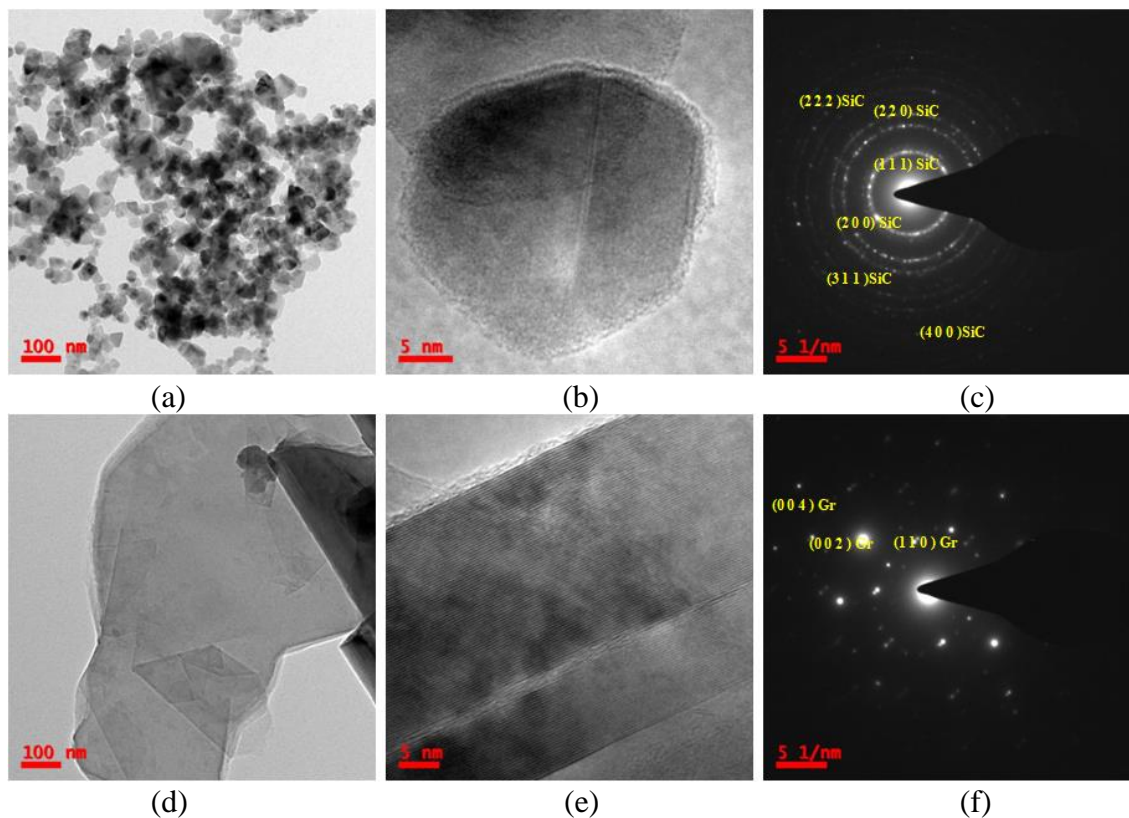


Figure 4.9: (a) SiCp nanoparticles, (b) SiCp nanoparticle, (c) SAD pattern of SiCp particles, (d) graphite particles, (e) graphite particle and (f) SAD pattern of graphite particles

The SiCp and graphitenanoparticles were analyzed under transmission electron microscopy (TEM). Figure 4.9 shows the TEM images of SiCp and graphite nanoparticles and its Selected Area Diffraction (SAD) pattern. The single SiCp and graphite particles are shown in figure 4.10 (b) and (e). It can be seen that the as-received SiCp nanoparticles are relatively spherical. The SAD pattern confirmed the SiCp and graphite nanoparticles with zero impurities in the composition. The size distribution of nanoparticles are shown in figure 4.10 (b) and (d). The average size of SiCp and graphite reinforcement particles are 50 nm and 500 nm respectively.

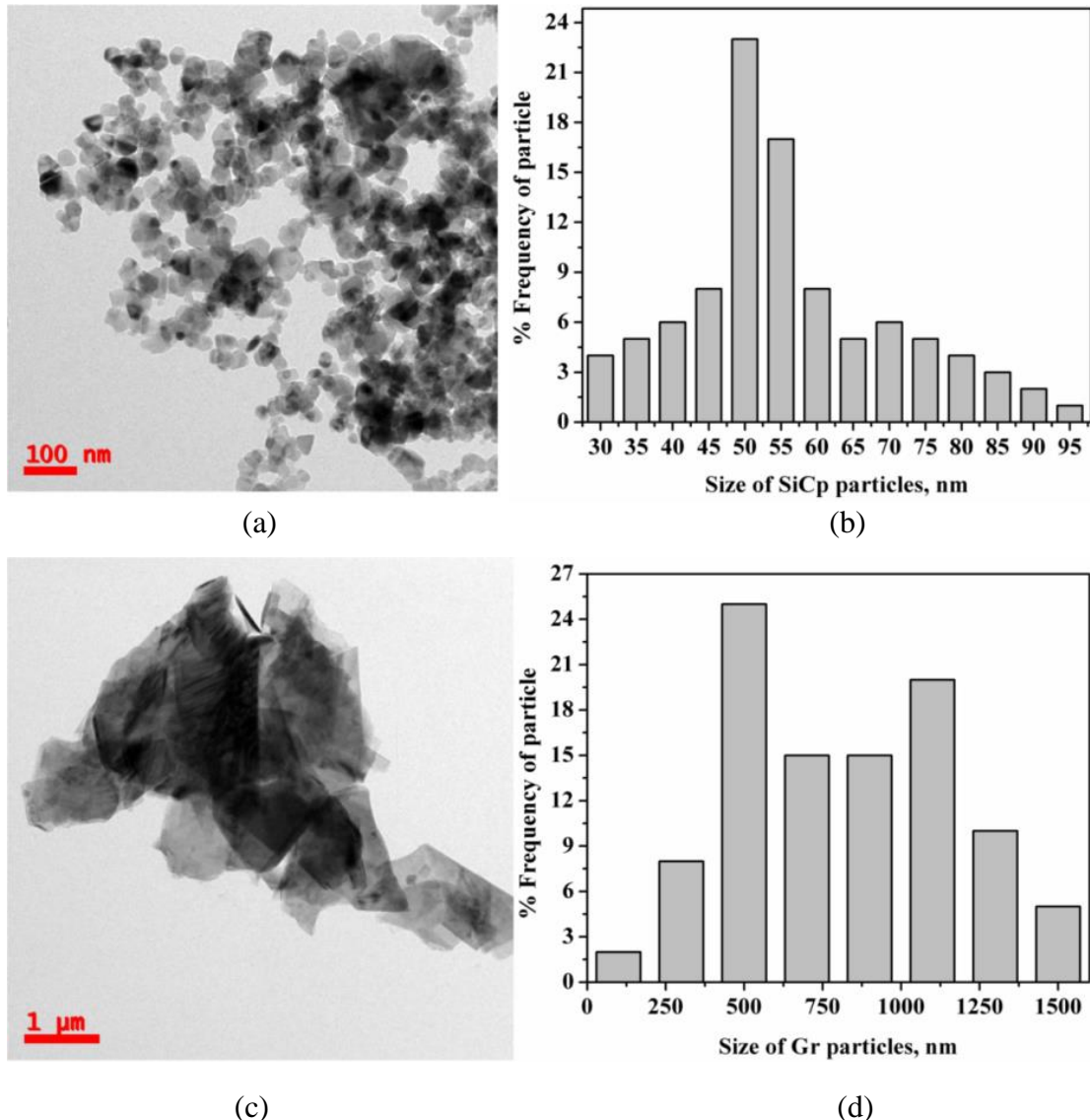


Figure 4.10: (a) TEM image of SiCp, (b) distribution of various sizes of SiCp nanoparticles, (c) TEM image of graphite and (d) distribution of various sizes of Gr nanoparticles

4.6 Scanning Electron Microscopy

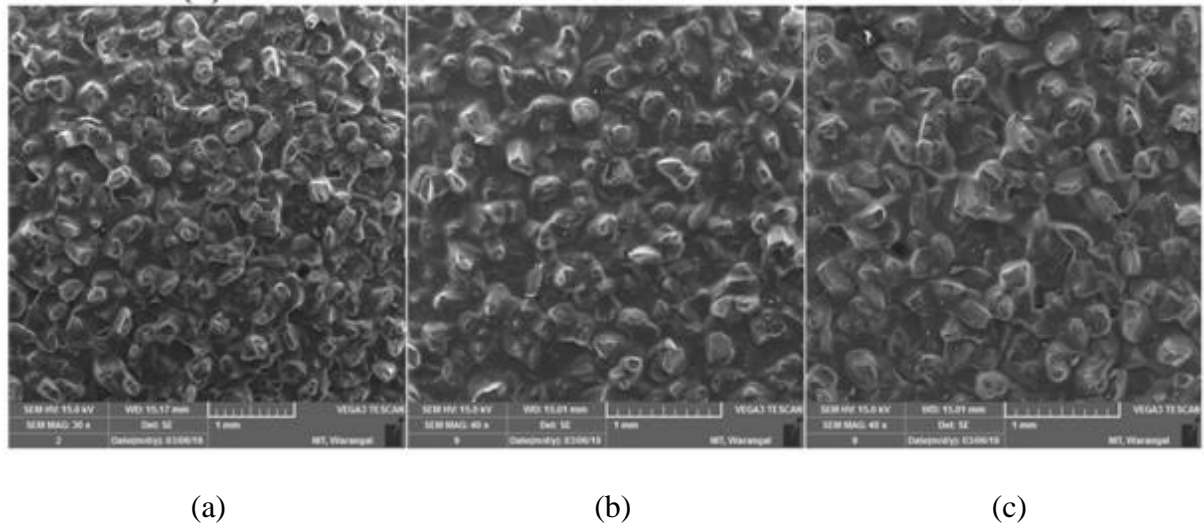


Figure 4.11: Morphology of different abrasive grit papers (a) 50 μm (b) 100 μm (c) 150 μm

The SEM images of 50, 100, and 150 μm fresh abrasive grit papers are presented in figure 4.11. The abrasive grit particles are oriented in different directions with individual rake angle. Figure 4.12 represents the SEM micrographs of AA6061 aluminium alloy, 0.5NC, 1NC, 1.5NC and 2NC nanocomposites. Figure 4.12 (a) indicates the unreinforced AA6061 aluminium alloy. Figure 4.12 (b)-(e) shows the microstructure of 0.5NC, 1NC, 1.5NC and 2NC nanocomposites. The grayish white SiCp nanoparticles are present in AA6061 aluminium alloy matrix. However, few smaller SiCp particle clusters are observed in the matrix. It reveals that SiCp nano-reinforcements are dispersed uniformly in the AA6061 aluminium alloy matrix. However, small scale clusters appeared in the microstructure with rise of SiCp quantity in the matrix. Figure 4.13 denotes the SEM micrographs of 2NC nanocomposite, 0.5HNC, 1HNC, 1.5HNC, 2HNC, and 3HNC hybrid nanocomposites. Figure 4.13 (b) shows the microstructure of 2NC nanocomposite. The grayish white SiCp nanoparticles are present in AA6061 aluminium alloy matrix and uniformly distributed in the matrix. However, few smaller SiC particle clusters are observed in the matrix. Figure 4.13 (c)-(f) depicts the microstructure of 0.5HNC, 1HNC, 1.5HNC, 2HNC, and 3HNC hybrid nanocomposites. It reveals that SiCp and graphite reinforcements are dispersed uniformly in the AA6061 aluminium alloy matrix. However, small scale clusters appeared in the microstructure with rise of graphite quantity in the matrix.

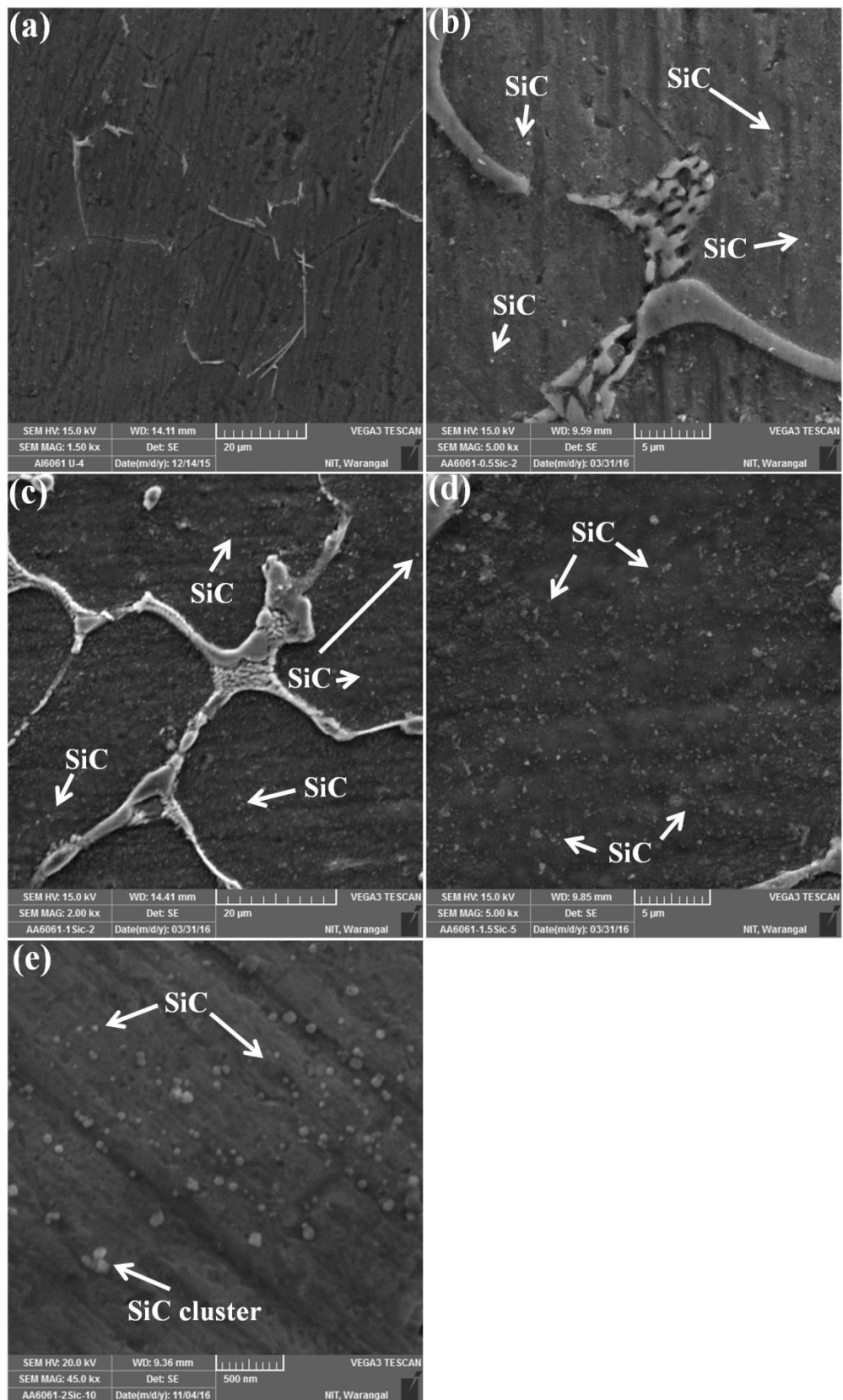


Figure 4.12: SEM micrographs (a) AA6061 aluminium alloy, (b) 0.5NC, (c) 1NC, (d) 1NC and (e) 2NC

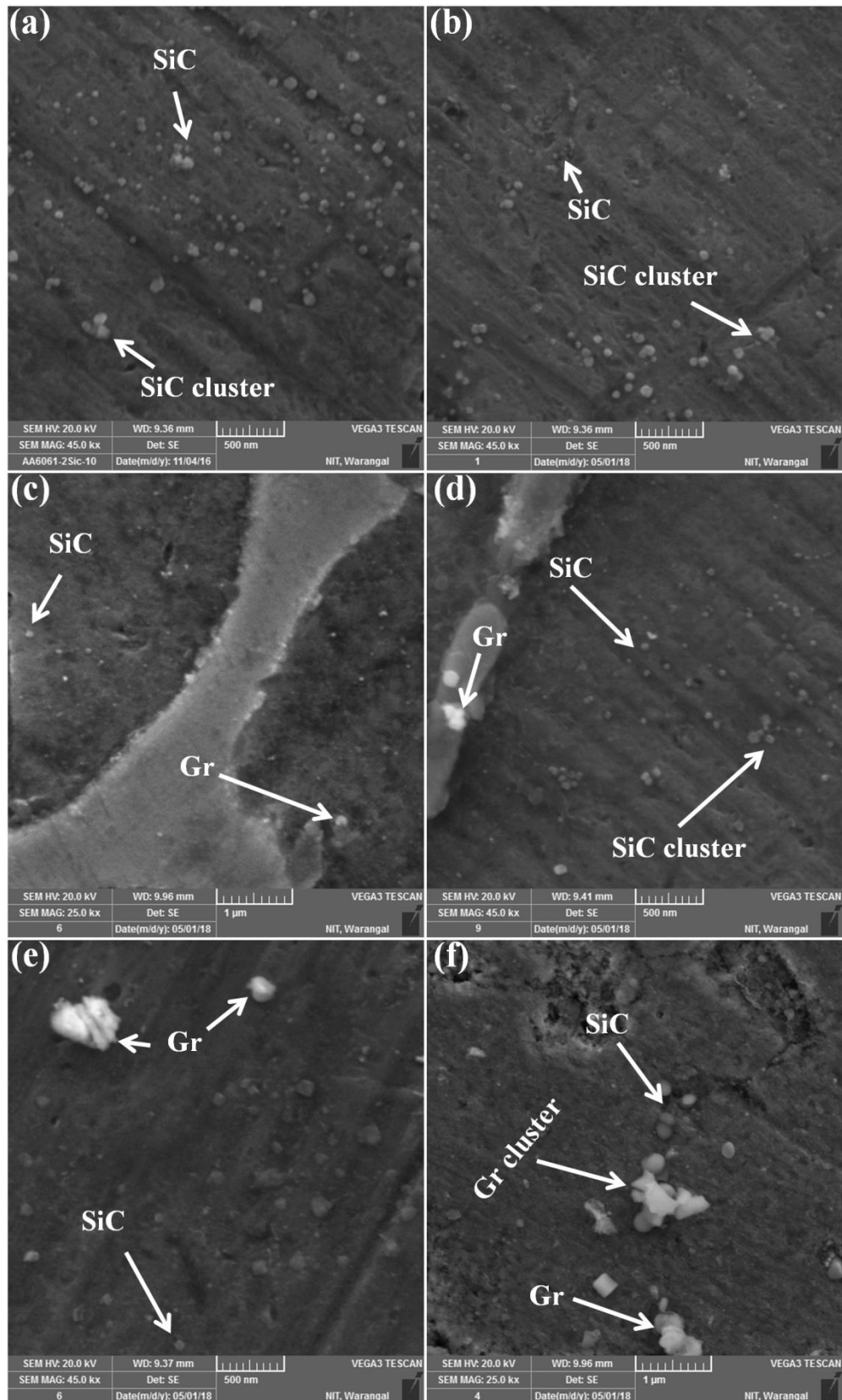


Figure 4.13: SEM micrographs (a) 2NC, (b) 0.5HNC, (c) 1HNC, (d) 1.5HNC, (e) 2HNC, and (f) 3HNC

4.7 Summary

In present chapter the ultrasonically assisted stir casted samples are characterized using XRD, SEM and TEM. Density increased with SiCp and decreased with graphite. The XRD intensity peak is lower for graphite and SiCp due to lower content. Uniform distribution of SiCp and graphite is observed. However small nanoparticle clusters formed with increase in weight percent of reinforcement. Average particle size of SiCp and graphite is 50 nm and 500 nm respectively.

Chapter 5

Mechanical Properties

5.1 Introduction

In this chapter, the mechanical properties of AA6061 aluminium alloy, 0.5NC, 1NC, 1.5NC and 2NC nanocomposites and 0.5HNC, 1HNC, 1.5HNC, 2HNC and 3HNC hybrid nanocomposites are studied and discussed briefly. The mechanical properties include the hardness and tensile characteristics of AA6061 aluminium alloy matrix, its nanocomposites and hybrid nanocomposites. The morphology of nanocomposites and hybrid nanocomposites fractured surface of tensile samples are analyzed and discussed briefly. The enhancement of yield strength of nanocomposites and hybrid nanocomposites is predicted using various strengthening mechanisms and yield strength prediction models including porosity. In the present study the relationship between average grain size, reinforcement particle diameter and volume fraction of nanoparticles is developed for nanocomposites using experimental value and literature data. The experimental and predicted yield strength of various models is compared and discussed.

5.2 Microhardness

Microhardness of AA6061 aluminium alloy, 0.5NC, 1NC, 1.5NC and 2NC nanocomposites is presented in figure 5.1. The microhardness of nanocomposites is more than the base alloy and improved with increasing SiCp nano-reinforcements in the AA6061 aluminium alloy matrix. The microhardness of the ultrasonically assisted stir casted samples

is significantly improved. The microhardness is 52 ± 3 HV for AA6061 aluminium alloy, 65 ± 2 HV for 0.5NC, 73 ± 3 HV for 1NC, 82 ± 3 HV for 1.5NC and 91 ± 4.12 HV for 2NC. The enhancement of microhardness for 0.5NC, 1NC, 1.5NC and 2NC nanocomposite compared to AA6061 aluminium alloy is 25%, 40%, 58% and 78% respectively. The increase in microhardness is due to increase in content of SiCp nano-reinforcement particles in the AA6061 aluminium alloy matrix that attain good resistance to the lattice displacement.

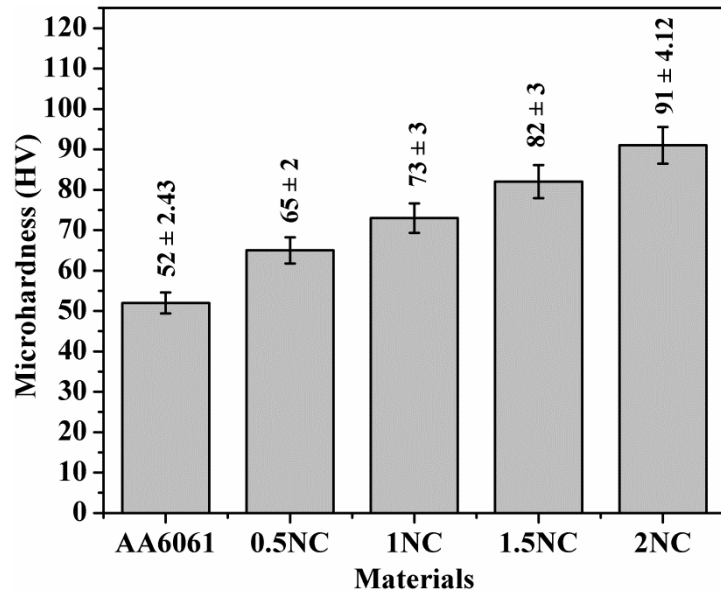


Figure 5.1: Microhardness of AA6061 aluminium alloy and its nanocomposites

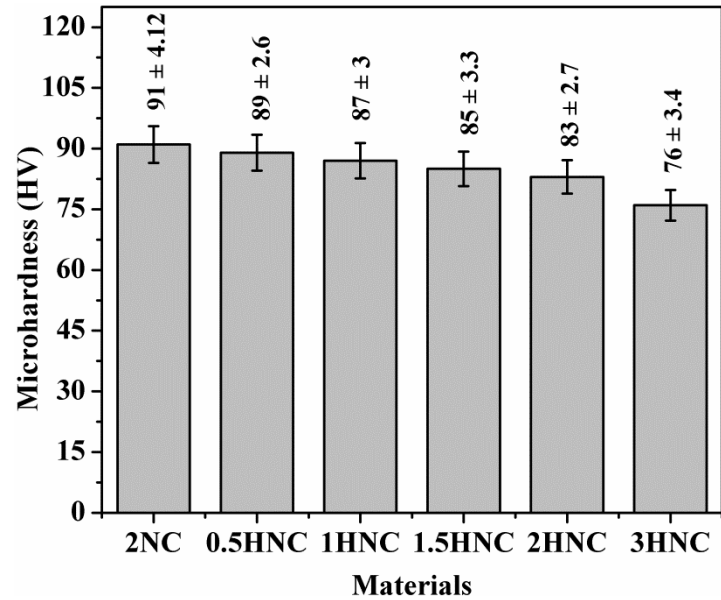


Figure 5.2: Microhardness of AA6061 aluminium alloy and its hybrid nano-composites

The average microhardness of AA6061 aluminium alloy, 0.5HNC, 1HNC, 1.5HNC, 2HNC and 3HNC hybrid nanocomposites is shown in figure 5.2. The microhardness is 91 ± 4.12 HV for 2NC, 89 ± 2.6 HV for 0.5HNC, 87 ± 3 HV for 1HNC, 85 ± 3.3 HV for 1.5HNC, 83 ± 2.7 HV for 2HNC and 76 ± 3.4 HV for 3HNC. The microhardness of the composites decreased with increasing graphite nano-reinforcement particles in the matrix. The enhancement of microhardness for 0.5HNC, 1HNC, 1.5HNC, 2HNC and 3HNC hybrid nanocomposites compared to base alloy are 71%, 67%, 64%, 60%, and 46% respectively. Microhardness of hybrid nanocomposites increased compared to base alloy and decreased compared to nanocomposite. The reduction in microhardness of the hybrid nanocomposite could be due to presence of graphite. The graphite being soft allotrope of carbon acts as a solid lubricant. The graphite will ease the grain movement along slip planes due to its weak van der waals forces of parallel thin plates [128].

5.3 Tensile Properties

Figure 5.3 shows the stress verses strain diagram of 0.5NC, 1NC, 1.5NC and 2NC nanocomposites. The mechanical properties (average value of five samples) of AA6061 aluminium alloy, 0.5NC, 1NC, 1.5NC and 2NC nanocomposites are shown in figure 5.4. The improvement in the yield strength of nanocomposites compared to the AA6061 aluminium alloy is 96% for 0.5NC, 127% for 1NC, 158% for 1.5NC and 206% for 2NC nanocomposites respectively. The increase of yield strength is due to the addition of SiCp nano-reinforcements and its homogenous dispersion in the AA6061 aluminium alloy matrix. The dispersed nano-sized SiCp particles create obstacles to plastic flow and increase dislocation density in the AA6061 aluminium alloy matrix. The dislocation density increased with increase in the weight percentage of nano-sized SiCp reinforcements in the matrix. The resistance of the nanocomposites against the applied tensile load increases with increase in the dislocation density [129]. The enhancement of ultimate tensile strength of the nanocomposites compared to AA6061 aluminium alloy is 29.63% for 0.5NC, 51.11% for 1NC, 73.33% for 1.5NC and 77.7% for 2NC. The increment of ultimate tensile strength is due to the strengthening of AA6061 aluminium alloy matrix, reduction in grain size of the nanocomposites, difference in thermal expansion coefficient between the AA6061 aluminium alloy matrix and SiCp nano-reinforcement, and initiation of higher dislocation density [129]. The ductility of the 0.5NC, 1NC, 1.5NC and 2NC nanocomposites is decreased by 9.3, 17.33,

25.33, and 33.3% with increasing SiCp nanoparticles in the AA6061 aluminium alloy matrix respectively. Researchers have reported that the ductility of the composites decreases with the increase of ceramic reinforcements in the aluminium matrix. The brittle behaviour of nano-sized SiCp reinforcement particles plays a significant role in the reduction of ductility [16].

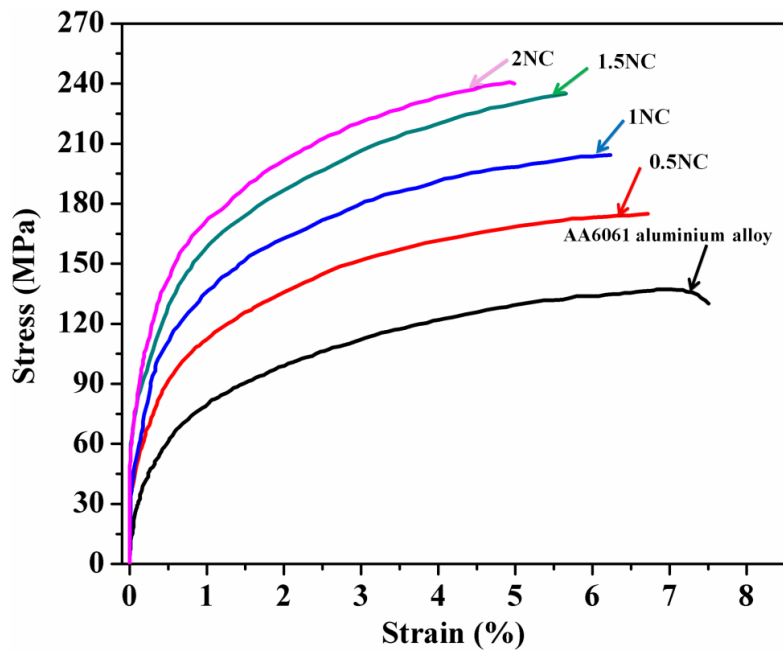


Figure 5.3: Stress-strain curves of AA6061 aluminium alloy and its nanocomposites

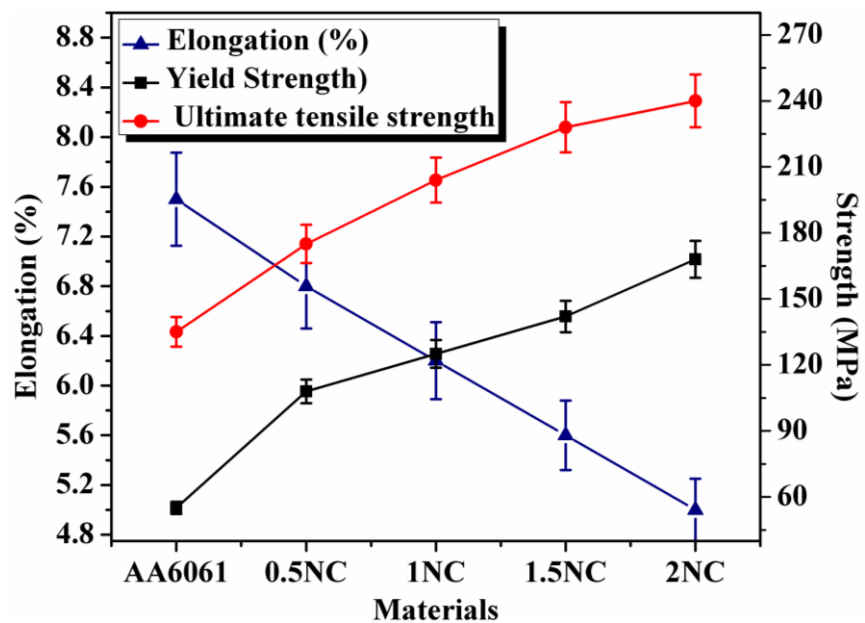


Figure 5.4: Mechanical properties of AA6061 aluminium alloy and its composites

The percentage of elongation of the AA6061 aluminium alloy, 0.5NC, 1NC, 1.5NC and 2NC nanocomposites is 7.5%, 6.7%, 6.2%, 5.6% and 5% respectively. The percentage of elongation of the nanocomposites decreased with increase in the nano-sized SiCp reinforcements in the AA6061 alloy matrix. This is because of the SiCp nano-reinforcement's brittleness and they extend the brittleness in the manufactured nanocomposites. However, increasing the weight percentage of nano-sized SiCp reinforcements in the nanocomposites repels the plastic flow of AA6061 aluminium alloy matrix and decreases the ductility which resulted in the reduction of the percentage of elongation. Figure 5.5 represents the stress verses strain diagram of AA6061 aluminium alloy, 0.5HNC, 1HNC, 1.5HNC, 2HNC, and 3HNC hybrid nanocomposites.

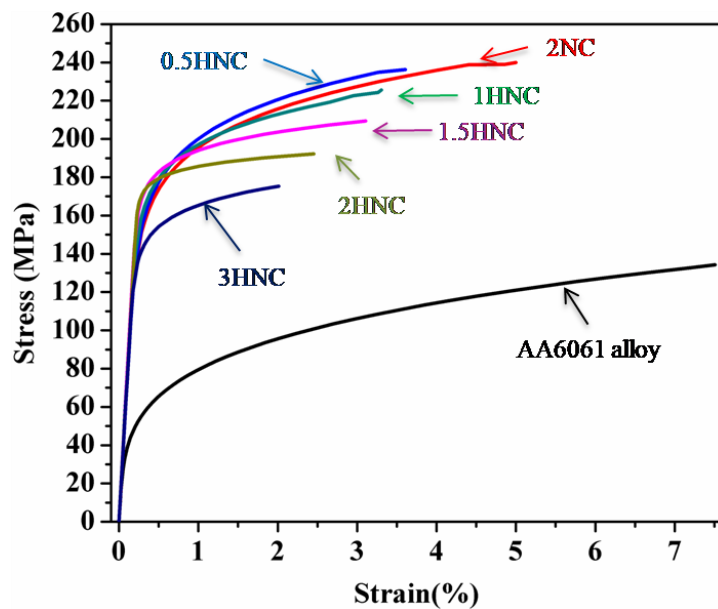


Figure 5.5: Stress-strain curves of AA6061 aluminium alloy and its hybrid nanocomposites

The mechanical properties of AA6061 aluminium alloy, 0.5HNC, 1HNC, 1.5HNC, 2HNC, and 3HNC hybrid nanocomposites are shown in figure 5.6. The improvement in the yield strength of hybrid nanocomposites compared to the base AA6061 aluminium alloy is 209% for 0.5HNC, 218% for 1HNC, 227% for 1.5HNC, 240% for 2HNC and 173% for 3HNC. Enhancement of yield strength is attributed to the rise of dislocation density, uniform distribution and combined strengthening effect of SiCp and graphite nano-reinforcements in the AA6061 aluminium alloy matrix. The enhancement of the yield strength increases up to 2HNC and suddenly decreases for 3HNC hybrid nanocomposite. This would be attributed due to the formation of nano-reinforcement clusters and higher amount graphite in the alloy

matrix. The results specify that the ultimate tensile strength increased by 76% for 0.5HNC, 64% for 1HNC, 57% for 1.5HNC, 49% for 2HNC and 33% for 3HNC hybrid nanocomposites compared to base alloy. The addition of graphite content to the 2NC nanocomposite decreases the enhancement of ultimate tensile strength.

The ductility of the 0.5HNC, 1HNC, 1.5HNC, 2HNC, and 3HNC hybrid nanocomposites is decreased by 52%, 56%, 59%, 67% and 72% with increasing graphite nanoparticles in the AA6061 aluminium alloy matrix. The percentage of elongation is 7.5 for AA6061 aluminium alloy, 3.6 for 0.5HNC, 3.3 for 1HNC, 3.1 for 1.5HNC, 2.5 for 2HNC and 2.1 for 3HNC hybrid nanocomposites. The elongation of the hybrid nanocomposites decreased with increase in the graphite nano-reinforcements in the AA6061 aluminium alloy. This would be attributed to the increase of brittleness with increase of nano-reinforcements in the matrix. However, the increase of nano-reinforcements in the matrix repels the plastic flow of matrix and decreases the ductility which resulted in the reduction of the elongation percentage [16].

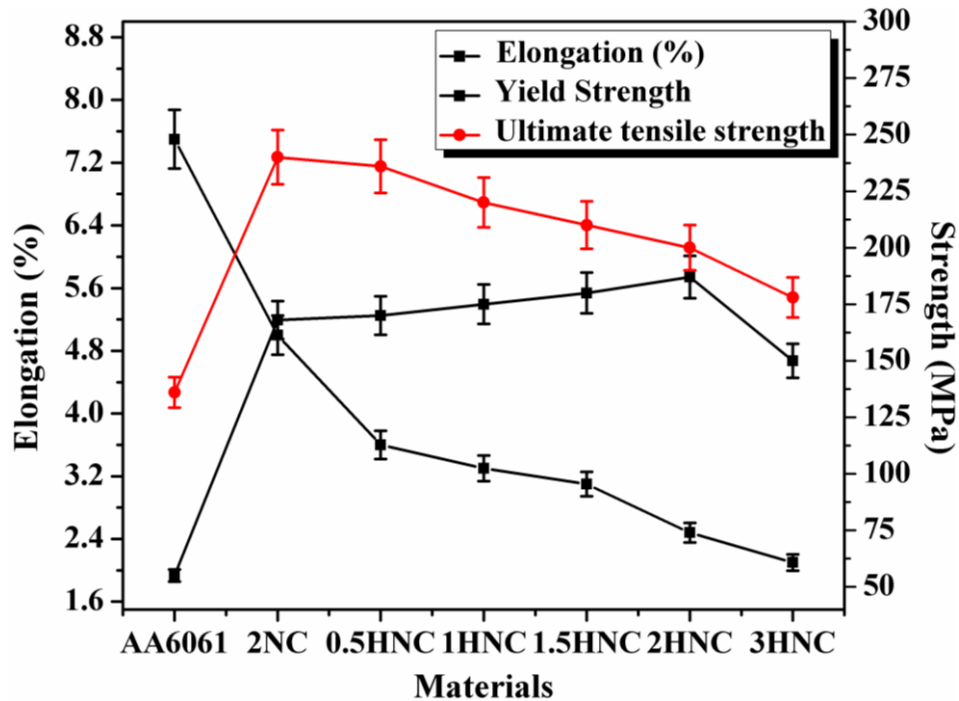


Figure 5.6: Mechanical properties of AA6061 aluminium alloy and its hybrid nanocomposites

5.4 Fractography

Figure 5.7 represents the fracture surfaces of AA6061 aluminium alloy, 0.5NC, 1NC, 1.5NC and 2NC nanocomposites. Fracture surface of AA6061 aluminium alloy shown in figure 5.7 (a) reveals the grape like dendrites in higher quantity, micro cracks, tear ridges, facets and tiny dimples in smaller quantity. The mode of fracture of AA6061 aluminium alloy is ductile fracture (i.e., 45°).

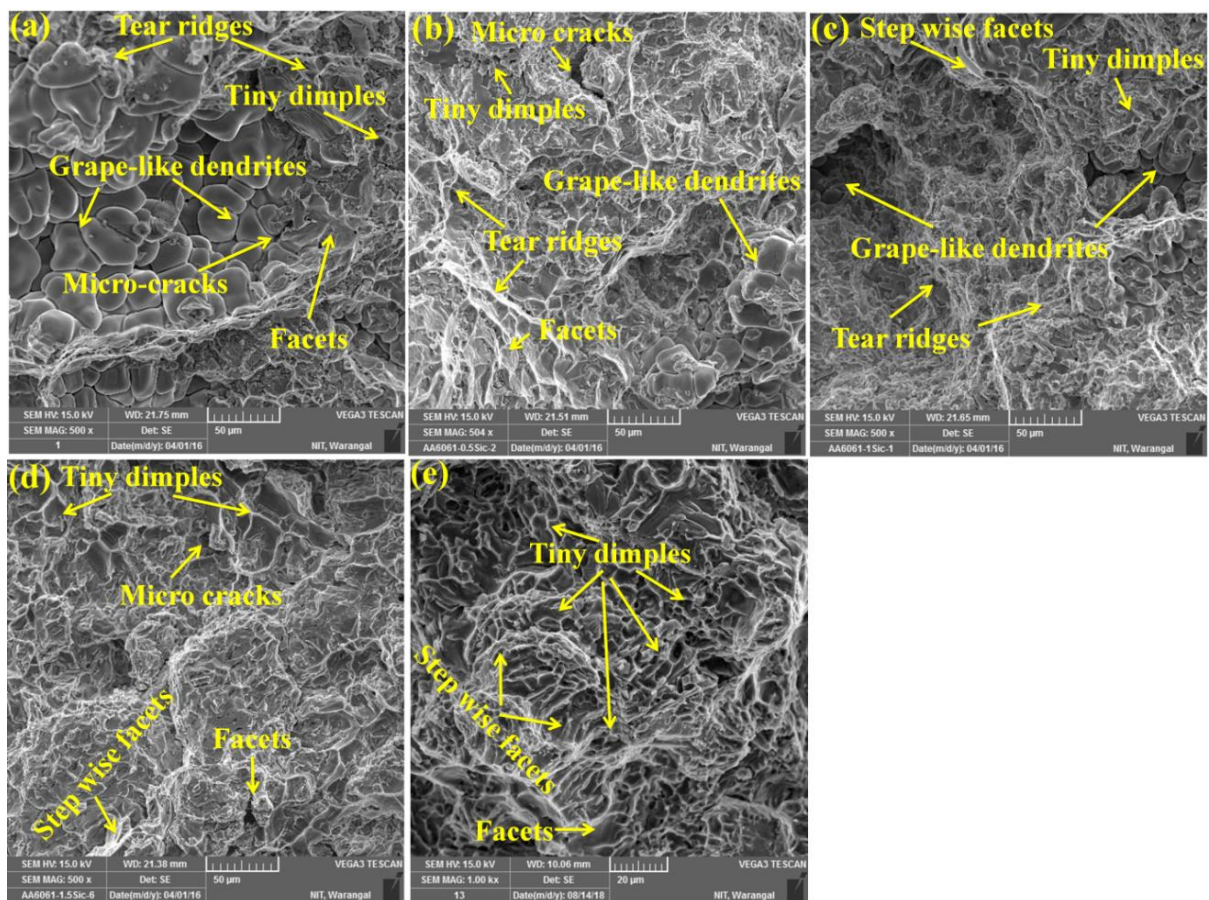


Figure 5.7: SEM micrographs of fractured surfaces of materials (a) AA6061 aluminium alloy, (b) 0.5NC, (c) 1NC, (d) 1.5NC, and (e) 2NC

Figure 5.7 (b) denotes the fracture surface of 0.5NC nanocomposite. It reveals the micro cracks, facets, tiny dimples and grape like dendrites in lower quantity. It would be due to the smaller quantity of SiCp nano-reinforcements in the AA6061 aluminium alloy matrix. Figure 5.7 (c) and (d) depicts the fracture surfaces of 1NC and 1.5NC nanocomposites respectively. It reveals the larger quantity of step wise facets and tiny dimples.

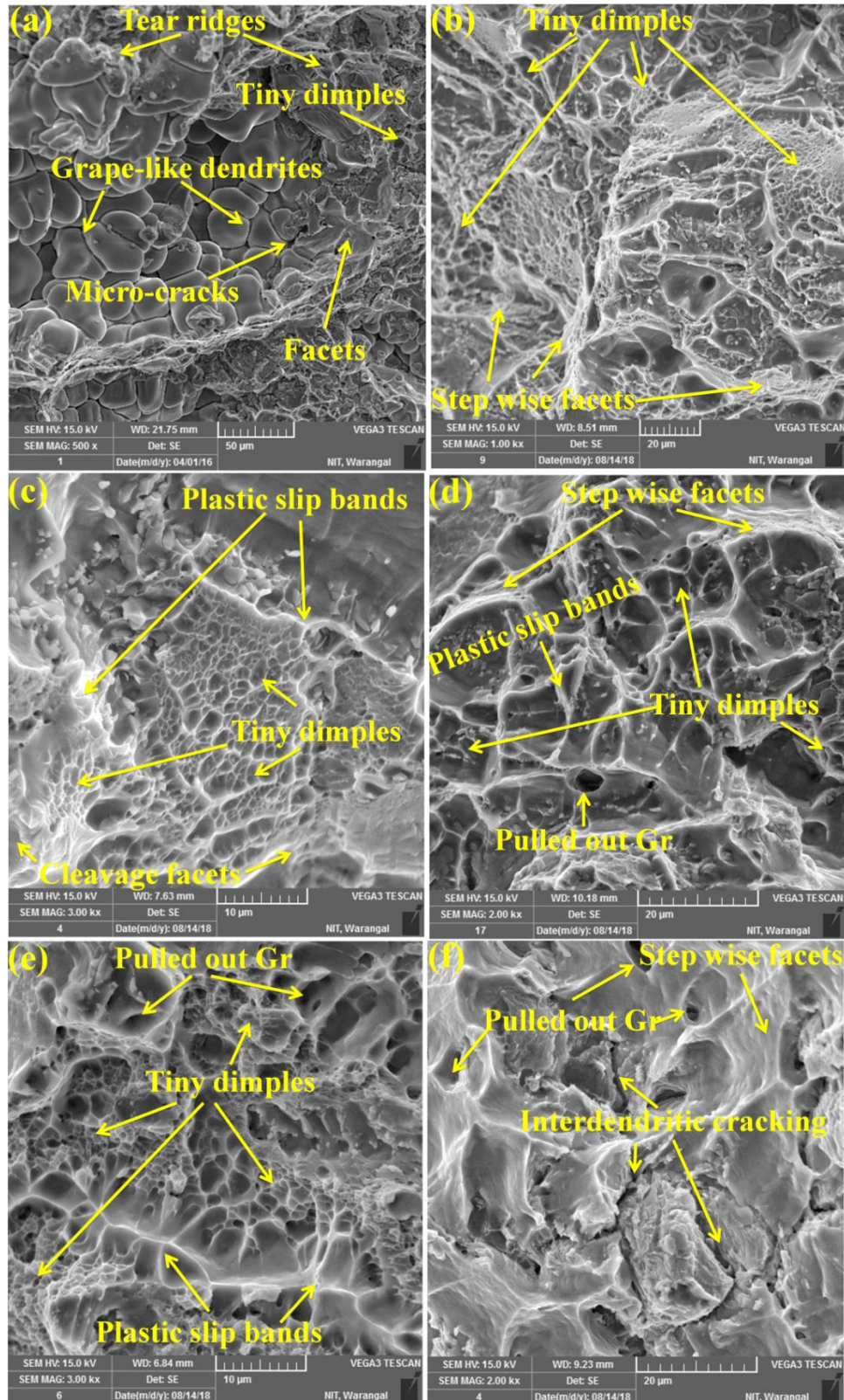


Figure 5.8: SEM micrographs of fractured surfaces of materials (a) AA6061 aluminium alloy, (b) 0.5HNC, (c) 1HNC, (d) 1.5HNC, (e) 2HNC, and (f) 3HNC

It would be attributed due to the presence of more quantity of SiCp nano-reinforcements in the AA6061 aluminium alloy matrix. The rise of dislocation density with increase of SiCp nano-reinforcements and ultra-sonication process decreases the formation of grape like dendrites in the AA6061 aluminium alloy matrix. Figure 5.7 (e) indicates the 2NC nanocomposite fracture surface that reveals more tiny dimples in smaller size and step wise facets. The appearance of larger quantity tiny dimples is an indication of ductile fracture mode of failure [34]. This ductile failure would be due to the nucleation of voids and voids growth. The voids will be growing up and form a crystalline boundary with the matrix and SiCp nanoparticles. The formation of voids will spread into a small dimple and finally cracks.

Figure 5.8 represents the fracture surfaces of AA6061 aluminium alloy, 0.5HNC, 1HNC, 1.5HNC, 2HNC and 3HNC hybrid nanocomposites. Fracture surface of AA6061 aluminium alloy as shown in figure 5.8 (a) reveals the grape like dendrites in higher quantity, micro cracks, tear ridges, facets and tiny dimples in smaller quantity. The mode of fracture of AA6061 aluminium alloy is ductile fracture (i.e., 45°). Figure 5.8 (b) shows the 0.5HNC hybrid nanocomposite fracture surface that reveals the smaller size tiny dimples and more step wise facets [130]. It can be seen that there are number of tiny dimples and its size reduced. The sudden reduction in the dimple size is an indication of lower ductility. This would be attributed to the rise of nano-reinforcement particles in the matrix. Figure 5.8 (c)-(f) shows the SEM images of fracture surfaces of 1HNC, 1.5HNC and 2HNC hybrid nanocomposites respectively. It reveals the plastic slip bonds, cleavage and step wise facets.

It is observed that the nano-reinforcements particles are pulled out from the matrix. The appearance of more cleavage facets is an indication of ductile-brittle fracture mode. Figure 5.8 (g) represents the SEM micrographs of fracture surface of 3HNC hybrid nanocomposite that exhibits the interdendritic cracking, step wise facets and particle pull out. The interdendritic cracking is an indication of typical brittle fracture mode [131]. This is due to the rise of graphite nano-reinforcement clusters along the grain boundaries. However, the crack nucleation may be started along the grain boundaries and triple junctions followed by their propagation along the weakest neighbour grains [132].

5.5 Yield Strength Prediction

5.5.1 Nanocomposites

The yield strength of AA6061/SiCp nanocomposites is predicted using four models (i) Ramakrishnan's model (ii) Zhang and Chen model (iii) Modified Clyne method (iv) Mirza and Chen model (considering porosity and Hall-Petch effect). Ramakrishnan suggested a mathematical model for prediction of the yield strength by considering the load bearing effect and thermal dislocation mismatch effect. In this model, the weight percentage of reinforcement increases the dislocations in the matrix and act as barriers, which are affected more by the particle size than the weight percentage. According to this method, yield strength is given by the following relation [84]:

$$\sigma_y(nc) = \sigma_y(m)(1 + f_{load})(1 + f_{\Delta CTE}) \quad (5.1)$$

Zhang and Chen developed a mathematical model to predict the yield strength by considering the Orowan strengthening effect, thermal dislocation mismatch, and load bearing effect. In this model Orowan strengthening effect is included and that is significant for nano-sized particles less than 100 nm. The significant improvements in yield strength of the nanocomposites with various contributing factors of strengthening mechanisms for Zhang and Chen model are as follows [85]:

$$\sigma_y(nc) = \sigma_y(m)(1 + f_{load})(1 + f_{\Delta CTE})(1 + f_{orowan}) \quad (5.2)$$

In modified Clyne method, the Hall-Petch effect is included due to the grain refinement of the molten metal, which effects the grain size. According to the Hall-Petch relationship, strength increases with decreasing grain size of the composites. The significant improvements in the maximum strength of nanocomposites with the various factors of strengthening mechanisms by including the Hall-Petch effect were expressed as [77]:

$$\sigma_y(nc) = \sigma_y(m) + \sqrt{(\Delta\sigma_{orowan})^2 + (\Delta\sigma_{HP})^2 + (\Delta\sigma_{Load})^2 + (\Delta\sigma_{\Delta CTE})^2} \quad (5.3)$$

In the Mirza and Chen model porosity effect is considered along with all strengthening mechanisms. The yield strength of the nanocomposites was calculated by considering the load bearing effect, coefficient of thermal expansion mismatch, Orowan

strengthening effect, modified Hall-Petch effect, and porosity. The yield strength of the metal matrix nanocomposites is expressed as follows [77]:

$$\sigma_{y(nc)} = \sigma_{y(m)}(1 + f_{load} - P)(1 + f_{\Delta CTE})(1 + f_{Orowan})(1 + f_{mHP})(e^{-nP}) \quad (5.4)$$

where ' $\sigma_{y(m)}$ ' is yield strength of the matrix, ' f_{load} ' is load bearing contribution factor, ' $f_{\Delta CTE}$ ' is coefficient of thermal expansion mismatch contribution factor, ' f_{Orowan} ' is Orowan strengthening contribution factor, ' f_{mHP} ' is Hall-Petch modified improvement factor, and 'P' is porosity. The equation for yield strength improvement factors is given by the following relations:

$$f_{load} = \frac{\Delta\sigma_{load}}{\sigma_{y(m)}} \quad (5.5)$$

$$f_{\Delta CTE} = \frac{\Delta\sigma_{\Delta CTE}}{\sigma_{y(m)}} \quad (5.6)$$

$$f_{Orowan} = \frac{\Delta\sigma_{Orowan}}{\sigma_{y(m)}} \quad (5.7)$$

Hall-Petch developed a relationship between yield stress and grain size. According to Hall-Petch strengthening effect, the yield strength of the nanocomposites improved with decrease in grain size. The average grain size of 0.5NC, 1NC, 1.5NC and 2NC nanocomposites decrease significantly from 120 μm (AA6061 aluminium alloy) to 47 μm with the increase of the SiCp content and which is evident from figure 4.6. The incremental yield strength due to grain refinement is calculated to be 1.784 MPa (for 0.5NC), 2.152 MPa (for 1NC), 3.23 MPa (for 1.5NC) and 4.038 MPa (for 2NC). The Hall-Petch equation for nanocomposites is given by [16]:

$$\sigma_{y(nc)} = \sigma_{y(m)} + k \frac{1}{\sqrt{d_{grainsize}}} \quad (5.8)$$

where ' $\sigma_{y(nc)}$ ' is yield strength of the nanocomposite, ' $\sigma_{y(m)}$ ' is yield strength of base matrix, and ' $d_{grainsize}$ ' is grain size of the nanocomposite.

The grain size of the matrix is affected by the particle size and volume fraction of reinforcement. Hence, Zener modified the Hall-Petch equation and developed the empirical

relation between grain size, reinforcement particle size and its volume fraction [77], which is given by:

$$d_{grainsize} = \frac{4\alpha d_p}{3V_f} \quad (5.9)$$

where ‘ α ’ is proportional constant, ‘ d_p ’ is reinforcement nanoparticle size, and ‘ V_f ’ is volume fraction of reinforcement nanoparticles.

Proportionality constant (α) is based on the type of nanocomposite, type of reinforcement and fabrication technique. Hence, in the present work, (α) is evaluated from volume fraction of particles, average particle size and average grain size of the different samples. An attempt made to calculate the relation between grain size of the matrix and reinforcement particle size and its volume fraction by using literature and experimental data is shown in Table 5.1.

Table 5.1: Average grain size of nanoparticle reinforced AA6061 nanocomposites

Nanocomposite	Average grain size (μm)	Average particle size (nm)
AA6061/0.007 volume fraction of Al ₂ O ₃ [16]	67	56
AA6061/0.007 volume fraction of Al ₂ O ₃ [16]	72	80
AA6061/0.007 volume fraction of Al ₂ O ₃ [16]	80	107
AA6061/0.007 volume fraction of Al ₂ O ₃ [16]	190	156
AA6061/0.007 volume fraction of Al ₂ O ₃ [70]	65	50
AA6061/0.014 volume fraction of Al ₂ O ₃ [70]	80	95
AA6061/0.021 volume fraction of Al ₂ O ₃ [70]	170	228
AA6061/0.004 volume fraction of SiCp	75	50
AA6061/0.008 volume fraction of SiCp	69	50
AA6061/0.012 volume fraction of SiCp	55	50
AA6061/0.016 volume fraction of SiCp	47	50

Figure 5.9 represents the grain size of the matrix as a function of reinforcement particle size and its volume fraction. In this plot, the slope shows the constant (α). The linear relationship extracted from the graph is as follows:

$$d_{grainsize} (nm) = 4.68 \left[\frac{4d_p}{3V_f} \right] + 27013 \quad (5.10)$$

From equation 5.10, the proportionality constant (α) is approximately 4.68 for the AA6061 aluminium alloy based nanocomposites. The intercept shows the initial grain size of the AA6061 aluminium alloy matrix, which is constant in this equation. Hall-Petch equation is modified using the equations 5.8 and 5.10 and the resultant equation 5.11 is applicable to AA6061/SiCp nanocomposites. Equation 5.11 is used as the Hall-Petch effect on the strength of AA6061 aluminium alloy based nanocomposites.

$$\sigma_{y(nc)} = \sigma_{y(m)} + \frac{k}{\sqrt{4.68 \left[\frac{4d_p}{3V_f} \right] + 27013}} \quad (5.11)$$

$$\sigma_{y(nc)} = \sigma_{y(m)}(1 + f_{mHP}) \quad (5.12)$$

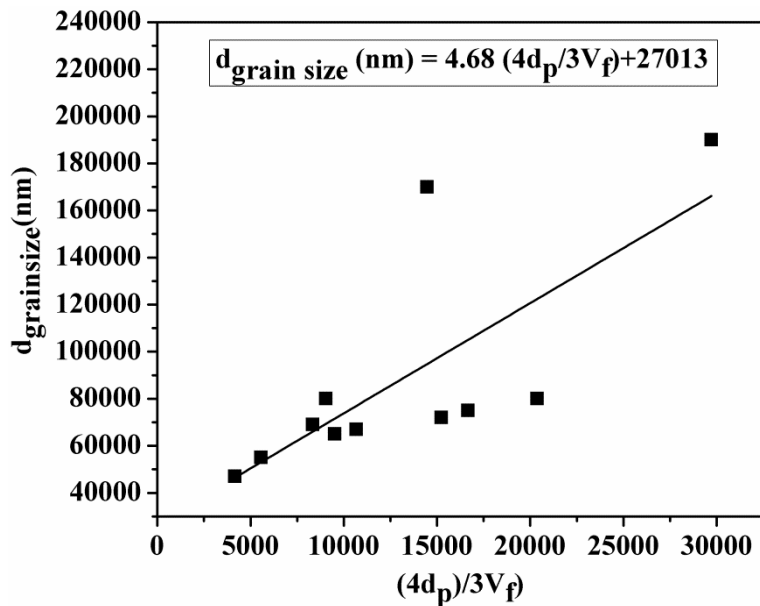


Figure 5.9: Grain size of AA6061 aluminium alloy based nanocomposites as a function of nano particle size and its volume fraction

In this study, where $f_{mHP} = \frac{k}{\sqrt{4.68 \left[\frac{4d_p}{3V_f} \right] + 27013}}$ = modified Hall-Petch improvement factor, ‘ $\sigma_{y(m)}$ ’ is yield strength of base material, ‘ d_p ’ is SiCp nano-reinforcement particle size, ‘ V_f ’ is volume fraction of SiCp nano-reinforcement particles, and ‘ k ’ is material constant for AA6061 aluminium alloy (74 MPa $\mu\text{m}^{1/2}$) [16]. Figure 5.10 shows the analytical results of predicted yield strength by using various models for the SiCp reinforced AA6061

nanocomposites as a function of volume fractions of reinforcement nanoparticles. The data used for yield strength prediction of the nano-sized SiCp particles reinforced AA6061 nanocomposites tested at room temperature is as follows: $\sigma_y(m) = 55 \text{ MPa}$, $G_m = 26 \text{ GPa}$, $d_p = 50 \text{ nm}$, $b_m = 0.286 \text{ nm}$, $\alpha_m = 25.2 \times 10^{-6} (\text{ }^\circ\text{C})^{-1}$ [16], $\alpha_p = 4.5 \times 10^{-6} (\text{ }^\circ\text{C})^{-1}$ [133].

It is assumed that the dislocation punching starts at a stress-free homologous temperature of 0.59 value and which is resulted in good agreement with previous studies by various researchers [134]. The melting point temperature of AA6061 aluminium alloy is to be ($T_{mp} = 855 \text{ K}$) and the measured room temperature during casting process is ($T_{room} = 298 \text{ K}$). During cooling from a high annealing temperature to a room temperature the SiCp nanoparticles and the matrix are stress-free by diffusion until stress free homologous temperature is reached.

$$\frac{T_{sf}}{T_{mp}} = 0.59 \quad (5.13)$$

$$\frac{T_{sf}}{855} = 0.59$$

$$\text{Therefore, } T_{sf} = 504 \text{ K}$$

$$\Delta T = T_{sf} - T_{room} = (504 - 298) \text{ K} = 206 \text{ K}$$

where ' T_{sf} ' is the stress-free homologous temperature and ' T_{room} ' is the room temperature.

From figure 5.10, the yield strength increased with the volume fraction of reinforcement particles in the alloy matrix. A small amount of volume fraction of reinforcement nanoparticles less than 0.06 significantly improved the yield strength of the metal matrix nanocomposites. The yield strength of the AA6061/SiCp nanocomposites predicted using the various models, i.e., equations 5.1-5.4, in a nano-sized SiCp particle reinforced AA6061 nanocomposite as a function of particle size is presented in figure 5.11. The yield strength of the metal matrix nanocomposites becomes very strong when the reinforcement particle size is less than 100 nm. The incremental yield strength due to Orowan strengthening mechanism for 50 nm size particles reinforced nanocomposites is calculated to be 21.6 MPa (for 0.5NC), 29.12 MPa (for 1NC), 35.1 MPa (for 1.5NC) and 37.7 MPa (for

2NC). The reinforcement particle of size of 50 nm is much affected on yield strength of the nanocomposites is proven from experiments shown in figure 5.6.

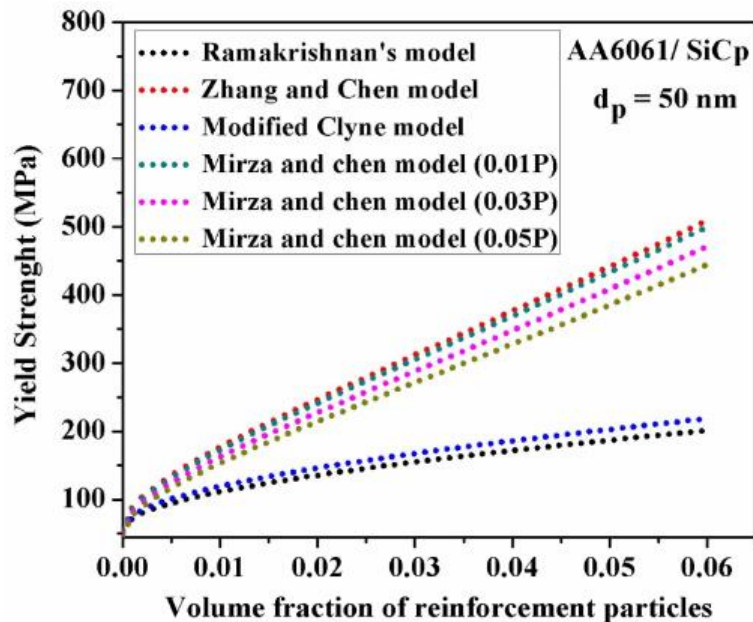


Figure 5.10: Predicted yield strength as a function of volume fraction of reinforcement particles for various particles sizes in nano-SiCp particulate-reinforced AA6061 aluminium alloy nanocomposites tested at 20 °C

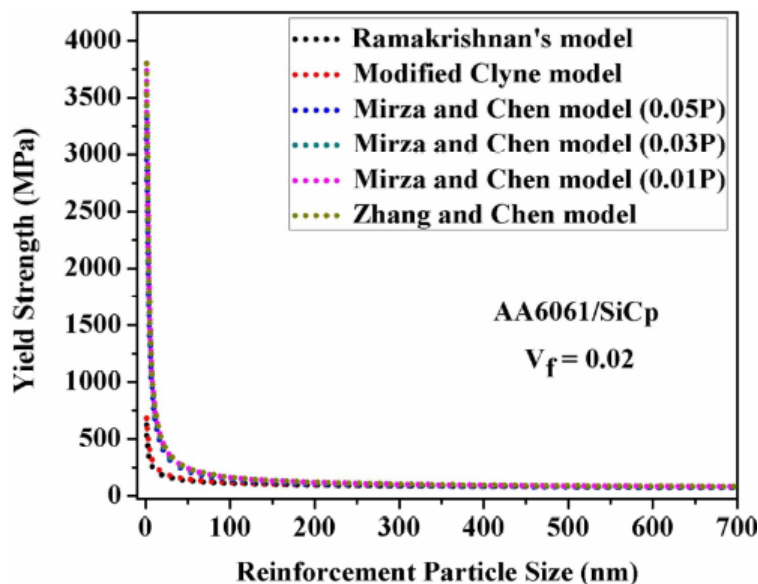


Figure 5.11: Predicted yield strength as a function of reinforcement particle size for a volume fraction of 0.02 in nano-SiCp particulate-reinforced AA6061 aluminium alloy nanocomposites tested at 20 °C

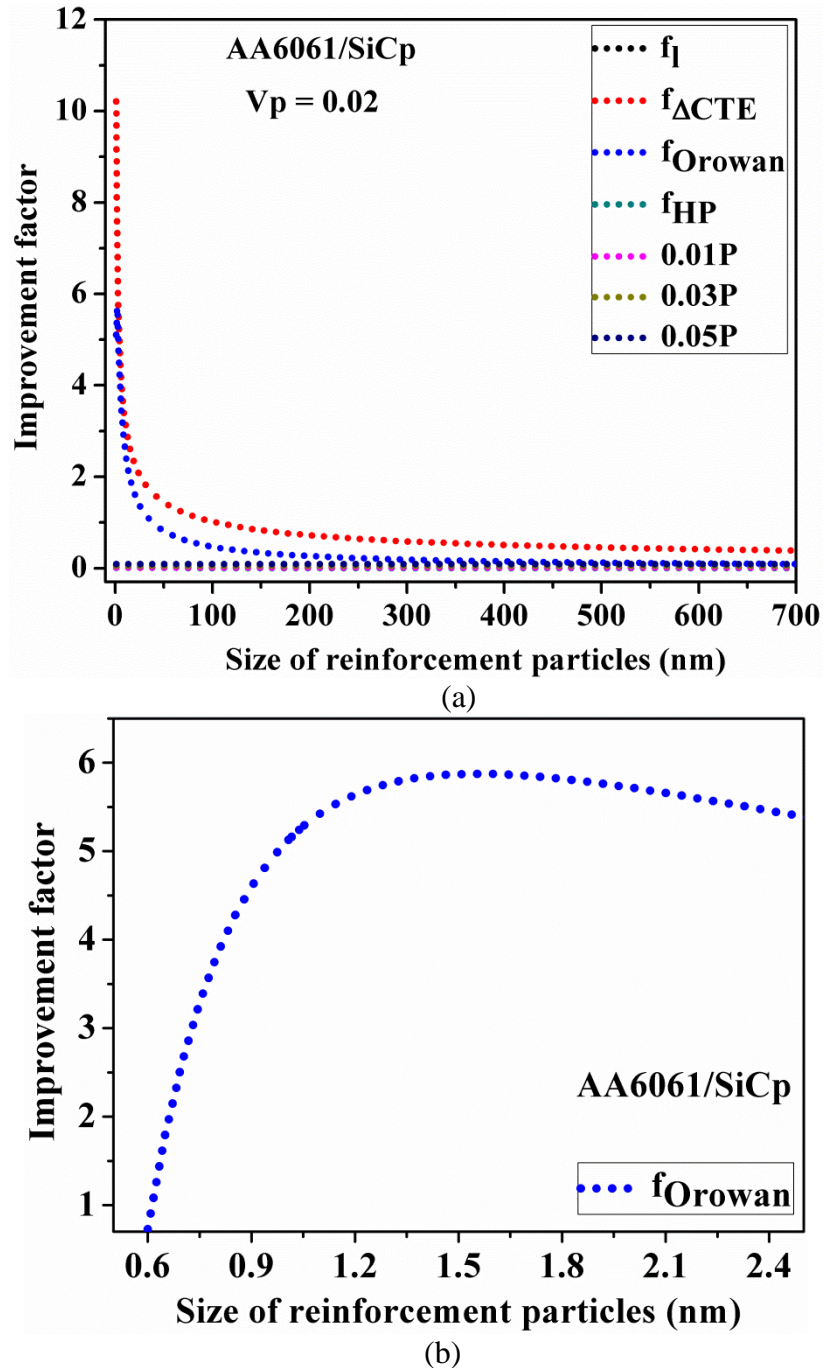


Figure 5.12: Factors as a function of reinforcement particle size for a volume fraction of 0.02 in nano-SiCp particulate-reinforced AA6061 alloy nanocomposites tested at 20°C (a) Different improvement factors (b) Orowan strengthening improvement factor between 2.5 nm and 0.6 nm

The contribution of thermal mismatch effect is larger than the other mechanisms with respect to the reinforcement particle size. As the size of the reinforcement particle decreases from 100 nm to 1 nm the contribution of thermal mismatch strengthening factor $f_{\Delta\text{CTE}}$

increases monotonically. The incremental yield strength due to coefficient of thermal mismatch strengthening mechanism for 50 nm size particles reinforced nanocomposites is calculated to be 35.3 MPa (for 0.5NC), 49.93 MPa (for 1NC), 61.3 MPa (for 1.5NC) and 70.9 MPa (for 2NC). The reinforcement particle of size of 50 nm is much affected on yield strength of the nanocomposites is proven from experiments shown in figure 5.6. The variation of improvement factors with respect to the size of reinforcement particles for a volume fraction of 0.02 in AA6061/SiCp nanocomposites is shown in figure 5.12 (a). The contribution of Hall-Petch effect and load bearing effect is very small in the AA6061/SiCp nanocomposites. The contribution of Orowan strengthening improvement factor f_{Orowan} is shown in figure 5.12 (b) for less than 2.5 nm particle sizes. The contribution of Orowan strengthening factor f_{Orowan} increases with decrease in the size of reinforcement particles up to a critical size of 1.56 nm for AA6061/SiCp nanocomposites, below which f_{Orowan} decreases continuously. For further analysis the ratios of $(f_l/f_{\Delta CTE})$, and $(f_{Orowan}/f_{\Delta CTE})$ plotted are shown in figure 5.13. Results revealed that the critical size is independent of the volume fraction of nano-reinforcement particles. The reduction of Orowan strengthening factor f_{Orowan} below the critical nano-reinforcement particle size is observed. As the size of the nano-reinforcement particles decreases, the proportion of Orowan strengthening effect increases, and thus the amount of the load bearing effect decreases in the AA6061/SiCp nanocomposites.

As shown in figure 5.12, with decreasing nano-reinforcement particles in the matrix the Orowan strengthening effect in AA6061/SiCp metal matrix nanocomposites increases up to the critical size of the nano-reinforcement particles. The Orowan strengthening effect below the critical size declines suddenly. Thus the breakdown of the Orowan strengthening effect occurs below the critical size of nano-reinforcement particles. The critical size of the nano-reinforcement particles depends on the atomic diameter (d_{atom}) of the aluminium matrix, with a ratio of $(d_{critical}/d_{atom})$ of about 5.46 for AA6061/SiCp nanocomposites, where ($d_{atom} = 0.286$ nm) for aluminium. The breakdown of Orowan strengthening effect for (< 2 nm) size reinforcement particles is due to the change in the deformation mechanism. The load bearing effect in aluminium metal matrix nanocomposites is small due to the low volume fraction of nano-reinforcement particles, large difference in the coefficient of thermal expansion of AA6061 alloy and the nano-sized SiCp particles i.e. $\Delta\alpha = 20.7 \times 10^{-6}$ $(^{\circ}\text{C})^{-1}$, leading to a greater $f_{\Delta CTE}$ contribution in AA6061/SiCp nanocomposites.

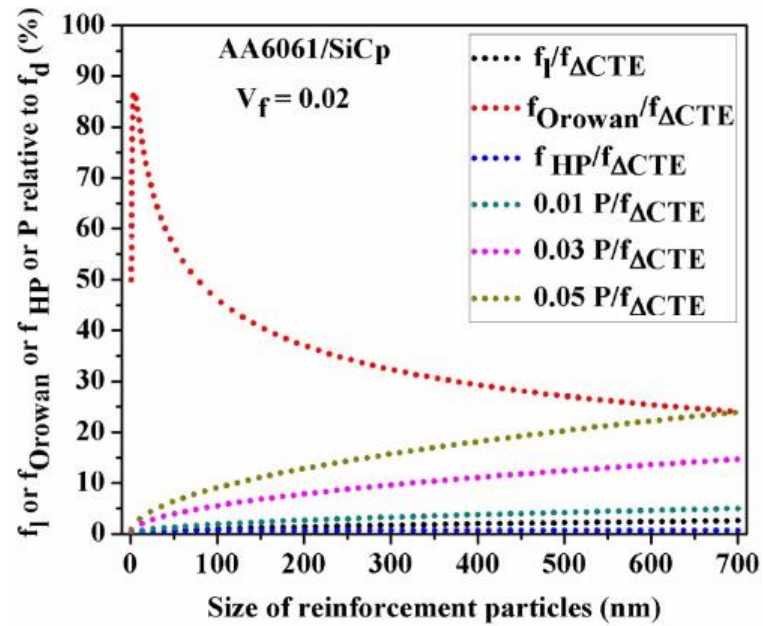


Figure 5.13: Relative contribution of factors as a function of reinforcement particle size for a volume fraction of 0.02 in nano-SiCp particulate-reinforced AA6061alloy nanocomposites tested at 20 °C

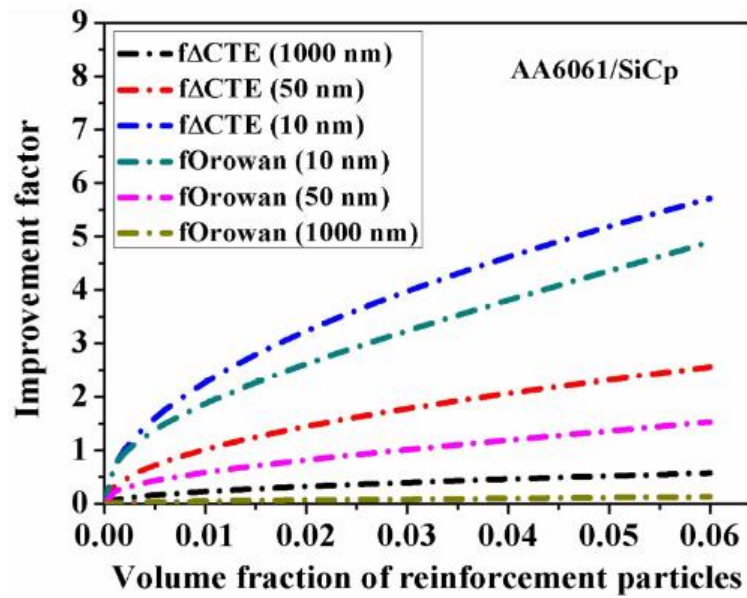


Figure 5.14: Orowan and dislocation mismatch improvement factors as a function of volume fraction of reinforcement particles with sizes of ($d_p = 10, 50, \text{ and } 1000 \text{ nm}$) in AA6061/SiCp nanocomposites tested at 20 °C

The incremental yield strength due to load bearing effect for 50 nm size particles reinforced nanocomposites is calculated to be 0.11 MPa (for 0.5NC), 0.22 MPa (for 1NC),

0.33 MPa (for 1.5NC) and 0.44 MPa (for 2NC). The reinforcement particle of size of 50 nm is much affected on yield strength of the nanocomposites is proven from experiments shown in figure 5.6. From figure 5.13, the effect of porosity increases with increase in size of the reinforcement particles. This in turn reduces the yield strength. The Hall-Petch effect is very small on the yield strength with respect to the reinforcement particle size. The size of reinforcement particles is the most significant parameter on the Orowan strengthening effect as shown in figure 5.14. As the size of the reinforcement particles increases from 10 nm to 1 μm , f_{Orowan} decreases quickly than $f_{\Delta\text{CTE}}$. When the reinforcement particle size is in microns, the effect of Orowan strengthening improvement factor f_{Orowan} is small and the thermal mismatch improvement factor $f_{\Delta\text{CTE}}$ has major effect at the same size. Because of this, Orowan strengthening effect is negligible for metal matrix composites when the particle size is in terms of microns. It is only to be considered for metal matrix nanocomposites. From figure 5.14, it reveals that both the improvement factors $f_{\Delta\text{CTE}}$ and f_{Orowan} increase with decreasing particle size and increasing volume fraction of nano-reinforcement particles.

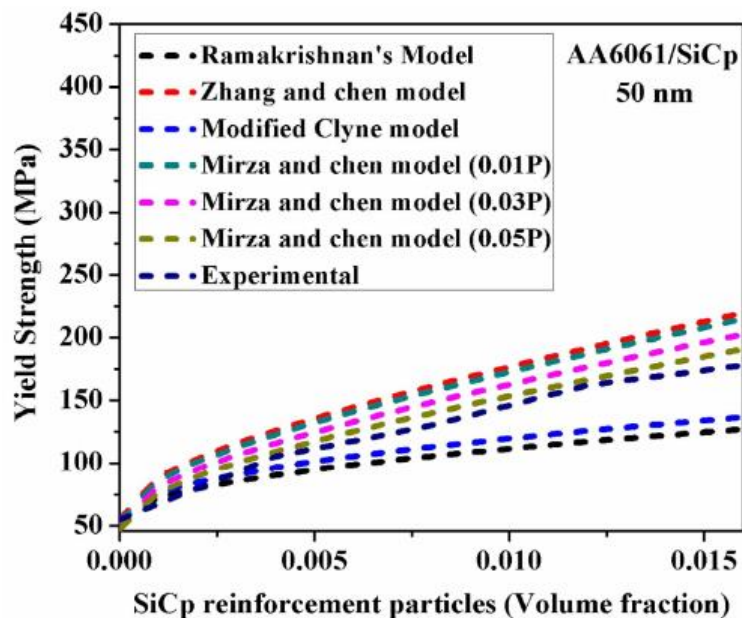


Figure 5.15: The yield strength of various models compared with the experimental data in AA6061/SiCp nanocomposites tested at 20 °C

The yield strength of the AA6061/SiCp nanocomposites is predicted using Ramakrishnan's model, Zhang and Chen, Modified Clyne, and Mirza and Chen model (consideration of porosity, (P = 1, 3, and 5%)) and is presented in figure 5.15. The yield

strength of the nanocomposites is raised with increasing weight percentage of SiCp reinforcements in the matrix. The Zhang and Chen model give rise to higher yield strength and Ramakrishnan's model resulted in lower yield strength. The experimental data points are between the predicted data points from all the methods. The experimental data points are slightly near to 5% porosity data points. The scatter of the experimental data points is due to the formation of clusters and agglomeration of nano-sized SiCp in the matrix. The five data points reflected a close agreement with the Mirza and Chen model. By incorporating the effect of porosity and grain growth, the predictability of various analytical models will be improved.

5.5.2 Hybrid Nanocomposites

The yield strength of AA6061 aluminium alloy based hybrid nanocomposites is influenced by SiCp and graphite nano-reinforcements. There are various strengthening mechanism that were implemented by researchers to evaluate the yield strength properties of nanocomposites i.e., Hall-Petch effect [16], Orowan strengthening mechanism [16], Dislocation mismatch effect [16], Load bearing effect [135], and porosity effect [74]. The grain size is refined with addition of SiCp and graphite nano-reinforcements in the AA6061aluminium alloy matrix. The grain size refinement enhances the yield strength of the hybrid nanocomposites [136].

Hall-Petch developed a relationship between grain size and yield strength of nanocomposite due to grain refinement of AA6061 aluminium alloy that is follows [136]:

$$\Delta\sigma_{HP} = k \left[\frac{1}{\sqrt{d_c}} - \frac{1}{\sqrt{d_m}} \right] \quad (5.14)$$

where, ' d_m ' is the average grain size of AA6061 aluminium alloy matrix, ' d_c ' is the average grain size of SiCp and graphite reinforced AA6061hybrid nanocomposites and 'k' is equal to 74 MPa $\mu\text{m}^{1/2}$ [16]. The SiCp and graphite second phase nanoparticles can act as obstacles to the dislocations movement and thus enhance the yield strength of the hybrid nanocomposites [85].

Orowan strengtheining effect due to combination of SiCp and graphite nanoparticles is described as follows [74]:

$$\Delta\sigma_{Orowan} = 0.13G_m b_m \left[\frac{\ln\left(\frac{d_{SiC}}{2b_m}\right)}{\tau_{SiC}} + \frac{\ln\left(\frac{d_{Gr}}{2b_m}\right)}{\tau_{Gr}} \right] \quad (5.15)$$

$$\tau_{SiC} = d_{SiC} \left(\left(\frac{1}{2V_{SiC}} \right)^{\frac{1}{3}} - 1 \right) \quad (5.16)$$

$$\tau_{Gr} = d_{Gr} \left(\left(\frac{1}{2V_{Gr}} \right)^{\frac{1}{3}} - 1 \right) \quad (5.17)$$

where, ‘ $\Delta\sigma_{Orowan}$ ’ is the change in yield strength due to Orowan effect, ‘ G_m ’ is shear modulus of alloy, ‘ V_{SiC} ’ is volume fraction of SiCp nano-reinforcements, ‘ V_{Gr} ’ is volume fraction of graphite nano-reinforcements, ‘ b_m ’ is the magnitude of burgers vector of matrix material, ‘ d_{SiC} ’ is average diameter of the SiCp nano-reinforcements, ‘ d_{Gr} ’ is average diameter of the graphite nano-reinforcements, ‘ τ_{SiC} ’ is the average interparticle spacing of SiCp and ‘ τ_{Gr} ’ is the average interparticle spacing of graphite.

The large difference of coefficient of thermal expansion between matrix and graphite nano-reinforcements induces the thermal mismatch strengthening effect during cooling of the molten metal from the initial fabrication conditions. The induced thermal stresses near the interface around the nano-reinforcement particles are sufficient for plastic strain in the alloy matrix. Therefore, the developed thermal stress due to geometrically mismatched dislocations $\Delta\sigma_{CTE}$ is obtained from the empirical relation [74].

$$\Delta\sigma_{CTE} = \beta G_m b_m (\rho^{CTE})^{\frac{1}{2}} \quad (5.18)$$

$$\rho^{CTE} = \frac{A\Delta T}{b_m} \left[\frac{(\alpha_m - \alpha_{SiC})V_{SiC}}{d_{SiC}(1-V_{SiC})} + \frac{(\alpha_m - \alpha_{Gr})V_{Gr}}{d_{Gr}(1-V_{Gr})} \right] \quad (5.19)$$

where ‘ $\Delta\sigma_{CTE}$ ’ is change in yield strength due to thermal mismatch effect, ‘ β ’ is a constant equal to 1.25 [135], ‘ b_m ’ is the magnitude of burgers vector of matrix material, ‘ G_m ’ is the shear modulus of matrix, ‘ ρ^{CTE} ’ is dislocation density, ‘ V_{SiC} ’ is volume fraction of SiCp nano-reinforcements, ‘ V_{Gr} ’ is volume fraction of graphite nano-reinforcements, ‘ A ’ is constant equal to 12, ‘ d_{SiC} ’ is average SiCp particle size, ‘ d_{Gr} ’ is average graphite particle size, $(\alpha_m - \alpha_{SiC})$ is difference of thermal expansion coefficient between the alloy matrix and SiCp nano-reinforcement particle, $(\alpha_m - \alpha_{Gr})$ is difference of thermal expansion coefficient between the alloy matrix and graphite nano-reinforcement particle and ‘ ΔT ’ is the

temperature change from the stress free homologous temperature. It is assumed that the dislocation punching starts at a stress-free homologous temperature of 0.59 value and which is resulted in good agreement with previous studies by various researchers [16, 134]. The melting point temperature of AA6061 aluminium alloy is to be ($T_{mp} = 855$ K) and the measured room temperature during casting process is ($T_{room} = 298$ K). During cooling from a high annealing temperature to a room temperature the SiCp, graphite particles and the matrix are stress-free by diffusion until stress free homologous temperature is reached.

$$\frac{T_{sf}}{T_{mp}} = 0.59 \quad (5.20)$$

$$\frac{T_{sf}}{855} = 0.59$$

$$\text{Therefore, } T_{sf} = 504 \text{ K}$$

$$\Delta T = T_{sf} - T_{room} = (504 - 298) \text{ K} = 206 \text{ K}$$

where ' T_{sf} ' is the stress-free homologous temperature and ' T_{room} ' is the room temperature.

The good interface bonding between SiCp and graphite nano-reinforcements and the AA6061 aluminium alloy matrix make the nano-reinforcements to contribute to the external applied load. The load bearing effect of nano-reinforcement particles is given by the following relation [75].

$$\Delta\sigma_{load} = 0.5(V_{SiC} + V_{Gr})\sigma_m \quad (5.21)$$

where ' $\Delta\sigma_{load}$ ' is change in yield strength due to load bearing effect, ' V_{SiC} ' is volume fraction of SiCp nano-reinforcements, ' V_{Gr} ' is volume fraction of graphite reinforcement particles, and ' σ_m ' is yield strength of AA6061 aluminium alloy. The porosity of the metal matrix hybrid nanocomposites plays an important role on the yield strength. The porosity of the hybrid nano-composites increased with increase of volume fraction of the nano-reinforcement particles in the AA6061 aluminium alloy matrix and reduces the yield strength [74]. The porosity of hybrid nanocomposites may interrupt load balance between the nano-reinforcement particles and matrix material, which results in stress concentration, crack initiation and crack propagation. Based on the literature, ' f_p ' is the degradation factor represented as a function of porosity in the hybrid nanocomposites, which is as follows [74]:

$$f_p = 1 - e^{-np} \quad (5.22)$$

where 'n' is empirical constant equal to 1.943 and 'p' is porosity.

Strengthening contributions of 0.5HNC, 1HNC, 1.5HNC, 2HNC, and 3HNC hybrid nanocomposites is presented in Table 5.3, which is calculated using the parameters given in Table 5.2. Various strengthening contributions of SiCp nanoparticles are effectively more than that of graphite nanoparticles. This would be attributed to the addition of smaller size SiCp particles and increase of dislocation density in the matrix. Size factor also affects the yield strength of the matrix where as in this case SiCp nanoparticles are 10 times smaller than the graphite nanoparticles. The various strengthening effects are calculated for hybrid nanocomposites by fixing the SiCp nanoparticles content in the AA6061 aluminium alloy matrix and by varying the graphite nanoparticles content. The Hall-Petch effect $\Delta\sigma_{HP}$ for 3HNC hybrid nanocomposite is more than 2.64, 2.14, 1.53 and 1.27 times for 0.5HNC, 1HNC, 1.5HNC, and 2HNC hybrid nanocomposites respectively. This would be attributed due to the decrease of grain size of hybrid nanocomposites and combined strengthening effect of SiCp and graphite nanoparticles in the matrix. The load bearing effect $\Delta\sigma_{load}$ for 5HNC hybrid nanocomposites is more than 2.4, 1.9, 1.6, and 1.3 times for 0.5HNC, 1HNC, 1.5HNC, and 2HNC hybrid nanocomposites respectively.

Table 5.2: Yield strength of hybrid nanocomposites are predicted using these parameters

Material	E (GPa)	G (GPa)	$\alpha (10^{-6}/K)$	ν	b (nm)	d (nm)	V_f
β -SiCp			4.5 [133]			50	0.01684
Graphite			4.06 [137]			500	
AA6061 aluminium alloy	69	26	25.2 [16]	0.33[16]	0.286		

The Orowan effect $\Delta\sigma_{Orowan}$ for 3HNC hybrid nanocomposite is more than 1.12, 1.08, 1.05 and 1 times for 0.5HNC, 1HNC, 1.5HNC, and 2HNC hybrid nanocomposites respectively. The thermal dislocation mismatch effect $\Delta\sigma_{\Delta CTE}$ for 5HNC hybrid nanocomposite is more than 1.08, 1.06, 1.05, and 1.03 times than 0.5HNC, 1HNC, 1.5HNC, and 2HNC hybrid nanocomposites respectively. The contribution of load bearing effect is much lower than the other strengthening mechanisms (Table 5.4). The enhancement of yield strength is more influenced by $\Delta\sigma_{\Delta CTE}$ followed by $\Delta\sigma_{Orowan}$, $\Delta\sigma_{HP}$ and $\Delta\sigma_{load}$ respectively.

Table 5.3: Yield strength contribution from various strengthening mechanisms

Materials/ Strengthening mechanisms	0.5HNC	1HNC	1.5HNC	2HNC	3HNC
$\Delta\sigma_{HP}$ (MPa)	4.7	5.8	8.1	9.8	12.4
$\Delta\sigma_{load}$ (MPa)	0.63	0.79	0.95	1.2	1.5
$\Delta\sigma_{\Delta CTE}$ (MPa)	74.1	75.2	76.62	77.9	80.4
$\Delta\sigma_{Orowan}$ (MPa)	45.1	46.52	47.7	48.7	50.51

Different prediction models are described for studying the enhancement of yield strength of nanocomposites i.e., Ramakrishnan's model [84], Zhang and Chen model [85], Mirza and chen model [74], Modified clyne model [16], arithmetic model [16], quadratic summation model [16], compounding models [16]. Ramakrishnan introduced a model to predict yield strength as a function of load bearing effect and dislocation mismatch effect. According to Ramakrishnan's model the yield strength of the composite is given by the relation [84].

$$\sigma_{ync} = (\sigma_m) \left(1 + \frac{\Delta\sigma_{load}}{\sigma_m}\right) \left(1 + \frac{\Delta\sigma_{\Delta CTE}}{\sigma_m}\right) \quad (5.23)$$

Zhang and Chen implemented yield strength prediction model as a function of Orowan effect, thermal mismatch effect and load bearing effect. Rise of yield strength of the hybrid nanocomposites can be described as follows [85]:

$$\sigma_{ync} = (\sigma_m) \left(1 + \frac{\Delta\sigma_{load}}{\sigma_m}\right) \left(1 + \frac{\Delta\sigma_{\Delta CTE}}{\sigma_m}\right) \left(1 + \frac{\Delta\sigma_{Orowan}}{\sigma_m}\right) \quad (5.24)$$

Mirza and Chen developed a model to predict the yield strength of hybrid nanocomposites including load bearing effect, thermal dislocation mismatch effect, Orowan effect, Hall-Petch effect and porosity effect. Then the yield strength of the hybrid nanocomposites is given below [84]:

$$\sigma_{ync} = (\sigma_m) \left(1 + \frac{\Delta\sigma_{load}}{\sigma_m} - P\right) \left(1 + \frac{\Delta\sigma_{\Delta CTE}}{\sigma_m}\right) \left(1 + \frac{\Delta\sigma_{Orowan}}{\sigma_m}\right) \left(1 + \frac{\Delta\sigma_{HP}}{\sigma_m}\right) (e^{-nP}) \quad (5.25)$$

Clyne et al. [16] suggested the quadratic summation model for prediction of yield strength of nanocomposites. This model is proposed for micron size particles reinforced

composites. Several reports specify that the nanocomposite properties significantly improved and the assumptions for micron size particle reinforced composites cannot be applied to nanocomposites. This model assumes that the total enhancement of yield strength is proportional to the sum of the squares of each strengthening effect under square root. The yield strength of nanocomposites is theoretically calculated using equation 5.24 given below.

$$\sigma_{ync} = \sigma_m + \sqrt{\Delta\sigma_{HP}^2 + \Delta\sigma_{Orowan}^2 + \Delta\sigma_{\Delta CTE}^2 + \Delta\sigma_{load}^2} \quad (5.26)$$

Orowan and thermal mismatch effect played a major role in the increment of yield strength of hybrid nanocomposites. Hall-Petch and load bearing effect is negligible compared to other strengthening mechanisms. Orowan and thermal mismatch strengthening mechanisms are directly influencing yield strength of hybrid nanocomposites. So that it is required to take the sum of squares of Orowan and thermal mismatch effect under square root. Considering these two strengthening mechanisms under square root is known as Modified clyne model [84].

$$\sigma_{ync} = \sigma_m + \Delta\sigma_{HP} + \Delta\sigma_{load} + \sqrt{\Delta\sigma_{Orowan}^2 + \Delta\sigma_{\Delta CTE}^2} \quad (5.27)$$

Summation of contribution of each strengthening mechanism is known as arithmetic summation model. According to this model the various strengthening effect acts and independently contribute to the yield strength of the hybrid nanocomposites [16].

$$\sigma_{ync} = \sigma_m + \Delta\sigma_{HP} + \Delta\sigma_{Orowan} + \Delta\sigma_{\Delta CTE} + \Delta\sigma_{load} \quad (5.28)$$

According to compounding model the enhancement of yield strength due nano-reinforcements is multiplied to σ_{ync} and is given equation 5.27 below [84].

$$\sigma_{ync} = (\sigma_m) \left(1 + \frac{\Delta\sigma_{HP}}{\sigma_m}\right) \left(1 + \frac{\Delta\sigma_{load}}{\sigma_m}\right) \left(1 + \frac{\Delta\sigma_{\Delta CTE}}{\sigma_m}\right) \left(1 + \frac{\Delta\sigma_{Orowan}}{\sigma_m}\right) \quad (5.29)$$

The predicted yield strength of 2NC nanocomposite, 1HNC, 2HNC, 3HNC, 4HNC and 5HNC hybrid nanocomposites are compared with the experimental results is shown in fig 5.16. Predicted yield strength of hybrid nanocomposites obtained from the modified Clyne model and quadratic summation model are close to the experimental yield strength values. But there is a sudden decrement in yield strength for 5HNC hybrid nanocomposites. This is

due to the presence of maximum amount of porosity and nanoparticle cluster formation in the 5HNC hybrid nanocomposite.

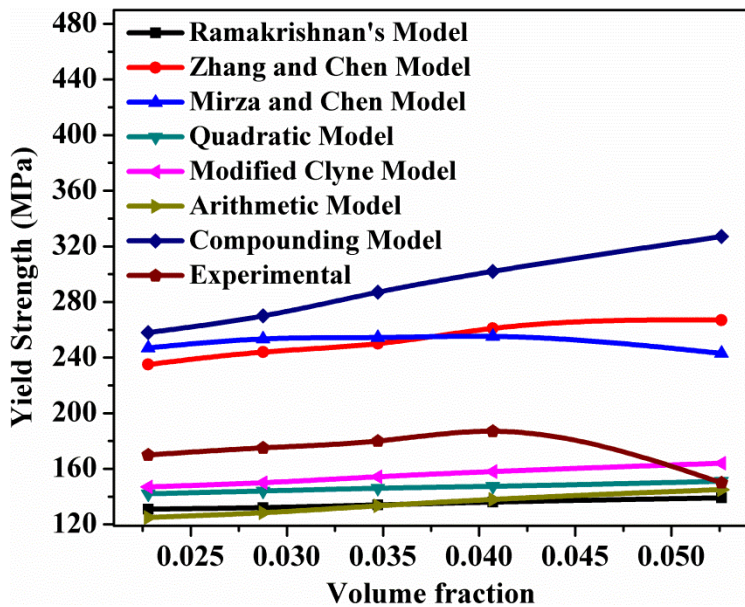


Figure 5.16: The yield strength of various models compared with the experimental data in Hybrid nanocomposites tested at 20 °C

5.6 Summary

This chapter presents the mechanical properties including hardness, yield strength, ultimate tensile strength and ductility of nanocomposites and hybrid nanocomposites. The yield strength of 0.5NC, 1NC, 1.5NC and 2NC nanocomposites and 0.5HNC, 1HNC, 1.5HNC, 2HNC and 3HNC hybrid nanocomposites is predicted using various strengthening mechanisms and yield strength prediction models. From the present chapter the following conclusions were drawn.

- Microhardness increased with SiCp and decreased with increase of graphite content for same SiCp content.
- Yield strength and ultimate tensile strength increased with SiCp and decreased after 2wt. % of graphite for same SiCp.
- Fracture surface indicates ductile to brittle fracture mode with increase in SiCp and more brittle fracture mode with increase in graphite content.

- Orowan strengthening effect and thermal dislocation mismatch density effect is found to play a significant role in the metal matrix nanocomposites. The contribution of Hall-Petch and load bearing effect is negligible in the AA6061/SiCp nanocomposites.
- The experimental data points are slightly near the 5% porosity data points of the Mirza and Chen model.
- Enhancement of yield strength value of the strengthening mechanisms follows the trend ($\Delta\sigma_{\Delta CTE} > \Delta\sigma_{Orowan} > \Delta\sigma_{HP} > \Delta\sigma_{Load}$) for hybrid nanocomposites.
- Predicted yield strength of hybrid nanocomposites obtained from the modified Clyne model and quadratic summation model are close to the experimental values.

Chapter 6

Tribological Properties

6.1 Introduction

In this chapter, the dry sliding wear behaviour of AA6061 aluminium alloy, 0.5NC, 1NC, 1.5NC, and 2NC nanocomposites, 0.5HNC, 1HNC, 1.5HNC, 2HNC, and 3HNC hybrid nanocomposites on EN31 steel counter face was studied as a function of applied normal load, sliding distance and sliding velocity. The two body abrasive wear characteristics of the AA6061 aluminium alloy, 2NC nanocomposite, and 2HNC hybrid nanocomposite were studied as a function of applied normal load, sliding distance, sliding velocity, and abrasive grit particle size. The investigation on worn surfaces of pin specimens, wear debris and abrasive grit papers was done to understand the possible wear mechanisms in dry sliding wear and abrasive wear process.

6.2 Tribological Properties of AA6061/SiCp Nanocomposites

6.2.1 Volumetric Wear Rate

The volumetric wear rate of the AA6061 aluminium alloy, 0.5NC, 1NC, 1.5NC, and 2NC nanocomposites was calculated from wear loss (g) data after the dry sliding wear tests on EN31 steel and reported in Table 6.1 to 6.4. The effect of SiCp particles, applied normal load, sliding velocity and sliding distance on volumetric wear rate is discussed in the following sub sections. The wear rate of the materials is a function of its metallurgical characteristics, operating and environmental conditions, and nature of counter surface.

Among these, hardness of the pin material, EN31 steel disc and silicon carbide grit paper will play a significant role on the type of wear mechanism [148].

Table 6.1: Volumetric wear rate of different materials obtained at 0.5 m/s sliding velocity

Load (N)	Sliding distance (m)	Volumetric Wear Rate (mm ³ /m)				
		0.5 m/s (sliding velocity)				
		AA6061 alloy	0.5NC	1NC	1.5NC	2NC
5	1000	0.0056	0.00513	0.00477	0.00443	0.0042
5	2000	0.0068	0.0062	0.00563	0.00516	0.0046
5	3000	0.0074	0.00695	0.00643	0.00604	0.0056
10	1000	0.0061	0.00586	0.00541	0.00495	0.0045
10	2000	0.0072	0.00674	0.00636	0.00576	0.0054
10	3000	0.0082	0.00783	0.00725	0.00682	0.0063
15	1000	0.0068	0.00653	0.00618	0.00583	0.0061
15	2000	0.0076	0.00739	0.00716	0.00692	0.0068
15	3000	0.0085	0.00815	0.00782	0.00743	0.0071
20	1000	0.0071	0.00694	0.00680	0.00672	0.0066
20	2000	0.0078	0.00756	0.00736	0.00718	0.007
20	3000	0.0098	0.00956	0.00933	0.00915	0.009

Table 6.2: Volumetric wear rate of different materials obtained at 1 m/s sliding velocity

Load (N)	Sliding distance (m)	Volumetric Wear Rate (mm ³ /m)				
		1 m/s (sliding velocity)				
		AA6061 alloy	0.5NC	1NC	1.5NC	2NC
5	1000	0.0057	0.00534	0.00497	0.00458	0.0043
5	2000	0.0071	0.00664	0.00616	0.00559	0.0053
5	3000	0.0095	0.00866	0.00775	0.00663	0.0059
10	1000	0.0062	0.00585	0.00552	0.00526	0.0049
10	2000	0.0077	0.00723	0.00672	0.00627	0.0056
10	3000	0.0103	0.00948	0.0086	0.00752	0.0067
15	1000	0.0069	0.00674	0.00658	0.00646	0.0062
15	2000	0.0083	0.008	0.00763	0.00726	0.007
15	3000	0.0111	0.0101	0.00936	0.00839	0.0074
20	1000	0.0075	0.00734	0.00716	0.00703	0.0068
20	2000	0.0086	0.00823	0.00798	0.00758	0.0073
20	3000	0.0115	0.0109	0.0105	0.010	0.0095

Table 6.3: Volumetric wear rate of different materials obtained at 1.5 m/s sliding velocity

Load (N)	Sliding distance (m)	Volumetric Wear Rate (mm ³ /m)				
		1.5 m/s (sliding velocity)				
		AA6061 alloy	0.5NC	1NC	1.5NC	2NC
5	1000	0.0065	0.00603	0.00566	0.00487	0.0044
5	2000	0.0077	0.00727	0.00674	0.00629	0.0054
5	3000	0.0099	0.00918	0.00878	0.00833	0.0069
10	1000	0.0079	0.00711	0.00627	0.00546	0.0048
10	2000	0.0083	0.00766	0.00703	0.00656	0.0059
10	3000	0.0108	0.0103	0.00953	0.00873	0.0082
15	1000	0.0085	0.00762	0.00685	0.00605	0.0063
15	2000	0.0092	0.00873	0.00825	0.00774	0.0073
15	3000	0.0116	0.0111	0.0106	0.0102	0.0088
20	1000	0.0096	0.00849	0.00757	0.00672	0.0069
20	2000	0.0102	0.00968	0.00904	0.00838	0.0076
20	3000	0.0126	0.0121	0.0116	0.0112	0.0108

Table 6.4: Volumetric wear rate of different materials obtained at 2 m/s sliding velocity

Load (N)	Sliding distance (m)	Volumetric Wear Rate (mm ³ /m)				
		2 m/s (sliding velocity)				
		AA6061 alloy	0.5NC	1NC	1.5NC	2NC
5	1000	0.00696	0.00652	0.00625	0.0059	0.0055
5	2000	0.0079	0.0075	0.00692	0.00639	0.0058
5	3000	0.011	0.0098	0.0088	0.00851	0.0073
10	1000	0.0082	0.00775	0.00726	0.00658	0.0061
10	2000	0.00872	0.00824	0.00776	0.00734	0.007
10	3000	0.0112	0.0103	0.00966	0.00861	0.0079
15	1000	0.0085	0.00813	0.00758	0.00697	0.0064
15	2000	0.0112	0.0107	0.00926	0.00865	0.0081
15	3000	0.0123	0.0114	0.0106	0.0104	0.0094
20	1000	0.009	0.00849	0.00793	0.00737	0.0071
20	2000	0.012	0.0113	0.0105	0.00935	0.0085
20	3000	0.0136	0.013	0.0126	0.0123	0.0119

6.2.1.1 Effect of applied normal load

Figure 6.1 represents the wear rate of AA6061 aluminium alloy, 0.5NC, 1NC, 1.5NC, and 2NC nanocomposites as a function of applied normal loads. Figure 6.1 (a) denotes the wear rate of materials at 2 m/s sliding velocity. It is observed that the decrement in volumetric wear rate of 0.5NC, 1NC, 1.5NC, and 2NC nanocomposites at 5 N applied normal load and 1000 m sliding distance is 6.4%, 10.3%, 15.3%, and 21% respectively. It revealed that the decrement in volumetric wear rate of 0.5NC, 1NC, 1.5NC, and 2NC nanocomposites at 10 N applied normal load and 1000 m sliding distance is 5.5%, 11.5%, 19.76%, and 25.6% respectively. It can be seen that the decrement in volumetric wear rate of 0.5NC, 1NC, 1.5NC, and 2NC nanocomposites at 15 N applied normal load and 1000 m sliding distance is 4.4%, 10.82%, 18%, and 24.71% respectively. The decrement in volumetric wear rate of 0.5NC, 1NC, 1.5NC, and 2NC nanocomposites at 20 N applied normal load and 1000 m sliding distance is 5.7%, 11.9%, 18.1%, and 21.1% respectively.

Figure 6.1 (b) indicates the volumetric wear rate of materials at 2000 m sliding distances and at 2 m/s sliding velocity. It is observed that the decrement in volumetric wear rate of 0.5NC, 1NC, 1.5NC, and 2NC nanocomposites at 5 N applied normal load and 2000 m sliding distance is 5.1%, 12.4%, 19.1%, and 26.58% respectively. It revealed that the decrement in volumetric wear rate of 0.5NC, 1NC, 1.5NC, and 2NC nanocomposites at 10 N applied normal load and 2000 m sliding distance is 5.5%, 11%, 15.83%, and 19.73% respectively. It can be seen that the decrement in volumetric wear rate of 0.5NC, 1NC, 1.5NC, and 2NC nanocomposites at 15 N applied normal load and 2000 m sliding distance is 4.5%, 17.3%, 22.77%, and 27.68% respectively. The decrement in volumetric wear rate of 0.5NC, 1NC, 1.5NC, and 2NC nanocomposites at 20 N applied normal load and 2000 m sliding distance is 5.83%, 12.5%, 22.1%, and 29.2% respectively.

Figure 6.1 (c) represents the volumetric wear rate of materials at 3000 m sliding distances and at 2 m/s sliding velocity. It is observed that the decrement in volumetric wear rate of 0.5NC, 1NC, 1.5NC, and 2NC nanocomposites at 5 N applied normal load and 3000 m sliding distance is 10.9%, 20.36%, 29%, and 36.64% respectively. It revealed that the decrement in volumetric wear rate of 0.5NC, 1NC, 1.5NC, and 2NC nanocomposites at 10 N applied normal load and 3000 m sliding distance is 8.04%, 13.8%, 23.1%, and 29.47% respectively. It can be seen that the decrement in volumetric wear rate of 0.5NC, 1NC,

1.5NC, and 2NC nanocomposites at 15 N applied normal load and 3000 m sliding distance is 7.31%, 13.82%, 20.33%, and 23.58% respectively. The decrement in volumetric wear rate of 0.5NC, 1NC, 1.5NC, and 2NC nanocomposites at 20 N applied normal load and 3000 m sliding distance is 4.41%, 7.36%, 9.56%, and 12.5% respectively.

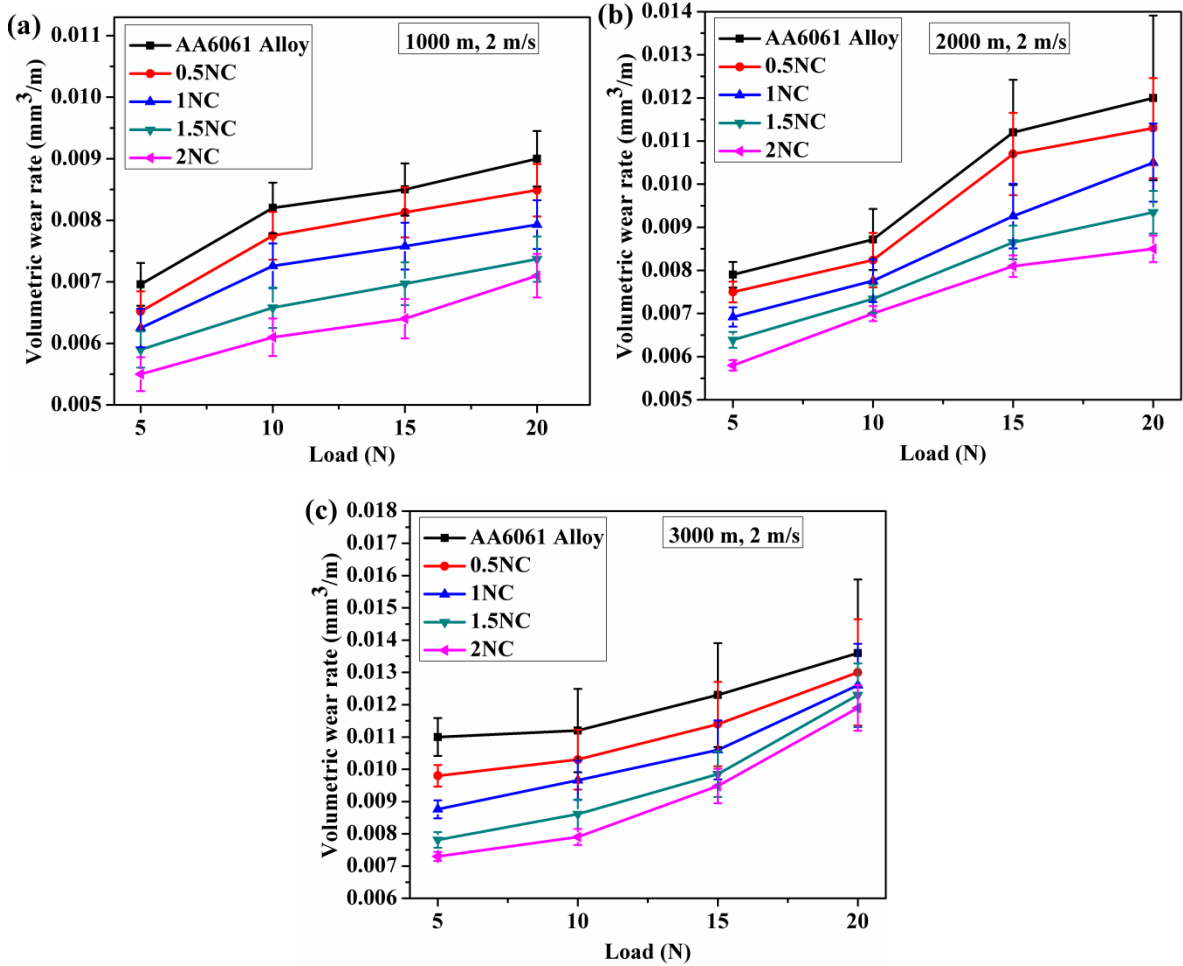


Figure 6.1: Volumetric wear rate of AA6061 aluminium alloy, 0.5NC, 1NC, 1.5NC, and 2NC nanocomposites as a function of applied normal load (a) 1000 m (b) 2000 m and (c) 3000 m

It is identified that the volumetric wear rate of all materials increased gradually with rise of applied normal loads [98]. The higher volumetric wear rate is found in unreinforced AA6061 aluminium alloy compared to nanocomposite materials. This would be attributed due to less wear resistance of unreinforced AA6061 aluminium alloy at all applied normal load conditions. The rise of applied normal loads on base alloy increases the more depth of penetration of EN31 steel and breaks matrix. During dry sliding, counteracting of hard asperities would lead to formation of large grooves with higher depth of penetration and larger deformation of surface leads to more wear rate [138].

6.2.1.2 Effect of sliding distance

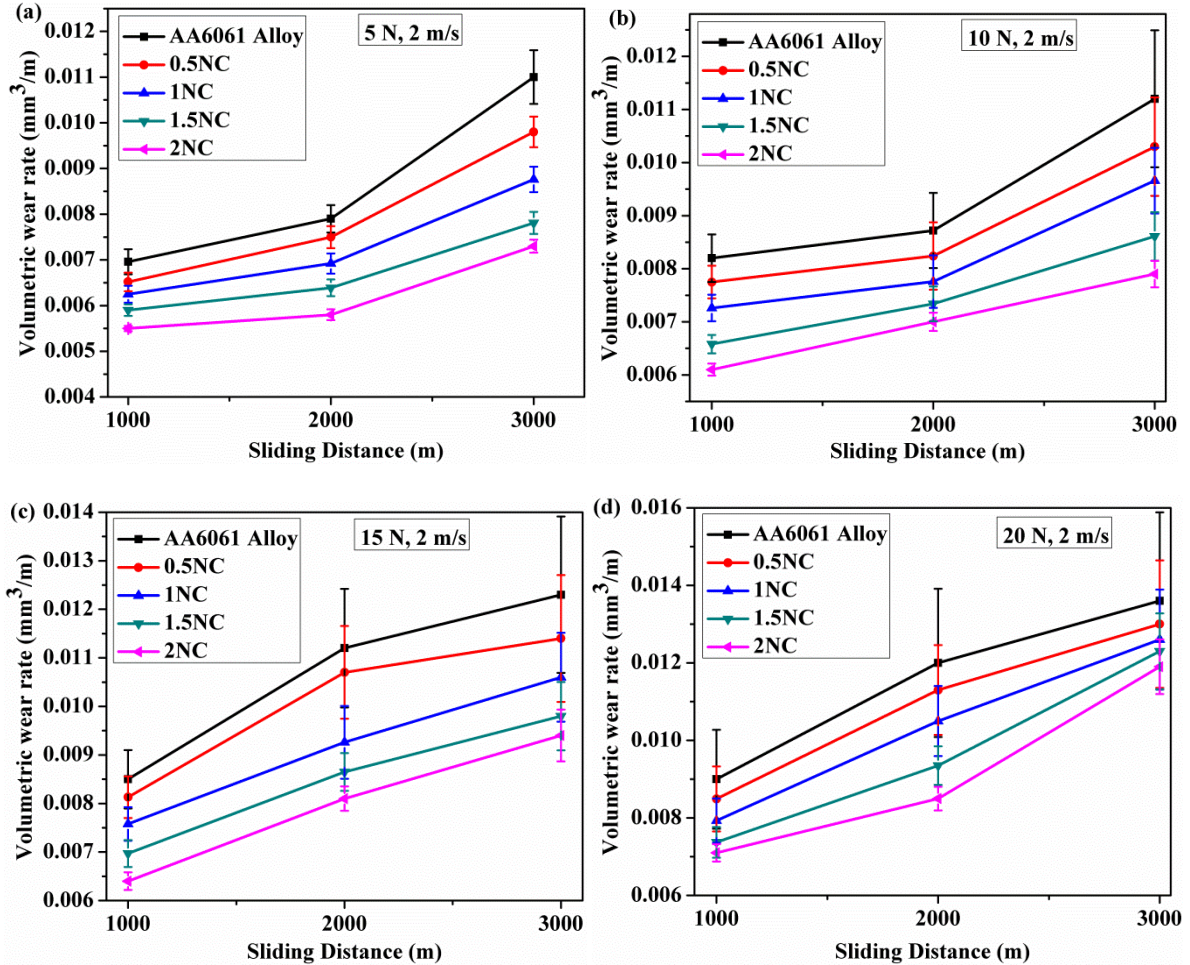


Figure 6.2: Volumetric wear rate of AA6061 aluminium alloy, 0.5NC, 1NC, 1.5NC, and 2NC nanocomposites as a function of sliding distance (a) 5 N (b) 10 N and (c) 15 N and (d) 20 N

Figure 6.2 represents the volumetric wear rate of AA6061 aluminium alloy, 0.5NC, 1NC, 1.5NC, and 2NC nanocomposites as a function of sliding distance. Figure 6.2 (a) denotes the volumetric wear rate of materials at 5 N normal load and 2 m/s sliding velocity. It is observed that the decrement in volumetric wear rate of 0.5NC, 1NC, 1.5NC, and 2NC nanocomposites at 1000 m sliding distance was 6.3%, 10.2%, 15.23%, and 20.98% respectively. It is observed that the decrement in volumetric wear rate of 0.5NC, 1NC, 1.5NC, and 2NC nanocomposites at 2000 m sliding distance was 5.1%, 12.41%, 19.11%, and 26.6% respectively. It is observed that the decrement in volumetric wear rate of 0.5NC, 1NC, 1.5NC, and 2NC nanocomposites at 3000 m sliding distance was 10.9%, 20.4%, 29%, and 33.64% respectively.

Figure 6.2 (b) indicates the volumetric wear rate of materials at 10 N applied normal loads and at 2 m/s sliding velocity. It revealed that the decrement in volumetric wear rate of 0.5NC, 1NC, 1.5NC, and 2NC nanocomposites at 10 N applied normal load and 1000 m sliding distance was 5.5%, 11.5%, 19.8%, and 25.6% respectively. It revealed that the decrement in volumetric wear rate of 0.5NC, 1NC, 1.5NC, and 2NC nanocomposites at 2000 m sliding distance was 5.5%, 11%, 15.83%, and 19.73% respectively. It revealed that the decrement in volumetric wear rate of 0.5NC, 1NC, 1.5NC, and 2NC nanocomposites at 3000 m sliding distance was 8.04%, 13.8%, 23.2%, and 29.5% respectively.

Figure 6.2 (c) represents the volumetric wear rate of materials at 15 N applied normal load and at 2m/s sliding velocity. It can be seen that the decrement in volumetric wear rate of 0.5NC, 1NC, 1.5NC, and 2NC nanocomposites at 1000 m sliding distance was 4.3%, 10.8%, 18%, and 24.7% respectively. It can be seen that the decrement in volumetric wear rate of 0.5NC, 1NC, 1.5NC, and 2NC nanocomposites at 2000 m sliding distance was 4.5%, 17.32%, 22.8%, and 27.7% respectively. It can be seen that the decrement in volumetric wear rate of 0.5NC, 1NC, 1.5NC, and 2NC nanocomposites at 3000 m sliding distance was 7.32%, 13.82%, 20.32%, and 23.58% respectively.

Figure 6.2 (d) represents the volumetric wear rate of materials at 20 N applied normal load and at 2 m/s sliding velocity. The decrement in volumetric wear rate of 0.5NC, 1NC, 1.5NC, and 2NC nanocomposites at 1000 m sliding distance was 5.7%, 11.9%, 18.1%, and 21.1% respectively. The decrement in volumetric wear rate of 0.5NC, 1NC, 1.5NC, and 2NC nanocomposites at 2000 m sliding distance was 5.83%, 12.5%, 22.1%, and 29.2% respectively. The decrement in volumetric wear rate of 0.5NC, 1NC, 1.5NC, and 2NC nanocomposites at 3000 m sliding distance was 4.4%, 7.4%, 9.6%, and 12.5% respectively.

It is identified that the volumetric wear rate rises with the increase of sliding distance for all materials. Temperature increases at contact surface of pin and disc with rise of sliding distance, which promotes the oxidation process and formation of tribo-layer, which reflects on microstructural changes such as dissolution of precipitates [139]. The tribo-layer gets worn off with increase of contact surface temperature and thus results in higher wear rate [140]. It is identified that highest volumetric wear rate is observed for unreinforced AA6061 aluminium alloy for all sliding distances.

6.2.1.3 Effect of sliding velocity

The volumetric wear rate of ultrasonically assisted casted materials is plotted in figure 6.3 as a function of sliding velocity at various applied normal loads and constant sliding distance of 3000 m. Figure 6.3 (a) depicts the volumetric wear rate of AA6061 aluminium alloy, 0.5NC, 1NC, 1.5NC, and 2NC nanocomposites at 5 N applied normal load and 3000 m sliding distance. It is observed that the decrement in volumetric wear rate of 0.5NC, 1NC, 1.5NC, and 2NC nanocomposites at 0.5 m/s sliding velocity was 6.1%, 13.2%, 18.4%, and 24.32% respectively. It is observed that the decrement in volumetric wear rate of 0.5NC, 1NC, 1.5NC, and 2NC nanocomposites at 1 m/s sliding velocity was 8.84%, 18.42%, 30.21%, and 37.9% respectively. It can be seen that the decrement in volumetric wear rate of 0.5NC, 1NC, 1.5NC, and 2NC nanocomposites at 1.5 m/s sliding velocity was 7.3%, 11.3%, 15.86%, and 30.3% respectively. It is identified that the decrement in volumetric wear rate of 0.5NC, 1NC, 1.5NC, and 2NC nanocomposites at 2 m/s sliding velocity was 10.91%, 20%, 22.64%, and 33.64 respectively.

Figure 6.3 (b) depicts the volumetric wear rate of AA6061 aluminium alloy, 0.5NC, 1NC, 1.5NC, and 2NC nanocomposites at 10 N applied normal load and 3000 m sliding distance. It is observed that the decrement in volumetric wear rate of 0.5NC, 1NC, 1.5NC, and 2NC nanocomposites at 0.5 m/s sliding velocity was 4.51%, 11.6%, 16.83%, and 23.17% respectively. It is observed that the decrement in volumetric wear rate of 0.5NC, 1NC, 1.5NC, and 2NC nanocomposites at 1 m/s sliding velocity was 7.96%, 16.51%, 26.99%, and 34.95% respectively. It is observed that the decrement in volumetric wear rate of 0.5NC, 1NC, 1.5NC, and 2NC nanocomposites at 1.5 m/s sliding velocity was 4.63%, 11.76%, 19.17%, and 24.1% respectively. It was found that the decrement in volumetric wear rate of 0.5NC, 1NC, 1.5NC, and 2NC nanocomposites at 2 m/s sliding velocity was 8.1%, 13.8%, 20%, and 22.32% respectively.

Figure 6.3 (c) depicts the volumetric wear rate of AA6061 aluminium alloy, 0.5NC, 1NC, 1.5NC, and 2NC nanocomposites at 15 N applied normal load and 3000 m sliding distance. It is identified that the decrement in volumetric wear rate of 0.5NC, 1NC, 1.5NC, and 2NC nanocomposites at 0.5 m/s sliding velocity was 4.1%, 8%, 12.6%, and 16.5% respectively. It is observed that the decrement in volumetric wear rate of 0.5NC, 1NC, 1.5NC, and 2NC nanocomposites at 1 m/s sliding velocity was 9%, 15.7%, 24.4%, and

33.33% respectively. It can be seen that the decrement in volumetric wear rate of 0.5NC, 1NC, 1.5NC, and 2NC nanocomposites at 1.5 m/s sliding velocity was 4.3%, 8.63%, 12.1%, and 24.14% respectively. It is identified that the decrement in volumetric wear rate of 0.5NC, 1NC, 1.5NC, and 2NC nanocomposites at 2 m/s sliding velocity was 7.32%, 12.2%, 15.5%, and 23.6% respectively.

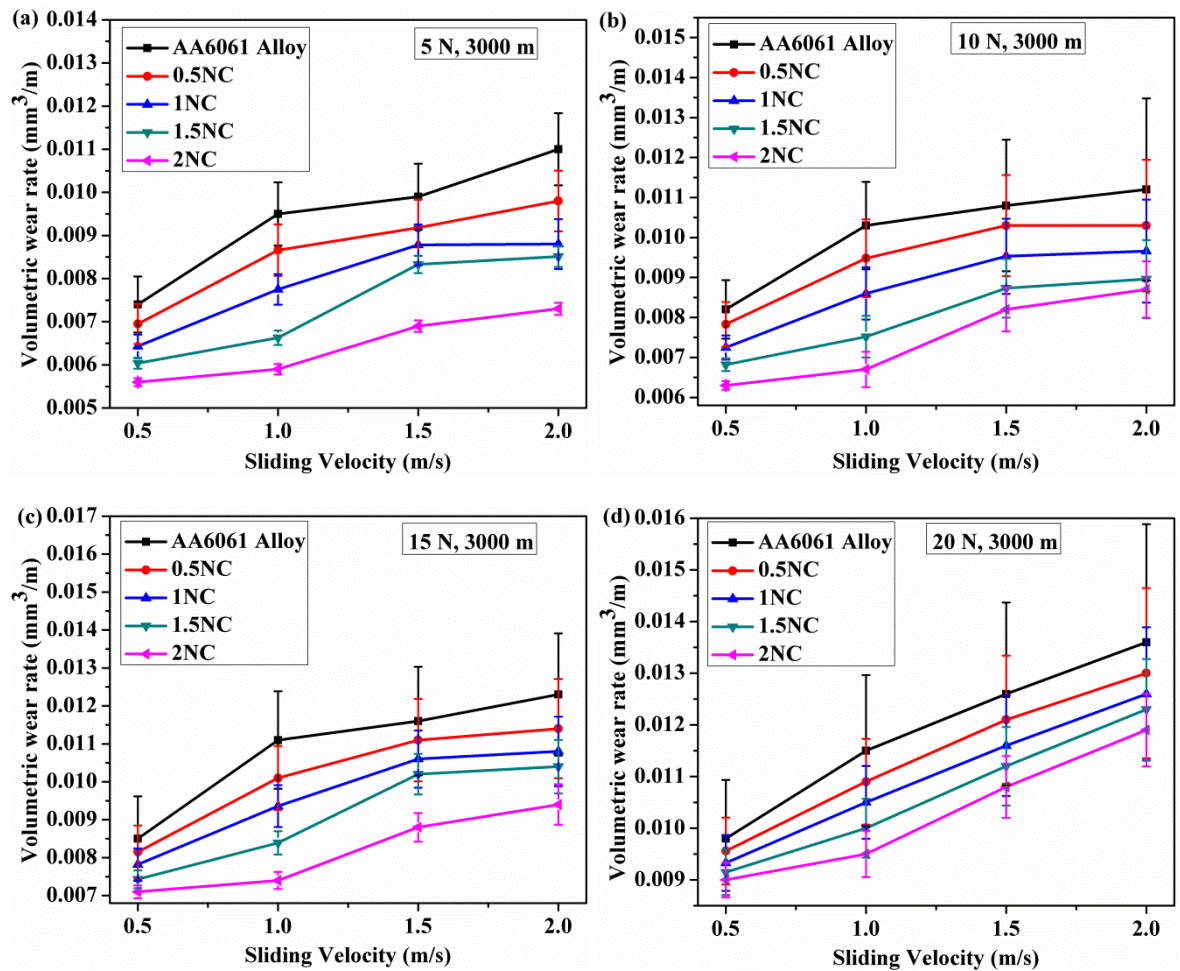


Figure 6.3: Volumetric wear rate of AA6061 aluminium alloy, 0.5NC, 1NC, 1.5NC, and 2NC nanocomposites as a function of sliding velocity (a) 5 N (b) 10 N and (c) 15 N and (d) 20 N

Figure 6.3 (d) depicts the wear rate of AA6061 aluminium alloy, 0.5NC, 1NC, 1.5NC, and 2NC nanocomposites at 20 N applied normal load and 3000 m sliding distance. It is identified that the decrement in volumetric wear rate of 0.5NC, 1NC, 1.5NC, and 2NC nanocomposites at 0.5 m/s sliding velocity was 2.5%, 4.8%, 6.63%, and 8.17% respectively. It is observed that the decrement in volumetric wear rate of 0.5NC, 1NC, 1.5NC, and 2NC nanocomposites at 1 m/s sliding velocity was 5.2%, 8.7%, 13.1%, and 17.4% respectively. It

can be seen that the decrement in volumetric wear rate of 0.5NC, 1NC, 1.5NC, and 2NC nanocomposites at 1.5 m/s sliding velocity was 3.97%, 7.94%, 11.1%, and 14.3% respectively. It is observed that the decrement in volumetric wear rate of 0.5NC, 1NC, 1.5NC, and 2NC nanocomposites at 2 m/s sliding velocity was 4.4%, 7.4%, 9.6%, and 12.5% respectively.

It is identified that the volumetric wear rate rises with the increase of sliding velocity for all materials. Temperature increases at contact surface of pin and disc with rise of sliding velocity, which promotes the oxidation process and formation of tribo-layer, which reflects on microstructural changes such as dissolution of precipitates [139]. The tribo-layer worn off with increase of contact surface temperature and thus results in higher wear rate [140]. It is identified that highest wear rate is observed for unreinforced AA6061 aluminium alloy for all sliding velocities.

6.2.2 Wear Coefficients

The wear coefficients of AA6061 aluminium alloy, 0.5NC, 1NC, 1.5NC, and 2NC nanocomposites are represented in figure 6.4 as a function of applied normal load, sliding distance, sliding velocity and SiCp reinforcements. The wear coefficients are shown in figure 6.4 (a) as a function of applied normal load. It is noticed that the wear coefficients decreased for 5 N to 15 N and increased for 20 N applied normal load for all tested materials. It would be attributed due to the higher depth of penetration of hard asperites into the soft nanocomposites pin surface at higher loads. Similar trends were observed in the previous studies mentioned by Das et al. [126], Yang et al. [88], and Kaushik et al. [141]. The wear coefficients are shown in figure 6.4 (b) as a function of materials. It is noticed that the wear coefficients of AA6061 aluminium alloy, 0.5NC, 1NC, 1.5NC, and 2NC nanocomposites decreased with increase of SiCp nano-reinforcements in the alloy matrix at all conditions. It would be attributed due to the addition of SiCp nano-reinforcements particles in to the matrix that increases the wear resistance of nanocomposites. The wear coefficients are represented in figure 6.4 (c) as a function of sliding distance. It can be seen that the wear coefficients of materials increased with increase of sliding distance. This would be attributed due to the occurrence of more damaged wear tracks caused by fractured SiCp nanoparticles when a longer sliding distance is used.

The wear coefficients of AA6061 aluminium alloy, 0.5NC, 1NC, 1.5NC, and 2NC nanocomposites are shown in figure 6.4 (d) as a function of sliding velocity. It is observed that the wear coefficients of the AA6061 aluminium alloy, 0.5NC, 1NC, 1.5NC, and 2NC nanocomposites increased with increase of sliding velocity. This would be attributed due to the occurrence of more damage of wear tracks caused by fractured SiCp when higher sliding velocity was used [108].

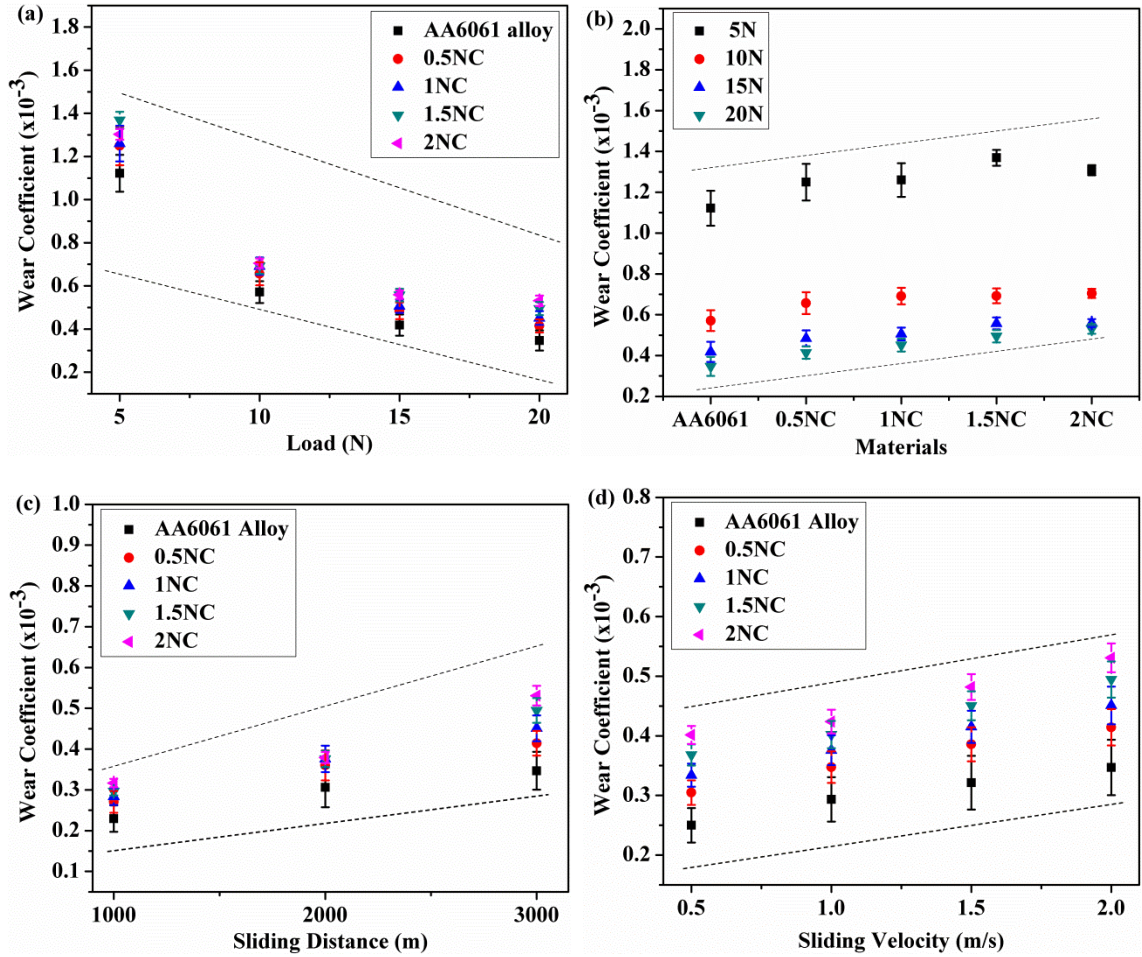


Figure 6.4: Wear coefficient of AA6061 aluminium alloy, 0.5NC, 1NC, 1.5NC, and 2NC nanocomposites as a function of (a) applied normal load, (b) material, (c) sliding distance, and (d) sliding velocity

The hard asperities quickly penetrate into the soft material with increase of sliding velocity at all applied normal load conditions. The wear coefficient decreased with increase of applied normal loads and increase of SiCp nano-reinforcement particles in the matrix. The wear coefficient increased with increase of sliding distance and sliding velocity for all materials. It is because the hardness of the SiCp reinforced nanocomposites materials

dominated the wear coefficients. Observed trend is according to the Archard's wear equation given in equation 6.1 as follows.

$$K = \frac{Q_{v/l} H_m}{W} \quad (6.1)$$

where, ' $Q_{v/l}$ ' is the volume loss per unit sliding distance (mm^3/m), ' H_m ' is the hardness of the material surface (N/mm^2), ' W ' is the applied load (N) and ' K ' is the dimensionless wear coefficient less than unity. But the hardness of the nanocomposites increased with increase of SiCp nano-reinforcements in the AA6061 aluminium alloy matrix. It is further noticed that the wear coefficients of the 0.5NC, 1NC, 1.5NC, and 2NC nanocomposites i.e., formation probability of wear particle is found to be lower than AA6061 aluminium alloy matrix. This would be attributed to the nanocomposites surface being protected by reducing the material plastic flow by SiCp nano-reinforcements [142]. At lower applied normal loads, higher wear coefficients indicate that the probability formation of wear particle could be mainly due to the crack nucleation and its propagation in to micro level crack even through the level of depth of penetration of hard asperities. But at higher applied normal loads the level of depth of penetration of specimen will be more and increases the material removal rate with higher plastic deformation [143]. At higher applied normal loads, it can be noted that the asperities formed during dry sliding wear process could be due to fragmentation either from the pin surface or counter surface. These hard asperities consist of hard debris present on the counter surface that penetrates deeper into the softer pin surface in the very initial stages of the dry sliding wear.

6.2.3 Coefficient of Friction

Coefficient of friction of AA6061 aluminium alloy, 0.5NC, 1NC, 1.5NC, and 2NC nanocomposites is shown in figure 6.5. It is observed that from figure 6.5 (a) the coefficient of friction increased with rising loads on pin irrespective of material. The increase of coefficient of friction would be attributed due to the increase in depth of penetration with rise of tangential loads on pin. The friction coefficient changed linearly for all conditions as a function of applied normal loads on pin materials. The friction coefficient increased with increase in the addition of the SiCp nano-reinforcements in the matrix material. The cubic structured beta SiCp particles in nanocomposite are attributed to rise in the friction coefficient which is more with increase in the nano-reinforcements wieght percentage in the

matrix [121]. Figure 6.5 (b) represents the coefficient of friction as a function of sliding velocity. The coefficient of friction decreased with increase of sliding velocities for all materials. This would be attributed due to the formation of MML on contact surface at higher sliding velocity. The lower friction coefficient is obtained at a large amount of sliding velocities [95]. At higher sliding velocities time for the individual asperity contacts and asperities deformation is less. This results in decrease of the real area of contact and decrease of the friction force with increasing velocity. Hence, the rate of volumetric wear and coefficient of friction decreases with extreme sliding velocity and sliding distance.

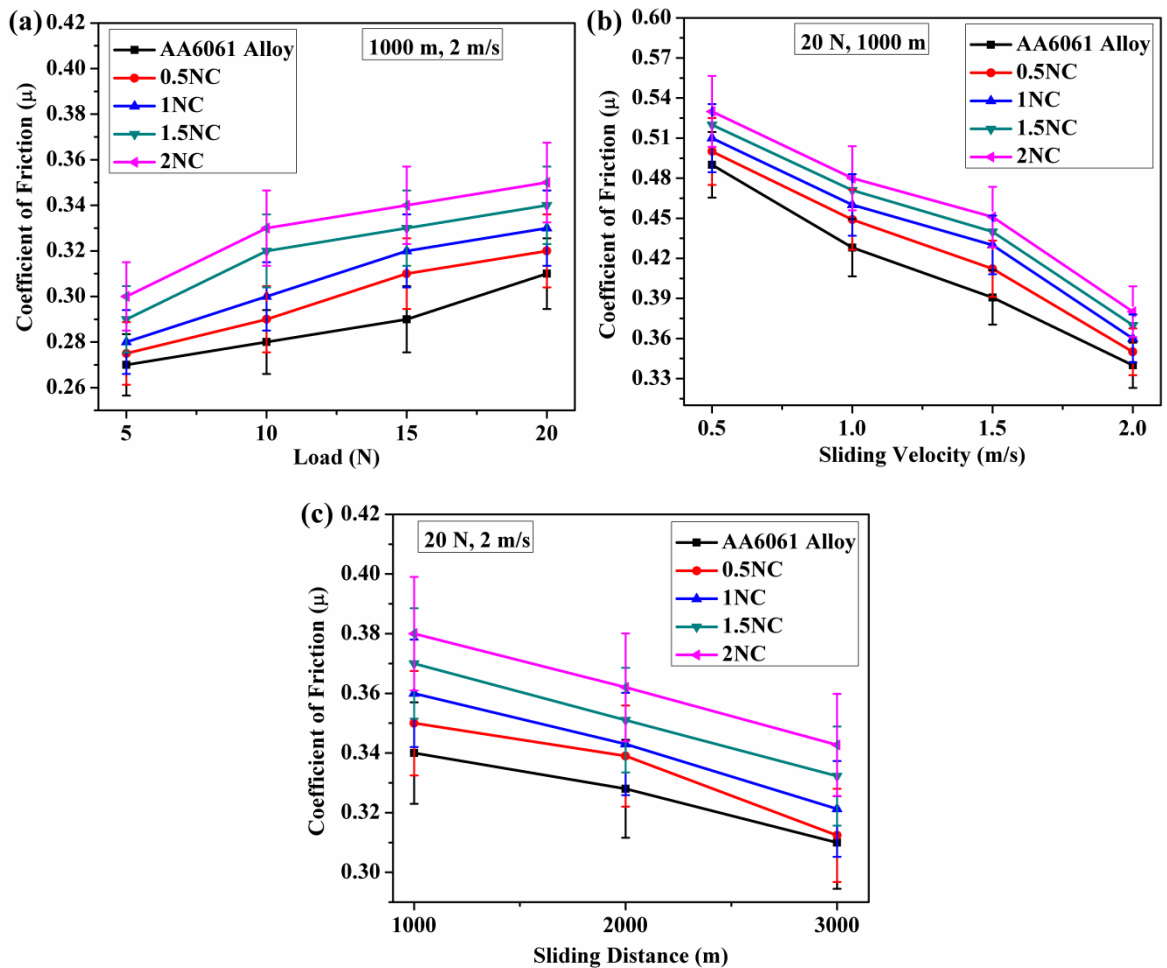


Figure 6.5: Coefficient of friction of AA6061 aluminium alloy, 0.5NC, 1NC, 1.5NC and 2NC nanocomposites (a) applied normal load, (b) sliding velocity, and (c) sliding distance

Figure 6.5 (c) depicts the variation in coefficient of friction with respect to sliding distance. The formation of oxide film on the worn surface rises with increase of sliding distance. This led to a nonlinear friction coefficient due to the hard asperities in between the nanocomposite pin surface and EN31 steel disc. The results revealed that the coefficient of

friction increased with the addition of SiCp nano-reinforcements in the AA6061 aluminium alloy matrix. This would be attributed to the presence of cubic structured beta SiCp nanoparticles in the alloy matrix [121].

The exhibited results shown in figure 6.6 reveals higher friction coefficient for 2NC nanocomposite compared to all materials. The increase of coefficient of friction of 0.5NC, 1NC, 1.5NC, and 2NC nanocomposites compared to AA6061 aluminium alloy at 20 N normal load, 1000 m sliding distance and at 2 m/s sliding velocity is 3.3%, 6.5%, 9.7%, and 13% respectively. The experimental results also confirm the increase of coefficient of friction for nanocomposites with increase of SiCp nanoparticles. The wear resistance of the aluminium based materials increased with the addition of SiCp nano-reinforcement particles and which increase the frictional heat at the interface [64].

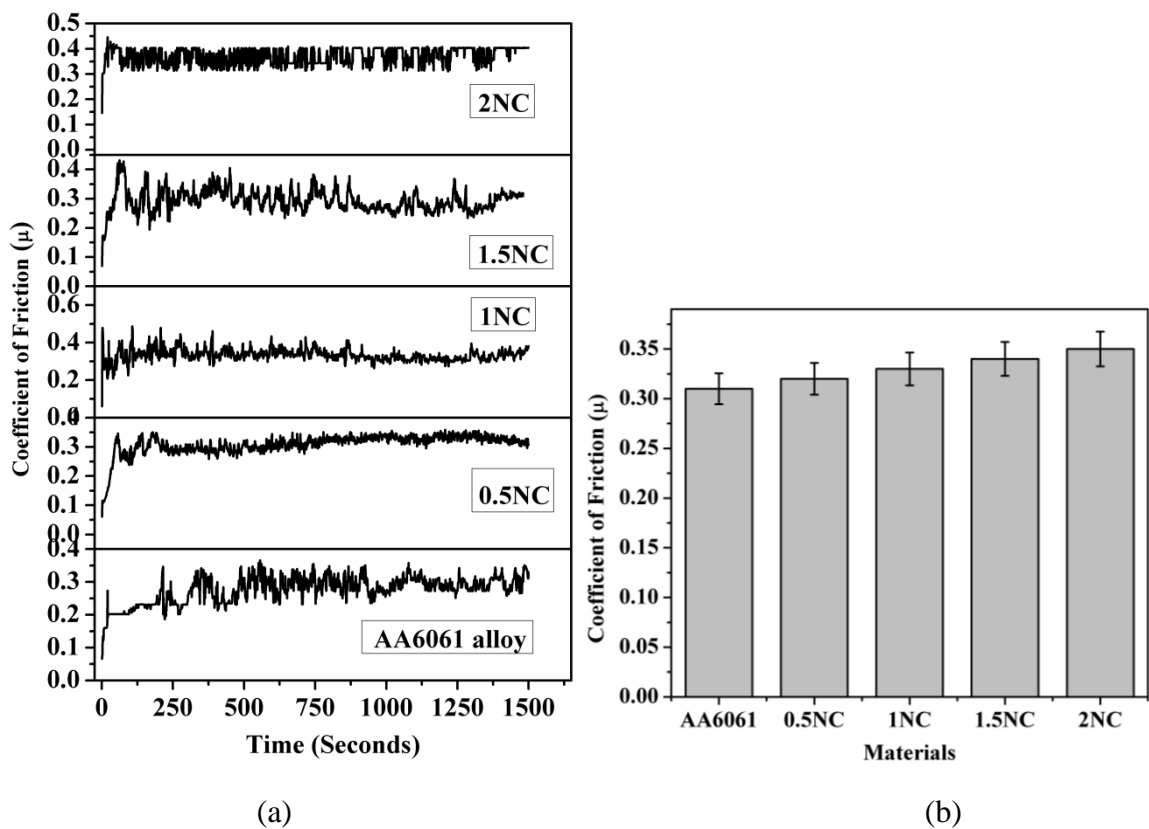


Figure 6.6: Coefficient of friction of AA6061 aluminium alloy based materials at 20N normal loads, 2 m/s sliding distance and 1000 m sliding distance (a) time and (b) materials

6.2.4 Worn Surfaces of Pin Specimens

In this study, three types of wear mechanisms were observed during wear testing at dry condition i.e., abrasion, oxidation, and delamination. Figures 6.7, 6.8, 6.9, and 6.10 represent the worn surfaces of the AA6061 aluminium alloy, 0.5NC, 1NC, 1.5NC and 2NC nanocomposites tested at 5 N, 1000 m and 0.5 m/s (named as $L_L D_L V_L$); 5 N, 3000 m and 2 m/s (named as $L_L D_H V_H$); 20 N, 1000 m and 0.5 m/s (named as $L_H D_L V_L$); and 20 N, 3000 m and 2 m/s (named as $L_H D_H V_H$) conditions respectively. Figures 6.7 (a) and 6.8 (a) indicate the worn surfaces of AA6061 aluminium alloy at 5 N applied normal load, lower and higher sliding distance, and sliding velocity conditions respectively. In the SEM images 'GR' represents the grooves, 'D' denotes the delaminating layer on the worn surface.

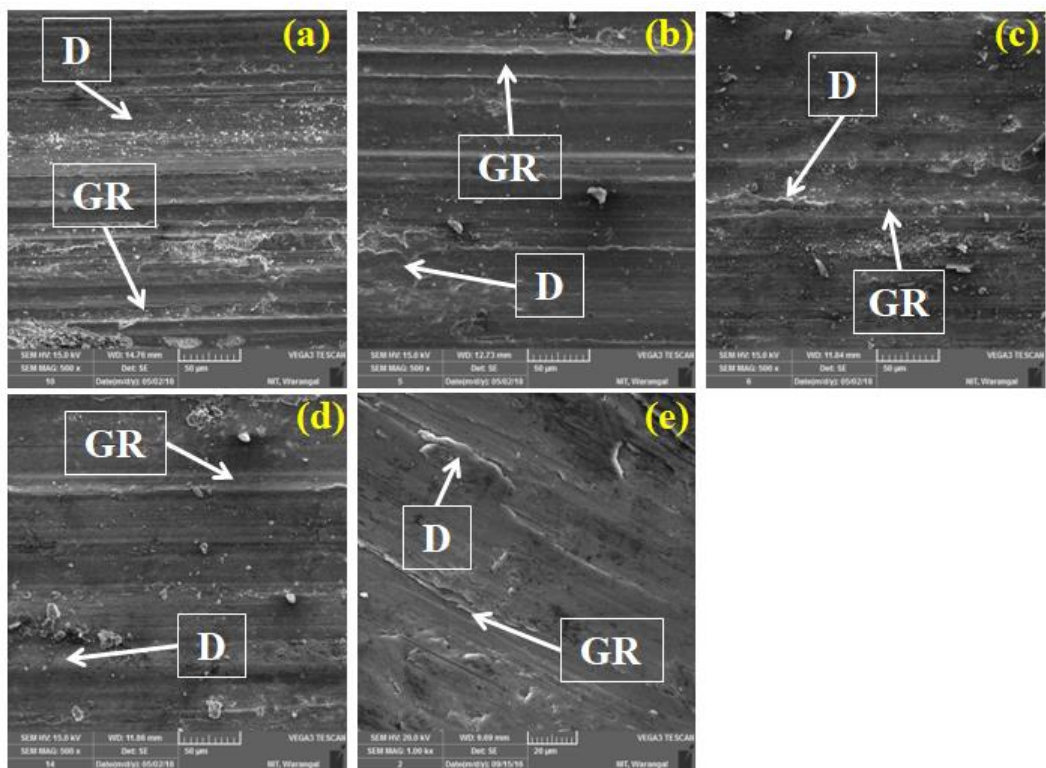


Figure 6.7: SEM images of worn surfaces of different materials at 5 N applied normal load, 0.5 m/s sliding velocity, and 1000 m sliding distance (a) AA6061 aluminium alloy, (b) 0.5NC, (c) 1NC, (d) 1.5NC and (e) 2NC

It can be observed that parallel grooves, scratches, and plastic deformation on AA6061 aluminium alloy worn surface in the sliding direction at $L_L D_L V_L$ condition. It can be seen that the deep grooves, shallower scratches and plastic flow of material on AA6061

aluminium alloy worn surface in the sliding direction at $L_L D_H V_H$ condition. Figure 6.9 (a) shows the worn surface of AA6061 aluminium alloy at $L_H D_L V_L$ condition. It can be seen that deeper parallel grooves, scratches and higher plastic flow at $L_H D_L V_L$ condition. The execution of grooves and scratches on pin surface would be the evidence of abrasive wear mechanism. The plastic flow occurred on the surface in the sliding direction with row of furrows as an indication of adhesive wear mechanism.

Figure 6.10 (a) shows the severe damage on the worn surface of AA6061 aluminium alloy and delamination is the dominant wear mechanism at $L_H D_H V_H$ conditions. The presence of oxide film on the wear surface of the AA6061 aluminium alloy and the relative motion between the disc materials introduce the frictional heat [144]. This frictional heat obviously affects the wear loss of the nanocomposites. However, the development of grooves and plastic deformation of the AA6061 aluminium alloy pin in the direction of sliding depends on the normal loads and sliding velocities.

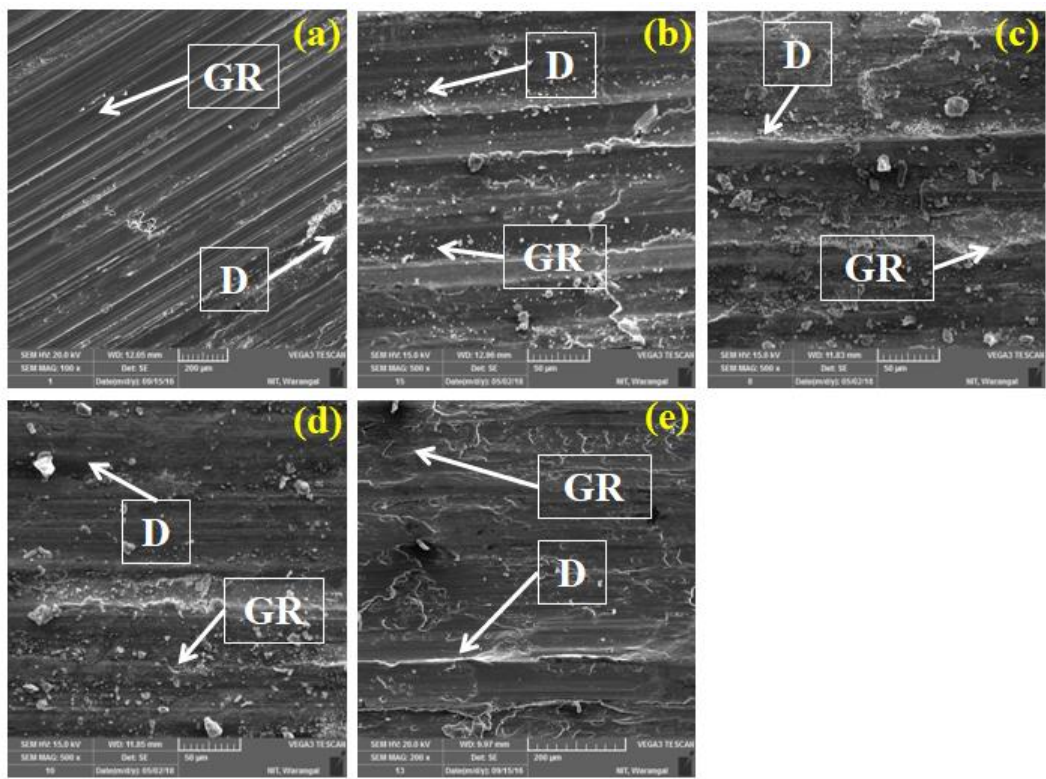


Figure 6.8: SEM images of worn surfaces of different materials at 5 N applied normal load, 2 m/s sliding velocity, and 1000 m sliding distance (a) AA6061 aluminium alloy (b) 0.5NC, (c) 1NC, (d) 1.5NC and (e) 2NC

The increase of applied normal loads on the pin at the constant sliding velocity leads to the transformation of the fine grooves into larger v-shape scratches. Due to the increase of sliding velocity at constant normal loads on pin, the fine grooves have transformed into v-shape grooves on the wear surface of the AA6061 aluminium alloy. The increase of either load or sliding velocity increases the plastic deformation with the higher depth of penetration [145]. Figures 6.7 (b) and 6.8 (b) indicate the worn surfaces of 0.5NC nanocomposite at 5 N applied normal load, lower and higher sliding distance, and sliding velocity conditions respectively. In the SEM images 'GR' represents the grooves, 'D' denotes the delaminating layer on the worn surface. It can be observed that fine grooves, delaminating layer and oxide debris are seen of 0.5NC nanocomposite worn surface in the sliding direction at $L_L D_L V_L$ condition. It can be seen that the shallower scratches and plastic flow of material on 0.5NC nanocomposite worn surface are observed in the sliding direction at $L_L D_H V_H$ condition. Figure 6.9 (b) shows the worn surface of 0.5NC nanocomposite at $L_H D_L V_L$ condition.

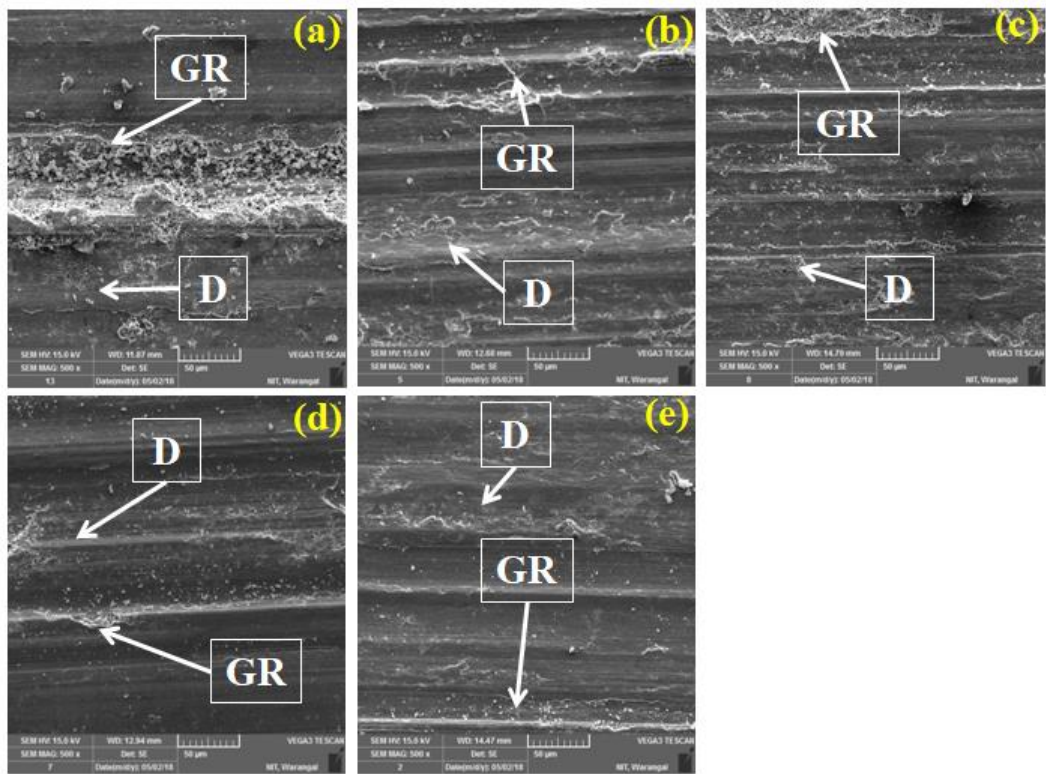


Figure 6.9: SEM images of worn surfaces of different materials at 20 N applied normal load, 0.5 m/s sliding velocity, and 1000 m sliding distance (a) AA6061 aluminium alloy (b) 0.5NC, (c) 1NC, (d) 1.5NC and (e) 2NC

It can be seen that circular grooves, shallower scratches and higher plastic flow are observed L_HD_LV_L condition. Figure 6.10 (b) shows that oxidation is the dominant wear mechanism at higher applied normal loads 20 N on the pin. The presence of oxide film on the wear surface of the nanocomposites and the relative motion between the disc materials introduce the frictional heat [145]. This frictional heat obviously affects the wear loss of the nanocomposites. However, the development of grooves, oxide debris and plastic deformation of the nanocomposite pin in the direction of sliding depends on the normal loads and sliding velocities. The increase of normal loads on the pin at the constant sliding velocity has turned the fine grooves into shallower scratches. Due to the increase of sliding velocity at constant normal loads on pin, the fine grooves have transformed to circular scratches on the wear surface of the nanocomposites.

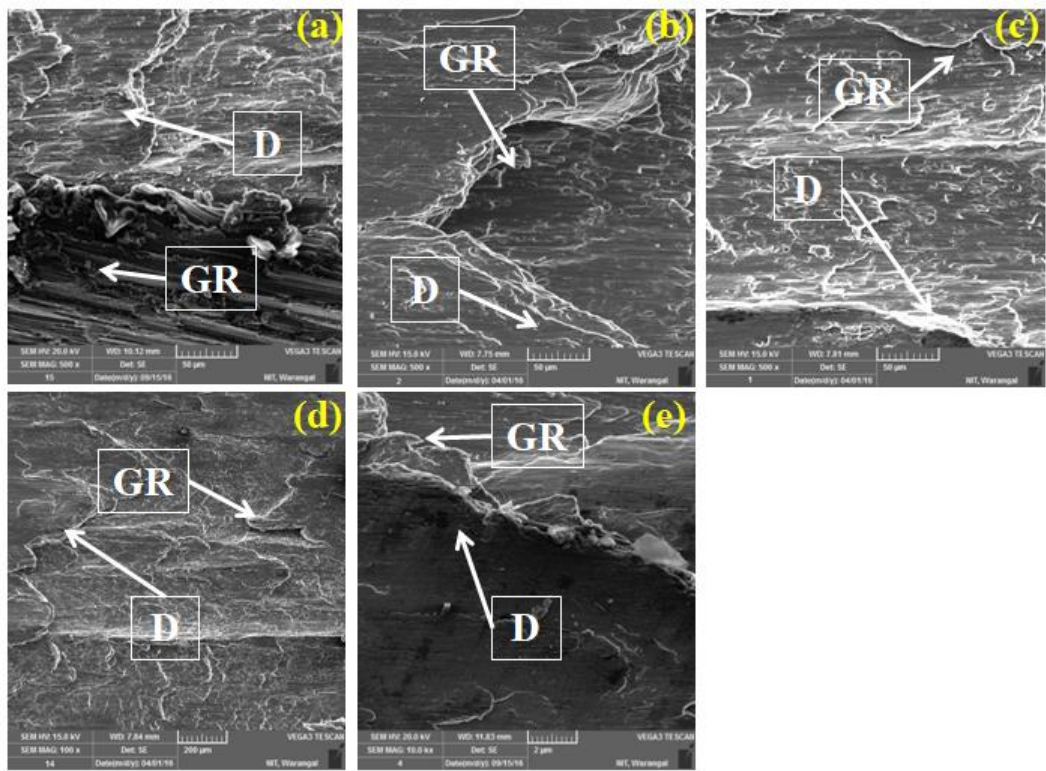


Figure 6.10: SEM images of worn surfaces at 20 N applied normal load, 2 m/s sliding velocity and 3000 m sliding distance (a) AA6061 aluminium alloy, (b) 0.5NC, (c) 1NC, (d) 1.5NC and (e) 2NC

Figures 6.7 (c) and 6.8 (c) indicate the worn surfaces of 1NC nanocomposite at 5 N applied normal load, lower and higher sliding distance, and sliding velocity conditions respectively. In the SEM images 'GR' represents the grooves, 'D' denotes the delaminating

layer on the worn surface. It can be observed that delaminating layer and oxide debris are present on 1NC nanocomposite worn surface in the sliding direction at $L_L D_L V_L$ condition. It can be seen that the shallower scratches and plastic flow of material are observed on 1NC nanocomposite worn surface in the sliding direction at $L_L D_H V_H$ condition. Figure 6.9 (b) shows the worn surface of 1NC nanocomposite at $L_H D_L V_L$ condition. It can be seen that circular scratches were found at $L_H D_L V_L$ condition. Fig. 6.10 (c) shows the worn surface it reveals higher amount of penetration with severe plastic deformation at 20 N normal loads.

Figures 6.7 (d) and 6.8 (d) indicate the worn surfaces of 1.5NC nanocomposite at 5 N applied normal load, lower and higher sliding distance, and sliding velocity conditions respectively. In the SEM images 'GR' represents the grooves, 'D' denotes the delaminating layer on the worn surface. It can be observed that delaminating layer and oxide debris are seen on 1.5NC nanocomposite worn surface in the sliding direction at $L_L D_L V_L$ condition. It can be seen that the deep shallower scratches and plastic flow of material on 1.5NC nanocomposite worn surface are observed in the sliding direction at $L_L D_H V_H$ condition. Figure 6.9 (d) shows the worn surface of 1.5NC nanocomposite at $L_H D_L V_L$ condition. It can be seen that circular scratches were found at $L_H D_L V_L$ condition. Figure 6.10 (d) shows the worn surface, it reveals higher amount of penetration with severe plastic deformation at 20 N normal loads. However, the deformation and development of oxide debris on the nanocomposite wear surfaces have decreased with the increase of SiCp reinforcement particles. The depth of penetration of hard disc material on the wear surfaces is rising with increasing applied normal loads on pins and decreased with increasing SiCp nano-reinforcement particles.

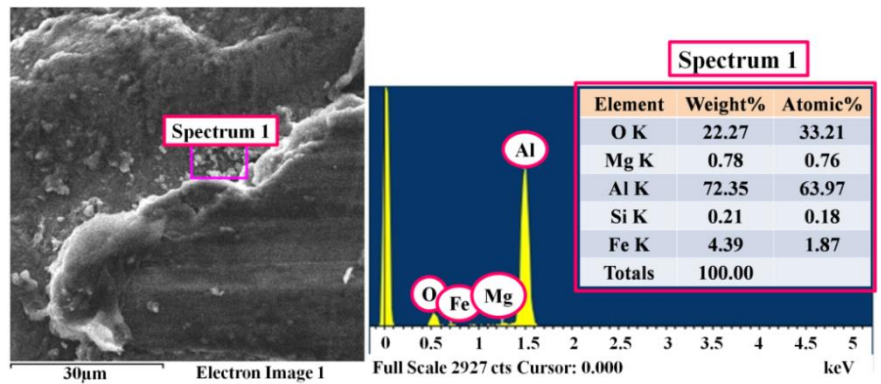
In figures 6.7 (e) and 6.8 (e) represent the worn surfaces of 2NC nanocomposite at $L_L D_L V_L$ condition. Formation of smaller scratches in the sliding direction is evident of abrasive wear mechanism. The SEM micrograph of the worn surface of 2NC nanocomposite reveals the delamination mechanism in the sliding direction. It reveals lower plastic deformation in the sliding direction which is lower than the unreinforced alloy and its lower content SiCp nanocomposites at $L_L D_H V_H$ condition. In figures 6.9 (e) and 6.10 (e) represent the worn surfaces of 2NC nanocomposite reveals that the shallower scratches with higher plastic deformation at $L_H D_L V_L$ condition. The worn surface of 2NC nanocomposite reveals the turbulent plastic flow of material in the sliding direction at $L_H D_H V_H$ condition. The depth of penetration is less compared to the unreinforced alloy at all conditions. This would be

attributed to the presence of nano-sized SiCp reinforcement particles in the matrix and which hinder the plastic flow of material during dry sliding.

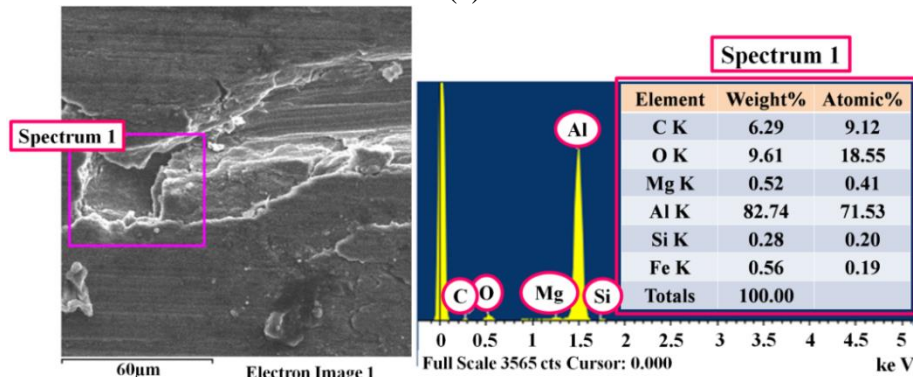
6.2.5 EDX Analysis

The worn surfaces of the nanocomposite at 20 N normal load, 2 m/s sliding velocity, and 3000 m sliding distance are analyzed by using EDX spectrum. EDX results of the nanocomposites revealed that the intensity peak is oxygen. It indicates that the oxide debris development is there on the worn surface at dry sliding conditions. During dry sliding of the nanocomposites on the hard steel disc (EN31) counter surface, heat generates due to the friction and leads to rise of temperature. The combination of temperature rise and environmental reaction causes the formation of the oxide debris at pin and disc contact surfaces [22]. The EDX spectrum analysis of the worn surface of 1NC nanocomposite at 20 N normal load and sliding velocity of 2 m/s is presented in figure 6.11 (a). The results revealed that the small intensity of silicon peak and a strong intensity of aluminium peak are present. The strong intensity peak of aluminium indicates more plastic flow of 0.5NC nanocomposite at dry sliding conditions.

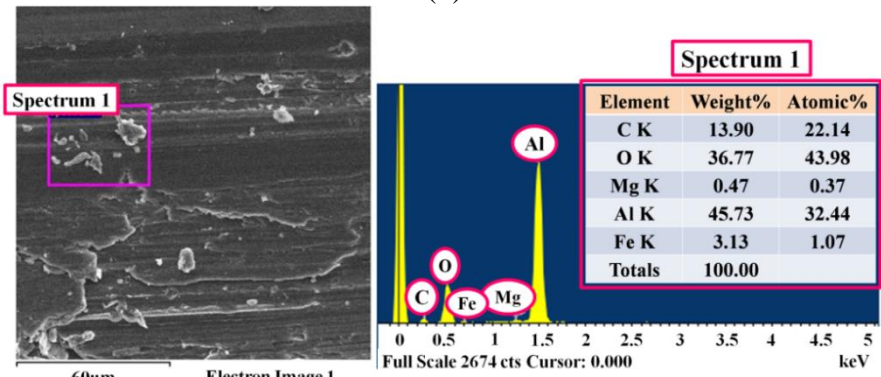
The EDX spectrum analysis of the worn surface of 1NC nanocomposite at normal load of 20 N and 2 m/s sliding velocity is presented in figure 6.11 (b). The low intensity of the carbon peak and average intensity of silicon peak specifies that SiCp reinforcement particles are dragged from the AA6061 alloy matrix. The EDX spectrum analysis of the worn surface of the 1.5NC nanocomposite at applied normal loads of 20 N and 2 m/s sliding velocity is represented in figure 6.11 (c). The EDX spectrum analysis of the worn surface of the 2NC nanocomposite at 20 N normal load and sliding velocity of 2 m/s is represented in figure 6.11 (d). The results revealed that the small intensity of silicon, carbon peaks and a strong intensity of aluminium peak are present. The higher intensity of aluminium peak indicates more plastic flow of 2NC nanocomposite at dry sliding conditions. It also observe the intensity of carbon, aluminium and silicon peaks. However, the noticeable iron and oxygen peak are also observed. The hard disc counter surface is eroded by the SiCp reinforcements. The oxygen and iron appeared in the EDX indicates the development of iron oxide on the worn surface of the contact parts. Because of the heat generation between the mating parts, the temperature is raised and causes the formation of oxide film on the mating surfaces [145].



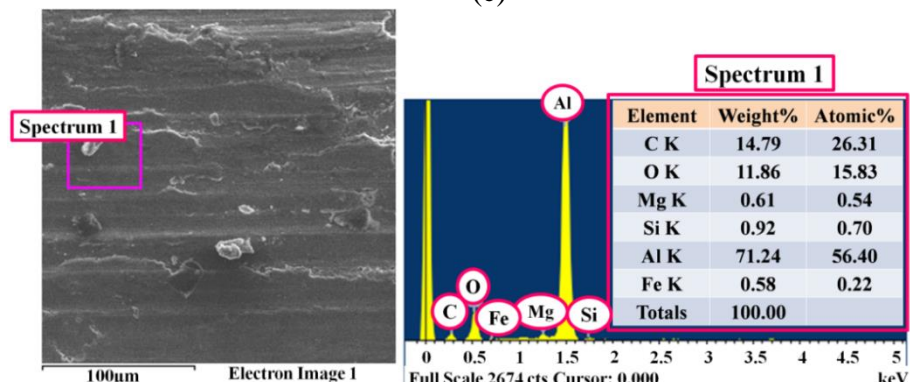
(a)



(b)



(c)



(d)

Figure 6.11: EDX of wear surfaces of AA6061/SiCp nanocomposites at applied normal loads 20 N at 2 m/s sliding speed (a) 0.5NC, (b) 1NC, (c) 1.5NC, and (d) 2NC

6.2.6 Wear Debris

Figure 6.12 represents the wear debris of AA6061 aluminium alloy and 2NC nanocomposite. In figure 6.12 (a), the larger size wear debris produced from AA6061 aluminium alloy during dry sliding condition is indicated. Formation of larger size wear debris would be attributed to the severe plastic deformation with higher depth of penetration of hard asperities during dry sliding condition. From figure 6.12 (b) represents the AA6061 aluminium alloy matrix filled with SiCp nano-reinforcements with lower inter particle spacing which increases the dislocation density. The medium size wear debris produced from 2NC nanocomposite. The production of medium size wear debris may be due to the application of external loads that starts yielding of dislocation pile up in the subsurface of the pin material [146]. The contact profile of 2NC nanocomposite shows the yielding of dislocation piles up which lead to crack initiation and propagates towards the subsurface layer. The SiCp nano-reinforcement particles may come out from the subsurface and combine with the MML and increases the wear resistance. The SiCp nano-reinforcement particles resist the hard asperities from the EN31 steel disc counter face and hence there is plastic deformation and higher depth of penetration.

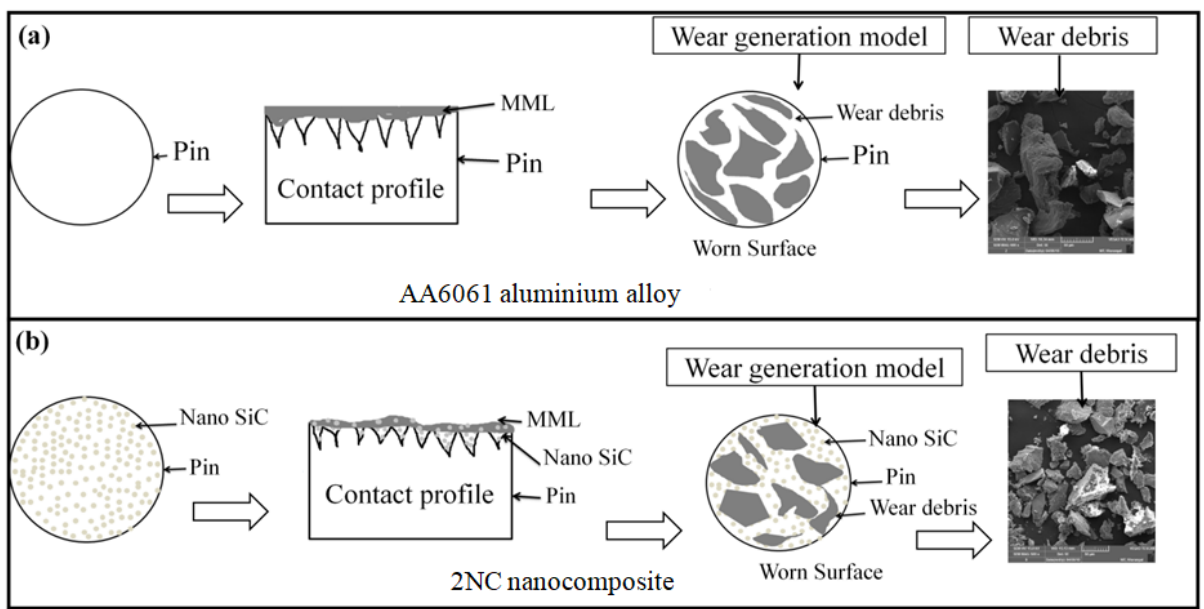


Figure 6.12: Schematic view of wear generation model including wear debris of AA6061 aluminium alloy and 2NC nanocomposite

6.2.7 Wear Mechanism

The wear mechanisms of the nanocomposites are defined by sliding velocity and normal loads. In the present test conditions, various groups of mechanisms are found to be gradual and the boundaries on the diagram are approximate (figure 6.13). At the lower sliding velocity, and lower normal loads, fine grooves are identified with oxidation, abrasion, and delamination wear mechanisms. At 15 N normal loads, with higher sliding velocities, the circular scratches are identified with oxidation, delamination, and abrasion wear mechanisms. At 20 N normal loads, with lower sliding velocities, smaller deep grooves are found with delamination and abrasion. At 20 N normal loads with higher sliding velocities, the larger size oxide debris with softened surfaces are identified, with delamination and abrasion wear mechanism.

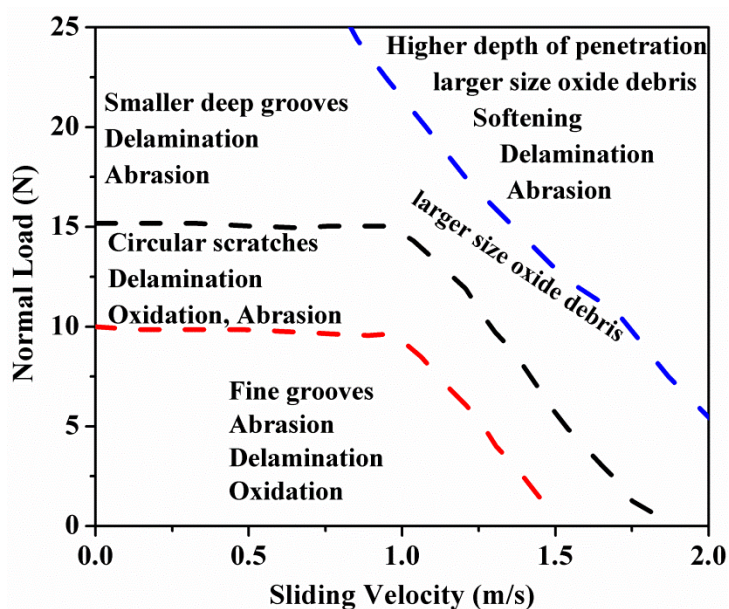


Figure 6.13: Wear mechanisms of the nanocomposites are drawn at various conditions and with approximate boundaries in the present study

6.3 Tribological Properties of Hybrid Nanocomposites

6.3.1 Volumetric Wear Rate

The volumetric wear rate of the AA6061 aluminium alloy, 2NC nanocomposite, and 0.5HNC, 1HNC, 1.5HNC, 2HNC and 3HNC hybrid nanocomposite was calculated from

wear loss (g) data after the dry sliding wear tests on EN31 steel and the same reported in the following Table 6.5 to 6.8. The effect of graphite particles, applied normal load, sliding velocity and sliding distance on volumetric wear rate was discussed in the following sub sections. The volumetric wear rate of the materials is a function of its metallurgical characteristics, operating and environmental conditions, and nature of counter surface. Among these, hardness of the pin material and EN31 steel disc will play a significant role on type of wear mechanism [147].

The volumetric wear rate of the AA6061 aluminium alloy, 2NC nanocomposite, and 0.5HNC, 1HNC, 1.5HNC, 2HNC and 3HNC hybrid nanocomposite was calculated from wear loss (g) data after the dry sliding wear tests on EN31 steel and the same reported in the following Table 6.5 to 6.8. The effect of graphite particles, applied normal load, sliding velocity and sliding distance on volumetric wear rate was discussed in the following sub sections. The wear rate of the materials is a function of its metallurgical characteristics, operating and environmental conditions, and nature of counter surface. Among these, hardness of the pin material and EN31 steel disc will play a significant role on type of wear mechanism [147].

Table 6.5: Volumetric wear rate of different materials obtained at 0.5 m/s sliding velocity

Load (N)	Sliding distance (m)	Volumetric Wear Rate (mm ³ /m)						
		0.5 m/s (sliding velocity)						
		AA6061 alloy	2NC	0.5HNC	1HNC	1.5HNC	2HNC	3HNC
5	1000	0.0056	0.0042	0.0024	0.0019	0.0012	0.0003	0.0007
5	2000	0.0068	0.0046	0.0027	0.0021	0.0013	0.0004	0.0009
5	3000	0.0074	0.0056	0.0034	0.0027	0.0017	0.0005	0.0011
10	1000	0.0061	0.0045	0.0027	0.0022	0.0014	0.0006	0.0011
10	2000	0.0072	0.0054	0.0032	0.0028	0.0019	0.0007	0.0012
10	3000	0.0082	0.0063	0.0042	0.0034	0.0024	0.0009	0.0015
15	1000	0.0068	0.0055	0.0029	0.0025	0.0016	0.0008	0.0013
15	2000	0.0076	0.0068	0.0034	0.0029	0.0021	0.001	0.0015
15	3000	0.0085	0.0071	0.0049	0.0041	0.0029	0.0014	0.0021
20	1000	0.0071	0.0066	0.0031	0.0026	0.0018	0.0013	0.0015
20	2000	0.0078	0.007	0.0035	0.0027	0.0022	0.0016	0.0018
20	3000	0.0098	0.009	0.0055	0.0033	0.0026	0.0019	0.0022

Table 6.6: Volumetric wear rate of different materials obtained at 1 m/s sliding velocity

Load (N)	Sliding distance (m)	Volumetric Wear Rate (mm ³ /m)						
		1 m/s (sliding velocity)						
		AA6061 alloy	2NC	0.5HNC	1HNC	1.5HNC	2HNC	3HNC
5	1000	0.0057	0.0043	0.0030	0.0022	0.0014	0.0011	0.0015
5	2000	0.0071	0.0053	0.0038	0.0029	0.0017	0.0013	0.0018
5	3000	0.0095	0.0059	0.0047	0.0036	0.0022	0.0017	0.0023
10	1000	0.0062	0.0049	0.0032	0.0024	0.0016	0.0012	0.0016
10	2000	0.0077	0.0056	0.0039	0.0032	0.0021	0.0016	0.0021
10	3000	0.0103	0.0067	0.0051	0.0039	0.0026	0.0019	0.0026
15	1000	0.0069	0.0062	0.0033	0.0028	0.0019	0.0014	0.0018
15	2000	0.0083	0.007	0.0041	0.0034	0.0023	0.0017	0.0022
15	3000	0.0111	0.0074	0.006	0.0041	0.003	0.0021	0.0028
20	1000	0.0075	0.0068	0.0034	0.0029	0.0021	0.0015	0.0019
20	2000	0.0086	0.0073	0.0043	0.0035	0.0026	0.0018	0.0023
20	3000	0.0115	0.0095	0.0063	0.0044	0.0034	0.0023	0.003

Table 6.7: Volumetric wear rate of different materials obtained at 1.5 m/s sliding velocity

Load (N)	Sliding distance (m)	Volumetric Wear Rate (mm ³ /m)						
		1.5 m/s (sliding velocity)						
		AA6061 alloy	2NC	0.5HNC	1HNC	1.5HNC	2HNC	3HNC
5	1000	0.0065	0.0044	0.0035	0.0028	0.0021	0.0014	0.0017
5	2000	0.0077	0.0054	0.0043	0.0035	0.0026	0.0017	0.0025
5	3000	0.0099	0.0069	0.0057	0.0047	0.0034	0.0022	0.0028
10	1000	0.0079	0.0048	0.0036	0.0027	0.0022	0.0015	0.0019
10	2000	0.0083	0.0059	0.0045	0.0033	0.0027	0.0018	0.0021
10	3000	0.0108	0.0082	0.006	0.0048	0.0036	0.0024	0.0030
15	1000	0.0085	0.0063	0.0038	0.0028	0.0024	0.0016	0.002
15	2000	0.0092	0.0073	0.0047	0.0035	0.0029	0.0019	0.0023
15	3000	0.0116	0.0088	0.0063	0.0049	0.0039	0.0025	0.0033
20	1000	0.0096	0.0069	0.004	0.0031	0.0027	0.0019	0.0021
20	2000	0.0102	0.0076	0.0049	0.0038	0.0033	0.0023	0.0026
20	3000	0.0126	0.0108	0.0066	0.0051	0.0044	0.0030	0.0035

Table 6.8: Volumetric wear rate of different materials obtained at 2 m/s sliding velocity

Load (N)	Sliding distance (m)	Volumetric Wear Rate (mm ³ /m)						
		2 m/s (sliding velocity)						
		AA6061 alloy	2NC	0.5HNC	1HNC	1.5HNC	2HNC	3HNC
5	1000	0.00696	0.0055	0.0042	0.0037	0.0021	0.0015	0.0019
5	2000	0.0079	0.0058	0.0046	0.0038	0.0029	0.0017	0.0023
5	3000	0.011	0.0073	0.0058	0.0048	0.0038	0.0026	0.0029
10	1000	0.0082	0.0061	0.0049	0.0041	0.0023	0.0016	0.0021
10	2000	0.00872	0.007	0.0057	0.0049	0.004	0.0024	0.0031
10	3000	0.0112	0.0079	0.0065	0.0055	0.0042	0.0029	0.0033
15	1000	0.0085	0.0064	0.0051	0.0045	0.0025	0.0018	0.0023
15	2000	0.0112	0.0081	0.0067	0.0058	0.0042	0.0029	0.0033
15	3000	0.0123	0.0094	0.0071	0.006	0.0051	0.0032	0.0043
20	1000	0.009	0.0071	0.0055	0.0048	0.0028	0.002	0.0025
20	2000	0.012	0.0085	0.007	0.0061	0.0045	0.0031	0.0035
20	3000	0.0136	0.0119	0.0081	0.0072	0.0059	0.0037	0.0049

6.3.1.1 Effect of applied normal load

Volumetric wear rate of AA6061 aluminium alloy, 2NC nanocomposite, 0.5HNC, 1HNC, 1.5HNC, 2HNC, and 3HNC hybrid nanocomposites is presented in figure 6.14. Figures 6.14 (a) and 6.14 (b) represent the volumetric wear rate of materials with respect to applied normal load at 0.5 m/s, 1000 m (named as V_{LD_L}) and 2 m/s, 3000 m (named as V_{HD_H}) conditions respectively. The test conditions 5 N, 1000 m and 0.5 m/s; 5 N, 3000 m and 2 m/s; 20 N, 1000 m and 0.5 m/s; 20 N, 3000 m and 2 m/s are named as $L_{LD_L}V_L$, $L_{LD_H}V_H$, $L_{HD_L}V_L$ and $L_{HD_H}V_H$ respectively. It is observed that decrement in volumetric wear rate of 2NC nanocomposite, 0.5HNC, 1HNC, 1.5HNC, 2HNC, and 3HNC hybrid nanocomposites at 5 N normal load, V_{LD_L} condition was 25%, 57.2%, 66.1%, 78.6%, 94.6%, and 87.5% respectively. It revealed that decrement in volumetric wear rate of 2NC nanocomposite, 0.5HNC, 1HNC, 1.5HNC, 2HNC, and 3HNC hybrid nanocomposites at 10 N applied normal load and V_{LD_L} condition was 26.2%, 55.74%, 63.94%, 77.1%, 90.2%, and 81.96% respectively. It can be seen that decrement in volumetric wear rate of 2NC nanocomposite, 0.5HNC, 1HNC, 1.5HNC, 2HNC, and 3HNC hybrid nanocomposites at 15 N applied normal load and V_{LD_L} condition was 19.2%, 57.4%, 63.24%, 76.5%, 88.24%, and 80.9% respectively. The decrement in volumetric wear rate of 2NC nanocomposite,

0.5HNC, 1HNC, 1.5HNC, 2HNC, and 3HNC hybrid nanocomposites at 20 N applied normal load and 1000 m sliding distance was 7.1%, 56.4%, 63.4%, 74.7%, 81.7%, and 78.9% respectively.

Figure 6.14 (b) represents the wear rate of materials at 3000 m sliding distances and V_{HDH} condition. It is observed that decrement in volumetric wear rate of 2NC nanocomposite, 0.5HNC, 1HNC, 1.5HNC, 2HNC, and 3HNC hybrid nanocomposites at 5 N applied normal load and 3000 m sliding distance was 33.64%, 47.3%, 56.4%, 65.5%, 76.4%, and 73.64% respectively. It revealed that decrement in volumetric wear rate of 2NC nanocomposite, 0.5HNC, 1HNC, 1.5HNC, 2HNC, and 3HNC hybrid nanocomposites at 10 N applied normal load and V_{HDH} condition was 28.83%, 41.44%, 50.45%, 62.7%, 73.87%, and 70.27% respectively.

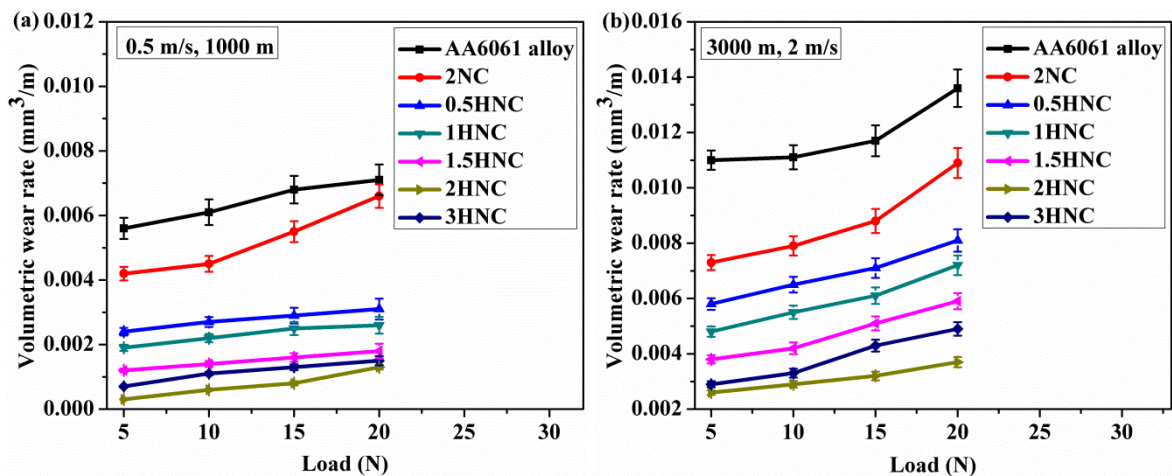


Figure 6.14: Volumetric wear rate of AA6061 aluminium alloy, nanocomposite, and hybrid nanocomposites as a function of applied normal load (a) V_{LDL} condition and (b) V_{HDL} condition

It can be seen that the enhancement of wear rate of 2NC nanocomposite, 0.5HNC, 1HNC, 1.5HNC, 2HNC, and 3HNC hybrid nanocomposites at 15 N applied normal load and V_{HDL} condition was 24.8%, 39.32%, 47.9%, 56.41%, 72.7%, and 63.3% respectively. The enhancement of wear rate of 2NC nanocomposite, 0.5HNC, 1HNC, 1.5HNC, 2HNC, and 3HNC hybrid nanocomposites at 20 N applied normal load and V_{HDL} condition was 19.9%, 40.44%, 47.1%, 56.62%, 72.8%, and 63.97% respectively.

It is identified that the wear rate of all materials increased gradually with the rise of applied normal loads [98]. The higher wear rate is found in unreinforced AA6061 aluminium alloy compared to nanocomposite materials. This would be attributed due to less wear resistance of unreinforced AA6061 aluminium alloy at all applied normal load conditions. During dry sliding, counteracting of hard asperities would lead to the formation of large grooves with a higher depth of penetration and larger deformation of surface leads to more wear rate [138]. It is identified that the wear rate of materials rises with the increase of sliding velocity and sliding distance. Temperature at the interface of the composite pin and EN31 steel disc increases with rise of sliding velocity and which induces the oxidation phenomenon. Heavy heat dissipation at the interfaces of the pin and EN31 steel counterface reflects on chemical structure of the pin material [139]. The rise of temperature at the interface would be resulting in higher wear rate of material due to the worn-off of lubricating film [148]. In many studies, researchers have reported that the tribo-layer worn off with the increase of contact surface temperature and thus results in higher wear rate [140]. It is identified that there was highest wear rate for unreinforced AA6061 aluminium alloy as compared to 2NC nanocomposites and hybrid nanocomposites at all conditions.

It is observed that 2NC nanocomposite revealed good wear resistance than base material. This would be due to the formation of mechanically mixed layer (MML) of soft AA6061 aluminium alloy matrix and hard ceramic nano-sized SiCp particles. SiCp nanoparticles mix with MML and reduce the transfer of material from the pin surface and hence improves the wear resistance. The SiCp nanoparticles act as a barrier to the external applied load and increase the hardness of nanocomposite. Due to the higher hardness and smaller size, the detached SiCp nanoparticles rolled between the surfaces and played a part in a three-body abrasion mechanism by contributing towards abrading the two mating surfaces. These hard asperities of EN31 steel chips and SiCp nanoparticles penetrate furthermore into the matrix with the rise of loads. The rise in temperature introduces the oxide layer formation with the mixer of SiCp nanoparticles at $L_H D_H V_H$ conditions. At the interface, harder asperities penetrate into the pin surface and damage the oxide layer at higher load and hence increase the wear rate [141, 149].

It is noticed from figure 6.14 (a) and 6.14 (b), the wear rate of 0.5HNC, 1HNC, 1.5HNC, 2HNC, and 3HNC hybrid nanocomposites reduced with increasing graphite content in the base material and raised with increasing applied normal loads. This would be attributed

due to the continuous supply of graphite, the formation of graphite thick film and spreading over the contact surface of the pin without peeling off. Incorporation of graphite as a secondary phase in the soft matrix result in the formation of a more stable lubricating layer on the tribo-surface of hybrid nanocomposites compared to the base alloy and nanocomposite [150]. Reduction in volumetric wear rate of the hybrid nanocomposites with rise of graphite content would be related to the dual phase effect of SiCp and graphite nanoparticles in the formation of stronger MML on the contact surface. The aluminium based hybrid composites consisting of dual phases of SiCp and graphite particles in the matrix possess better tribological properties than the Al-SiCp based composites and alloy. Another report specified that rise in sliding velocity as a function of load is expected to result in rise of surface temperature and leads to more severe wear [151].

6.3.1.2 Effect of sliding distance

Figure 6.15 represents the volumetric wear rate of AA6061 aluminium alloy, 2NC nanocomposite, and 0.5HNC, 1HNC, 1.5HNC, 2HNC, and 3HNC hybrid nanocomposites as a function of sliding distance. Figure 6.15 (a) denotes the volumetric wear rate of materials at 1000 m sliding distance, 5 N normal load and 2 m/s sliding velocity (named as $L_L V_L$) respectively.

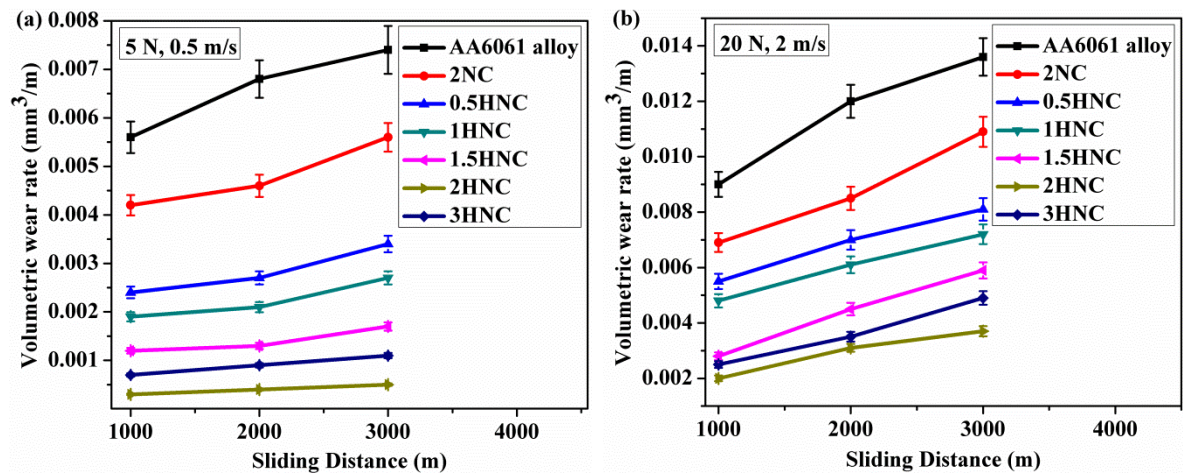


Figure 6.15: Volumetric wear rate of AA6061 aluminium alloy, 2NC nanocomposite, 0.5HNC, 1HNC, 1.5HNC, 2HNC, and 3HNC hybrid nanocomposites (a) $L_L V_L$ condition and (b) $L_H V_H$ condition

It is observed that decrement in volumetric wear rate of 2NC nanocomposite, 0.5HNC, 1HNC, 1.5HNC, 2HNC, and 3HNC hybrid nanocomposites at 1000 m sliding distance and L_{LV_L} condition was 25%, 57.2%, 66.1%, 78.6%, 94.64%, and 87.5% respectively. It is observed that decrement in wear rate of 2NC nanocomposite, 0.5HNC, 1HNC, 1.5HNC, 2HNC, and 3HNC hybrid nanocomposites at 2000 m sliding distance and at L_{LV_L} condition was 32.4%, 60.3%, 69.2%, 80.88%, 94.1%, and 86.8% respectively.

It is observed that the enhancement of wear rate of 2NC nanocomposite, 0.5HNC, 1HNC, 1.5HNC, 2HNC, and 3HNC hybrid nanocomposites at 3000 m sliding distance and at L_{LV_L} condition was 24.32%, 54.1%, 63.52%, 77.1%, 93.3%, and 85.2% respectively. Figure 6.15 (b) denotes the volumetric wear rate of materials at 20 N normal load and 2 m/s sliding velocity (named as L_{HV_H}) conditions respectively. The decrement in wear rate of 2NC nanocomposite, 0.5HNC, 1HNC, 1.5HNC, 2HNC, and 3HNC hybrid nanocomposites at 1000 m sliding distance and at L_{HV_H} condition was 23.3%, 38.9%, 46.7%, 68.8%, 77.7%, and 72.2% respectively.

The decrement in volumetric wear rate of 2NC nanocomposite, 0.5HNC, 1HNC, 1.5HNC, 2HNC, and 3HNC hybrid nanocomposites at 2000 m sliding distance and at L_{HV_H} condition was 29.2%, 41.7%, 49.2%, 62.5%, 74.2%, and 70.8% respectively. The decrement in volumetric wear rate of 2NC nanocomposite, 0.5HNC, 1HNC, 1.5HNC, 2HNC, and 3HNC hybrid nanocomposites at 3000 m sliding distance and at L_{HV_H} condition was 19.85%, 40.44%, 47.1%, 56.62%, 72.8%, and 63.97% respectively.

It is identified that the wear rate rises with the increase of sliding distance for all materials. Temperature increases at contact surface of pin and disc with rise of sliding distance that promotes the oxidation process and formation of tribo-layer, which reflects on microstructural changes such as dissolution of precipitates [139]. The tribo-layer worn off with increase of contact surface temperature and thus results in higher wear rate [140]. It is identified that highest wear rate is observed for unreinforced AA6061 aluminium alloy for sliding distances. It is identified that the wear rate of materials rise with the increase of sliding velocity and sliding distance. The sliding distance doesn't affect much on the volumetric wear rate compared to the effect of load and sliding velocity. Favourable effect of SiCp nanoparticles in improving the wear resistance has also been reported by other researchers [97].

6.3.1.3 Effect of sliding velocity

Figure 6.16 represents the volumetric wear rate of AA6061 aluminium alloy, 2NC nanocomposite, and 0.5HNC, 1HNC, 1.5HNC, 2HNC, and 3HNC hybrid nanocomposites as a function of sliding velocity. Figure 6.16 (a) denotes the volumetric wear rate of materials at 1000 m sliding distance and 5 N normal load (named as L_{LDL}) respectively. It is found that decrement in volumetric wear rate of 2NC nanocomposite, and 0.5HNC, 1HNC, 1.5HNC, 2HNC, and 3HNC hybrid nanocomposites at 0.5 m/s sliding velocity and at L_{LDL} condition was 25%, 57.14%, 66.1%, 78.6%, 94.64%, and 87.5% respectively. It is found that decrement in volumetric wear rate of 2NC nanocomposite, and 0.5HNC, 1HNC, 1.5HNC, 2HNC, and 3HNC hybrid nanocomposites at 1 m/s sliding velocity and at L_{LDL} condition was 26.2%, 55.74%, 63.93%, 77.1%, 90.2%, and 81.96% respectively.

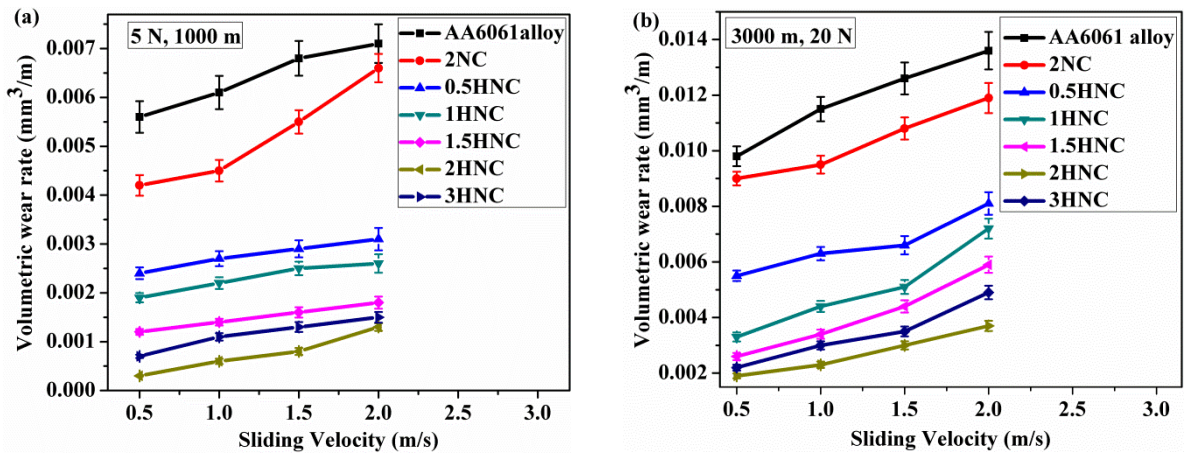


Figure 6.16: Volumetric wear rate of AA6061 aluminium alloy, 2NC nanocomposite, 0.5HNC, 1HNC, 1.5HNC, 2HNC, and 3HNC hybrid nanocomposites (a) L_{LDL} condition and (b) L_{HDL} condition

It is found that decrement in volumetric wear rate of 2NC nanocomposite, and 0.5HNC, 1HNC, 1.5HNC, 2HNC, and 3HNC hybrid nanocomposites at 1.5 m/s sliding velocity and at L_{LDL} condition was 19.2%, 57.4%, 63.24%, 76.5%, 88.23%, and 80.9% respectively. It is found that decrement in wear rate of 2NC nanocomposite, and 0.5HNC, 1HNC, 1.5HNC, 2HNC, and 3HNC hybrid nanocomposites at 2 m/s sliding velocity and at L_{LDL} condition was 7.1%, 56.34%, 63.4%, 74.7%, 81.7%, and 78.9% respectively.

Figure 6.16 (b) depicts the wear rate of AA6061 aluminium alloy, 2NC nanocomposite, and 0.5HNC, 1HNC, 1.5HNC, 2HNC, and 3HNC hybrid nanocomposites at

L_{HDH} condition. It is found that volumetric wear rate of 2NC nanocomposite, and 0.5HNC, 1HNC, 1.5HNC, 2HNC, and 3HNC hybrid nanocomposites at 0.5 m/s sliding velocity and at L_{HDH} condition was 8.2%, 43.9%, 66.33%, 73.47%, 80.61%, and 77.6% respectively. It is found that decrement in volumetric wear rate enhancement of 2NC nanocomposite, and 0.5HNC, 1HNC, 1.5HNC, 2HNC, and 3HNC hybrid nanocomposites at 1 m/s sliding velocity and at L_{HDH} condition was 17.4%, 45.21%, 61.74%, 70.44%, 80%, and 73.9% respectively. It is found that decrement in volumetric wear rate of 2NC nanocomposite, and 0.5HNC, 1HNC, 1.5HNC, 2HNC, and 3HNC hybrid nanocomposites at 1.5 m/s sliding velocity and at L_{HDH} condition was 14.3%, 47.62%, 59.5%, 65.1%, 76.2%, and 72.2% respectively. It is found that decrement in volumetric wear rate of 2NC nanocomposite, and 0.5HNC, 1HNC, 1.5HNC, 2HNC, and 3HNC hybrid nanocomposites at 2 m/s sliding velocity and at L_{HDH} condition was 12.5%, 40.44%, 47.1%, 56.62%, 72.7%, and 63.97% respectively.

It is identified that the volumetric wear rate of materials rise with the increase of sliding velocity. Temperature at the interface of the composite pin and EN31 steel disc increases with rise of sliding velocity which induces the oxidation phenomenon. Heavy heat dissipation at the interfaces of the pin and EN31 steel counterface reflects on chemical structure of the pin material [139]. The rise of temperature at the interface would be resulting in higher wear rate of material due to the worn-off of lubricating film. In many studies, researchers have reported that the tribo-layer has worn off with the increase of contact surface temperature and thus results in higher wear rate [140]. It is identified that there was highest wear rate for unreinforced AA6061 aluminium alloy as compared to 2NC nanocomposites and hybrid nanocomposites at all conditions.

The SiCp nanoparticles act as a barrier to the external applied load and increase the hardness of 2NC nanocomposite. Due to higher hardness and smaller size, as the detached SiCp nanoparticles rolled between the surfaces, they played a part in a three-body abrasion mechanism by contributing towards abrading the two mating surfaces. These hard asperities of EN31 steel chips and SiCp nanoparticles penetrate furthermore into the matrix with the rise of sliding velocity. The rise in temperature introduces the oxide layer formation with the mixer of SiCp nanoparticles at $L_{HDH}V_H$ conditions. At the interface, harder asperities penetrate into the pin surface and damage the oxide layer at higher sliding velocity, and hence increase the volumetric wear rate [152].

6.3.2 Wear Coefficients

The wear coefficients of AA6061 aluminium alloy, 2NC nanocomposite, and 0.5HNC, 1HNC, 1.5HNC, 2HNC and 3HNC hybrid nanocomposite are represented in figure 6.17 as a function of applied normal load, sliding distance, sliding velocity and different materials. The wear coefficients were shown in figure 6.17(a) as a function of applied normal load. It was noticed that the wear coefficients of materials decreased with increase of applied normal loads.

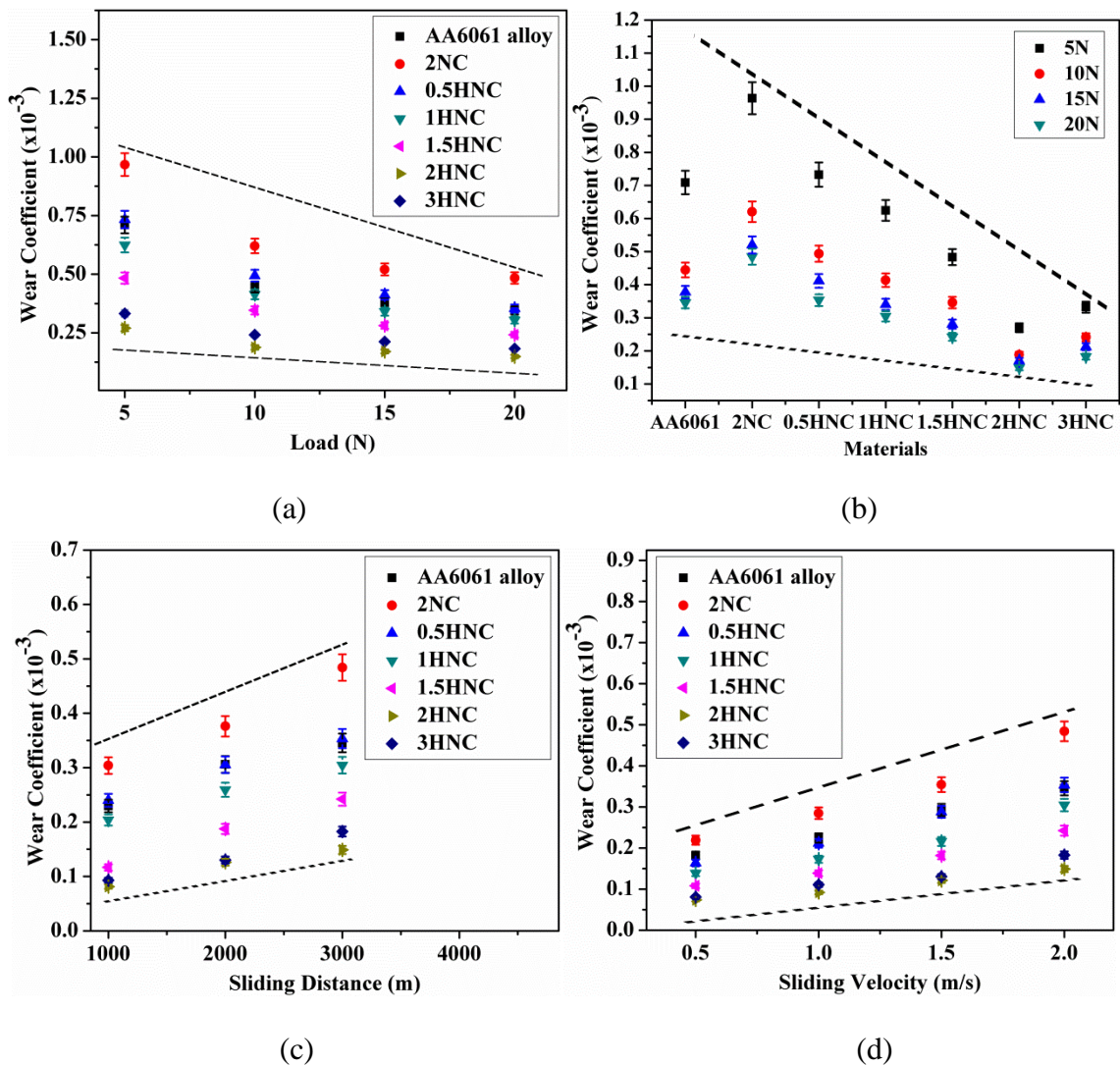


Figure 6.17: Wear coefficient of AA6061 aluminium alloy, 2NC nanocomposite and 2HNC hybrid nanocomposite as a function of (a) applied normal load (b) materials (c) sliding distance and (d) sliding velocity

It would be attributed due to the higher depth of penetration of hard asperites into the soft materials during higher applications of normal loads. Similar trends were observed in the previous studies mentioned by Das et al. [126], Yang et al. [88] and Kaushik et al. [141]. The wear coefficients were represented in figure 6.22(b) as a function of graphite content. It can be seen that the wear coefficients of materials decreased with the increase of graphite reinforcements in the AA6061 aluminium alloy matrix. It would be attributed due to the addition of solid lubricant graphite into the matrix that increases the wear resistance of hybrid nanocomposites. But the addition of graphite into the 2NC nanocomposite decreases the hardness of the hybrid nanocomposites which tends to decrease the wear coefficient.

Figure 6.17 (c) shows the wear coefficient of the materials as a function of sliding distance. It was observed that the wear coefficients of AA6061 aluminium alloy, 2NC nanocomposite and 0.5HNC, 1HNC, 1.5HNC, 2HNC and 3HNC hybrid nanocomposites increased with increase of sliding distances at all applied normal load conditions. This would be attributed due to the occurrence of more damaged wear tracks caused by fractured SiCp and graphite nanoparticles when a longer sliding distance was used. Figure 6.17(d) shows the wear coefficient of the materials as a function of sliding velocity. It was observed that the wear coefficients of AA6061 aluminium alloy, 2NC nanocomposite and 0.5HNC, 1HNC, 1.5HNC, 2HNC and 3HNC hybrid nanocomposites increased with increase of sliding velocities at all applied normal load conditions. This would be attributed due to the occurrence of more damage of wear tracks caused by fractured SiCp and graphite nanoparticles when higher sliding velocity was used [108]. The hard asperites quickly penetrate into the soft material with increase of sliding velocity at all applied normal load conditions. It was found that the wear coefficient of 2NC nanocomposite is larger than the AA6061 aluminium alloy, 0.5HNC, 1HNC, 1.5HNC, 2HNC and 3HNC hybrid nanocomposites at all conditions. The wear coefficient decreased with increase of applied normal loads and increase of graphite particles in the matrix. The wear coefficient increased with increase of sliding distance and sliding velocity of all materials. It is due to the hardness of the SiCp reinforced nanocomposite materials that dominated the wear coefficients. Observed trend was according to the Archard's wear equation given in equation 6.2 as follows.

$$K = \frac{Q_{v/l} H_m}{L} \quad (6.2)$$

where, ' $Q_{v/l}$ ' is the volume loss per unit sliding distance (mm^3/m), ' H_m ' is the hardness of the material surface (N/mm^2), ' L ' is the applied load (N) and ' K ' is the dimensionless wear coefficient less than unity. But the hardness in case of the AA6061 aluminium alloy, 0.5HNC, 1HNC, 1.5HNC, 2HNC and 3HNC hybrid nanocomposite was lower than 2NC nanocomposite. It was further noticed that the wear coefficients of the 0.5HNC, 1HNC, 1.5HNC, 2HNC and 3HNC hybrid nanocomposites i.e., formation probability of wear particle was found to be lower than AA6061 aluminium alloy matrix. This would be attributed to nanocomposite surface being protected by reducing the material plastic flow by SiCp nano-reinforcements and self-lubricating layer formed by graphite nano-reinforcement [142]. At lower applied normal loads, the higher wear coefficients indicate that the probability of formation of wear particle could be mainly due to the crack nucleation and its propagation into micro level crack even through the level of depth of penetration of hard asperities. But at higher applied normal loads the level of depth of penetration of specimen will be more and increases the material removal rate with higher plastic deformation [143]. At higher applied normal loads, it can be noted that the asperities formed during dry sliding wear process could be due to fragmentation either from the pin surface or counter surface. These hard asperities consist of hard debris present on the counter surface that penetrates deeper into the softer pin surface in the very initial stages of the dry sliding wear.

6.3.3 Coefficient of Friction of Pin Materials

The average friction coefficient values of AA6061 aluminium alloy, 2NC nanocomposite, 0.5HNC, 1HNC, 1.5HNC, 2HNC, and 3HNC hybrid nanocomposites is presented in figure 6.18. It is identified that from figure 6.18 (a) and 6.18 (b) the average coefficient of friction increased with increasing loads on pin irrespective of materials. Reports revealed that the friction coefficient increased by incorporation of SiCp nanoparticles in the base material. It would be attributed to the appearance of cubic structured beta-SiCp nanoparticles in the base material [121]. However, the friction coefficient reduced with rise of graphite nanoparticle content in the 2NC nanocomposite at a particular applied normal load. The average friction coefficient values of the hybrid nanocomposites is lower than the 2NC nanocomposite and base alloy. The hard SiCp nanoparticles withstand the load and graphite nanoparticles act as a solid lubricant and reduce the pin-counterface contact area that and resulted in reduction of the friction coefficient values [153].

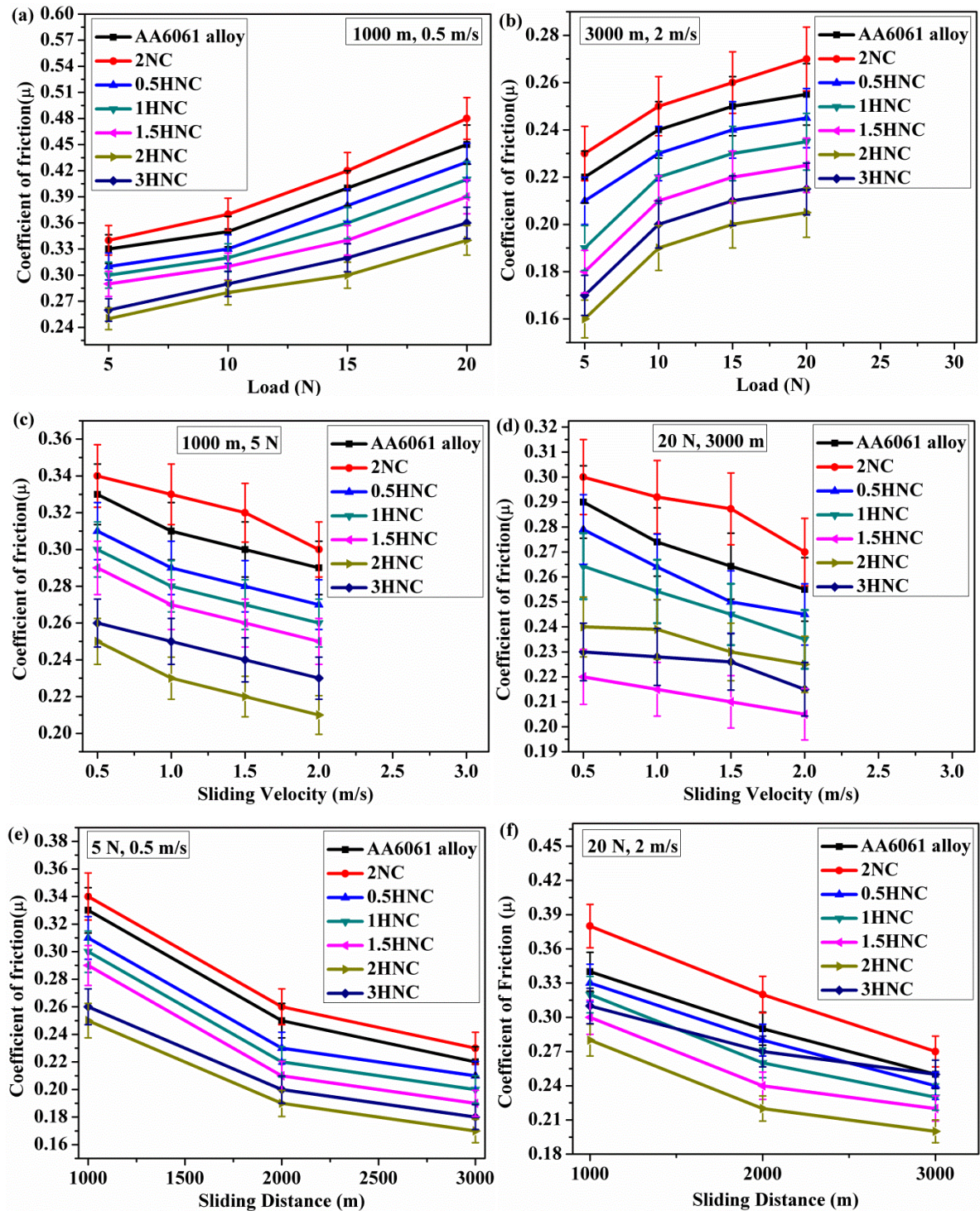


Figure 6.18: Friction coefficient (FC) values of Al6061 alloy based composite materials (a) FC versus load at V_{LDL} , (b) FC versus load at V_{HDL} , (c) FC versus sliding velocity at L_{LDL} , (d) FC versus sliding velocity at L_{HDH} , (e) FC versus sliding distance at V_{LL} , and (f) FC versus sliding distance at V_{HLH}

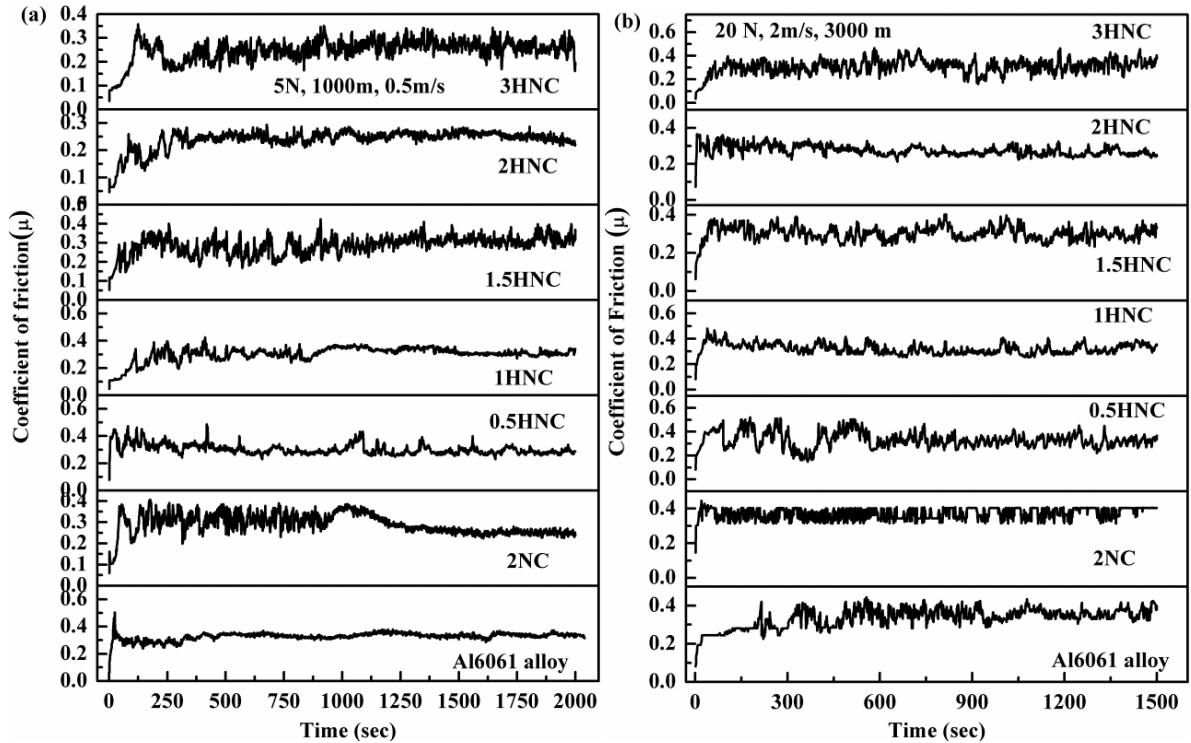


Figure 6.19: Friction coefficient of AA6061 aluminium alloy based materials (a) L_{LDLV_L} condition, and (b) L_{HDHV_H} condition

Increase of friction coefficient values would be attributed due to the rise of the depth of penetration with an increase of tangential loads on the pin. However, at higher applied normal load conditions, the strong interface bond between SiCp, graphite nanoparticles, and the matrix tends to break down and the average coefficient of friction values increases significantly. Figure 6.18 (c) and 6.18 (d) represent the friction coefficient values with respect to sliding velocity. Results reveal that the average friction coefficient values reduces slightly with rise of sliding velocity for all materials. It is identified that the friction coefficient values are lower at higher sliding velocity. It would be attributed to the softening of both the composite pin specimen and the EN 31 steel disc during dry sliding.

Incorporation of graphite nanoparticles minimizes the heat generation due to friction by its lubricity. Further reduction in the friction coefficient values in the case of hybrid nanocomposites at higher sliding velocities would be due to the introduction of graphite tribo-layer on the contact surface. Figure 6.18 (e) and 6.18 (f) depicts the friction coefficient values with respect to sliding distance. The variation of friction coefficient values is very

high throughout the beginning stages of sliding and decrease with sliding distance, as seen in figure 18. The friction coefficient values reduce slightly with the increase of sliding distance.

The decrease in the friction coefficient values is related to the type of wear mechanism [154]. Interactions of hard asperities at the interface would influence the friction coefficient values during dry sliding period [148]. This would be due to the formation of the mixer of SiCp and graphite nanoparticles with the MML layer which reduces the friction coefficient. Decrease of friction coefficient of hybrid nanocomposite is due to the hexagonal structure of graphite which acts as a solid lubricant [152]. The exhibited results shown in figure 6.19 (a) and 6.19 (b) reveal lower friction coefficient for 2HNC hybrid nanocomposite compared to all materials. The reduction of the coefficient of friction of 0.5HNC, 1HNC, 1.5HNC, 2HNC, and 3HNC hybrid nanocomposites compared to AA6061 aluminium alloy at $L_H D_H V_H$ is 3%, 5.9%, 11.8%, 17.7%, and 9% respectively. The experimental results also confirm the increase of coefficient of friction for 3HNC hybrid nanocomposite with more than 2 wt. % of graphite addition. After reaching the critical value of graphite addition, there is increase in the formation of thick graphite tribo-layer on the worn surface that would be peeling-off from the surface and causes the higher depth of penetration of asperities on the counter surface and leads to larger resistance to its sliding movement. The wear resistance of the aluminium based materials increased by the addition of graphite reinforcement particles more than the critical value that resulted in increasing the coefficient of friction [155].

6.3.4 Worn Surfaces of Pin Specimens

Figures 6.20, 6.21, 6.22, and 6.23 represent the worn surfaces of AA6061 aluminium alloy, 2NC nanocomposite, 0.5HNC, 1HNC, 1.5HNC, 2HNC and 3HNC hybrid nanocomposites at $L_L D_L V_L$, $L_L D_H V_H$, $L_H D_L V_L$, and $L_H D_H V_H$ conditions. In figures 6.20 (a) and 6.21 (a) indicate the worn surface of AA6061 aluminium alloy at 5 N applied normal load, lower and higher sliding distance, and sliding velocity conditions respectively. It can be observed that parallel grooves, scratches and plastic deformation at $L_L D_L V_L$ condition. Deep grooves, shallower scratches and plastic flow are observed at $L_L D_H V_H$ condition. In figures 6.22 (a) and 6.23 (a) depict the worn surfaces of AA6061 aluminium alloy at $L_H D_L V_L$ and $L_H D_H V_H$ conditions. It can be seen that deeper grooves, scratches and higher plastic flow at $L_H D_L V_L$ condition. Deep grooves, shallower scratches and turbulent flow of material are observed at $L_H D_H V_H$ condition. The execution of parallel grooves and scratches on pin

surface would be the evidence of abrasive wear mechanism (denoted as A). The plastic flow occurred on the surface in the sliding direction with row of furrows as an indication of adhesive wear mechanism (denoted as B). The increase of either load or sliding velocity increases the plastic deformation with the higher depth of penetration [83]. It is attributed to the lower hardness of unreinforced AA6061 aluminium alloy.

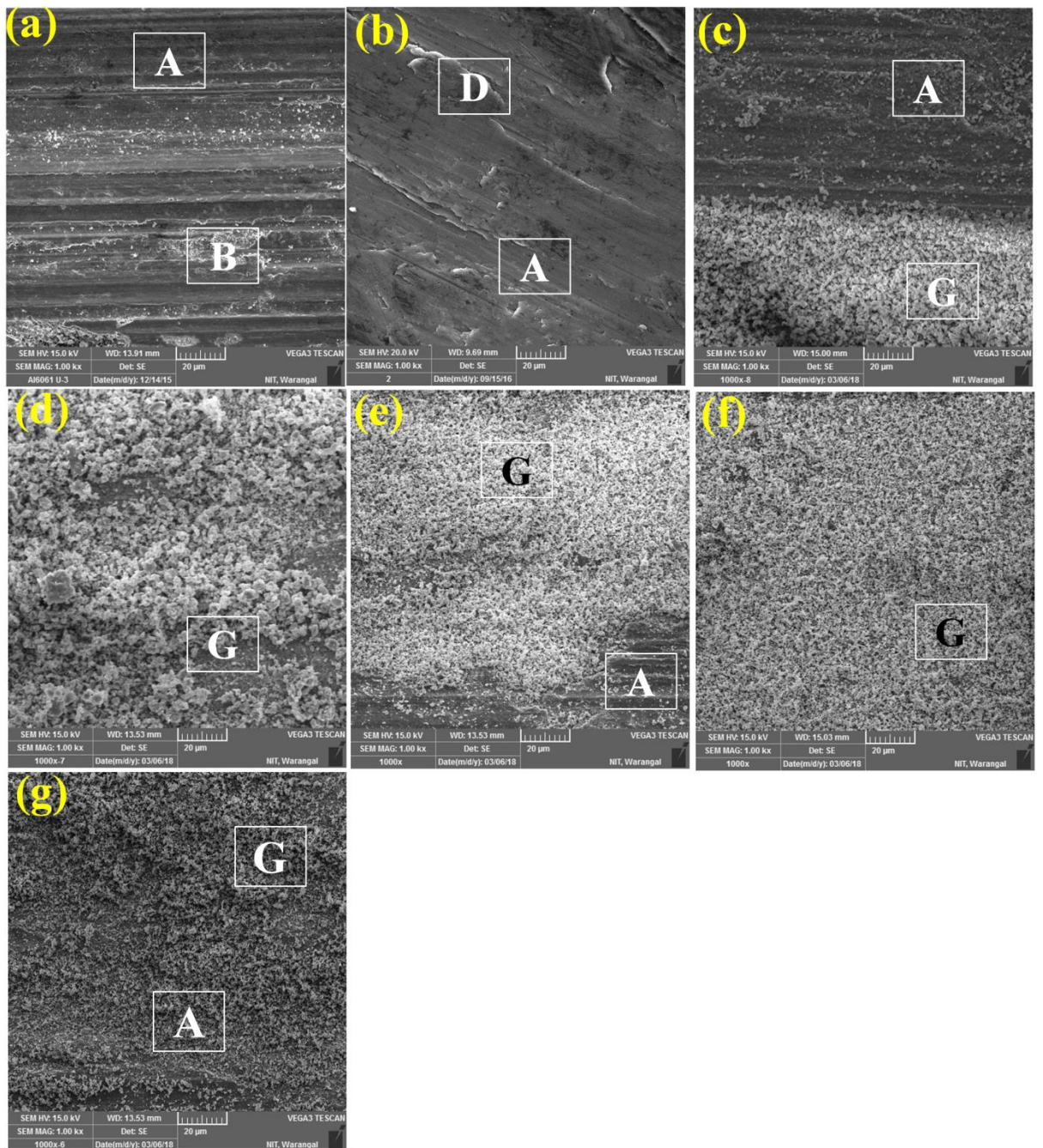


Figure 6.20: SEM micrographs of worn surfaces at LLDLV_L condition (a) AA6061 aluminium alloy, (b) 2NC, (c) 0.5HNC, (d) 1HNC, (e) 1.5HNC, (f) 2HNC, and (g) 3HNC

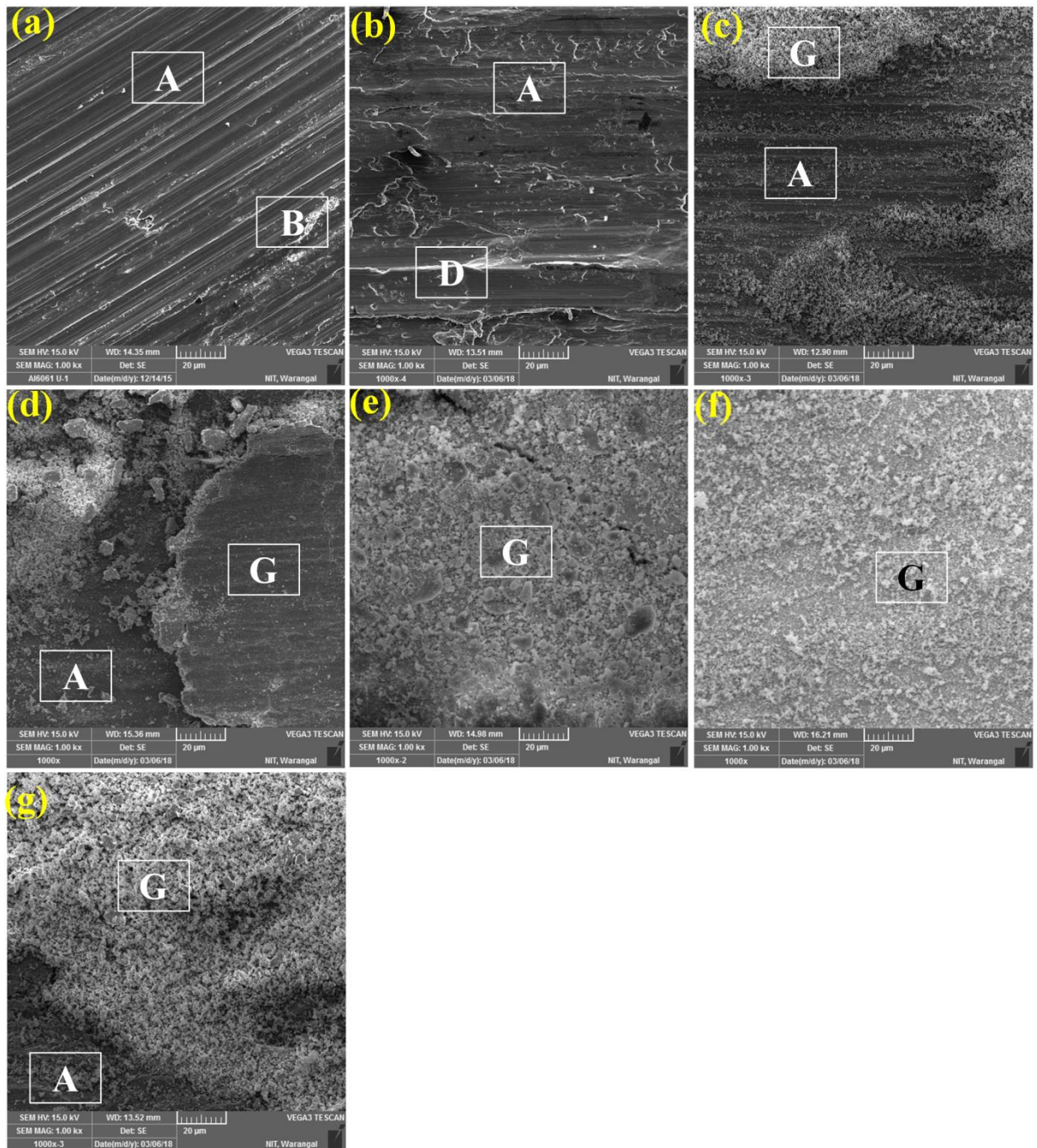


Figure 6.21: SEM images of worn surfaces at $LLDHV_H$ condition (a) AA6061 aluminium alloy, (b) 2NC, (c) 0.5HNC, (d) 1HNC, (e) 1.5HNC, (f) 2HNC, and (g) 3HNC

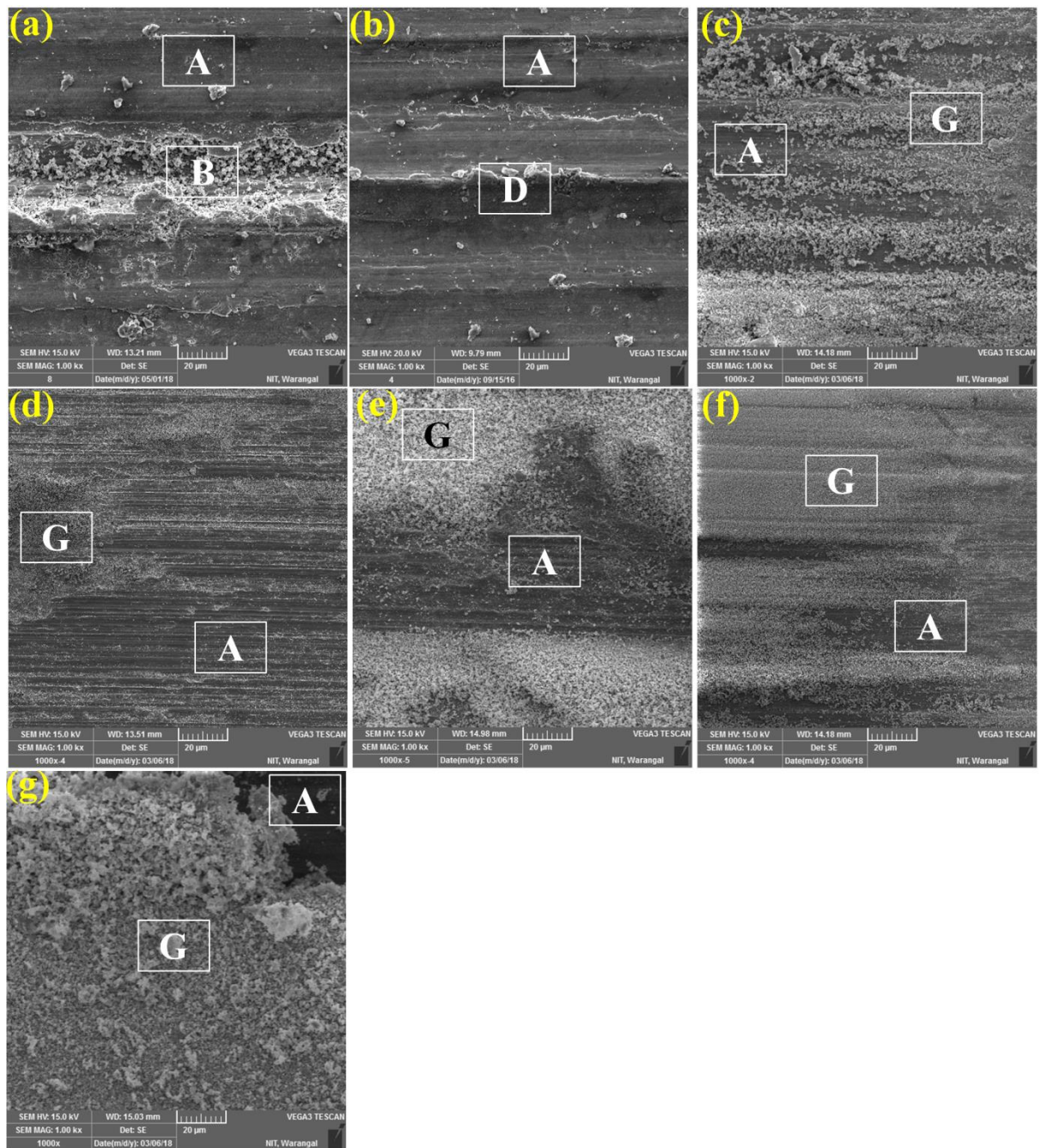


Figure 6.22: SEM images of worn surfaces at $L_H D_L V_L$ condition (a) AA6061 aluminium alloy, (b) 2NC, (c) 0.5HNC, (d) 1HNC, (e) 1.5HNC, (f) 2HNC, and (g) 3HNC

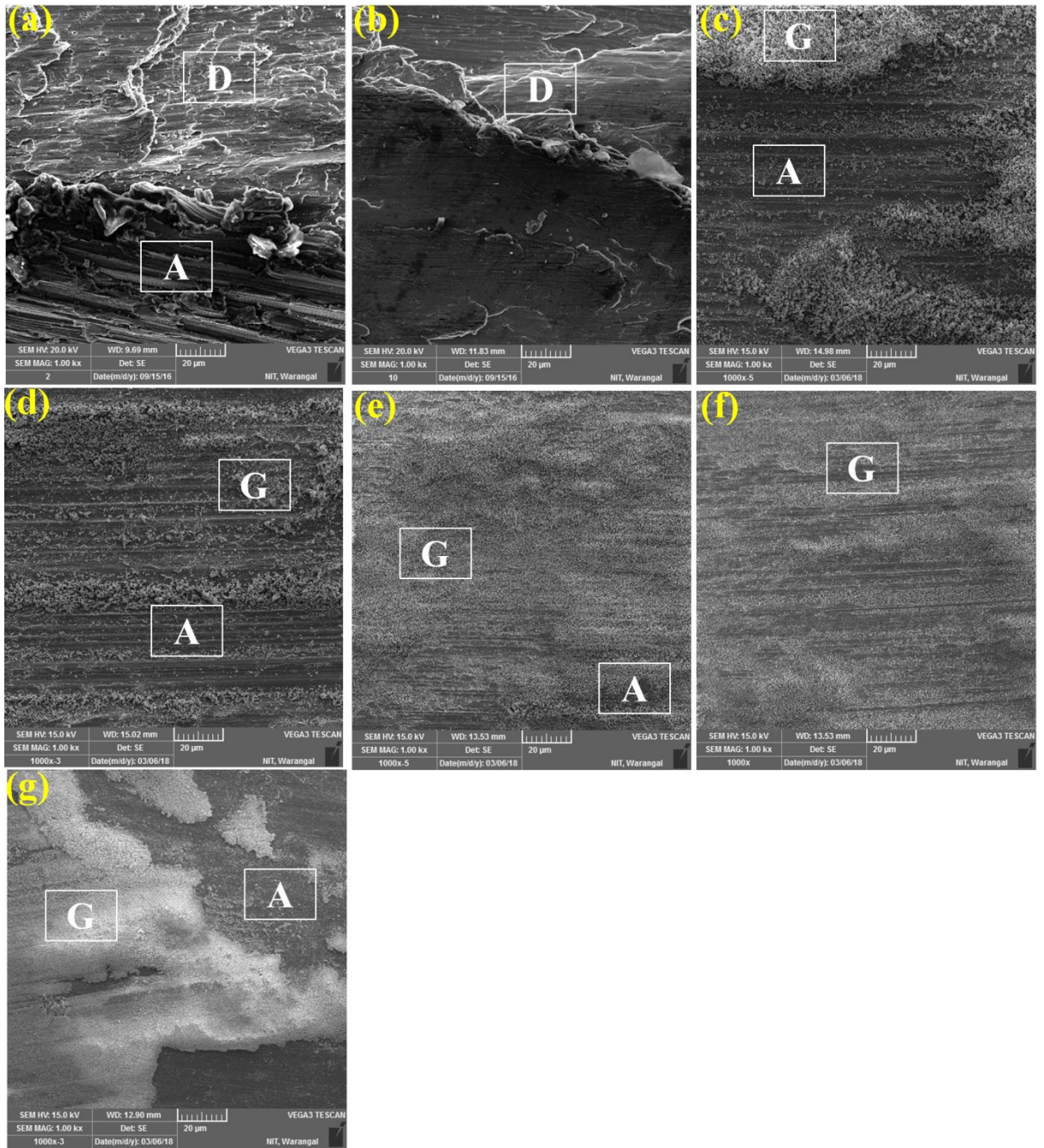


Figure 6.23: SEM images of worn surfaces at $L_H D_H V_H$ condition (a) AA6061 aluminium alloy, (b) 2NC, (c) 0.5HNC, (d) 1HNC, (e) 1.5HNC, (f) 2HNC, and (g) 3HNC

In figures 6.20 (b) and 6.21 (b) represent the worn surfaces of 2NC nanocomposite at $L_L D_L V_L$ and $L_L D_H V_H$ condition. Formation of smaller scratches in the sliding direction is evident of abrasive wear mechanism (denoted as A). The SEM micrograph of the worn surfaces of 2NC nanocomposite reveals the delamination mechanism (denoted as D) in the sliding direction. It reveals lower plastic deformation in the sliding direction which is lower

than the unreinforced AA6061 aluminium alloy at $L_LD_LV_L$ condition. It reveals the delamination of material in the sliding direction at $L_LD_HV_H$ condition. In figures 6.22 (b) and 6.23 (b) represent the worn surfaces of 2NC nanocomposite at $L_HD_LV_L$ and $L_HD_HV_H$ conditions. The worn surface of 2NC nanocomposite reveals the shallower scratches with higher plastic deformation at $L_HD_LV_L$ condition. The worn surface of 2NC nanocomposite reveals the severe plastic flow of material in the sliding direction at $L_HD_HV_H$ condition. The depth of penetration is less compared to the unreinforced alloy at all conditions. However, the flow of material shifted away from the sliding direction at $L_HD_HV_H$ condition, because the SiCp particles acted as obstacles to the flow and driven the material away from the sliding direction.

Figures 6.20 (c), (d) and (e), 6.21 (c), (d) and (e), 6.22 (c), (d) and (e), 6.23 (c), (d) and (e) shows the worn surface s of 0.5HNC, 1HNC, and 1.5HNC hybrid nanocomposites at $L_LD_LV_L$, $L_LD_HV_H$, $L_HD_LV_L$, and $L_HD_HV_H$ conditions. It is identified that the graphite film (denoted as G) spread over the surface but not covered the entire surface. The worn surface of hybrid nanocomposites reveals lower plastic deformation at $L_LD_LV_L$ condition. At this condition depth of penetration is lower than the unreinforced alloy and 2NC nanocomposite. It is observed that more depth of penetration is seen where the graphite thick layer is not present on the pin surface at $L_LD_HV_H$ condition. The uncovered surface reveals higher plastic deformation and obtained wear mechanism is abrasive wear at $L_HD_HV_H$ condition. It is observed that the graphite film is formed with gaps on the worn surface at $L_HD_HV_H$ condition. This is due to lack of continuous supply of graphite film on the pin surface during dry sliding wear. The increase of graphite content in the matrix decreases the groove formation and depth of penetration. Available graphite content on the worn surface acts as a solid lubricant which prevents the severe damage of the pin material. It is found that at low graphite content in the 2NC nanocomposite, the effect of graphite as a solid lubricant in dry sliding condition is less.

Figures 6.20 (f), 6.21 (f), 6.22 (f), and 6.23 (f) shows the worn surfaces of 2HNC hybrid nanocomposite at $L_LD_LV_L$, $L_LD_HV_H$, $L_HD_LV_L$, and $L_HD_HV_H$ conditions. On the worn surface of the hybrid nanocomposite, the thick graphite film is spread over the surface without gaps and cracks at all conditions. It is observed that the graphite thick film is well distributed over the worn surface and executed the abrasive wear mechanism. During dry sliding the sheared graphite particles form thick lubricating layer and reduce the direct

contact of pin and steel counter face. The depth of penetration is less compared to lower content graphite reinforced hybrid nanocomposite, unreinforced alloy and 2NC nanocomposite. Figures 6.20 (g), 6.21 (g), 6.22 (g), and 6.23 (g) shows the worn surfaces of 3HNC hybrid nanocomposite at $L_L D_L V_L$, $L_L D_H V_H$, $L_H D_L V_L$, and $L_H D_H V_H$ conditions.

It is observed that the graphite layer sheared and spread over the worn surface during dry sliding at 5 N load conditions. At 20 N load conditions the micrographs reveal that the graphite thick film spread over the surface and peeling off graphite film in some area. It would be attributed to oversupply of graphite on the surface $L_H D_H V_H$ condition. Due to the peeling off graphite thick film from the surface, it increases the depth of penetration which is less compared to the unreinforced AA6061 aluminium alloy and 2NC nanocomposite. Due to the continuous supply of graphite during dry sliding which turns into thick film on the surface and peels off from the worn surface then executed the abrasive wear mechanism. The addition of graphite content in the 2NC nanocomposite above the critical value leads to the release of graphite to the worn surface during dry sliding, graphite thick film forms and graphite film peels off from the pin surface and increases the wear rate.

6.3.5 EDX Analysis

Figures 6.24 and 6.25 represent the EDAX analysis of 2HNC hybrid nanocomposite at $L_L D_L V_L$ and $L_H D_H V_H$ conditions. The elemental analysis of the worn surface reveals the mixture of constituents from pin material, disc material and iron based oxide compounds. From the EDAX analysis it can be seen that the peaks of carbon (C), iron (Fe), aluminium (Al), silicon (Si), and oxygen (O). The EDAX analysis of graphite thick layer covered area of worn surface of hybrid nanocomposite tested at 5 N load condition reveals that the low intensity of Al, Fe, and O, high intensity of C peaks.

The higher intensity C peak reveals the presence of smeared nano graphite on pin worn surface. The presence of higher intensity of C peak minimizes the plastic deformation of AA6061 aluminium alloy matrix. The EDAX of graphite uncovered layer (named as spectrum 2) worn surface of hybrid nanocomposite reveals low intensity of C peak, higher intensity of Al, Fe, and O peaks at 5 N load condition. Worn surface of graphite thick layer covered hybrid nanocomposite tested at 20 N load condition reveals higher intensity of C, O, and Fe peaks and low intensity of Al peak. At similar conditions the uncovered (named as

spectrum 2) graphite thick film area exhibited high intensity of Al peak and low intensity of Fe and O peak at 20 N load condition. It indicates higher plastic deformation due to absence of graphite film on the worn surface.

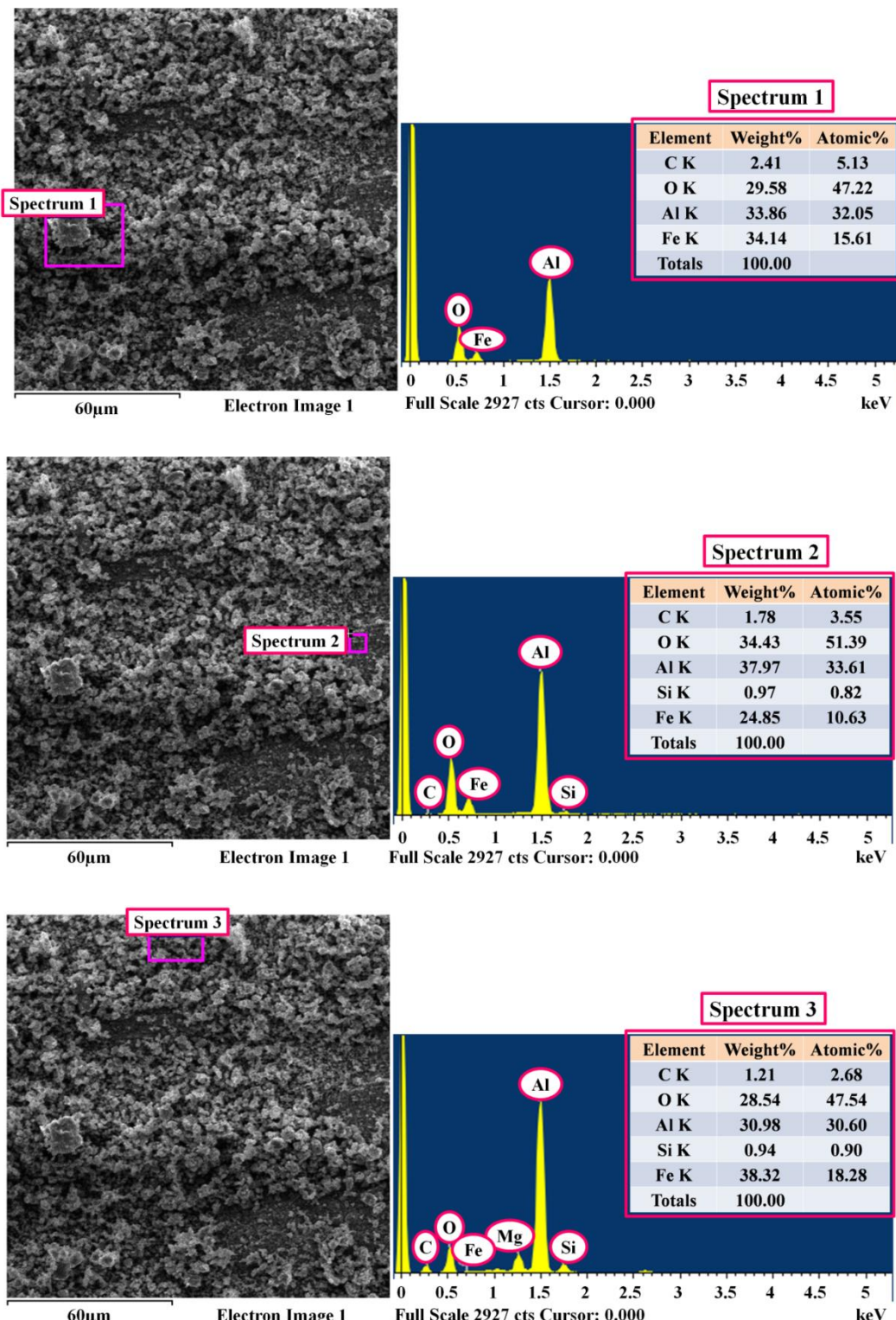


Figure 6.24: EDAX analysis of 2HNC hybrid nanocomposite worn surface at LLDLV_L

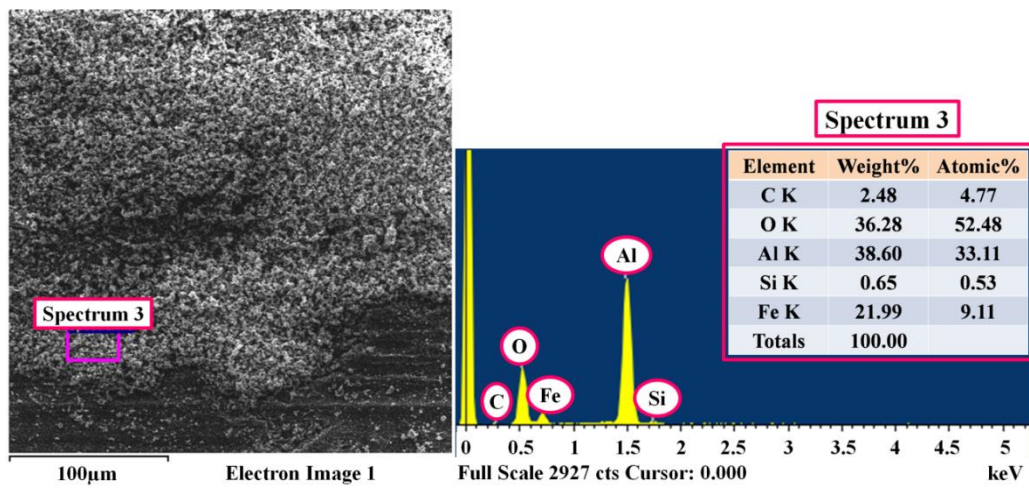
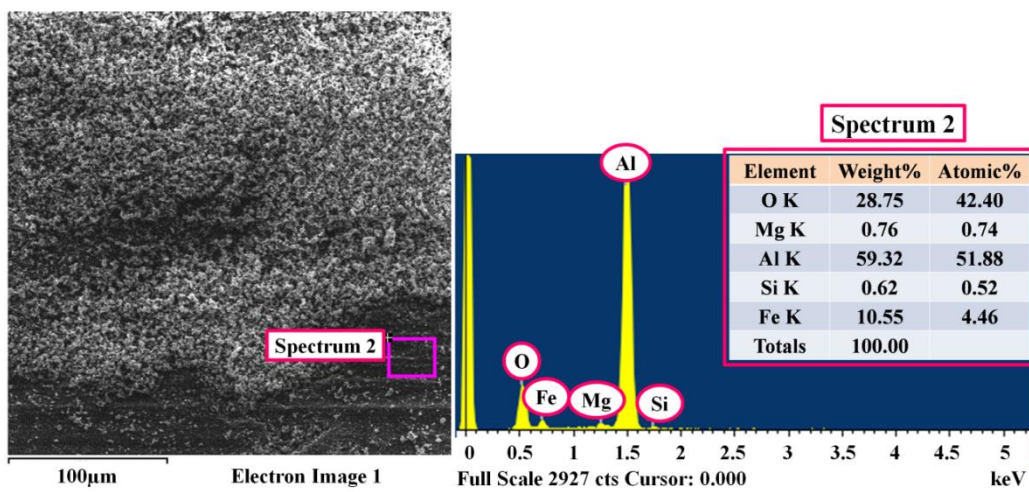
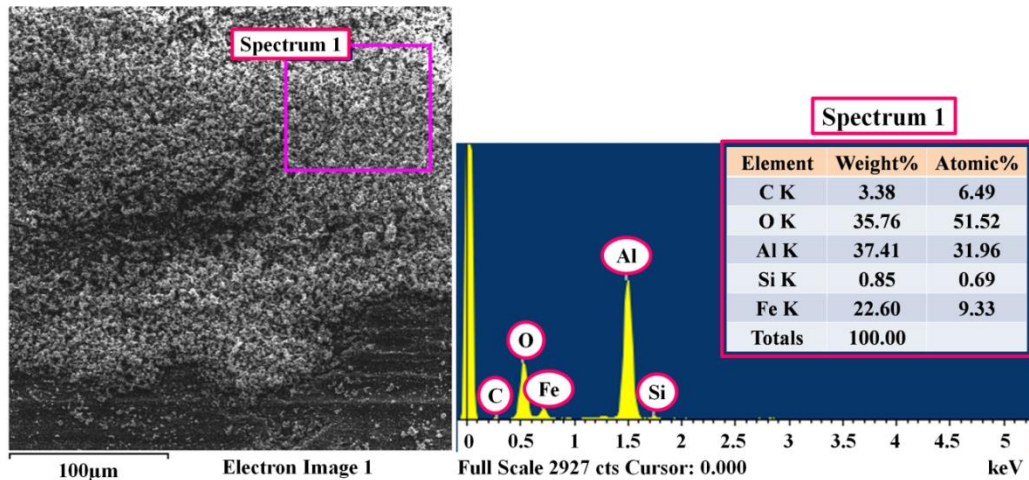


Figure 6.25: EDAX analysis of 2HNC hybrid nanocomposite worn surface at L_HD_HV_H

6.3.6 Wear Debris of Pin Materials

Figure 6.26 represents the wear debris of AA6061 aluminium alloy, 2NC nanocomposite and 2HNC hybrid nanocomposite. In figure 6.26 (a) indicates that the larger size wear debris is produced from AA6061 aluminium alloy during dry sliding condition. Formation of large size wear debris would be attributed to the severe plastic deformation with higher depth of penetration of hard asperities of steel disc counter face during dry sliding condition. From figure 6.26 (b) it represents that the AA6061 aluminium alloy matrix is filled with SiCp nano-reinforcements with lower inter particle spacing which increases the dislocation density. The medium size wear debris is produced from 2NC nanocomposite. The production of medium size wear debris may be due to the application of external loads that starts yielding of dislocation pile up in the subsurface of the pin material [146]. The contact profile of 2NC nanocomposite shows the yielding of dislocation piles up, which lead to crack initiation and propagates towards subsurface layer.

The SiCp nano-reinforcement particles come out from the subsurface combine with the MML and increase the wear resistance. The SiCp nano-reinforcement particles resist the hard asperities from the steel disc counter face and hence reduce the plastic deformation and higher depth of penetration. From figure 6.26 (c) it is observed that there is lower inter particle spacing for 2HNC hybrid nanocomposite. It would be due to the rise of dislocations with the addition SiCp and graphite nano-reinforcements in the matrix. It is seen that there is presence of lower depth of penetration and MML with SiCp and graphite nano-reinforcements in the contact profile of 2HNC hybrid nanocomposite. It is observed that the finer size wear debris is produced from 2HNC hybrid nanocomposite during dry sliding wear.

The size reduction of wear debris of 2HNC hybrid nanocomposite would be due to the production of continuous thick graphite layer on the pin contact surface mixed with MML and SiCp nano-reinforcements. The hard particle dislocation density increases in the thick graphite layer which leads to reduction of contact between the pin surface and steel disc counter face. Figure 6.27 shows the EDAX analysis of wear debris of 2HNC hybrid nanocomposite. It reveals the existence of iron and oxygen in the wear debris. The appearance of iron in the wear debris implies the transfer of iron from the EN31 steel disc to the worn surface of hybrid nanocomposite pin. Hard asperities at the interface of mating parts penetrate into the oxide layer and damage the oxide mixed layer. The presence of a high

oxygen peak confirmed the oxidation process and the iron indicates the material transition by adhesion at higher load 20 N.

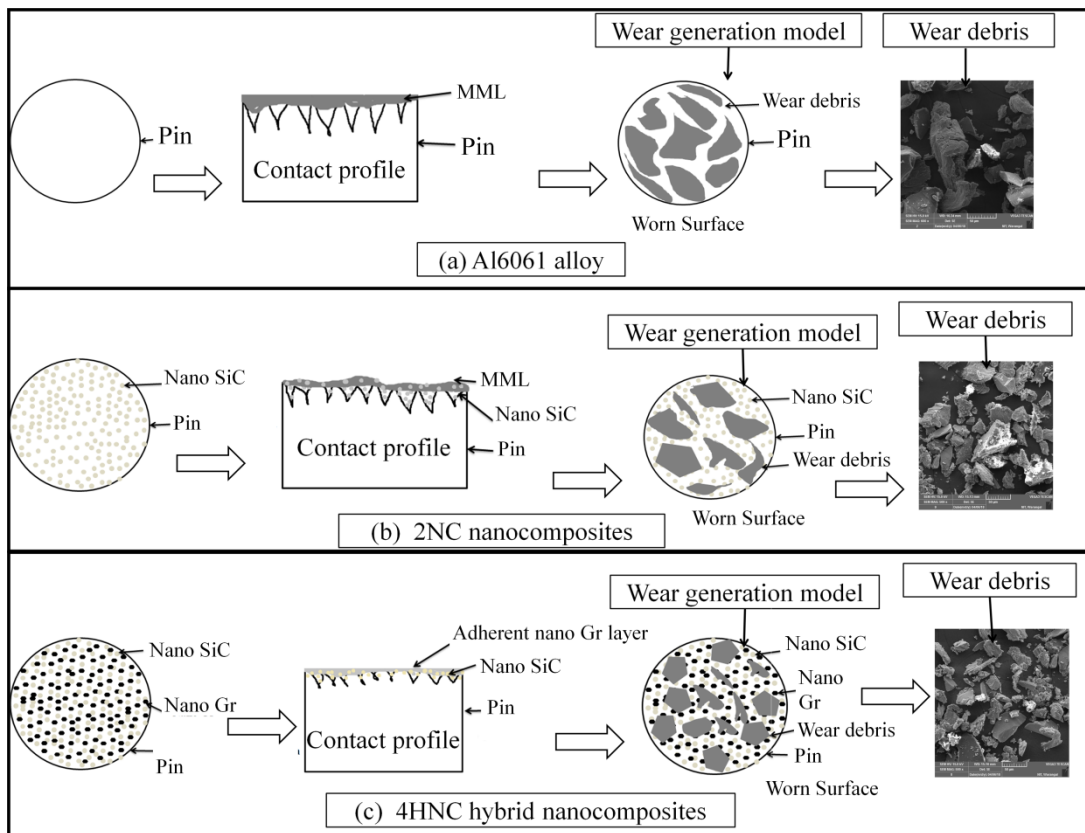


Figure 6.26: Schematic view of wear generation model including wear debris of AA6061 aluminium alloy, 2NC nanocomposite and 2HNC hybrid nanocomposite

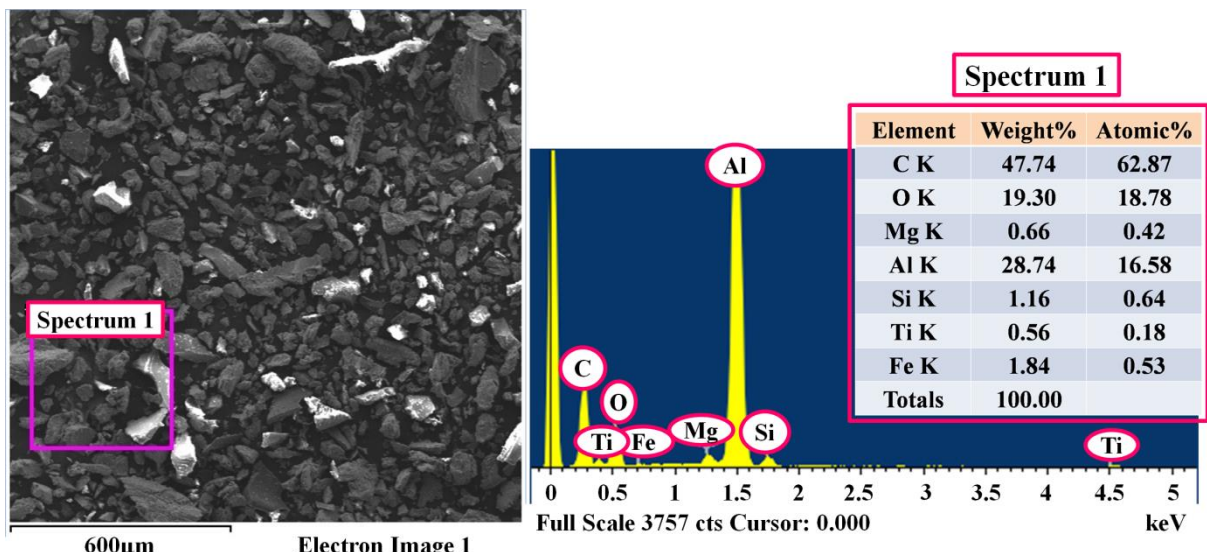


Figure 6.27: EDAX analysis of wear debris of 2HNC hybrid nanocomposite

6.3.7 Wear Mechanism

The wear mechanism of the 2HNC hybrid nanocomposite is defined by sliding velocity and applied normal loads. In the present test conditions, various groups of mechanisms are found to be gradual and the boundaries on the diagram are approximate (figure 6.28). At the lower sliding velocity and lower normal loads, graphite thin layer and smaller size oxide debris are identified (denoted as A). It is observed that the graphite thin layer with medium size oxide debris and lower delamination are seen at 15 N applied normal loads with lower sliding velocity up to 1.5 m/s (denoted as B). It is observed that the graphite peeling off from the worn surface with larger size oxide debris are seen at applied normal load above 15 N with higher sliding velocity (denoted as C). It reveals that there is severe oxidation, deeper grooves, smaller scratches with abrasion wear at applied normal loads above 20 N at all sliding velocity conditions (denoted as D). It is observed that there is severe abrasion wear with deeper grooves and delamination at higher sliding velocity and higher loads (denoted as E). It is observed that severe abrasion wear with higher depth of penetration, deeper grooves and oxide debris are found at higher sliding velocity and higher loads (denoted as F).

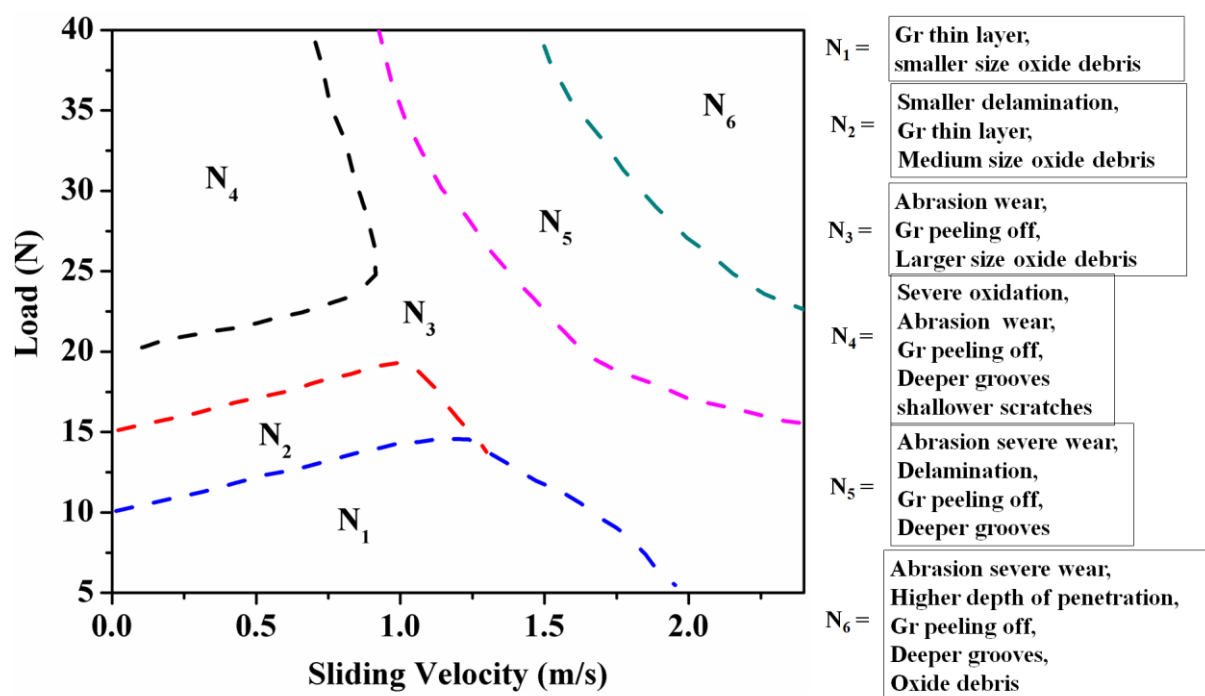


Figure 6.28: Wear mechanism of the 2HNC hybrid nanocomposite is drawn at various conditions with approximate boundaries in the present study

6.4 Two Body Abrasive Wear of Nanocomposites

6.4.1 Volumetric Wear Rate

The volumetric wear rate of the AA6061 aluminium alloy, 2NC nanocomposite and 2HNC hybrid nanocomposite was calculated from wear loss (g) data after the two body abrasion tests. The effect of applied normal load, abrasive grit size, sliding velocity and sliding distance on volumetric wear rate is discussed in the following sub sections. The volumetric wear rate of the materials is a function of its metallurgical characteristics, operating and environmental conditions, and nature of counter surface. Among these, hardness of the pin material and abrasive grit size on paper will play a significant role on type of wear mechanism [147].

6.4.1.1 Effect of applied normal load

Figure 6.29 represents the 2D bar graphs of volumetric wear rate of materials as a function of applied normal loads and sliding distances of 60 m, 120 m, and 180 m respectively. Figure 6.29 (a) denotes the volumetric wear rate of AA6061 aluminium alloy, 2NC nanocomposite and 2HNC hybrid nanocomposite at 150 μm abrasive grit size and 60 m sliding distance. At 5 N applied normal load, the volumetric wear rate was found to be 0.4302 mm^3/m , 0.35 mm^3/m , and 0.288 mm^3/m respectively. The decrease in volumetric wear rate at 5 N applied normal load is around 18.64% for 2NC nanocomposite and 33.1% for 2HNC hybrid nanocomposite compared to AA6061 aluminium alloy. At 10 N applied normal load, the volumetric wear rate is found to be 0.5643 mm^3/m for AA6061 aluminium alloy, 0.431 mm^3/m for 2NC nanocomposite and 0.351 mm^3/m for 2HNC hybrid nanocomposite. The decrease in volumetric wear rate at 10 N applied normal load is around 23.6% for 2NC nanocomposite and 38% for 2HNC hybrid nanocomposite compared to AA6061 aluminium alloy. At 15 N applied normal load, the volumetric wear rate was found to be 0.957 mm^3/m for AA6061 aluminium alloy, 0.686 mm^3/m for 2NC nanocomposite and 0.599 mm^3/m for 2HNC hybrid nanocomposite.

The decrease in volumetric wear rate at 15 N applied normal load is around 28.3% for 2NC nanocomposite and 37.4% for 2HNC hybrid nanocomposite compared to AA6061 aluminium alloy. At 20 N applied normal load, the volumetric wear rate was found to be

1.51 mm^3/m for AA6061 aluminium alloy, 0.871 mm^3/m for 2NC nanocomposite and 0.7594 mm^3/m for 2HNC hybrid nanocomposite. The decrease in volumetric wear rate at 15 N applied normal load is around 42.3% for 2NC nanocomposite and 49.7% for 2HNC hybrid nanocomposite compared to AA6061 aluminium alloy.

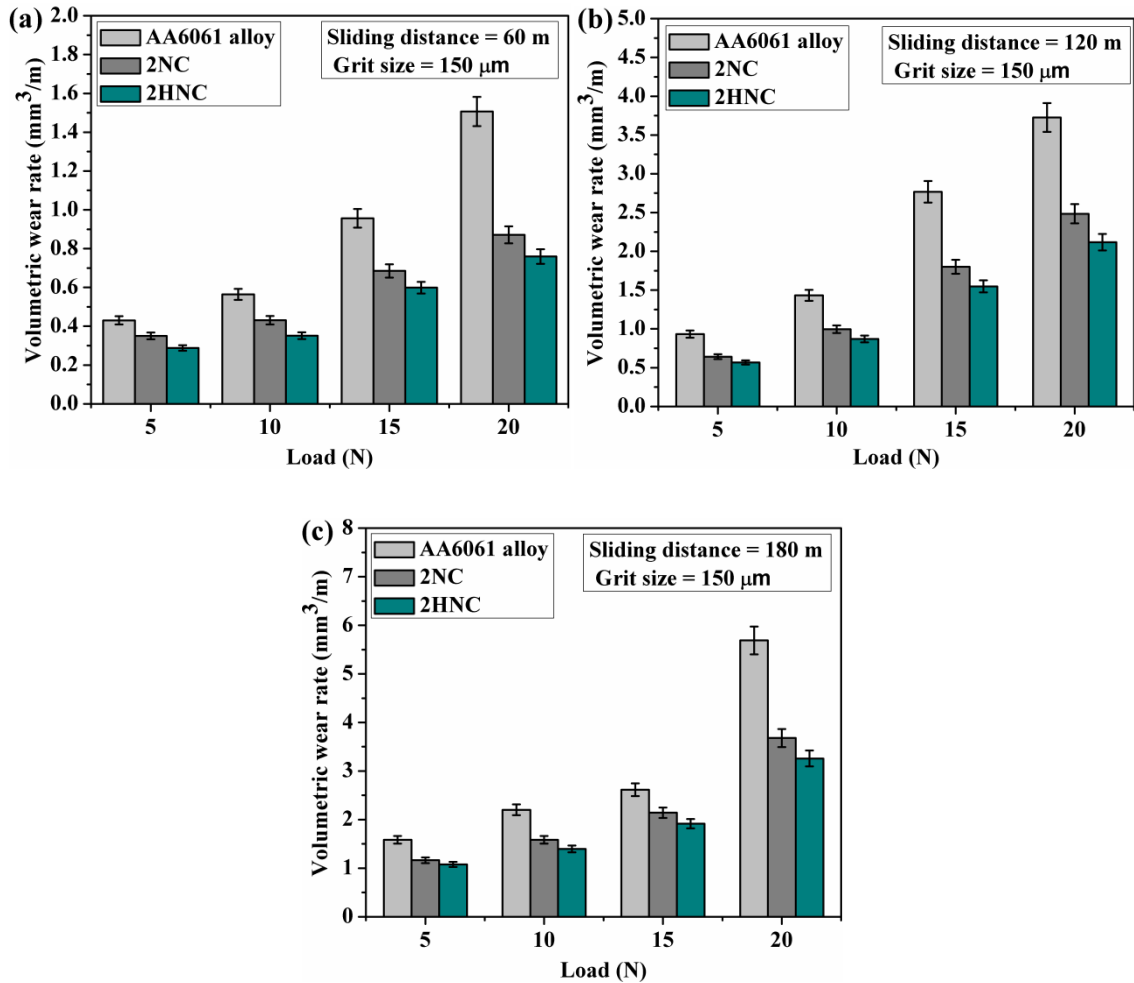


Figure 6.29: Volumetric wear rate of AA6061 aluminium alloy, 2NC nanocomposite and 2HNC hybrid nanocomposite as a function of applied normal load (a) 60 m, (b) 120 m, and (c) 180 m

Figure 6.29 (b) represents the volumetric wear rate of AA6061 aluminium alloy, 2NC nanocomposite and 2HNC hybrid nanocomposite at 150 μm abrasive grit size and 120 m sliding distance. At 5 N applied normal load, the volumetric wear rate was found to be 0.933 mm^3/m , 0.642 mm^3/m , and 0.568 mm^3/m respectively. The decrease in volumetric wear rate at 5 N applied normal load is around 31.1% for 2NC nanocomposite and 39.1% for 2HNC hybrid nanocomposite compared to AA6061 aluminium alloy. At 10 N applied

normal load, the volumetric wear rate was found to be $1.433 \text{ mm}^3/\text{m}$, $0.995 \text{ mm}^3/\text{m}$, and $0.871 \text{ mm}^3/\text{m}$ respectively. The decrease in volumetric wear rate at 10 N applied normal load is around 30.6% for 2NC nanocomposite and 39.2% for 2HNC hybrid nanocomposite compared to AA6061 aluminium alloy. At 15 N applied normal load, the volumetric wear rate was found to be $2.77 \text{ mm}^3/\text{m}$, $1.8 \text{ mm}^3/\text{m}$, and $1.55 \text{ mm}^3/\text{m}$ respectively. The decrease in volumetric wear rate at 15 N applied normal load is around 35% for 2NC nanocomposite and 44.1% for 2HNC hybrid nanocomposite compared to AA6061 aluminium alloy. At 20 N applied normal load, the volumetric wear rate was found to be $3.73 \text{ mm}^3/\text{m}$, $2.485 \text{ mm}^3/\text{m}$, and $2.118 \text{ mm}^3/\text{m}$ respectively. The decrease in volumetric wear rate at 20 N applied normal load is around 33.4% for 2NC nanocomposite and 43.2% for 2HNC hybrid nanocomposite compared to AA6061 aluminium alloy.

Figure 6.29 (c) represents the volumetric wear rate of AA6061 aluminium alloy, 2NC nanocomposite and 2HNC hybrid nanocomposite at $150 \mu\text{m}$ abrasive grit size and 180 m sliding distance. At 5 N applied normal load, the volumetric wear rate was found to be $1.5846 \text{ mm}^3/\text{m}$, $1.164 \text{ mm}^3/\text{m}$, and $1.078 \text{ mm}^3/\text{m}$ respectively. The decrease in volumetric wear rate at 5 N applied normal load is around 26.5% for 2NC nanocomposite and 31.2% for 2HNC hybrid nanocomposite compared to AA6061 aluminium alloy. At 10 N applied normal load, the volumetric wear rate was found to be $2.21 \text{ mm}^3/\text{m}$ for AA6061 aluminium alloy, $1.59 \text{ mm}^3/\text{m}$ for 2NC nanocomposite and $1.398 \text{ mm}^3/\text{m}$ for 2HNC hybrid nanocomposite. The decrease in volumetric wear rate at 10 N applied normal load is around 28.1% for 2NC nanocomposite and 36.8% for 2HNC hybrid nanocomposite compared to AA6061 aluminium alloy. At 15 N applied normal load, the volumetric wear rate was found to be $2.62 \text{ mm}^3/\text{m}$ for AA6061 aluminium alloy, $2.15 \text{ mm}^3/\text{m}$ for 2NC nanocomposite and $1.92 \text{ mm}^3/\text{m}$ for 2HNC hybrid nanocomposite. The decrease in volumetric wear rate at 15 N applied normal load is around 17.9% for 2NC nanocomposite and 26.7% for 2HNC hybrid nanocomposite compared to AA6061 aluminium alloy. At 20 N applied normal load, the volumetric wear rate was found to be $5.69 \text{ mm}^3/\text{m}$ for AA6061 aluminium alloy, $3.68 \text{ mm}^3/\text{m}$ for 2NC nanocomposite and $3.26 \text{ mm}^3/\text{m}$ for 2HNC hybrid nanocomposite. The decrease in volumetric wear rate at 20 N applied normal load is around 35.3% for 2NC nanocomposite and 42.7% for 2HNC hybrid nanocomposite compared to AA6061 aluminium alloy.

It is noticed that the volumetric wear rate increases with increase of applied normal load irrespective of the material. It would be attributed to the higher depth of penetration of

abrasive grit particles with increase of applied normal load on pin material. The increase of volumetric wear rate with respect to the applied normal load would be attributed to the rise of contact stress. The pin surface is worn away due to the cutting action of abrasive grit particles on the counter faces. Material removal rate is a function of elastic contact load and abrasive grit particle size [156]. The resistance force offered by the abrasive grit particles due to the external applied normal load is effectively transferred from the abrasive grit particles to the pin surface. The depth of penetration of abrasive grit particles rises with increase of applied normal load. The higher applied normal loads tends to create a higher stress concentration on the pin material and thus resulting in higher abrasion wear rate [87]. It is also observed that the volumetric wear rate of hybrid nanocomposite is less than the AA6061 aluminium alloy and 2NC nanocomposite at all applied normal loads.

6.4.1.2 Effect of abrasive grit size

Figure 6.30 denotes the 2D bar graphs of volumetric wear rate of materials as a function of abrasive grit particle size, at a sliding distance of 180 m and applied normal loads of 5 N, 10 N, 15 N, and 20 N respectively. Figure 6.30 (a) represents the volumetric wear rate of AA6061 aluminium alloy, 2NC nanocomposite and 2HNC hybrid nanocomposite at 5 N applied normal load and a sliding distance of 180 m. The volumetric wear rate of AA6061 aluminium alloy, 2NC nanocomposite, and 2HNC hybrid nanocomposite on 50 μm abrasive grit size at 5 N applied normal load is $0.597 \text{ mm}^3/\text{m}$, $0.544 \text{ mm}^3/\text{m}$, and $0.46 \text{ mm}^3/\text{m}$ respectively. The decrease in volumetric wear rate on 50 μm abrasive grit size at 5 N applied normal load is around 8.9% for 2NC nanocomposite and 22.9% for 2HNC hybrid nanocomposite compared to AA6061 aluminium alloy. The volumetric wear rate of AA6061 aluminium alloy, 2NC nanocomposite, and 2HNC hybrid nanocomposite on 100 μm abrasive grit size at 5 N applied normal load is $1.45 \text{ mm}^3/\text{m}$, $1.03 \text{ mm}^3/\text{m}$, and $0.92 \text{ mm}^3/\text{m}$ respectively. The decrease in volumetric wear rate on 50 μm abrasive grit size at 5 N applied normal load is around 28.9% for 4NC nanocomposite and 36.6% for 2HNC hybrid nanocomposite compared to AA6061 aluminium alloy. The volumetric wear rate of AA6061 aluminium alloy, 2NC nanocomposite, and 2HNC hybrid nanocomposite on 150 μm abrasive grit size at 5N applied normal load is $1.59 \text{ mm}^3/\text{m}$, $1.165 \text{ mm}^3/\text{m}$, and $1.08 \text{ mm}^3/\text{m}$ respectively. The decrease in volumetric wear rate on 150 μm abrasive grit size at 5 N applied normal load is around 26.7% for 2NC nanocomposite and 32.1% for 2HNC hybrid nanocomposite.

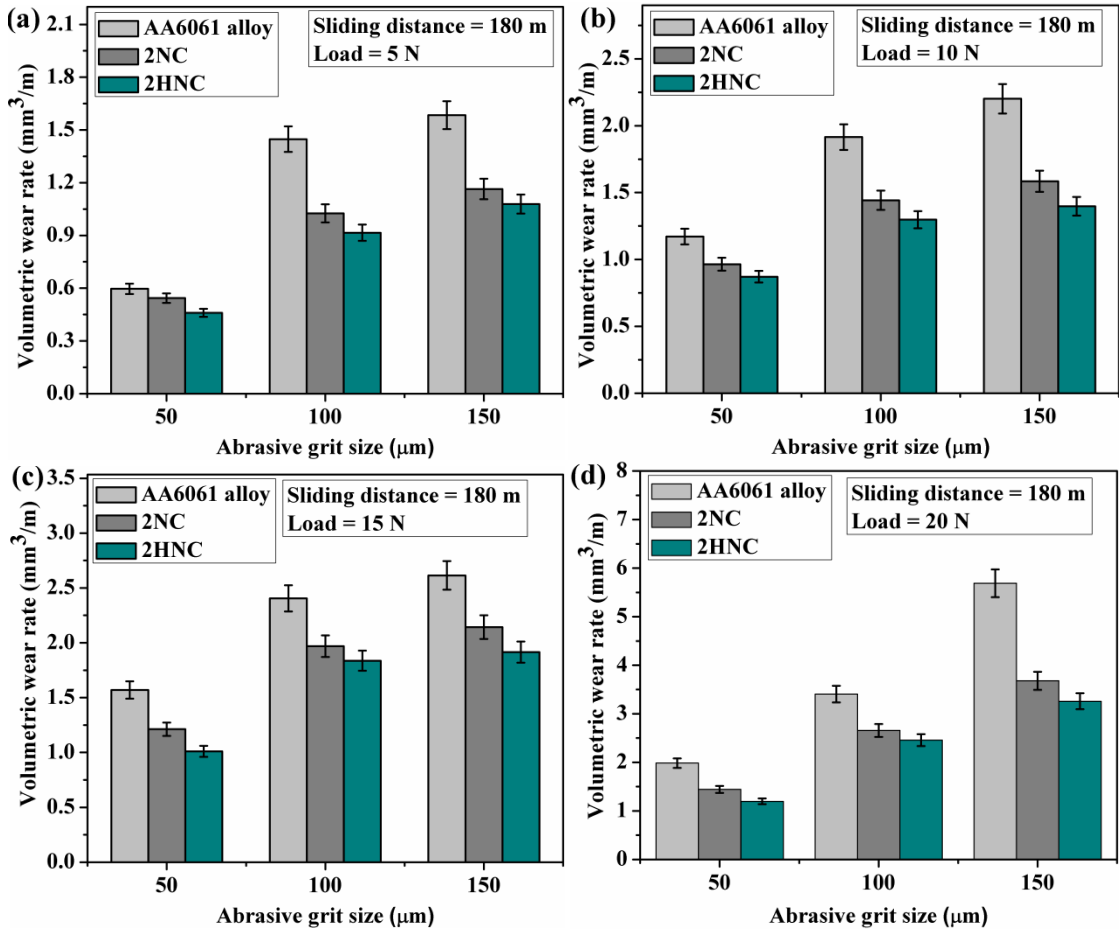


Figure 6.30: Volumetric wear rate of AA6061 aluminium alloy, 2NC nanocomposite and 2HNC hybrid nanocomposite as a function of grit size (a) 5 N, (b) 10 N, (c) 15 N, and (d) 20 N

Figure 6.30 (b) represents the volumetric wear rate of AA6061 aluminium alloy, 2NC nanocomposite and 2HNC hybrid nanocomposite at 10 N applied normal load and a sliding distance of 180 m. The volumetric wear rate of AA6061 aluminium alloy, 2NC nanocomposite, and 2HNC hybrid nanocomposite on 50 μm abrasive grit size at 10 N applied normal load is $1.171\text{mm}^3/\text{m}$, $0.965\text{ mm}^3/\text{m}$, and $0.871\text{ mm}^3/\text{m}$ respectively. The decrease in volumetric wear rate on 50 μm abrasive grit size at 10 N applied normal load is around 17.5% for 2NC nanocomposite and 25.6% for 2HNC hybrid nanocomposite compared to AA6061 aluminium alloy. The volumetric wear rate of AA6061 aluminium alloy, 2NC nanocomposite, and 2HNC hybrid nanocomposite on 100 μm abrasive grit size at 10 N applied normal load is $1.92\text{ mm}^3/\text{m}$, $1.443\text{ mm}^3/\text{m}$, and $1.298\text{ mm}^3/\text{m}$ respectively. The decrease in volumetric wear rate on 100 μm abrasive grit size at 10 N applied normal load is around 39.8% for 2NC nanocomposite and 32.4% for 2HNC hybrid nanocomposite

compared to AA6061 aluminium alloy. The volumetric wear rate of AA6061 aluminium alloy, 2NC nanocomposite, and 2HNC hybrid nanocomposite on 150 μm abrasive grit size at 10 N applied normal load is 2.21 mm^3/m , 1.585 mm^3/m , and 1.398 mm^3/m respectively.

The decrease in volumetric wear rate on 150 μm abrasive grit size at 10 N applied normal load is around 28.2% for 2NC nanocomposite and 36.8% for 2HNC hybrid nanocomposite compared to AA6061 aluminium alloy. Figure 6.30 (c) represents the volumetric wear rate of AA6061 aluminium alloy, 2NC nanocomposite and 2HNC hybrid nanocomposite at 15 N applied normal load and a sliding distance of 180 m. The volumetric wear rate of AA6061 aluminium alloy, 2NC nanocomposite, and 2HNC hybrid nanocomposite on 50 μm abrasive grit size at 15 N applied normal load is 1.57 mm^3/m , 1.22 mm^3/m , and 1.01 mm^3/m respectively. The decrease in volumetric wear rate on 50 μm abrasive grit size at 15 N applied normal load is around 22.3% for 2NC nanocomposite and 35.7% for 2HNC hybrid nanocomposite compared to AA6061 aluminium alloy. The volumetric wear rate of AA6061 aluminium alloy, 2NC nanocomposite, and 2HNC hybrid nanocomposite on 100 μm abrasive grit size at 15 N applied normal load is 2.41 mm^3/m , 1.97 mm^3/m , and 1.84 mm^3/m respectively. The decrease in volumetric wear rate on 100 μm abrasive grit size at 15 N applied normal load is around 18.3% for 2NC nanocomposite and 23.7% for 2HNC hybrid nanocomposite compared to AA6061 aluminium alloy. The volumetric wear rate of AA6061 aluminium alloy, 2NC nanocomposite, and 2HNC hybrid nanocomposite on 150 μm abrasive grit size at 15 N applied normal load is 2.62 mm^3/m , 2.143 mm^3/m , and 1.92 mm^3/m respectively. The decrease in volumetric wear rate on 150 μm abrasive grit size at 15 N applied normal load is around 18.2% for 2NC nanocomposite and 26.7% for 2HNC hybrid nanocomposite compared to AA6061 aluminium alloy.

Figure 6.30 (d) represents the volumetric wear rate of AA6061 aluminium alloy, 2NC nanocomposite and 2HNC hybrid nanocomposite at 20 N applied normal load and a sliding distance of 180 m. The volumetric wear rate of AA6061 aluminium alloy, 2NC nanocomposite, and 2HNC hybrid nanocomposite on 50 μm abrasive grit size at 20 N applied normal load is 1.985 mm^3/m , 1.443 mm^3/m , and 1.198 mm^3/m respectively. The decrease in volumetric wear rate on 50 μm abrasive grit size at 20 N applied normal load is around 27.3% for 2NC nanocomposite and 39.7% for 2HNC hybrid nanocomposite compared to AA6061 aluminium alloy. The volumetric wear rate of AA6061 aluminium alloy, 2NC

nanocomposite, and 2HNC hybrid nanocomposite on 100 μm abrasive grit size at 20 N applied normal load is 3.41 mm^3/m , 2.66 mm^3/m , and 2.46 mm^3/m respectively. The decrease in volumetric wear rate on 100 μm abrasive grit size at 20 N applied normal load is around 22% for 2NC nanocomposite and 28% for 2HNC hybrid nanocomposite compared to AA6061 aluminium alloy. The volumetric wear rate of AA6061 aluminium alloy, 2NC nanocomposite, and 2HNC hybrid nanocomposite on 150 μm abrasive grit size at 20 N applied normal load is 5.69 mm^3/m , 3.68 mm^3/m , and 3.26 mm^3/m respectively. The decrease in volumetric wear rate on 150 μm abrasive grit size at 20 N applied normal load is around 35.3% for 2NC nanocomposite and 42.7% for 2HNC hybrid nanocomposite compared to AA6061 aluminium alloy.

It is found that from the obtained results as abrasive grit size increases, the penetration of abrasive grit particles into the pin surface increases, hence the volumetric wear rate of both 2NC nanocomposite and 2HNC hybrid nanocomposite is increased [87]. Lower size abrasive grit particles are only in elastic contact with the pin material and supports the applied normal load without contributing to material removal rate. The grains in the lower size abrasive grit paper contain a large number of cracks which make them break easily and reduces their ability to remove material. The resistance force offered by the abrasive grit particles due to the external applied normal load is effectively transferred from the abrasive grit particles to the pin surface. The depth of penetration of abrasive grit particles rises with increase of size of grit particle and applied normal load. The increase of two body abrasive wear rate with respect to the abrasive paper grit size and applied normal load would be attributed to the rise of contact stress. The lower abrasive grit particle size tends to create a lower stress concentration on the pin material and thus resulting in higher abrasion wear resistance [87]. It can be seen that the SiCp reinforced AA6061 aluminium alloy based nanocomposite showed higher wear resistance compared to AA6061 aluminium alloy, whereas the SiCp and graphite dual nanoparticles reinforced AA6061 aluminium hybrid nanocomposite showed wear resistance further more compared to AA6061 aluminium alloy and 2NC nanocomposite.

6.4.1.3 Effect of sliding distance

The volumetric wear rate of ultrasonically assisted casted materials is plotted as a function of sliding distance at various loads and constant abrasive grit size of 150 μm is shown in figure 6.31. Figure 6.31 (a) depicts the volumetric wear rate of AA6061 aluminium

alloy, 2NC nanocomposite and 2HNC hybrid nanocomposite at 5 N applied normal load and abrasive grit size of 150 μm . The volumetric wear rate of materials at a sliding distance of 60 m and 5 N applied normal load is found to be $0.8852 \text{ mm}^3/\text{m}$ for AA6061 aluminium alloy, $0.62 \text{ mm}^3/\text{m}$ for 2NC nanocomposite and $0.56 \text{ mm}^3/\text{m}$ for 2HNC hybrid nanocomposite.

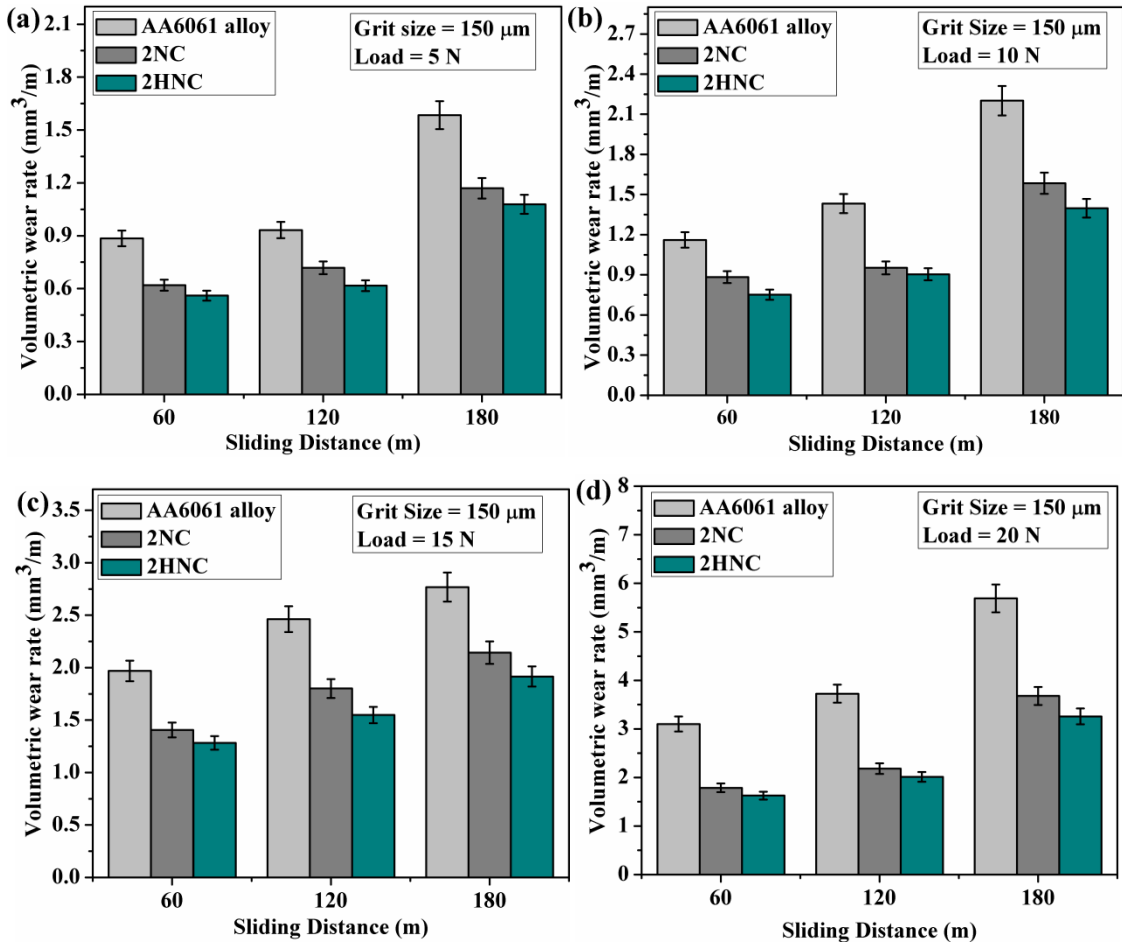


Figure 6.31: Volumetric wear rate of AA6061 aluminium alloy, 2NC nanocomposite and 2HNC hybrid nanocomposite as a function of abrasive grit size (a) 5 N, (b) 10 N, (c) 15 N, and (d) 20 N

The decrease in volumetric wear rate at 60 m sliding distance and 5 N applied normal load is around 30% for 2NC nanocomposite and 36.7% for 2HNC hybrid nanocomposite compared to AA6061 aluminium alloy. The volumetric wear rate of materials at a sliding distance of 120 m and 5 N applied normal load is found to be $0.933 \text{ mm}^3/\text{m}$ for AA6061 aluminium alloy, $0.72 \text{ mm}^3/\text{m}$ for 2NC nanocomposite and $0.62 \text{ mm}^3/\text{m}$ for 2HNC hybrid nanocomposite respectively. The decrease in volumetric wear rate at 120 m sliding distance

and 5 N applied normal load is around 23% for 2NC nanocomposite and 33.9% for 2HNC hybrid nanocomposite compared to AA6061 aluminium alloy. The volumetric wear rate of materials at a sliding distance of 180 m and 5 N applied normal load is found to be 1.59 mm³/m for AA6061 aluminium alloy, 1.17 mm³/m for 2NC nanocomposite and 1.08 mm³/m for 2HNC hybrid nanocomposite respectively. The decrease in volumetric wear rate at 120 m sliding distance and 5 N applied normal load is around 26.5% for 2NC nanocomposite and 32.1% for 2HNC hybrid nanocomposite compared to AA6061 aluminium alloy.

Figure 6.31 (b) depicts the volumetric wear rate of AA6061 aluminium alloy, 2NC nanocomposite and 2HNC hybrid nanocomposite at 10 N applied normal load and abrasive grit size of 150 μ m. The volumetric wear rate of materials at a sliding distance of 60 m and 10 N applied normal load is found to be 1.17 mm³/m for AA6061 aluminium alloy, 0.884 mm³/m for 2NC nanocomposite and 0.752 mm³/m for 2HNC hybrid nanocomposite. The decrease in volumetric wear rate at 60 m sliding distance and 10 N applied normal load is around 24.4% for 2NC nanocomposite and 35.7% for 2HNC hybrid nanocomposite compared to AA6061 aluminium alloy. The volumetric wear rate of materials at a sliding distance of 120 m and 10 N applied normal load is found to be 1.44 mm³/m for AA6061 aluminium alloy, 0.953 mm³/m for 2NC nanocomposite and 0.91 mm³/m for 2HNC hybrid nanocomposite. The decrease in volumetric wear rate at 120 m sliding distance and 10 N applied normal load is around 33.8% for 2NC nanocomposite and 36.8% for 2HNC hybrid nanocomposite compared to AA6061 aluminium alloy. The volumetric wear rate of materials at a sliding distance of 180 m and 10 N applied normal load is found to be 2.21 mm³/m for AA6061 aluminium alloy, 1.58 mm³/m for 2NC nanocomposite and 1.398 mm³/m for 2HNC hybrid nanocomposite. The decrease in volumetric wear rate at 180 m sliding distance and 10 N applied normal load is around 28.5% for 2NC nanocomposite and 36.7% for 2HNC hybrid nanocomposite compared to AA6061 aluminium alloy.

Figure 6.31 (c) represents the volumetric wear rate of AA6061 aluminium alloy, 2NC nanocomposite and 2HNC hybrid nanocomposite at 15 N applied normal load and abrasive grit size of 150 μ m. The volumetric wear rate of materials at a sliding distance of 60 m and 15 N applied normal load is found to be 1.97 mm³/m for AA6061 aluminium alloy, 1.41 mm³/m for 2NC nanocomposite and 1.283 mm³/m for 2HNC hybrid nanocomposite. The decrease in volumetric wear rate at 60 m sliding distance and 15 N applied normal load

is around 28.5% for 2NC nanocomposite and 34.9% for 2HNC hybrid nanocomposite compared to AA6061 aluminium alloy. The volumetric wear rate of materials at a sliding distance of 120 m and 15 N applied normal load is found to be $2.46 \text{ mm}^3/\text{m}$ for AA6061 aluminium alloy, $1.8 \text{ mm}^3/\text{m}$ for 2NC nanocomposite and $1.55 \text{ mm}^3/\text{m}$ for 2HNC hybrid nanocomposite. The decrease in volumetric wear rate at 120 m sliding distance and 15 N applied normal load is around 26.9% for 2NC nanocomposite and 37% for 2HNC hybrid nanocomposite compared to AA6061 aluminium alloy. The volumetric wear rate of materials at a sliding distance of 180 m and 15 N applied normal load is found to be $2.77 \text{ mm}^3/\text{m}$ for AA6061 aluminium alloy, $2.14 \text{ mm}^3/\text{m}$ for 2NC nanocomposite and $1.92 \text{ mm}^3/\text{m}$ for 2HNC hybrid nanocomposite. The decrease in volumetric wear rate at 180 m sliding distance and 15 N applied normal load is around 22.7% for 2NC nanocomposite and 30.7% for 2HNC hybrid nanocomposite compared to AA6061 aluminium alloy.

Figure 6.31 (d) denotes the volumetric wear rate of AA6061 aluminium alloy, 2NC nanocomposite and 2HNC hybrid nanocomposite at 20 N applied normal load and abrasive grit size of $150 \mu\text{m}$. The volumetric wear rate of materials at a sliding distance of 60 m and 20 N applied normal load is found to be $3.1 \text{ mm}^3/\text{m}$ for AA6061 aluminium alloy, $1.79 \text{ mm}^3/\text{m}$ for 2NC nanocomposite and $1.63 \text{ mm}^3/\text{m}$ for 2HNC hybrid nanocomposite. The decrease in wear rate at 60 m sliding distance and 20 N applied normal load is around 42.3% for 2NC nanocomposite and 47.4% for 2HNC hybrid nanocomposite compared to AA6061 aluminium alloy. The volumetric wear rate of materials at a sliding distance of 120 m and 20 N applied normal load is found to be $3.73 \text{ mm}^3/\text{m}$ for AA6061 aluminium alloy, $2.184 \text{ mm}^3/\text{m}$ for 2NC nanocomposite and $2.012 \text{ mm}^3/\text{m}$ for 2HNC hybrid nanocomposite. The decrease in volumetric wear rate at 120 m sliding distance and 20 N applied normal load is around 41.5% for 2NC nanocomposite and 34.5% for 2HNC hybrid nanocomposite compared to AA6061 aluminium alloy. The volumetric wear rate of materials at a sliding distance of 180 m and 20 N applied normal load is found to be $5.69 \text{ mm}^3/\text{m}$ for AA6061 aluminium alloy, $3.68 \text{ mm}^3/\text{m}$ for 2NC nanocomposite and $3.26 \text{ mm}^3/\text{m}$ for 2HNC hybrid nanocomposite. The decrease in volumetric wear rate at 180 m sliding distance and 20 N applied normal load is around 35.3% for 2NC nanocomposite and 42.7% for 2HNC hybrid nanocomposite compared to AA6061 aluminium alloy.

From the obtained results it is observed that the volumetric wear rate increases with increase of sliding distance for all the materials i.e., AA6061 aluminium alloy, 2NC

nanocomposite and 2HNC hybrid nanocomposite. It can be seen that the addition of SiCp nano-reinforcement to AA6061 aluminium alloy matrix exhibited superior resistance to wear compared to AA6061 aluminium alloy matrix. Whereas the SiCp and graphite dual reinforced AA6061 aluminium based hybrid nanocomposite has reduced wear compared to the base alloy and 2NC nanocomposite. During dry sliding of pin on the abrasive grit paper, the wear debris is released and tends to stay in between the valleys of pin specimen and the abrasive grit paper. The two body abrasive wear tests of longer sliding distances will lead to deterioration of abrasive grits on the emery paper which are in interaction with the pin specimen. The deterioration of abrasive grits would be blunting, fracture and even particle pick up. Hence it is found that the first few minutes of sliding on fresh emery paper decides the abrasive wear mechanism of material [157].

6.4.1.4 Effect of sliding velocity

The volumetric wear rate of ultrasonically assisted casted materials is plotted as a function of sliding velocity at various applied normal loads and constant abrasive grit size of 150 μm and constant sliding distance of 180 m is shown in figure 6.32. Figure 6.32 (a) depicts the wear rate of AA6061 aluminium alloy, 2NC nanocomposite, and 2HNC hybrid nanocomposite at 5 N applied normal load. It is found that the volumetric wear rate of these materials at 0.5 m/s sliding velocity and 5 N applied normal load is 1.24 mm^3/m for AA6061 aluminium alloy, 0.81 mm^3/m for 2NC nanocomposite, and 0.35 mm^3/m for 2HNC hybrid nanocomposite. The decrement in volumetric wear rate at these similar conditions is found to be around 34.7% for 2NC nanocomposite and 71.7% for 2HNC hybrid nanocomposite. It is found that the volumetric wear rate of these materials at 1 m/s sliding velocity and 5 N applied normal load is 1.31 mm^3/m for AA6061 aluminium alloy, 0.97 mm^3/m for 2NC nanocomposite, and 0.61 mm^3/m for 2HNC hybrid nanocomposite.

The decrement in volumetric wear rate at these similar conditions is found to be around 26% for 2NC nanocomposite and 53.4% for 2HNC hybrid nanocomposite. It is found that the volumetric wear rate of these materials at 1.5 m/s sliding velocity and 5 N applied normal load is 1.43 mm^3/m for AA6061 aluminium alloy, 1.06 mm^3/m for 2NC nanocomposite, and 0.94 mm^3/m for 2HNC hybrid nanocomposite. The decrement in volumetric wear rate at these similar conditions is found to be around 26% for 2NC nanocomposite and 34.3% for 2HNC hybrid nanocomposite. It is found that the volumetric

wear rate of these materials at 2 m/s sliding velocity and 5 N applied normal load is 1.59 mm³/m for AA6061 aluminium alloy, 1.17 mm³/m for 2NC nanocomposite, and 1.1 mm³/m for 2HNC hybrid nanocomposite. The decrement in volumetric wear rate at these similar conditions is found to be around 26.4% for 2NC nanocomposite and 30.8% for 2HNC hybrid nanocomposite.

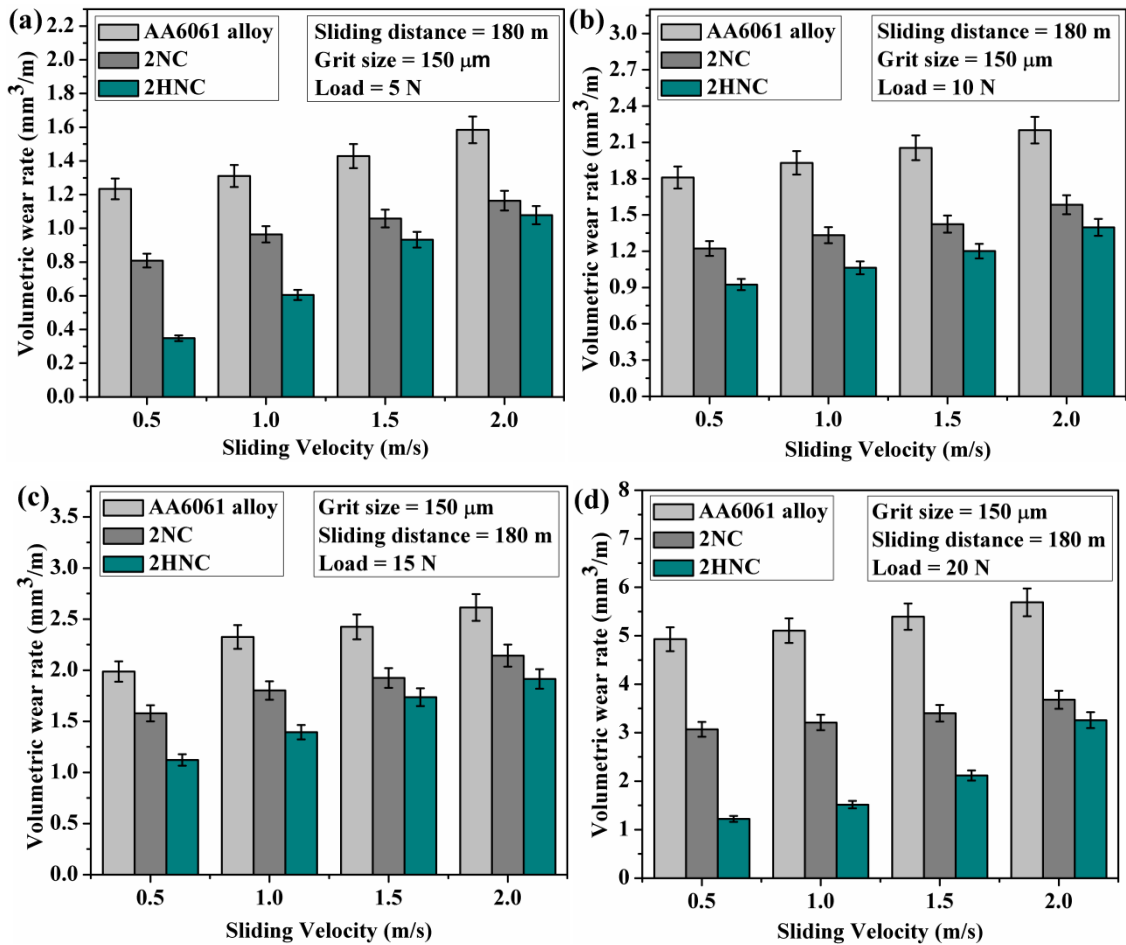


Figure 6.32: Volumetric wear rate of AA6061 aluminium alloy, 2NC nanocomposite and 2HNC hybrid nanocomposite as a function of sliding velocity (a) 5 N, (b) 10 N, (c) 15 N, and (d) 20 N

Figure 6.32 (b) represents the volumetric wear rate of AA6061 aluminium alloy, 2NC nanocomposite, and 2HNC hybrid nanocomposite at 10 N applied normal load. It is found that the volumetric wear rate of these materials at 0.5 m/s sliding velocity and 10 N applied normal load is 1.81 mm³/m for AA6061 aluminium alloy, 1.23 mm³/m for 2NC nanocomposite, and 0.93 mm³/m for 2HNC hybrid nanocomposite. The decrement in volumetric wear rate at these similar conditions is found to be around 32% for 2NC

nanocomposite and 48.62% for 2HNC hybrid nanocomposite. It is found that the volumetric wear rate of these materials at 1m/s sliding velocity and 10 N applied normal load is 1.931 mm³/m for AA6061 aluminium alloy, 1.33 mm³/m for 2NC nanocomposite, and 1.1 mm³/m for 2HNC hybrid nanocomposite. The decrement in volumetric wear rate at these similar conditions is found to be around 31% for 2NC nanocomposite and 43% for 2HNC hybrid nanocomposite. It is found that the volumetric wear rate of these materials at 1.5 m/s sliding velocity and 10 N applied normal load is 2.1 mm³/m for AA6061 aluminium alloy, 1.43 mm³/m for 2NC nanocomposite, and 1.2 mm³/m for 2HNC hybrid nanocomposite. The decrement in volumetric wear rate at these similar conditions is found to be around 31.9% for 2NC nanocomposite and 42.9% for 2HNC hybrid nanocomposite. It is found that the volumetric wear rate of these materials at 2 m/s sliding velocity and 10 N applied normal load is 2.2 mm³/m for AA6061 aluminium alloy, 1.59 mm³/m for 2NC nanocomposite, and 1.4 mm³/m for 2HNC hybrid nanocomposite. The decrement in volumetric wear rate at these similar conditions is found to be around 27.7% for 2NC nanocomposite and 36.4% for 2HNC hybrid nanocomposite.

Figure 6.32 (c) denotes the volumetric wear rate of AA6061 aluminium alloy, 2NC nanocomposite, and 2HNC hybrid nanocomposite at 15 N applied normal load. It is found that the volumetric wear rate of these materials at 0.5 m/s sliding velocity and 15 N applied normal load is 1.99 mm³/m for AA6061 aluminium alloy, 1.58 mm³/m for 2NC nanocomposite, and 1.12 mm³/m for 2HNC hybrid nanocomposite. The decrement in volumetric wear rate at these similar conditions was found to be around 20.6% for 2NC nanocomposite and 43.7% for 2HNC hybrid nanocomposite. It is found that the volumetric wear rate of these materials at 1m/s sliding velocity and 15 N applied normal load is 2.33 mm³/m for AA6061 aluminium alloy, 1.8 mm³/m for 2NC nanocomposite, and 1.4 mm³/m for 2HNC hybrid nanocomposite. The decrement in volumetric wear rate at these similar conditions is found to be around 22.8% for 2NC nanocomposite and 40% for 2HNC hybrid nanocomposite. It is found that the volumetric wear rate of these materials at 1.5 m/s sliding velocity and 15 N applied normal load is 2.43 mm³/m for AA6061 aluminium alloy, 1.93 mm³/m for 2NC nanocomposite, and 1.74 mm³/m for 2HNC hybrid nanocomposite. The decrement in wear rate at these similar conditions is found to be around 20.6% for 2NC nanocomposite and 28.4% for 2HNC hybrid nanocomposite. It is found that the volumetric wear rate of these materials at 2 m/s sliding velocity and 15 N applied normal load is

2.62 mm³/m for AA6061 aluminium alloy, 2.15 mm³/m for 2NC nanocomposite, and 1.92 mm³/m for 2HNC hybrid nanocomposite. The decrement in volumetric wear rate at these similar conditions is found to be around 18% for 2NC nanocomposite and 26.7% for 2HNC hybrid nanocomposite.

Figure 6.32 (d) represents the volumetric wear rate of AA6061 aluminium alloy, 2NC nanocomposite, and 2HNC hybrid nanocomposite at 20 N applied normal load. It is found that the volumetric wear rate of these materials at 0.5 m/s sliding velocity and 20 N applied normal load is 4.93 mm³/m for AA6061 aluminium alloy, 3.1 mm³/m for 2NC nanocomposite, and 1.22 mm³/m for 2HNC hybrid nanocomposite. The decrement in volumetric wear rate at these similar conditions is found to be around 37.1% for 2NC nanocomposite and 75.3% for 2HNC hybrid nanocomposite. It is found that the volumetric wear rate of these materials at 1 m/s sliding velocity and 20 N applied normal load is 5.1 mm³/m for AA6061 aluminium alloy, 3.2 mm³/m for 2NC nanocomposite, and 1.51 mm³/m for 2HNC hybrid nanocomposite. The decrement in volumetric wear rate at these similar conditions is found to be around 37.3% for 2NC nanocomposite and 70.4% for 2HNC hybrid nanocomposite. It is found that the volumetric wear rate of these materials at 1.5 m/s sliding velocity and 20 N applied normal load is 5.39 mm³/m for AA6061 aluminium alloy, 3.4 mm³/m for 2NC nanocomposite, and 2.12 mm³/m for 2HNC hybrid nanocomposite. The decrement in volumetric wear rate at these similar conditions is found to be around 37% for 2NC nanocomposite and 61% for 2HNC hybrid nanocomposite. It is found that the volumetric wear rate of these materials at 2 m/s sliding velocity and 20 N applied normal load is 5.69 mm³/m for AA6061 aluminium alloy, 3.68 mm³/m for 2NC nanocomposite, and 3.26 mm³/m for 2HNC hybrid nanocomposite. The decrement in volumetric wear rate at these similar conditions is found to be around 35.33% for 2NC nanocomposite and 42.7% for 2HNC hybrid nanocomposite.

From the obtained results it is observed that the volumetric wear rate increase with increase of sliding velocity for all the materials i.e., AA6061 aluminium alloy, 2NC nanocomposite and 2HNC hybrid nanocomposite. It can be seen that the addition of SiCp nano-reinforcement to AA6061 aluminium alloy matrix exhibited superior resistance to wear compared to AA6061 aluminium alloy matrix. Whereas the SiCp and graphite dual particles reinforced AA6061 aluminium based hybrid nanocomposite has reduced wear compared to the base alloy and 2NC nanocomposite. The increase of sliding velocity during dry sliding on

grit paper increases the blunting of abrasive grit particles and depth of penetration in to the specimen surface [157].

6.4.2 Wear Coefficients

The wear coefficients of AA6061 aluminium alloy, 2NC nanocomposite and 2HNC hybrid nanocomposite are represented in figure 6.33 as a function of applied normal load, sliding distance, sliding velocity and abrasive grit size. The wear coefficients are shown in figure 6.33 (a) as a function of applied normal load. It is noticed that the wear coefficients decreased from 5 N to 15 N and increased for 20 N applied normal load for all tested materials. It would be attributed due to the higher depth of penetration in to the nanocomposite pin surface at higher load and sliding distance. Similar trends were observed in the previous studies mentioned by Sawla [158] and Kaushik et al. [141].

The wear coefficients are shown in figure 6.33 (b) as a function of abrasive grit size. It is noticed that the wear coefficients of AA6061 aluminium alloy, 2NC nanocomposite and 2HNC hybrid nanocomposite increased with increase of abrasive grit size at all conditions. The wear coefficients are represented in figure 6.33 (c) as a function of sliding distance. It can be seen that the wear coefficients of materials decreased with increase of sliding distance. The wear coefficients of AA6061 aluminium alloy, 2NC nanocomposite and 2HNC hybrid nanocomposite materials is shown in figure 6.33 (d) as a function of sliding velocity. It is observed that the wear coefficients of the AA6061 aluminium alloy, 2NC nanocomposite and 2HNC hybrid nanocomposite decreased with increase of sliding velocity. It is found that the wear coefficient of 2NC nanocomposite is larger than the base alloy and 2HNC hybrid nanocomposite. The wear coefficients of AA6061 aluminium alloy, 2NC nanocomposite and 2HNC hybrid nanocomposite decreased with increase of applied normal load up to 15 N and then increased.

The wear coefficient decreased with increase of sliding distance and sliding velocity for all materials. It is due to the hardness of the SiCp reinforced nanocomposite materials that dominated the abrasive wear coefficients. Observed trend is according to the Archard's wear equation given in equation (6.3) as follows.

$$K = \frac{Q_v/lH_m}{L} \quad (6.3)$$

where, ' $Q_{v/l}$ ' is the volume loss per unit sliding distance (mm^3/m), ' H_m ' is the hardness of the material surface (N/mm^2), ' L ' is the applied load (N) and ' K ' is the dimensionless wear coefficient less than unity. But in case of the 2HNC hybrid nanocomposite, hardness is lower than 2NC nanocomposite.

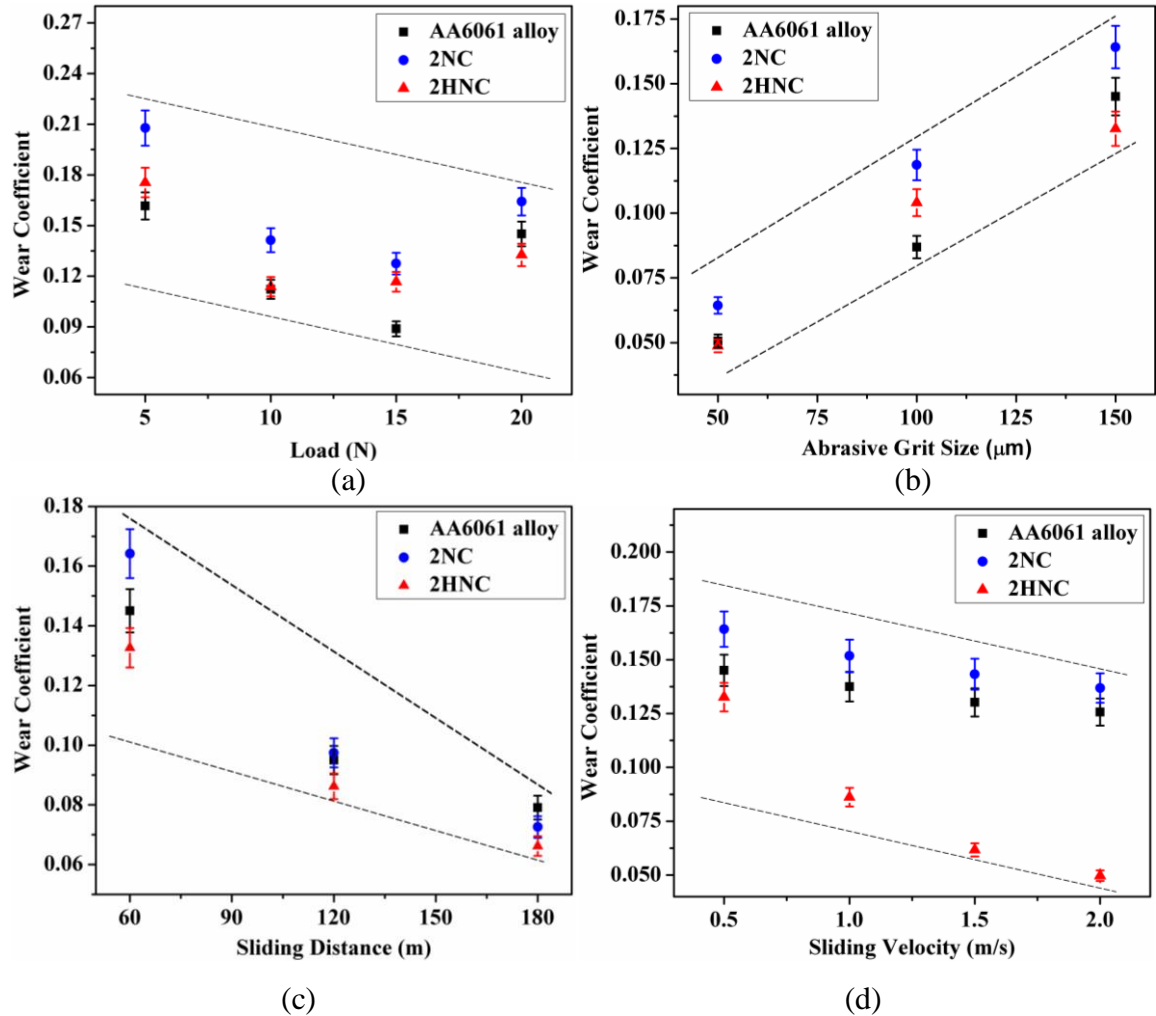


Figure 6.33: Wear coefficient of AA6061 aluminium alloy, 2NC nanocomposite and 2HNC hybrid nanocomposite as a function of (a) applied normal load, (b) abrasive grit size, (c) sliding distance and (d) sliding velocity

It is further noticed that the wear coefficients of the 2HNC hybrid nanocomposite i.e., formation probability of wear particle is found to be lower than AA6061 aluminium alloy matrix. This would be attributed to 2NC nanocomposite surface being protected by reducing the material plastic flow by SiCp nano-reinforcements and self-lubricating layer formed by graphite nano-reinforcement [159-161].

At lower applied normal loads, the higher wear coefficients indicate that the probability of formation of wear particle could be mainly due to crack nucleation and its propagation in to micro level crack even though the level of depth of penetration of abrasive grit is low. But at higher applied normal loads the level of depth of penetration of abrasive grit particle will be more and increases the material removal rate with higher plastic deformation [117, 160]. At higher loads, it can be noted that the asperities formed during abrasive wear process could be due to fragmentation either from the pin surface or counter surface. These hard asperities consist of abrasive grit particles present on the counter surface that penetrate deeper into the softer pin surface in the very initial stages of the abrasive wear. The grit particles itself act as a micro cutting tool when it approaches the pin surface and it depends on the orientation of abrasive grit particles bonded over the grit paper.

6.4.3 Worn Surface Analysis

6.4.3.1 Pin Specimen

Figures 6.34 and 6.35 shows the worn surfaces of AA6061 aluminium alloy, 2NC nanocomposite, and 2HNC hybrid nanocomposite pin tested on abrasive grit paper of size 50 μm , 100 μm , and 150 μm at 5 N and 20 N of applied normal load respectively, at sliding distance of 180 m and sliding velocity of 2 m/s. The worn surfaces of AA6061 aluminium alloy at lower load and lower grit paper size reveals long narrow cracks (denoted as A) on the worn surface and more plastic deformation. At higher load and lower grit size it reveals higher depth of penetration and more plastic deformation on the worn surface of pin material. The extended lips and craters are observed in the abrasive grit sliding direction. The pin surface of base alloy is more damaged with higher depth of penetration in case of larger grit size. More the depth of penetration, less is the wear resistance of pin material and hence increases the wear rate. It is observed that the fractured abrasive grit particles displacement on the material is vertical to the abrasive grit paper sliding direction when tested on 100 μm size abrasive grit paper. It can be seen that the parallel grooves with higher depth of penetration in the sliding direction are observed on the worn surface during the abrasion process when tested on 150 μm size abrasive grit paper. In case of 2NC nanocomposite it is found that the depth of penetration of abrasive grit particles into the pin material is less compared to the matrix material at lower load and lower grit size.

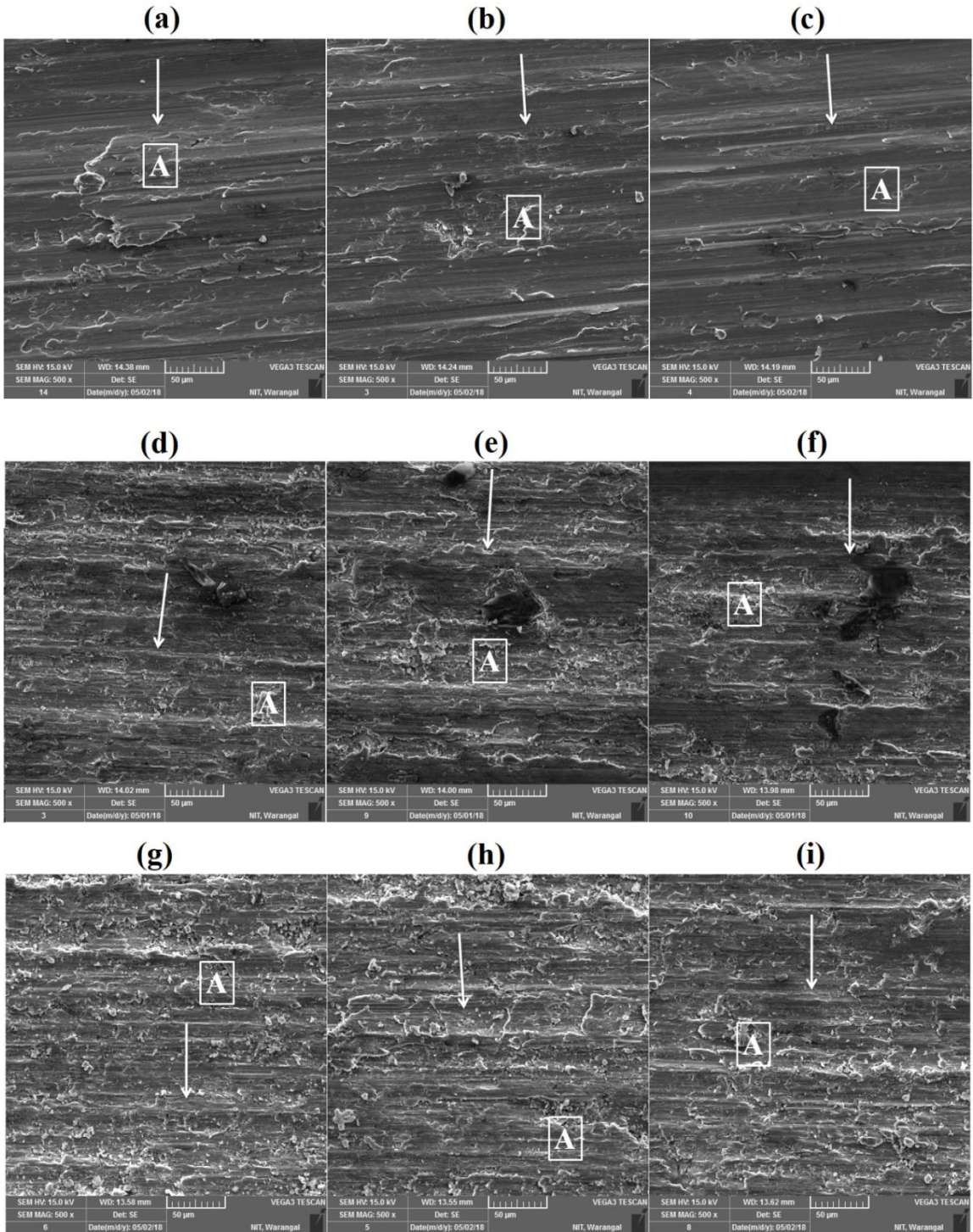


Figure 6.34: Worn surface of pin materials tested on abrasive grit papers at 5 N applied normal load (a) AA6061 alloy at grit size of $50\text{ }\mu\text{m}$, (b) AA6061 alloy at grit size of $100\text{ }\mu\text{m}$, (c) AA6061 alloy at grit size of $150\text{ }\mu\text{m}$, (d) 2NC at grit size of $50\text{ }\mu\text{m}$, (e) 2NC at grit size of $100\text{ }\mu\text{m}$, (f) 2NC at grit size of $150\text{ }\mu\text{m}$, (g) 2HNC at grit size of $50\text{ }\mu\text{m}$, (h) 2HNC at grit size of $100\text{ }\mu\text{m}$, and (i) 2HNC at grit size of $150\text{ }\mu\text{m}$

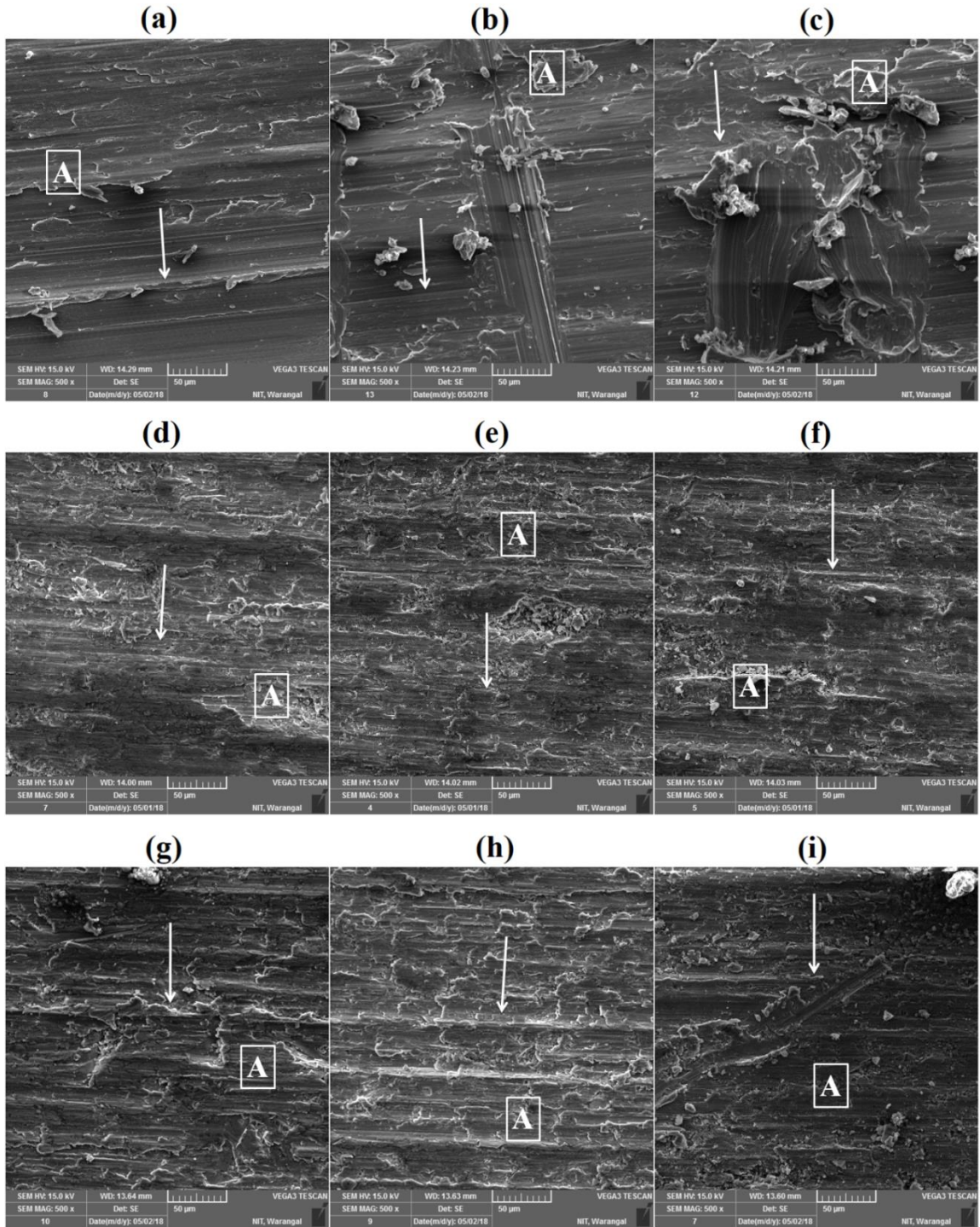


Figure 6.35: Worn surface of pin materials tested on abrasive grit papers at 20 N applied normal load (a) AA6061 alloy at grit size of 50 μm , (b) AA6061 alloy at grit size of 100 μm , (c) AA6061 alloy at grit size of 150 μm , (d) 2NC at grit size of 50 μm , (e) 2NC at grit size of 100 μm , (f) 2NC at grit size of 150 μm , (g) 2HNC at grit size of 50 μm , (h) 2HNC at grit size of 100 μm , and (i) 2HNC at grit size of 150 μm

It is because of the resistance force offered by the hard SiCp nano-reinforcement particles in the matrix. It can be seen that the shallower scratches on the nanocomposite worn surface are observed when tested on lower abrasive grit particle size. Long narrow cracks with lower depth of penetration are observed when tested on lower abrasive grit paper at higher load for nanocomposite. The worn surface of nanocomposite tested on 100 μm abrasive grit size showed fine grooves along the wear track at lower load and the long narrow cracks with higher depth of penetration at higher load. Circular grooves with higher depth of penetration are found when tested on higher abrasive grit paper size at higher load. The depth of penetration of nanocomposite is less compared to the base alloy due to presence of hard SiCp nano-reinforcement particles in the matrix.

It is found that the 2HNC hybrid nanocomposite exhibited smoother worn surfaces compared to the matrix material and 2NC nanocomposite tested on lower grit size at lower load. The depth of penetration is less in case of hybrid nanocomposite. It can be seen that the circular cracks with lower depth of penetration are present on worn surface when tested on lower abrasive grit paper at higher load. It is noticed to have longer smooth scratches on the abrasive worn surface in case of 100 μm abrasive grit paper at lower load and the hallow cracks with higher depth of penetration at higher load. Longer smooth scratches are present on the abrasive worn surface tested on higher abrasive grit size at lower load and long scratches are present with higher depth of penetration at higher load. It is found that the depth of penetration is more at higher grit size compared to lower grit size. The depth of penetration is less compared to the base alloy and 2NC nanocomposite because of the presence of hard SiCp nano-reinforcement and self lubricating nano graphite particles in the matrix.

For 2HNC hybrid nanocomposite graphite film could have been formed on the pin surface and expected to act as a solid lubricating layer on the pin surface [142]. The fractured abrasive grit particles are scratched perpendicular to the sliding direction on the pin surface during abrasion process. Initially the thin graphite layer chip away from the pin surface and later primary reinforcement SiCp takes lead in bearing the applied normal load on pin. This could be a reason for improving the wear resistance of the hybrid nanocomposites. It is observed that better wear properties are achieved by reinforcing graphite powder in case of 2HNC hybrid nanocomposite.

6.4.3.2 Abrasive grit paper

The SEM micrographs of worn surfaces of abrasive grit papers of sizes 50 μm , 100 μm , and 150 μm tested on AA6061 aluminium alloy, 2NC nanocomposite, and 2HNC hybrid nanocomposite at 5 N and 20 N applied normal load are represented in figures 6.36 and 6.37 respectively. It is noticed that the abrasive particles are debonded from the abrasive grit paper and fractured (denoted as PF) during abrasive wear process. The abrasive grit particle would be getting less sharp (blunting) during the abrasion process (denoted as BG). There is presence of the debris (denoted as DR) on the abrasive grit worn surfaces and particle pick up (denoted as P) from the worn surfaces of abrasive grit papers tested on AA6061 aluminium alloy at 5 N and 20 N applied normal load.

Particle pick up, fractured abrasive grit particles, blunting of abrasive grit particles, and lower size debris are observed on the abrasive worn surface. In this case the particle pick up and blunting of abrasive grit particles are more because of deterioration of abrasive grit particles rapidly during the abrasion process [157]. The depth of penetration is low at lower load and high at higher load. This would result in less wear rate for smaller size abrasive grits. From the worn surfaces of abrasive grit papers tested on 2NC nanocomposite, it is noticed that at lower load and 50 μm abrasive grit paper, blunting of abrasive grit particles, particle pick up, and fractured abrasive grit particles are observed. At higher load and 50 μm abrasive grit paper, major grit particles are fractured with introduction of cracks on the worn surface. It is observed that the abrasive grit particle pick-up, large quantity of grit particles are fractured, and more cracks are found on abrasive grit paper for both lower and higher load when tested on 100 μm abrasive grit paper. In case of 150 μm abrasive grit paper tested at lower load and higher load reveals that the abrasive grit particle pick-up and large quantity of grit particles are fractured. In this case the larger size abrasive grit particle tends to more penetration into the pin material. During abrasion process at some time the orientation of grit particle changes which tends to decrease in the wear resistance of the abrasive grit paper. As abrasive grit size increases, depth of penetration into the pin material during abrasion process is more, which decreases the wear resistance of the pin material. Presence of hard SiC nano-reinforcement particles in the matrix bear the load offered by the abrasive grit particles and result in more damage of abrasive grit particles.

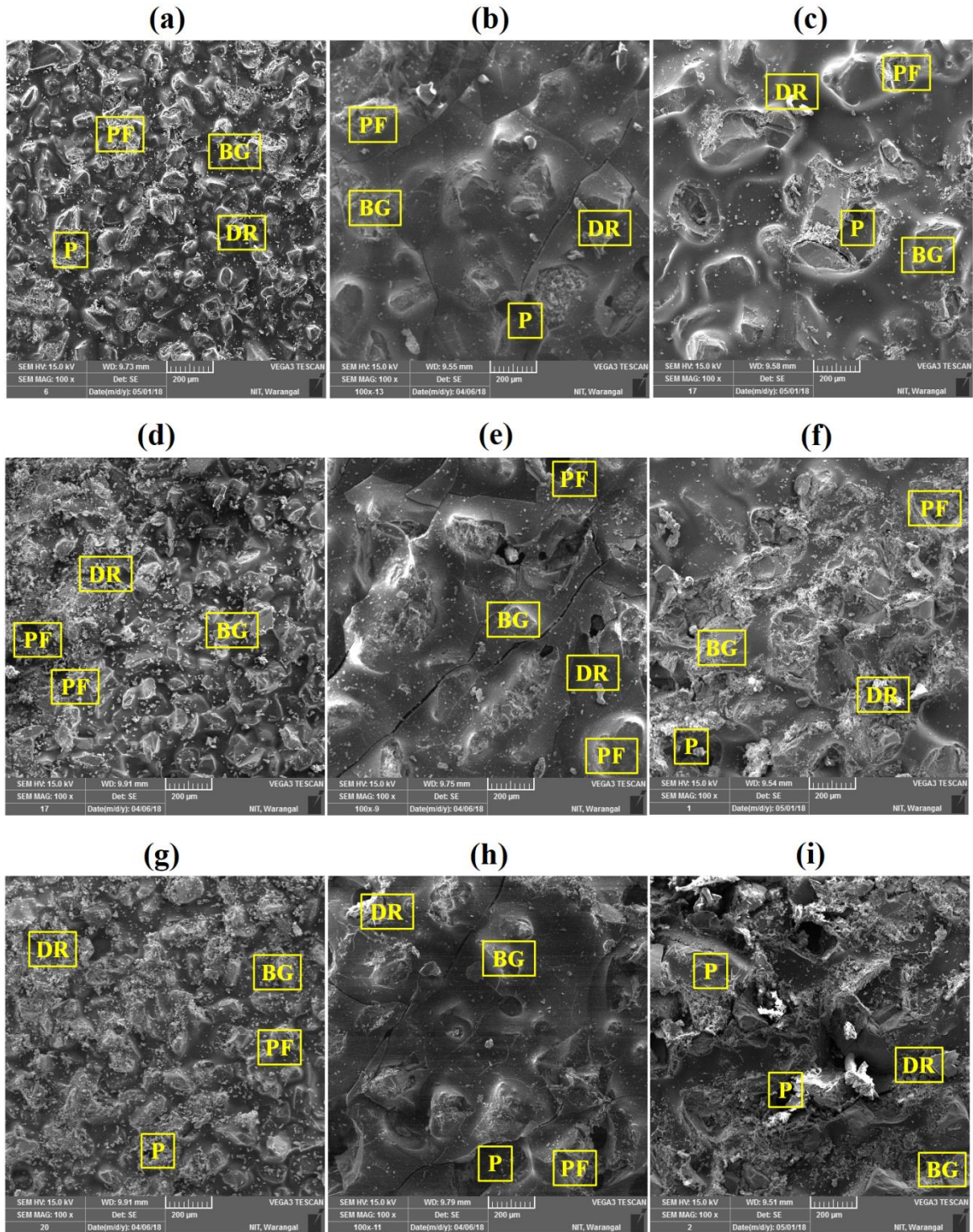


Figure 6.36: Worn surface of abrasive grit papers tested at 5 N applied normal load. AA6061 alloy tested on (a) 50 μm size grit paper, (b) 100 μm size grit paper, and (c) 150 μm size grit paper. 2NC nanocomposite tested on (d) 50 μm size grit paper, (e) 100 μm size grit paper, and (f) 150 μm size grit paper. 2HNC hybrid nanocomposite tested on (g) 50 μm size grit paper, (h) 100 μm size grit paper, and (i) 150 μm size grit paper

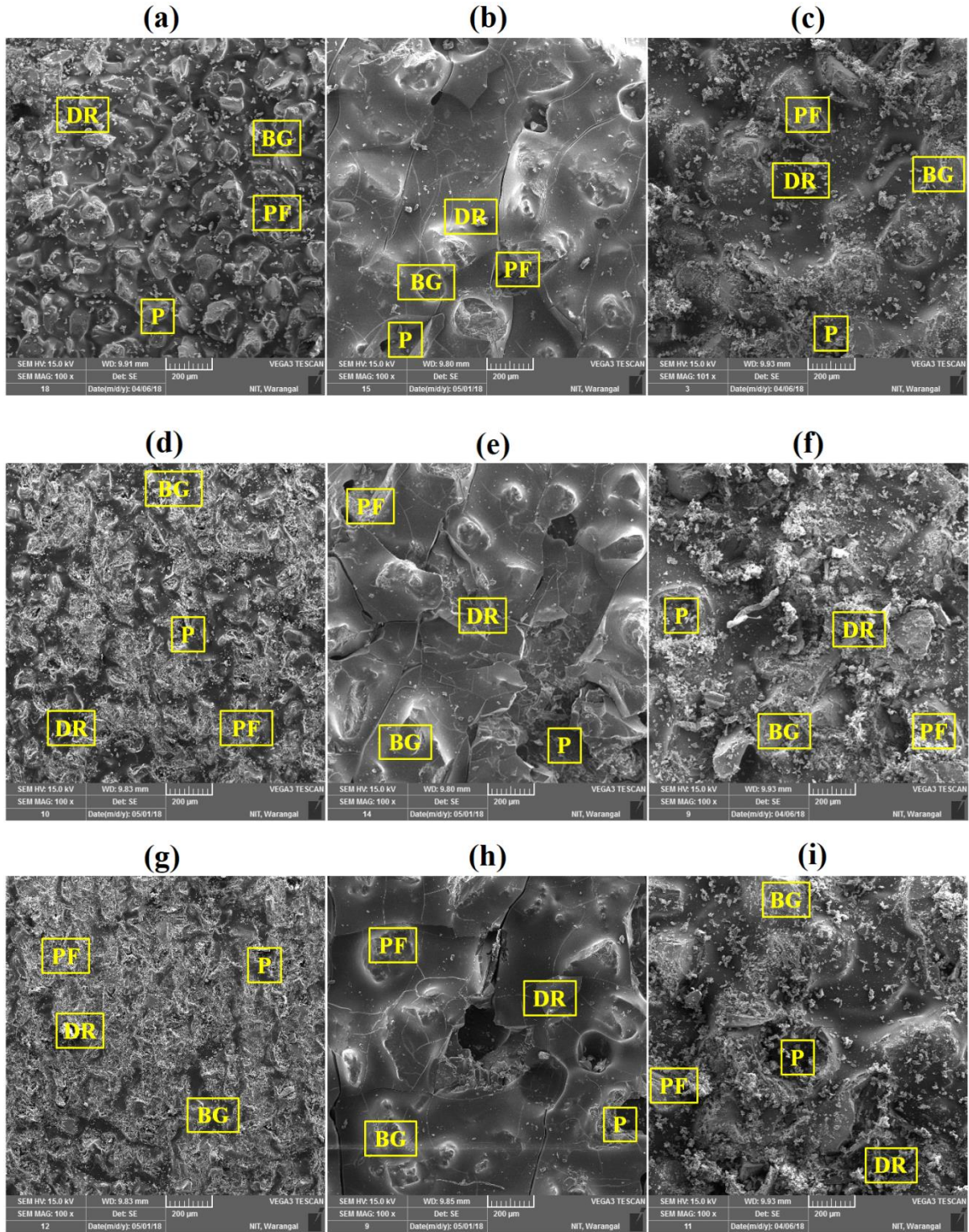


Figure 6.37: Worn surface of abrasive grit papers tested at 20 N applied normal load. AA6061 alloy tested on (a) 50 μm size grit paper, (b) 100 μm size grit paper, and (c) 150 μm size grit paper. 2NC nanocomposite tested on (d) 50 μm size grit paper, (e) 100 μm size grit paper, and (f) 150 μm size grit paper. 2HNC hybrid nanocomposite tested on (g) 50 μm size grit paper, (h) 100 μm size grit paper, and (i) 150 μm size grit paper

The worn surfaces of abrasive grit papers tested on 2HNC hybrid nanocomposite shows the blunting of abrasive grit particles, particle pick up, and fractured of abrasive grit particles with 50 μm abrasive grit at lower and higher load. More cracks are observed on 100 μm abrasive grit paper at minimum and maximum applied load. The abrasive grit particle pick-up and large quantity of grit particles are fractured at lower load and higher load on 150 μm abrasive grit surface. In this case the abrasive grit particle size is more and tend to penetration in to the pin material. The presence of reinforcement particles in the pin material resist the load and tend to fracture the grit particles on the abrasive grit paper. The applied normal load, SiCp and graphite nano-reinforcements in the matrix increases, the particle pick up also increases. This is due to the increase of stress concentration levels at the contact of pin surface and the abrasive grit paper. For higher applied normal loads on pin material and for larger abrasive grit sizes, the depth of penetration of pin material would be more and causes severe damage to the pin surface. However, the depth of penetration trend on abrasion grit papers is increasing with the addition of SiCp and graphite nano-reinforcements in the matrix. The abrasion wear debris is increasing with the increase of applied normal load and reinforcement particles in the matrix. The abrasion wear resistance is more in case of hybrid nanocomposites due to the presence of hard SiCp and graphite nano-reinforcement particles in the matrix compared to the AA6061 aluminium alloy.

6.4.4 Wear Debris

Figures 6.38 and 6.39 represents the SEM micro graphs of wear debris collected after abrasion wear process at 5 N and 20 N applied normal load respectively tested on abrasive paper grit size of 50 μm , 100 μm , and 150 μm . The area noted as 'CR' specifies the chips removed from pin material and the area 'GF' indicates the abrasive grit particle fractured or separated from the abrasive grit paper. The wear debris produced from AA6061 aluminium alloy pin material on 50 μm and 100 μm abrasive grit paper are large continuous chips with fractured grit particles at lower load and higher load. Discontinuous chips are produced from base alloy tested on 150 μm abrasive grit paper at lower load and higher load. The wear debris produced from 2NC nanocomposite pin are smaller in size on 50 μm abrasive grit paper with fractured abrasive grit particles at lower load and major fracture at higher load. The wear debris produced from nanocomposite are larger size continuous chips with fractured grit particles tested on 100 μm at lower load. These debris are related with higher number of microcracks which looks like card deck type.

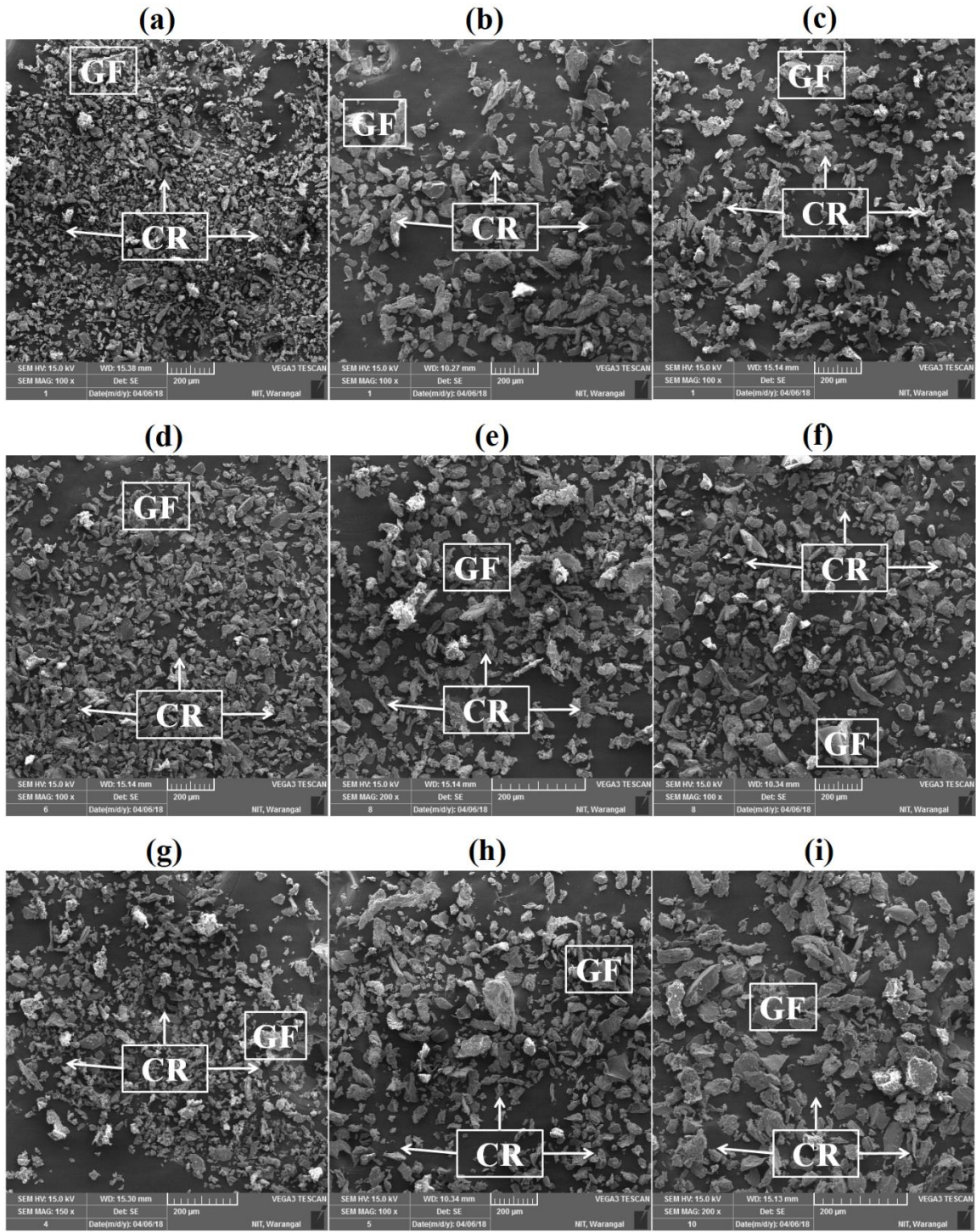


Figure 6.38: SEM micrographs of various wear debris collected after abrasion process. AA6061 alloy tested at 5 N (a) 50 μm size grit paper, (b) 100 μm size grit paper, and (c) 150 μm size grit paper. 2NC nanocomposite tested at 5 N (d) 50 μm size grit paper, (e) 100 μm size grit paper, and (f) 150 μm size grit paper. 2HNC hybrid nanocomposite tested at 5 N (g) 50 μm size grit paper, (h) 100 μm size grit paper, and (i) 150 μm size grit paper

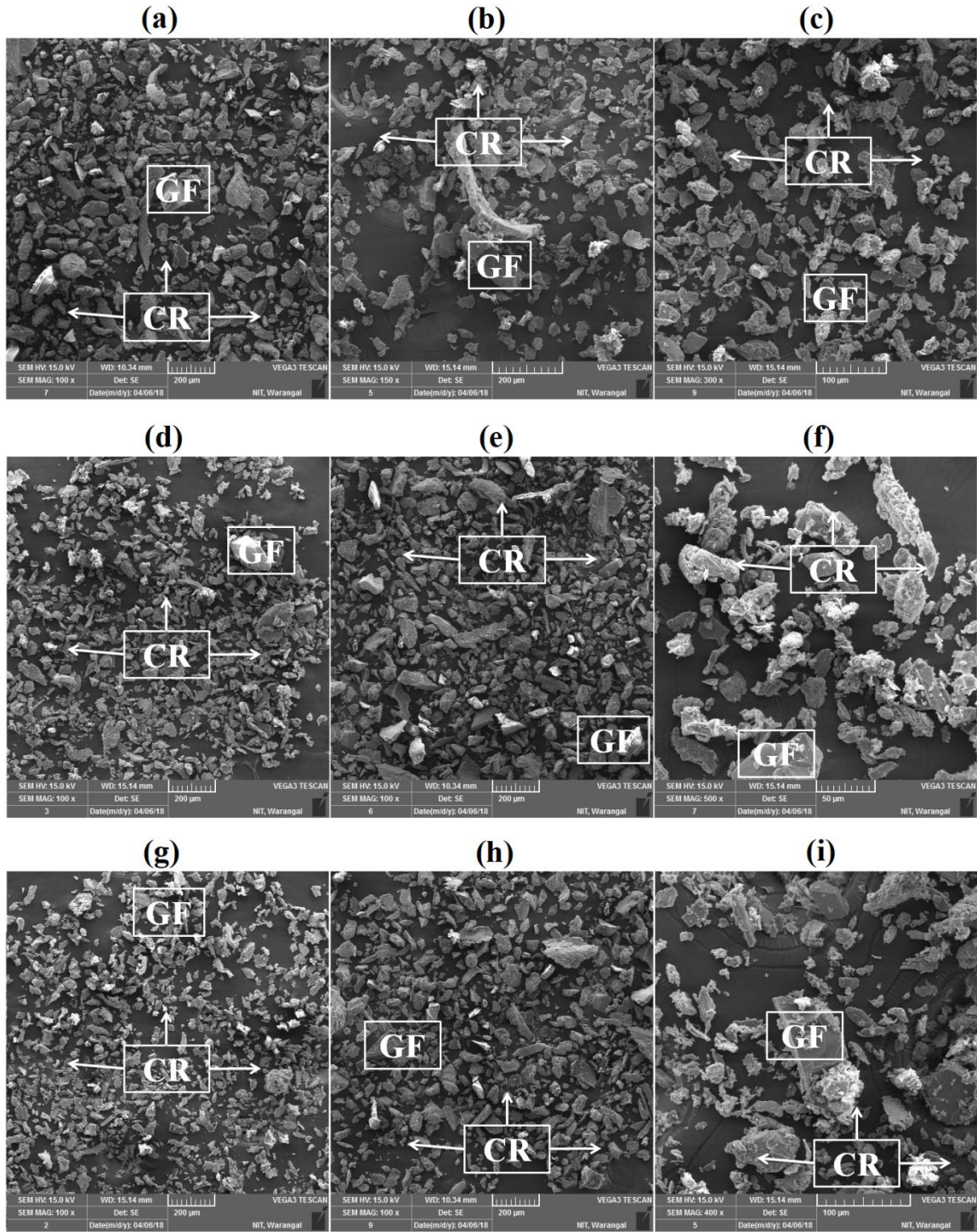


Figure 6.39: SEM micrographs of various wear debris collected after abrasion process. AA6061 alloy tested at 20 N (a) 50 μm size grit paper, (b) 100 μm size grit paper, and (c) 150 μm size grit paper. 2NC nanocomposite tested at 20 N (d) 50 μm size grit paper, (e) 100 μm size grit paper, and (f) 150 μm size grit paper. 2HNC hybrid nanocomposite tested at 20 N (g) 50 μm size grit paper, (h) 100 μm size grit paper, and (i) 150 μm size grit paper

The wear debris produced from nanocomposite are larger size continuous chips with more fractured abrasive grit particles when tested on 100 μm abrasive grit paper at higher load. The discontinuous chips with more fractured abrasive grit particles are produced from nanocomposite tested on 150 μm abrasive grit paper at lower and higher load. The wear debris of 2HNC hybrid nanocomposite pin produces more number of fractured abrasive grit particles of tiny size when tested on 50 μm abrasive grit paper at lower load and higher load. The discontinuous chips with major amount of fractured abrasive grit particles are produced on 100 μm and 150 μm abrasive grit paper at lower load and higher load. It is found that with the increase of nano-reinforcements in the matrix alloy, the wear debris size decreases and there is increase of fractured abrasive grit particles. The increase of abrasive grit particle size and applied normal load, the chip size decreases with increase of fractured abrasive grit particles or dispersoids.

6.4.5 Coefficient of Friction

Coefficient of friction of AA6061 aluminium alloy, 2NC nanocomposite and 2HNC hybrid nanocomposite are shown in figure 6.40 (a) as a function of applied normal loads. It is observed that the coefficient of friction values decreased with rise of applied normal loads on pin irrespective of material. Figure 6.40 (b) represents the coefficient of friction values of AA6061 aluminium alloy, 2NC nanocomposite and 2HNC hybrid nanocomposite as a function of abrasive grit particle size. It is observed that from figure 6.40 (b) the coefficient of friction decreased with rise of abrasive grit particle size irrespective of material. The decrease in coefficient of friction values is observed with increase of abrasive grit particle size due to higher depth of penetration in a short duration of time. Figure 6.40 (c) depicts the coefficient of friction values of AA6061 aluminium alloy, 2NC nanocomposite and 2HNC hybrid nanocomposite as a function of sliding velocity. It is observed that the coefficient of friction decreased with increase of sliding velocity irrespective of material. The decrease in coefficient of friction values is due to the rise of depth of penetration into the material. The coefficient of friction values of 2HNC hybrid nanocomposite increases with increase of sliding velocity. It would be attributed due to the lower depth of penetration and solid lubricating effect of graphite. Figure 6.40 (d) depicts the coefficient of friction values of AA6061 aluminium alloy, 2NC nanocomposite and 2HNC hybrid nanocomposite as a function of sliding distance. It is observed that the coefficient of friction values decrease with increase of sliding distance. It would be attributed due to the introduction of more hard

asperities in between the nanocomposite pin and abrasive grit paper. The slight increase of coefficient of friction value was observed in the case of 2NC nanocomposite compared to the 2HNC hybrid nanocomposite and AA6061 aluminium alloy. The presence of the SiCp nano-reinforcements also increase the hardness of the nanocomposite and it is difficult to cut down the picks of roughness, thus it is expected to have more abrasion wear mechanism.

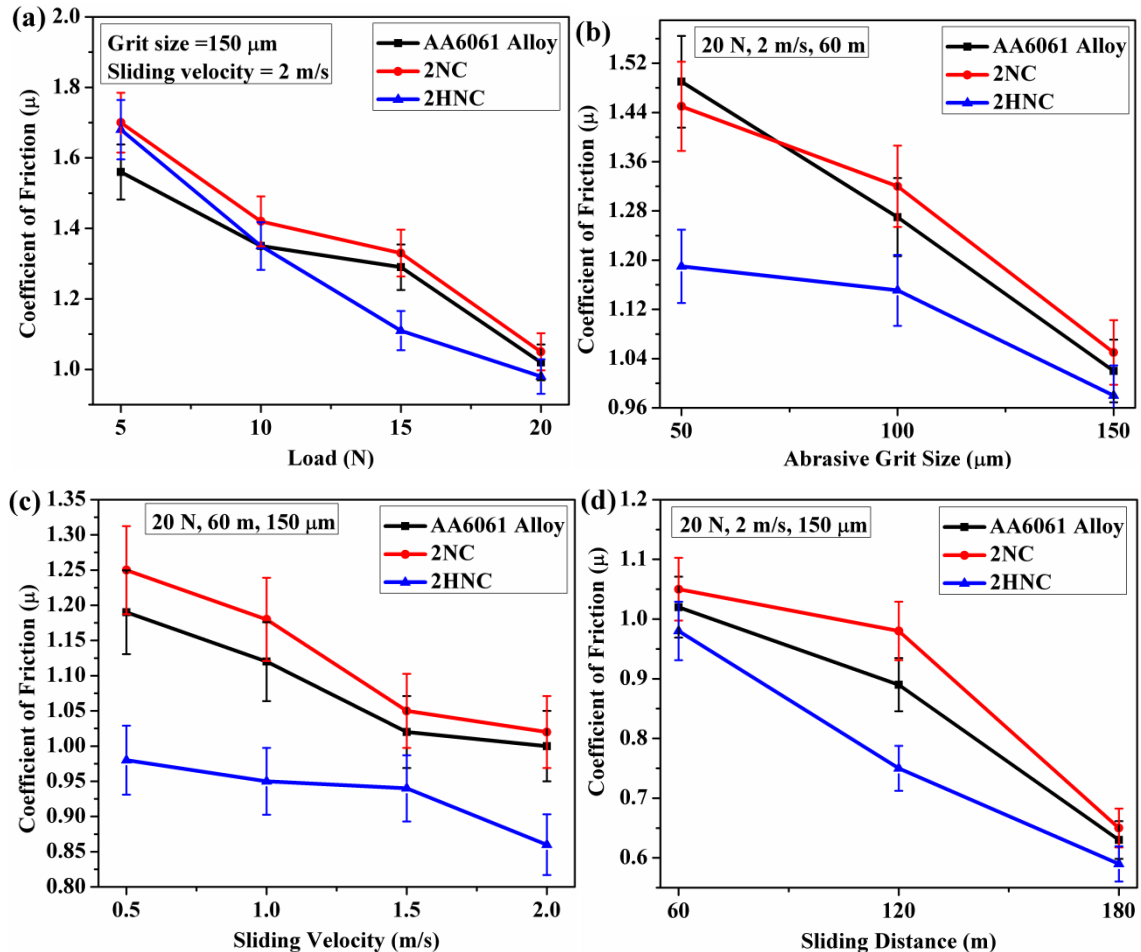


Figure 6.40: Coefficient of friction of AA6061 aluminium alloy, 2NC nanocomposite and 2HNC hybrid nanocomposite tested abrasive grit paper (a) applied normal load, (b) abrasive grit size, (c) sliding velocity and (d) sliding distance

Therefore, it is expected to have less adhesion and more abrasion wear mechanism between the nanocomposite pin and abrasive grit paper. The abrasive grits penetrate more into the nanocomposite pin and increases the coefficient of friction value of 2NC nanocomposite [162]. The decrease in coefficient of friction value of 2HNC hybrid nanocomposite is due to the load bearing effect of SiCp and solid lubricating effect of graphite [153]. The exhibited results shown in figure 6.46 reveals that the lower friction

coefficient is observed for 2HNC hybrid nanocomposite compared to all materials. The increase in coefficient of friction of 2NC nanocomposite compared to AA6061 aluminium alloy for 150 μm , 100 μm , and 50 μm abrasive grit sizes at 20 N, 2 m/s sliding velocity, and 60 m sliding distance is 5%, 4%, and 2.6% respectively.

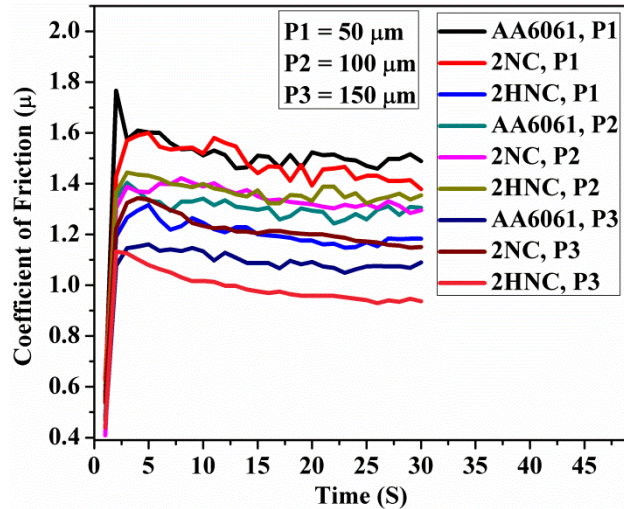


Figure 6.41: Coefficient of friction of AA6061 aluminium alloy, 2NC nanocomposite and 2HNC hybrid nanocomposite tested abrasive grit papers of sizes 150 μm , 100 μm , and 50 μm as a function of sliding duration

The reduction in coefficient of friction of 2HNC hybrid nanocomposite compared to AA6061 aluminium alloy for 150 μm , 100 μm and 50 μm abrasive grit sizes at 20 N, 2 m/s sliding velocity, and 60 m sliding distance is 4%, 11.8%, and 18% respectively. The presence of graphite solid lubricant in the hybrid nanocomposite improved the friction stability which was evident from figures 6.40 and 6.41. The coefficient of friction was low for the 2HNC hybrid nanocomposite even at higher applied normal loads as compared to that of 2NC nanocomposite and AA6061 aluminium alloy, suggesting the good sliding stability on abrasive grit paper.

6.4.6 Wear Mechanism

The two body abrasive wear mechanisms of the 2HNC hybrid nanocomposite are defined by sliding velocity and normal loads. In the present test conditions, various groups of mechanisms are found to be gradual and the boundaries on the diagram are approximate (figure 6.42). It is observed that smaller scratches, delamination and abrasive wear

mechanism are noticed at applied normal loads below 15 N and with respect to sliding velocity.

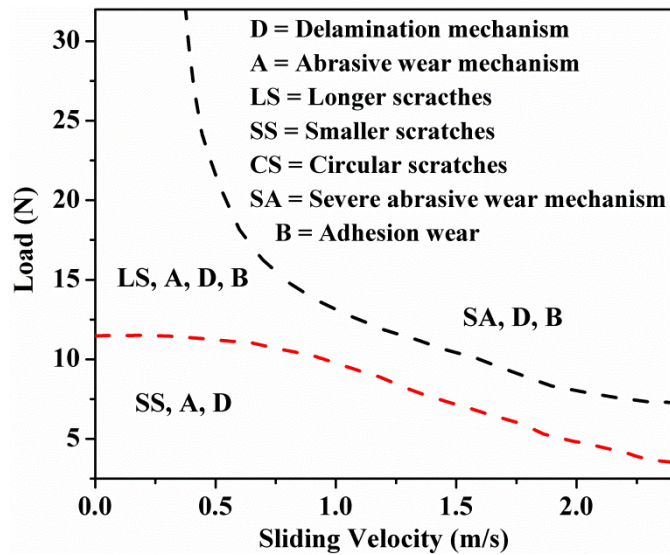


Figure 6.42: Two body abrasive wear mechanism of the 2HNC hybrid nanocomposite is drawn at various conditions and with approximate boundaries in the present study

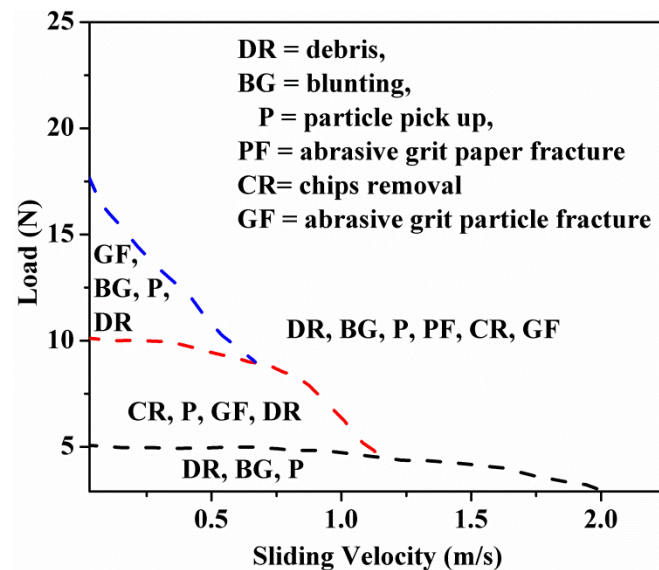


Figure 6.43: The mechanism of abrasive grit particle removal on 150 μm abrasive grit paper is drawn at various conditions and with approximate boundaries in the present study tested on 2HNC hybrid nanocomposites

It reveals longer scratches, lower adhesion wear, delamination and higher abrasive wear mechanism at applied normal loads above 15 N and lower sliding velocity. It is observed that the circular scratches, delamination and severe abrasive wear mechanism are

noticed at higher applied normal loads and sliding velocities. The mechanism of abrasive grit particle removal on 150 μm abrasive grit paper is drawn at various conditions and with approximate boundaries in the present study as shown in figure 6.43.

In the present test conditions, the abrasive grit particle removal mechanisms are found to be gradual and the boundaries on the diagram are approximate (figure 6.43). It is observed that the debris, blunting and particle pick up are found at 2 m/s sliding velocity below 5 N applied normal load. It is observed that the debris, chips, abrasive grit particle fracture and particle pick up are noticed at applied normal load below 10 N and 1 m/s sliding velocity. It reveals that the fractured abrasive grit particle, blunting, particle pick up and debris are observed at applied normal load above 10 N and below sliding velocity 1.75 m/s. It is observed that the debris, blunting, particle pick up, fractured abrasive grit particles, chips removal and fracture of abrasive grit paper are noticed at applied normal loads above 15 N with increase of sliding velocity.

6.5 Summary

The dry sliding wear behaviour of AA6061 aluminium alloy, 0.5NC, 1NC, 1.5NC and 2NC nanocomposite, 0.5HNC, 1HNC, 1.5HNC, 2HNC, and 3HNC hybrid nanocomposites on EN31 steel counter face is studied. The higher wear resistance and wear coefficient is obtained for 2NC nanocomposite among all nanocomposites. The lower wear rate, higher wear resistance and lower wear coefficient is obtained for 2HNC hybrid nanocomposites compared to all nanocomposites. The coefficient of friction values were higher for 2NC nanocomposites compared to all materials. The lower coefficient of friction values are obtained for 2HNC hybrid nanocomposite compared to all materials. In case of two body abrasive wear, the lower coefficient of friction values and higher wear rate are obtained for higher grit size. The wear resistance is higher for 2HNC hybrid nanocomposite in case of two body abrasive wear compared to all materials. It can be seen that the lower depth of penetration and MML with SiCp and graphite nano-reinforcements in the contact profile of 2HNC hybrid nanocomposite are observed. It is due to the strengthening effect of SiCp nanoparticles and graphite solid lubricants effect. The worn surfaces revealed severe oxidation, deeper grooves and abrasive wear mechanism at higher applied normal loads and higher sliding velocities. The size of wear debris reduces with increase of graphite nano-reinforcements in the matrix. In case of two body abrasive wear, the size of wear debris

increases with increase of abrasive grit particle size and applied normal loads on nanocomposites pin.

Chapter 7

Conclusions and Future Scope

In this chapter, the overall conclusions are drawn and future scope of research work is briefly reported.

7.1 Conclusions

The AA6061 aluminium alloy, 0.5NC, 1NC, 1.5NC, and 2NC nanocomposites and 0.5HNC, 1HNC, 1.5HNC, 2HNC, and 3HNC hybrid nanocomposites are successfully fabricated through ultrasonic assisted stir casting process. Summary of the research work observed from the present study is:

- The results proved that microstructures are greatly refined with the addition of SiCp and graphite nano-reinforcement particles. The average grain size of AA6061 aluminium alloy is 120 μm . The optical micrographs reveal the variation of grain size i.e., 47 μm for 2NC, 42 μm for 0.5HNC, 35 μm for 1HNC, 25 μm for 1.5HNC, 20 μm for 2HNC, 15 μm for 3HNC respectively. The reduction of average grain size compared to base alloy is 58% for 2NC, 65% for 0.5HNC, 71% for 1HNC, 79% for 1.5HNC, 83% for 2HNC, 88% for 3HNC respectively.
- The SEM micrographs of 0.5HNC, 1HNC, 1.5HNC, 2HNC, and 3HNC hybrid nanocomposites revealed the SiCp and graphite nano-reinforcement particles in the matrix. Small clusters appeared in the microstructure with rise of graphite quantity in the matrix.

- The phase analysis through XRD for 2NC nanocomposite has revealed smaller intensity SiCp peaks. The phase analysis by XRD for 0.5HNC, 1HNC, 1.5HNC, 2HNC, and 3HNC hybrid nanocomposites observed the smaller intensity peaks of carbon and SiCp. The intensity of peak is lower for C and SiCp due to its lower content in the matrix.
- The microhardness of 2NC, 0.5HNC, 1HNC, 1.5HNC, 2HNC, and 3HNC hybrid nanocomposites are 91 ± 4 HV, 89 ± 2 HV, 87 ± 3 HV, 85 ± 2 HV, 83 ± 3 HV, and 76 ± 4 HV respectively. The enhancement of microhardness of hybrid nanocomposites compared to the base alloy is 78% for 2NC, 71% for 0.5HNC, 67% for 1HNC, 64% for 1.5HNC, 60% for 2HNC, and 46% for 3HNC respectively. It is observed that there is decrease in microhardness with increase in wt. % of graphite in the matrix.
- The yield strength increased by 206% for 2NC, 209% for 0.5HNC, 218% for 1HNC, 227% for 1.5HNC, 240% for 2HNC and 173% for 3HNC hybrid nanocomposites compared to base alloy. The results specify that the ultimate tensile strength increased by 77.7% for 2NC, 76% for 0.5HNC, and 64% for 1HNC, 57% for 1.5HNC, 49% for 2HNC and 33% for 3HNC hybrid nanocomposites compared to base alloy.
- The Orowan strengthening effect and thermal dislocation mismatch density effect is found to play a significant role in the metal matrix nanocomposites. The contribution of thermal mismatch effect is larger than the other mechanisms with respect to the reinforcement particle size.
- As the size of the nano-reinforcement particles decreased from 100 nm to 1 nm the contribution of thermal mismatch strengthening factor $f_{\Delta CTE}$ increased monotonically. The contribution of Orowan strengthening factor f_{Orowan} increased up to a critical size of 1.56 nm for AA6061/SiCp nanocomposites, above which f_{Orowan} decreased slightly. The contribution of Hall-Petch and load bearing effect is negligible in the AA6061/SiCp nanocomposites.
- Enhancement of yield strength value of the strengthening mechanisms follows the trend of $\Delta\sigma_{\Delta CTE} > \Delta\sigma_{Orowan} > \Delta\sigma_{HP} > \Delta\sigma_{load}$ for hybrid nanocomposites.
- Predicted yield strength of hybrid nanocomposites obtained from the modified Clyne model and quadratic summation model are close to the experimental values.
- The fracture surface of AA6061 aluminium alloy reveals grape like dendrites in higher quantity whereas micro cracks, tear ridges, facets and tiny dimples are in smaller quantity. The fracture surfaces of 0.5NC, 1NC, 1.5NC and 2NC nanocomposites reveal

tiny dimples, facets and tear ridges in higher quantity and the grape like dendrites reduced with increase of SiCp nano-reinforcements in the matrix.

- Fracture surfaces of hybrid nanocomposites revealed the interdendritic cracking, step wise facets and particle pull out. Increase of graphite content in the matrix exhibited brittle fracture mode. Crack nucleated at triple junctions along the grain boundaries followed by their propagation along weakest neighbour grains.
- It is noticed that the wear coefficients of hybrid nanocomposites decreased with increase of applied normal loads and wt. % of graphite in the matrix. It can be seen that the wear coefficients increased with increase of sliding distances and sliding velocities at all load conditions.
- The deeper grooves are identified at lower content of worn surfaces of graphite hybrid nanocomposites. The depth of grooves increased with increase of applied normal loads and sliding velocity. The thin graphite layer is found on the worn surfaces which protected the surface from hard asperities during dry sliding. The graphite peeling off is found with increase of graphite in the matrix at higher loads and higher sliding velocity.
- The reduction of two body wear rate at higher load conditions for higher grit size is 35.3% for 2NC nanocomposite and 42.7% for 2HNC hybrid nanocomposite.
- Wear resistance is better in 2HNC hybrid nanocomposite compared to AA6061alloy and 2NC nanocomposite. This is due to the formation of thin graphite layer between composite pin and abrasive grit paper.
- Larger wear debris with more fractured abrasive grit particles at higher grit size and higher load on 2HNC hybrid nanocomposite is observed.

7.2 Other Observations

- It is observed that there is severe abrasion wear with higher depth of penetration, deeper grooves and oxide debris at higher sliding velocity and higher loads.
- It reveals longer scratches, lower adhesion wear, delamination and higher abrasive wear mechanism at above 10 N load and lower sliding velocity.
- It is observed that the circular scratches, delamination and severe abrasive wear mechanism are found at higher applied normal loads and sliding velocities.

- It is observed that the debris, blunting, particle pick up, fractured abrasive grit particles, chips removal and fracture of abrasive grit paper are seen at higher loads above 15 N with increase of sliding velocity.

7.3 Future Scope for this research work

- There is a good scope to study the dispersion of nano-reinforcement particles in the matrix slurry by varying ultrasonic intensity.
- Computational fluid dynamics (CFD) technique can be used for dispersion of nano-reinforcement particles based on ultrasonic stirring effect.
- The microstructural studies, dry sliding wear and abrasive wear behaviour of hybrid nanocomposites at T6 heat treatment condition can be examined.
- The tribological behaviour of T6 heat treated nanocomposite and hybrid nanocomposite materials can be tested under cryogenic conditions. The sub surface deformation of T6 heat treated specimens can be studied.

REFERENCES

- [1] P. Mukhopadhyay, Alloy Designation, Processing, and Use of AA6XXX Series Aluminium Alloys, ISRN Metall. 2012 (2012) 1-15.
<https://dx.doi.org/10.5402/2012/165082>
- [2] Y. Sato, A. Iwabuchi, M. Uchidate, H. Yashiro, Dynamic corrosion properties of impact-fretting wear in high-temperature pure water, Mater. Sci. Eng. A. 2012 (2012) 517-523. <https://doi.org/10.1016/j.matdes.2011.07.037>
- [3] P. Rambabu et al., Aerospace Materials and Material Technologies-Vouolume 1 Aerospace Materials, Springer. 1 (2017) 199-228. <https://doi.org/10.1007/978-981-10-2134-3>
- [4] M. Javidani, D. Larouche, Application of cast Al–Si alloys in internal combustion engine components, Int. Mater. Rev. 59 (2014) 132-158.
<https://doi.org/10.1179/1743280413y.0000000027>
- [5] C. Rontescu, T. Cicic, C. Amza, O. Chivu, D. Dobrotă, Choosing the optimum material for making a bicycle frame, Metalurgija. 54 (2015) 679-682.
- [6] S. V. Prasad, R. Asthana, Aluminum metal-matrix composites for automotive applications: Tribological considerations, Tribol. Lett. 17 (2004) 445-453.
<https://doi.org/10.1023/B:TRIL.0000044492.91991.f3>
- [7] Y.B. Liu, S.C. Lim, S. Ray, P.K. Rohatgi, Friction and wear of aluminium-graphite composites: the smearing process of graphite during sliding, Wear. 159 (1992) 201-205. [https://doi.org/10.1016/0043-1648\(92\)90303-P](https://doi.org/10.1016/0043-1648(92)90303-P)
- [8] P. Radha, G. Chandrasekaran, N. Selvakumar, Simplifying the powder metallurgy manufacturing process using soft computing tools, Appl. Soft Comput. J. 27 (2015) 191-204. <https://doi.org/10.1016/j.asoc.2014.11.011>
- [9] C. Yan, D. Xiong, J. Li, Synthesis of Ni-Al-Ta composite coatings on Al alloy plates and the transfer of Al powder via mechanical milling technique, Powder Technol. 340 (2018) 234-242. <https://doi.org/10.1016/j.powtec.2018.09.024>
- [10] T. Inoue, A. Yanagida, J. Yanagimoto, Finite element simulation of accumulative roll-bonding process, Mater. Lett. 106 (2013) 37-40.
<https://doi.org/10.1016/j.matlet.2013.04.093>

[11] U. Anselmi-Tamburini, J.E. Garay, Z.A. Munir, Fundamental investigations on the spark plasma sintering/synthesis process, *Mater. Sci. Eng. A.* 407 (2005) 24-30. <https://doi.org/10.1016/j.msea.2005.06.066>

[12] S.A. Sajjadi, H.R. Ezatpour, M. Torabi Parizi, Comparison of microstructure and mechanical properties of A356 aluminum alloy/Al₂O₃ composites fabricated by stir and compo-casting processes, *Mater. Des.* 34 (2012) 106-111. <https://doi.org/10.1016/j.matdes.2011.07.037>

[13] X. Zhou, D. Su, C. Wu, L. Liu, Tensile Mechanical Properties and Strengthening Mechanism of Hybrid Carbon Nanotube and Silicon Carbide Nanoparticle-Reinforced Magnesium Alloy Composites, *J. Nanomater.* 2012 (2012) 1-7. <https://doi.org/10.1155/2012/851862>

[14] C. Sauter, M.A. Emin, H.P. Schuchmann, S. Tavman, Influence of hydrostatic pressure and sound amplitude on the ultrasound induced dispersion and de-agglomeration of nanoparticles, *Ultrason. Sonochem.* 15 (2008) 517-523. <https://doi.org/10.1016/j.ultsonch.2007.08.010>

[15] X. Liu, S. Jia, L. Nastac, On Ultrasonic Cavitation-Assisted Molten Metal Processing of A356-Nanocomposites, 8 (2012) 120-127. <https://doi.org/10.1007/BF03355591>

[16] N. Srivastava, G.P. Chaudhari, Strengthening in Al alloy nano composites fabricated by ultrasound assisted solidification technique, *Mater. Sci. Eng. A.* 651 (2016) 241-247. <https://doi.org/10.1016/j.msea.2015.10.118>.

[17] J.H. Shin, H.J. Choi, D.H. Bae, The structure and properties of 2024 aluminum composites reinforced with TiO₂ nanoparticles, *Mater. Sci. Eng. A.* 607 (2014) 605-610. <https://doi.org/10.1016/j.msea.2014.04.038>.

[18] A. Salehi, A. Babakhani, S.M. Zebarjad, Microstructural and mechanical properties of Al-SiO₂ nanocomposite foams produced by an ultrasonic technique, *Mater. Sci. Eng. A.* 638 (2015) 54-59. <https://doi.org/10.1016/j.msea.2015.04.024>.

[19] H.R. Ezatpour, M. Torabi Parizi, S.A. Sajjadi, G.R. Ebrahimi, A. Chaichi, Microstructure, mechanical analysis and optimal selection of 7075 aluminum alloy based composite reinforced with alumina nanoparticles, *Mater. Chem. Phys.* 178 (2016) 119-127. <https://doi.org/10.1016/j.matchemphys.2016.04.078>.

[20] P. Yuan, D. Gu, D. Dai, Particulate migration behavior and its mechanism during selective laser melting of TiC reinforced Al matrix nanocomposites, *Mater. Des.* 82 (2015) 46-55. <https://doi.org/10.1016/j.matdes.2015.05.041>.

[21] Z. Zhang, T. Topping, Y. Li, R. Vogt, Y. Zhou, C. Haines, J. Paras, D. Kapoor, J.M. Schoenung, E.J. Lavernia, Mechanical behavior of ultrafine-grained Al composites reinforced with B₄C nanoparticles, *Scr. Mater.* 65 (2011) 652-655. <https://doi.org/10.1016/j.scriptamat.2011.06.037>.

[22] P. Ravindran, K. Manisekar, S. Vinoth Kumar, P. Rathika, Investigation of microstructure and mechanical properties of aluminum hybrid nano-composites with the additions of solid lubricant, *Mater. Des.* 51 (2013) 448-456. <https://doi.org/10.1016/j.matdes.2013.04.015>.

[23] R. Shen, Y. Du, B. Guo, J. Yi, S. Ni, Z. Tang, M. Song, Microstructures and mechanical properties of carbon nanotubes reinforced pure aluminum composites synthesized by spark plasma sintering and hot rolling, *Mater. Sci. Eng. A.* 698 (2017) 282-288. <https://doi.org/10.1016/j.msea.2017.05.068>.

[24] H. Zhang, X. Zhao, L. Xi, C. Ma, D. Gu, Microstructure characteristics and its formation mechanism of selective laser melting SiC reinforced Al-based composites, *Vacuum.* 160 (2018) 189-196. <https://doi.org/10.1016/j.vacuum.2018.11.022>.

[25] W. Wang, Y.Q. Liu, H.M. Cheng, H.T. Cong, C.H. Sun, AlN nanoparticle-reinforced nanocrystalline Al matrix composites: Fabrication and mechanical properties, *Mater. Sci. Eng. A.* 505 (2008) 151-156. <https://doi.org/10.1016/j.msea.2008.12.045>.

[26] O. Tapasztó, C. Balázs, The effect of milling time on the sintering kinetics of Si₃N₄ based nanocomposites, *Ceram. Int.* 36 (2010) 2247-2251. <https://doi.org/10.1016/j.ceramint.2010.06.006>

[27] W.Y. Li, C. Yang, H. Liao, Effect of vacuum heat treatment on microstructure and microhardness of cold-sprayed TiN particle-reinforced Al alloy-based composites, *Mater. Des.* 32 (2011) 388-394. <https://doi.org/10.1016/j.matdes.2010.06.002>.

[28] T. Xing, C. Zhang, L.H. Li, D. Lahiri, Y. Chen, A. Hadjikhani, A. Agarwal, Boron nitride nanotubes reinforced aluminum composites prepared by spark plasma sintering: Microstructure, mechanical properties and deformation behavior, *Mater. Sci. Eng. A.* 574 (2013) 149-156. <https://doi.org/10.1016/j.msea.2013.03.022>.

[29] J. Nampoothiri, R.S. Harini, S.K. Nayak, B. Raj, K.R. Ravi, Post in-situ reaction ultrasonic treatment for generation of Al-4.4Cu/TiB₂ nanocomposite: A route to enhance the strength of metal matrix nanocomposites, *J. Alloys Compd.* 683 (2016) 370-378. <https://doi.org/10.1016/j.jallcom.2016.05.067>.

[30] G.H. Fan, Q.W. Wang, L. Geng, G.S. Wang, Y.C. Feng, Preparation and characterization of aluminum matrix composites based on Al-WO₃ system, *J. Alloys Compd.* 545 (2012) 130-134. <https://doi.org/10.1016/j.jallcom.2012.07.132>.

[31] A. Evirgen, M.L. Öveçoğlu, Characterization investigations of a mechanically alloyed and sintered Al-2 wt%Cu alloy reinforced with WC particles, *J. Alloys Compd.* 496 (2010) 212-217. <https://doi.org/10.1016/j.jallcom.2010.02.136>.

[32] A. Dehghan Hamedan, M. Shahmiri, Production of A356-1wt% SiC nanocomposite by the modified stir casting method, *Mater. Sci. Eng. A.* 556 (2012) 921-926. <https://doi.org/10.1016/j.msea.2012.07.093>.

[33] Q. Li, F. Qiu, B.X. Dong, R. Geng, M.M. Lv, Q.L. Zhao, Q.C. Jiang, Fabrication, microstructure refinement and strengthening mechanisms of nanosized SiC_P/Al composites assisted ultrasonic vibration, *Mater. Sci. Eng. A.* 735 (2018) 310-317. <https://doi.org/10.1016/j.msea.2018.08.060>

[34] X. Yao, Z. Zhang, Y.F. Zheng, C. Kong, M.Z. Quadir, J.M. Liang, Y.H. Chen, P. Munroe, D.L. Zhang, Effects of SiC Nanoparticle Content on the Microstructure and Tensile Mechanical Properties of Ultrafine Grained AA6063-SiCnp Nanocomposites Fabricated by Powder Metallurgy, *J. Mater. Sci. Technol.* 33 (2017) 1023-1030. <https://doi.org/10.1016/j.jmst.2016.09.022>

[35] M. Alizadeh, H.A. Beni, Strength prediction of the ARBed Al/Al₂O₃/B₄C nanocomposites using Orowan model, *Mater. Res. Bull.* 59 (2014) 290-294. <https://doi.org/10.1016/j.materresbull.2014.07.034>

[36] A.F. Boostani, R.T. Mousavian, S. Tahamtan, S. Yazdani, R.A. Khosroshahi, D. Wei, J.Z. Xu, D. Gong, X.M. Zhang, Z.Y. Jiang, Graphene sheets encapsulating SiC nanoparticles: A roadmap towards enhancing tensile ductility of metal matrix composites, *Mater. Sci. Eng. A.* 648 (2015) 92-103. <https://doi.org/10.1016/j.msea.2015.09.050>

[37] X. Zhang, S. Li, D. Pan, B. Pan, K. Kondoh, Microstructure and synergistic-

strengthening efficiency of CNTs-SiC_dual-nano reinforcements in aluminum matrix composites, *Compos. Part A Appl. Sci. Manuf.* 105 (2018) 87-96.
<https://doi.org/10.1016/j.compositesa.2017.11.013>

[38] S. Kumar, T. Siew, M. Gupta, Microwave synthesis and characterization of metastable (Al/Ti) and hybrid (Al/Ti+SiC) composites, 453 (2007) 61-69.
<https://doi.org/10.1016/j.msea.2006.10.156>

[39] J. Li, G. Zhao, S. Wu, Z. Huang, S. Lü, Q. Chen, F. Li, A Preparation of hybrid particulates SiC np and Mg₂Si reinforced Al-Cu matrix composites, *Mater. Sci. Eng. A.* 751 (2019) 107-114. <https://doi.org/10.1016/j.msea.2019.02.076>

[40] L. J. Zhang, F. Qiu, J. Wang, H. Wang, Q. Jiang, Microstructures and mechanical properties of the Al2014 composites reinforced with bimodal sized SiC particles, *Mater. Sci. Eng. A.* 637 (2015) 70-74. <https://doi.org/10.1016/j.msea.2015.04.012>

[41] M.C. Şenel, M. Gürbüz, E. Koç, Fabrication and characterization of synergistic Al-SiC-GNPs hybrid composites, *Compos. Part B Eng.* 154 (2018) 1-9.
<https://doi.org/10.1016/j.compositesb.2018.07.035>

[42] L. Poovazhagan, K. Kalaichelvan, A. Rajadurai, V. Senthilvelan, Characterization of hybrid silicon carbide and boron carbide nanoparticles-reinforced aluminum alloy composites, in: *Procedia Eng.*, Elsevier B.V., 2013: pp. 681-689.
<https://doi.org/10.1016/j.proeng.2013.09.143>

[43] A. Kumar, K. Pal, S. Mula, Simultaneous improvement of mechanical strength , ductility and corrosion resistance of stir cast Al7075-2 % SiC micro-and nanocomposites by friction stir processing, *J. Manuf. Process.* 30 (2017) 1-13.
<https://doi.org/10.1016/j.jmapro.2017.09.005>

[44] R.T. Mousavian, R.A. Khosroshahi, S. Yazdani, D. Brabazon, A.F. Boostani, Fabrication of aluminum matrix composites reinforced with nano- to micrometer-sized SiC particles, *JMADE*. 89 (2016) 58-70. <https://doi.org/10.1016/j.matdes.2015.09.130>

[45] L. Kollo, C. R. Bradbury, R. Veinthal, C. Jaggi, E. C. Morelli, M. Leparoux, Nano-silicon carbide reinforced aluminium produced by high-energy milling and hot consolidation, 528 (2011) 6606–6615. <https://doi.org/10.1016/j.msea.2011.05.037>

[46] F. Khodabakhshi, A. Simchi, A.H. Kokabi, A.P. Gerlich, Similar and dissimilar friction-stir welding of an PM aluminum-matrix hybrid nanocomposite and commercial pure aluminum: Microstructure and mechanical properties, *Mater. Sci. Eng. A.* 666 (2016) 225-237. <https://doi.org/10.1016/j.msea.2016.04.078>

[47] H. Tazari, M.H. Siadati, Synthesis and mechanical properties of aluminum alloy 5083 / SiCnp nanocomposites, *J. Alloys Compd.* 729 (2017) 960-969. <https://doi.org/10.1016/j.jallcom.2017.09.130>

[48] M.R. Mattli, P.R. Matli, A. Shakoor, Structural and Mechanical Properties of Amorphous Si_3N_4 Nanoparticles Reinforced Al Matrix Composites Prepared by Microwave Sintering, (2019) 126-134. <https://doi.org/10.3390/ceramics2010012>

[49] M.P. Reddy, R.A. Shakoor, G. Parande, V. Manakari, F. Ubaid, A.M.A. Mohamed, M. Gupta, Enhanced performance of nano-sized SiC reinforced Al metal matrix nanocomposites synthesized through microwave sintering and hot extrusion techniques, *Prog. Nat. Sci. Mater. Int.* 27 (2017) 606-614. <https://doi.org/10.1016/j.pnsc.2017.08.015>

[50] J. Li, G. Zhao, S. Wu, Z. Huang, S. Lü, Q. Chen, F. Li, Preparation of hybrid particulates SiC np and Mg_2Si reinforced Al-Cu matrix composites, *Mater. Sci. Eng. A.* 751 (2019) 107–114. doi:10.1016/j.msea.2019.02.076.

[51] C. Wu, K. Ma, J. Wu, P. Fang, G. Luo, F. Chen, Influence of particle size and spatial distribution of B_4C reinforcement on the microstructure and mechanical behavior of precipitation strengthened Al alloy matrix composites, *Mater. Sci. Eng. A.* 675 (2016) 421-430. <https://doi.org/10.1016/j.msea.2016.08.062>

[52] Ö. Balci, D. AĞaoğullari, H. Gökçe, I. Duman, M.L. Öveçoğlu, Influence of TiB_2 particle size on the microstructure and properties of Al matrix composites prepared via mechanical alloying and pressureless sintering, *J. Alloys Compd.* 16 (2016) 147-158. <https://doi.org/10.1016/j.jallcom.2013.03.007>

[53] R. Harichandran, N. Selvakumar, Effect of nano/micro B_4C particles on the mechanical properties of aluminium metal matrix composites fabricated by ultrasonic cavitation-assisted solidification process, *Arch. Civ. Mech. Eng.* 16 (2016) 147-158. <https://doi.org/10.1016/j.acme.2015.07.001>

[54] Z. Wang, M. Song, C. Sun, Y. He, Effects of particle size and distribution on the

mechanical properties of SiC reinforced Al–Cu alloy composites, *Mater. Sci. Eng. A.* 528 (2011) 1131-1137. <https://doi.org/10.1016/j.msea.2010.11.028>

[55] C. Sun, M. Song, Z. Wang, Y. He, Effect of particle size on the microstructures and mechanical properties of SiC-reinforced pure aluminum composites, *J. Mater. Eng. Perform.* 20 (2011) 1606-1612. <https://doi.org/10.1007/s11665-010-9801-3>

[56] O. El-Kady, A. Fathy, Effect of SiC particle size on the physical and mechanical properties of extruded Al matrix nanocomposites, *Mater. Des.* 54 (2014) 348-353. <https://doi.org/10.1016/j.matdes.2013.08.049>

[57] Z. Zhang, D.L. Chen, Consideration of Orowan strengthening effect in particulate-reinforced metal matrix nanocomposites: A model for predicting their yield strength, *Scr. Mater.* 54 (2006) 1321–1326. doi:10.1016/j.scriptamat.2005.12.017.

[58] K. Amouri, S. Kazemi, A. Momeni, M. Kazazi, Microstructure and mechanical properties of Al-nano/micro SiC composites produced by stir casting technique, *Mater. Sci. Eng. A.* 674 (2016) 569-578. <https://doi.org/10.1016/j.msea.2016.08.027>

[59] G. Cao, H. Konishi, X. Li, Mechanical properties and microstructure of SiC-reinforced Mg-(2,4)Al-1Si nanocomposites fabricated by ultrasonic cavitation based solidification processing, *Mater. Sci. Eng. A.* 486 (2008) 357-362. <https://doi.org/10.1016/j.msea.2007.09.054>

[60] M.F. Ibrahim, H.R. Ammar, A.M. Samuel, M.S. Soliman, F.H. Samuel, On the impact toughness of Al-15 vol.% B₄C metal matrix composites, *Compos. Part B Eng.* 79 (2015) 83-94. <https://doi.org/10.1016/j.compositesb.2015.04.018>

[61] I. Ganesh, I. Advanced, Correlation between the characteristics of the mechanically mixed layer and wear behaviour of aluminium, Al-7075 alloy and Al-MMCs and wear behaviour of aluminium, Al-7075 alloy and Al-MMCs, 245 (2016) 22-38. [https://doi.org/10.1016/S0043-1648\(00\)00463-4](https://doi.org/10.1016/S0043-1648(00)00463-4)

[62] C.S. Ramesh, S.K. Seshadri, Tribological characteristics of nickel based composite coatings, *Wear.* 255 (2003) 893-902. [https://doi.org/10.1016/S0043-1648\(03\)00080-2](https://doi.org/10.1016/S0043-1648(03)00080-2)

[63] A. Wagih, A. Fathy, D. Ibrahim, O. Elkady, M. Hassan, Experimental investigation on strengthening mechanisms in Al-SiC nanocomposites and 3D FE simulation of Vickers indentation, *J. Alloys Compd.* 752 (2018) 137-147. <https://doi.org/10.1016/j.jallcom.2018.04.167>

[64] A. Mazahery, M.O. Shabani, Microstructural and abrasive wear properties of SiC reinforced aluminum-based composite produced by compocasting, *Trans. Nonferrous Met. Soc. China* (English Ed. 23 (2013) 1905-1914. [https://doi.org/10.1016/S1003-6326\(13\)62676-X](https://doi.org/10.1016/S1003-6326(13)62676-X)

[65] M.R. Dehnavi, B. Niroumand, F. Ashra, P.K. Rohatgi, Effects of continuous and discontinuous ultrasonic treatments on mechanical properties and microstructural characteristics of cast Al413-SiCnp nanocomposite, *Mater. Sci. Eng. A.* 617 (2014) 73-83. <https://doi.org/10.1016/j.msea.2014.08.042>

[66] A. Melaibari, A. Fathy, M. Mansouri, M.A. Eltaher, Experimental and numerical investigation on strengthening mechanisms of nanostructured Al-SiC composites, *J. Alloys Compd.* 774 (2019) 1123-1132. <https://doi.org/10.1016/j.jallcom.2018.10.007>

[67] G. Bajpai, R. Purohit, R.S. Rana, S. Singh Rajpurohit, A. Rana, Investigation and Testing of Mechanical Properties of Al-Nano SiC Composites through Cold Isostatic Compaction Process, *Mater. Today Proc.* 4 (2017) 2723-2732. <https://doi.org/10.1016/j.matpr.2017.02.149>

[68] S. Lü, P. Xiao, D. Yuan, K. Hu, S. Wu, Preparation of Al matrix nanocomposites by diluting the composite granules containing nano-SiCp under ultrasonic vibration, *J. Mater. Sci. Technol.* 34 (2018) 1609-1617. <https://doi.org/10.1016/j.jmst.2018.01.003>

[69] Y. Yang, J. Lan, X. Li, Study on bulk aluminum matrix nano-composite fabricated by ultrasonic dispersion of nano-sized SiC particles in molten aluminum alloy, *Mater. Sci. Eng. A.* 380 (2004) 378-383. <https://doi.org/10.1016/j.msea.2004.03.073>

[70] N. Srivastava, G.P. Chaudhari, Microstructural evolution and mechanical behavior of ultrasonically synthesized Al6061-nano alumina composites, *Mater. Sci. Eng. A.* 724 (2018) 199-207. <https://doi.org/10.1016/j.msea.2018.03.092>

[71] S. Queyreau, G. Monnet, B. Devincre, Orowan strengthening and forest hardening superposition examined by dislocation dynamics simulations, *Compos. Part B.* 4 (2017) 2927-2936. <https://doi.org/10.1016/j.matpr.2017.02.174>

[72] A. Bisht, M. Srivastava, R.M. Kumar, I. Lahiri, D. Lahiri, Strengthening mechanism in graphene nanoplatelets reinforced aluminum composite fabricated through spark plasma sintering, *Mater. Sci. Eng. A.* 695 (2017) 20-28. <https://doi.org/10.1016/j.msea.2017.04.009>

[73] Z. Zhang, D.L. Chen, Contribution of Orowan strengthening effect in particulate-reinforced metal matrix nanocomposites, *Mater. Sci. Eng. A*. 483-484 (2008) 148-152. <https://doi.org/10.1016/j.msea.2006.10.184>

[74] F.A. Mirza, D.L. Chen, A unified model for the prediction of yield strength in particulate-reinforced metal matrix nanocomposites, *Materials (Basel)*. 8 (2015) 5138-5153. <https://doi.org/10.3390/ma8085138>

[75] K. Deng, J. Shi, C. Wang, X. Wang, Y. Wu, K. Nie, K. Wu, Microstructure and strengthening mechanism of bimodal size particle reinforced magnesium matrix composite, *Compos. Part A Appl. Sci. Manuf.* 43 (2012) 1280-1284. <https://doi.org/10.1016/j.compositesa.2012.03.007>

[76] A. Alizadeh, E. Taheri-Nassaj, Mechanical properties and wear behavior of Al-2 wt.% Cu alloy composites reinforced by B₄C nanoparticles and fabricated by mechanical milling and hot extrusion, *Mater. Charact.* 67 (2012) 119-128. <https://doi.org/10.1016/j.matchar.2012.02.006>

[77] A. Sanaty-Zadeh, Comparison between current models for the strength of particulate-reinforced metal matrix nanocomposites with emphasis on consideration of Hall-Petch effect, *Mater. Sci. Eng. A*. 531 (2012) 112-118. <https://doi.org/10.1016/j.msea.2011.10.043>

[78] J.G. Park, D.H. Keum, Y.H. Lee, Strengthening mechanisms in carbon nanotube-reinforced aluminum composites, *Carbon N. Y.* 95 (2015) 690-698. <https://doi.org/10.1016/j.carbon.2015.08.112>

[79] K. M. Sree Manu, S. Arun Kumar, T. P. D. Rajan, M. Riyas Mohammed, B.C. Pai, Effect of alumina nanoparticle on strengthening of Al-Si alloy through dendrite refinement, interfacial bonding and dislocation bowing, *J. Alloys Compd.* 712 (2017) 394-405. <https://doi.org/10.1016/j.jallcom.2017.04.104>

[80] X. Zhang, S. Li, B. Pan, D. Pan, S. Zhou, S. Yang, L. Jia, K. Kondoh, A novel strengthening effect of in-situ nano Al₂O₃w on CNTs reinforced aluminum matrix nanocomposites and the matched strengthening mechanisms, *J. Alloys Compd.* 764 (2018) 279-288. <https://doi.org/10.1016/j.jallcom.2018.06.006>

[81] A. Bhaduria, L.K. Singh, T. Laha, Combined strengthening effect of nanocrystalline matrix and graphene nanoplatelet reinforcement on the mechanical properties of spark

plasma sintered aluminum based nanocomposites, *Mater. Sci. Eng. A.* 749 (2019) 14-26. <https://doi.org/10.1016/j.msea.2019.02.007>

[82] S. Amirkhanlou, S. Ji, Y. Zhang, D. Watson, Z. Fan, High modulus Al Si Mg Cu/Mg₂Si/TiB₂ hybrid nanocomposite: Microstructural characteristics and micromechanics-based analysis, *J. Alloys Compd.* 694 (2016) 313-324. <https://doi.org/10.1016/j.jallcom.2016.10.016>

[83] G.H. Fan, Q. W. Wang, L. Geng, G. S. Wang, Y. C. Feng, Preparation and characterization of aluminum matrix composites based on Al-WO₃ system, *J. Alloys Compd.* 545 (2012) 130-134. <https://doi.org/10.1016/j.jallcom.2012.07.132>

[84] N. Ramakrishnan, An analytical study on strengthening of particulate reinforced metal matrix composites, *Acta Mater.* 44 (1996) 69-77. [https://doi.org/10.1016/1359-6454\(95\)00150-9](https://doi.org/10.1016/1359-6454(95)00150-9)

[85] Z. Zhang, D.L. Chen, Consideration of Orowan strengthening effect in particulate-reinforced metal matrix nanocomposites: A model for predicting their yield strength, *Scr. Mater.* 54 (2006) 1321-1326. <https://doi.org/10.1016/j.scriptamat.2005.12.017>

[86] A. Khandelwal, K. Mani, N. Srivastava, R. Gupta, G.P. Chaudhari, Mechanical behavior of AZ31/Al₂O₃ magnesium alloy nanocomposites prepared using ultrasound assisted stir casting, *Compos. Part B Eng.* 123 (2017) 64-73. <https://doi.org/10.1016/j.compositesb.2017.05.007>

[87] P. Xiao, Y. Gao, C. Yang, Z. Liu, Y. Li, F. Xu, Microstructure, mechanical properties and strengthening mechanisms of Mg matrix composites reinforced with in situ nanosized TiB₂ particles, *Mater. Sci. Eng. A.* 710 (2018) 251-259. <https://doi.org/10.1016/j.msea.2017.10.107>

[88] N.C. Kaushik, R.N. Rao, Effect of grit size on two body abrasive wear of Al 6082 hybrid composites produced by stir casting method, *Tribol. Int.* 102 (2016) 52-60. <https://doi.org/10.1016/j.triboint.2016.05.015>

[89] R. Iredale, Manufacturing Composites for Automotive Applications, Univ. Bristol. (n.d.) 10-11.

[90] A.P. Sannino, H.J. Rack, Dry sliding wear of discontinuously reinforced aluminum composites: review and discussion, 189 (1995) 1-19. <https://doi.org/10.1016/0043->

[91] W. Aiguo, H.J. Rack, Abrasive wear of silicon carbide particulate and whisker-reinforced 7091 aluminum matrix composites, *Wear.* 146 (1991) 337-348.
[https://doi.org/10.1016/0043-1648\(91\)90073-4](https://doi.org/10.1016/0043-1648(91)90073-4)

[92] K. Soorya Prakash, P. Balasundar, S. Nagaraja, P.M. Gopal, V. Kavimani, Effect of reinforcement, compact pressure and hard ceramic coating on aluminium rock dust composite performance, *Int. J. Refract. Met. Hard Mater.* 54 (2017) 223-229.
<https://doi.org/10.1108/ACMM-09-2017-1837>

[93] I. Manivannan, S. Ranganathan, S. Gopalakannan, S. Suresh, K. Nagakarthigan, R. Jubendradass, Tribological and surface behavior of silicon carbide reinforced aluminum matrix nanocomposite, *Surfaces and Interfaces.* 8 (2017) 127-136.
<https://doi.org/10.1016/j.surfin.2017.05.007>

[94] X.G. Zou, H. Miyahara, K. Yamamoto, K. Ogi, Sliding wear behaviour of Al-Si-Cu composites reinforced with SiC particles, *Mater. Sci. Technol.* 19 (2003) 1519-1526.
<https://doi.org/10.1179/026708303225007997>

[95] M. Moazami-Goudarzi, F. Akhlaghi, Wear behavior of Al 5252 alloy reinforced with micrometric and nanometric SiC particles, *Tribol. Int.* 102 (2016) 28-37.
<https://doi.org/10.1016/j.triboint.2016.05.013>

[96] I. Manivannan, S. Ranganathan, S. Gopalakannan, S. Suresh, Mechanical Properties and Tribological Behavior of Al6061-SiC-Gr Self-Lubricating Hybrid Nanocomposites, *Trans. Indian Inst. Met.* 71 (2018) 1-15.
<https://doi.org/10.1007/s12666-018-1321-0>

[97] S. MOSLEH-SHIRAZI, F. AKHLAGHI, D. yang LI, Effect of SiC content on dry sliding wear, corrosion and corrosive wear of Al/SiC nanocomposites, *Trans. Nonferrous Met. Soc. China* (English Ed. 26 (2016) 1801-1808.
[https://doi.org/10.1016/S1003-6326\(16\)64294-2](https://doi.org/10.1016/S1003-6326(16)64294-2)

[98] X. Zeng, J. Yu, D. Fu, H. Zhang, J. Teng, Wear characteristics of hybrid aluminum-matrix composites reinforced with well-dispersed reduced graphene oxide nanosheets and silicon carbide particulates, *Vacuum.* 155 (2018) 364-375.
<https://doi.org/10.1016/j.vacuum.2018.06.033>

[99] B. Hekner, J. Myalski, N. Valle, A. Botor-Probierz, M. Sopicka-Lizer, J. Wieczorek,

Friction and wear behavior of Al-SiC(n) hybrid composites with carbon addition, Compos. Part B Eng. 108 (2017) 291-300.

<https://doi.org/10.1016/j.compositesb.2016.09.103>

[100] P. Hariharasakthisudhan, S. Jose, K. Manisekar, Dry sliding wear behaviour of single and dual ceramic reinforcements premixed with Al powder in AA6061 matrix, J. Mater. Res. Technol. (2018) 1-9. <https://doi.org/10.1016/j.jmrt.2018.01.005>

[101] J. Leng, G. Wu, Q. Zhou, Z. Dou, X.L. Huang, Mechanical properties of SiC/Gr/Al composites fabricated by squeeze casting technology, Scr. Mater. 59 (2008) 619-622. <https://doi.org/10.1016/j.scriptamat.2008.05.018>

[102] O. Carvalho, M. Buciumeanu, S. Madeira, D. Soares, F.S. Silva, G. Miranda, Dry sliding wear behaviour of AlSi-CNTs-SiCp hybrid composites, Tribol. Int. 90 (2015) 148-156. <https://doi.org/10.1016/j.triboint.2015.04.031>

[103] J. Babu, C. Kang, H. Kim, Dry sliding wear behavior of aluminum based hybrid composites with graphite nanofiber-alumina fiber, Materials & Design, 32, 3920-3925 (2011). <https://doi.org/10.1016/j.matdes.2011.02.064>

[104] D. Aruri, K. Adepu, K. Adepu, K. Bazavada, Wear and mechanical properties of 6061-T6 aluminum alloy surface hybrid composites [(SiC+Gr) and (SiC+Al₂O₃)] fabricated by friction stir processing, J. Mater. Res. Technol. 2 (2013) 362-369. <https://doi.org/10.1016/j.jmrt.2013.10.004>

[105] P. Ravindran, K. Manisekar, P. Rathika, P. Narayanasamy, Tribological properties of powder metallurgy - Processed aluminium self lubricating hybrid composites with SiC additions, Mater. Des. 45 (2013) 561-570. <https://doi.org/10.1016/j.matdes.2012.09.015>

[106] W. Chen, Y. Liu, C. Yang, D. Zhu, Y. Li, (SiCp+Ti)/7075Al hybrid composites with high strength and large plasticity fabricated by squeeze casting, 2014. <https://doi.org/10.1016/j.msea.2014.05.008>

[107] W. Ames, A.T. Alpas, Wear mechanisms in hybrid composites of graphite-20% SiC in A356 aluminium alloy (Al-7% Si-0.3% Mg), Met. Mater. Trans. A. 26 (1995) 85-98. <https://doi.org/10.1007/BF02669796>

[108] A. Mostafapour Asl, S.T. Khandani, Role of hybrid ratio in microstructural, mechanical and sliding wear properties of the Al5083/Graphitep/Al₂O_{3p} a surface hybrid nanocomposite fabricated via friction stir processing method, Mater. Sci. Eng. A. 559

(2013) 549-557. <https://doi.org/10.1016/j.msea.2012.08.140>

[109] S. Suresha, B.K. Sridhara, Effect of addition of graphite particulates on the wear behaviour in aluminium-silicon carbide-graphite composites, *Mater. Des.* 31 (2010) 1804-1812. <https://doi.org/10.1016/j.matdes.2009.11.015>

[110] J. Singh, Fabrication characteristics and tribological behavior of Al/SiC/Gr hybrid aluminum matrix composites: A review, *Friction.* 4 (2016) 191-207. <https://doi.org/10.1007/s40544-016-0116-8>

[111] S. Basavarajappa, G. Chandramohan, A. Mahadevan, M. Thangavelu, R. Subramanian, P. Gopalakrishnan, Influence of sliding speed on the dry sliding wear behaviour and the subsurface deformation on hybrid metal matrix composite, *Wear.* 262 (2007) 1007-1012. <https://doi.org/10.1016/j.wear.2006.10.016>

[112] S.T. Mavhungu, E.T. Akinlabi, M.A. Onitiri, F.M. Varachia, Aluminum Matrix Composites for Industrial Use: Advances and Trends, *Procedia Manuf.* 7 (2017) 178-182. <https://doi.org/10.1016/j.promfg.2016.12.045>

[113] S.C. Tung, Y. Huang, Modeling of abrasive wear in a piston ring and engine cylinder bore system©, *Tribol. Trans.* 47 (2004) 17-22. <https://doi.org/10.1080/05698190490279074>

[114] P.K. Rohatgi, B.C. Pai, S.C. Panda, Preparation of cast aluminium-silica particulate composites, *J. Mater. Sci.* 14 (1979) 2277-2283. <https://doi.org/10.1007/BF00737014>

[115] M. Singh, D.P. Mondal, O.P. Modi, A.K. Jha, Two-body abrasive wear behaviour of aluminium alloy-sillimanite particle reinforced composite, *Wear.* 253 (2002) 357-368. [https://doi.org/10.1016/S0043-1648\(02\)00153-9](https://doi.org/10.1016/S0043-1648(02)00153-9)

[116] A. Canakci, F. Arslan, Abrasive wear behaviour of B₄C particle reinforced Al2024 MMCs, *Int. J. Adv. Manuf. Technol.* 63 (2012) 785-795. <https://doi.org/10.1007/s00170-012-3931-8>

[117] A.G. Wang, I.M. Hutchings, Wear of alumina fibre-aluminium metal matrix composites by two-body abrasion, *Mater. Sci. Technol.* 5 (1989) 71-76. <https://doi.org/10.1179/mst.1989.5.1.71>

[118] A.T. Alpas, J.D. Embury, Sliding and abrasive wear behaviour of an aluminum (2014)-SiC particle reinforced composite, *Scr. Metall. Mater.* 24 (1990) 931-935.

[https://doi.org/10.1016/0956-716X\(90\)90140-C](https://doi.org/10.1016/0956-716X(90)90140-C)

[119] N. Axén, A. Alahelsten, S. Jacobson, Abrasive wear of alumina fibre-reinforced aluminium, *Wear.* 173 (1994) 95-104. [https://doi.org/10.1016/0043-1648\(94\)90261-5](https://doi.org/10.1016/0043-1648(94)90261-5)

[120] Y. Sahin, K. Özdin, A model for the abrasive wear behaviour of aluminium based composites, *Mater. Des.* 29 (2008) 728-733.
<https://doi.org/10.1016/j.matdes.2007.02.013>

[121] S. Wilson, A.T. Alpas, Wear mechanism maps for metal matrix composites, *Wear.* 212 (1997) 41-49. [https://doi.org/10.1016/S0043-1648\(97\)00142-7](https://doi.org/10.1016/S0043-1648(97)00142-7)

[122] S. Turenne, Y. Châtigny, D. Simard, S. Caron, J. Masounave, The effect of abrasive particle size on the slurry erosion resistance of particulate-reinforced aluminium alloy, *Wear.* 141 (1990) 147-158. [https://doi.org/10.1016/0043-1648\(90\)90199-K](https://doi.org/10.1016/0043-1648(90)90199-K)

[123] Z. Ma, J. Bi, Y. Lu, H. Shen, Y. Gao, Abrasive wear of discontinuous SiC reinforced aluminum alloy composites, *Wear.* 148 (1991) 287-293.
[https://doi.org/10.1016/0043-1648\(91\)90290-B](https://doi.org/10.1016/0043-1648(91)90290-B)

[124] A.B. Gurcan, T.N. Baker, A.B. Gurcan, T.N. Baker, Wear behaviour of AA6061 aluminium alloy and its composites, 188 (1995) 185-191.

[125] M.G. Hamblin, G.W. Stachowiak, Description of Abrasive Particle Shape and Its Relation to Two-Body Abrasive Wear, *Tribol. Trans.* 39 (1996) 803-810.
<https://doi.org/10.1080/10402009608983598>

[126] S. Das, D.P. Mondal, S. Sawla, N. Ramakrishnan, Synergic effect of reinforcement and heat treatment on the two body abrasive wear of an Al-Si alloy under varying loads and abrasive sizes, *Wear.* 264 (2008) 47-59. <https://doi.org/10.1016/j.wear.2007.01.039>

[127] R. Gupta, G.P. Chaudhari, B.S.S. Daniel, Strengthening mechanisms in ultrasonically processed aluminium matrix composite with in-situ Al₃Ti by salt addition, *Compos. Part B Eng.* 140 (2018) 27-34. <https://doi.org/10.1016/j.compositesb.2017.12.005>

[128] P. Sharma, S. Sharma, D. Khanduja, Effect of graphite reinforcement on physical and mechanical properties of aluminum metal matrix composites, *Part. Sci. Technol.* 34 (2016) 17-22. <https://doi.org/10.1080/02726351.2015.1031924>

[129] S. Suresh, N.S.V. Moorthi, Process development in stir casting and investigation on microstructures and wear behavior of TiB₂ on A16061 MMC, *Procedia Eng.* 64 (2013)

1183-1190. <https://doi.org/10.1016/j.proeng.2013.09.197>

[130] M.P. Reddy, R.A. Shakoor, G. Parande, V. Manakari, F. Ubaid, A.M.A. Mohamed, M. Gupta, Enhanced performance of nano-sized SiC reinforced Al metal matrix nanocomposites synthesized through microwave sintering and hot extrusion techniques, *Prog. Nat. Sci. Mater. Int.* 27 (2017) 606-614.
<https://doi.org/10.1016/j.pnsc.2017.08.015>

[131] K.R. Ramkumar, S. Sivasankaran, A.S. Alaboodi, Effect of alumina content on microstructures, mechanical, wear and machining behavior of Cu-10Zn nanocomposite prepared by mechanical alloying and hot-pressing, *J. Alloys Compd.* 709 (2017) 129-141. <https://doi.org/10.1016/j.jallcom.2017.03.153>

[132] S. Ozkaya, A. Canakci, Effect of the B₄C content and the milling time on the synthesis, consolidation and mechanical properties of AlCuMg-B₄C nanocomposites synthesized by mechanical milling, *Powder Technol.* 297 (2016) 8-16.
<https://doi.org/10.1016/j.powtec.2016.04.004>

[133] D.N. Talwar, On the pressure-dependent phonon characteristics and anomalous thermal expansion coefficient of 3C-SiC, *Mater. Sci. Eng. B Solid-State Mater. Adv. Technol.* 226 (2017) 1-9. <https://doi.org/10.1016/j.mseb.2017.08.018>

[134] D.C. Dunand, A. Mortensen, On plastic relaxation of thermal stresses in reinforced metals, *Acta Metall. Mater.* 39 (1991) 127-139. [https://doi.org/10.1016/0956-7151\(91\)90261-X](https://doi.org/10.1016/0956-7151(91)90261-X)

[135] P. Xiao, Y. Gao, C. Yang, Z. Liu, Y. Li, F. Xu, Microstructure, mechanical properties and strengthening mechanisms of Mg matrix composites reinforced with in situ nanosized TiB₂ particles, *Mater. Sci. Eng. A.* 710 (2018) 251-259.
<https://doi.org/10.1016/j.msea.2017.10.107>

[136] B. Chen, J. Shen, X. Ye, L. Jia, S. Li, J. Umeda, M. Takahashi, K. Kondoh, Length effect of carbon nanotubes on the strengthening mechanisms in metal matrix composites, *Acta Mater.* 140 (2017) 317-325.
<https://doi.org/10.1016/j.actamat.2017.08.048>

[137] D.K.L. Tsang, B.J. Marsden, S.L. Fok, G. Hall, Graphite thermal expansion relationship for different temperature ranges, *Carbon N. Y.* 43 (2005) 2902-2906.
<https://doi.org/10.1016/j.carbon.2005.06.009>

[138] N. Kumar, G. Gautam, R.K. Gautam, A. Mohan, S. Mohan, Wear, friction and profilometer studies of insitu AA5052/ZrB₂ composites, *Tribol. Int.* 97 (2016) 313-326. <https://doi.org/10.1016/j.triboint.2016.01.036>

[139] E. Omrani, A.D. Moghadam, P.L. Menezes, P.K. Rohatgi, Influences of graphite reinforcement on the tribological properties of self-lubricating aluminum matrix composites for green tribology, sustainability, and energy efficiency-A review, *Int. J. Adv. Manuf. Technol.* 83 (2016) 325-346. <https://doi.org/10.1007/s00170-015-7528-x>

[140] P.L. Menezes, P.K. Rohatgi, M.R. Lovell, Self-Lubricating Behavior of Graphite Reinforced Metal Matrix Composites, in: M. Nosonovsky, B. Bhushan (Eds.), *Green Tribol. Biomimetics, Energy Conserv. Sustain.*, Springer Berlin Heidelberg, Berlin, Heidelberg, 2012: pp. 445-480. https://doi.org/10.1007/978-3-642-23681-5_17

[141] N. C. Kaushik, R. N. Rao, Effect of applied load and grit size on wear coefficients of Al 6082-SiC-Gr hybrid composites under two body abrasion, *Tribol. Int.* 103 (2016) 298-308. <https://doi.org/10.1016/j.triboint.2016.07.018>

[142] M.L.T. Guo, C.Y.A. Tsao, Tribological behavior of self-lubricating aluminium/SiC/graphite hybrid composites synthesized by the semi-solid powder-densification method, *Compos. Sci. Technol.* 60 (2000) 65-74. [https://doi.org/10.1016/S0266-3538\(99\)00106-2](https://doi.org/10.1016/S0266-3538(99)00106-2)

[143] J. Rodríguez, P. Poza, M.A. Garrido, A. Rico, Dry sliding wear behaviour of aluminium-lithium alloys reinforced with SiC particles, *Wear.* 262 (2007) 292-300. <https://doi.org/10.1016/j.wear.2006.05.006>

[144] E.M. Sharifi, F. Karimzadeh, Wear behavior of aluminum matrix hybrid nanocomposites fabricated by powder metallurgy, *Wear.* 271 (2011) 1072-1079. <https://doi.org/10.1016/j.wear.2011.05.015>

[145] D.H. Buckley, R.L. Johnson, The influence of crystal structure and some properties of hexagonal metals on friction and adhesion, *Wear.* 11 (1968) 405-419. [https://doi.org/10.1016/0043-1648\(68\)90550-4](https://doi.org/10.1016/0043-1648(68)90550-4)

[146] N. Hosseini, F. Karimzadeh, M.H. Abbasi, M.H. Enayati, A comparative study on the wear properties of coarse-grained Al6061 alloy and nanostructured Al6061-Al₂O₃ composites, *Tribol. Int.* 54 (2012) 58-67. <https://doi.org/10.1016/j.triboint.2012.04.020>

[147] R.L. Deuis, C. Subramanian, J.M. Yellup, Abrasive wear of aluminium composites-a review, *Wear.* 201 (1996) 132-144. [https://doi.org/10.1016/S0043-1648\(96\)07228-6](https://doi.org/10.1016/S0043-1648(96)07228-6)

[148] S. Thirumalai Kumaran, M. Uthayakumar, Investigation on the dry sliding friction and wear behavior of AA6351-SiC-B₄C hybrid metal matrix composites, *Proc. Inst. Mech. Eng. Part J J. Eng. Tribol.* 228 (2014) 332-338.
<https://doi.org/10.1177/1350650113508103>

[149] A. Baradeswaran, A. Elaya Perumal, Influence of B₄C on the tribological and mechanical properties of Al 7075-B₄C composites, *Compos. Part B Eng.* 54 (2013) 146-152. <https://doi.org/10.1016/j.compositesb.2013.05.012>

[150] H. Fallahdoost, A. Nouri, A. Azimi, Dual functions of TiC nanoparticles on tribological performance of Al/graphite composites, *J. Phys. Chem. Solids.* 93 (2016) 137-144.
<https://doi.org/10.1016/j.jpcs.2016.02.020>

[151] M.M.H. Bastwros, A.M.K. Esawi, A. Wifi, Friction and wear behavior of Al-CNT composites, *Wear.* 307 (2013) 164-173. <https://doi.org/10.1016/j.wear.2013.08.021>

[152] F. Akhlaghi, A. Zare-Bidaki, Influence of graphite content on the dry sliding and oil impregnated sliding wear behavior of Al 2024-graphite composites produced by in situ powder metallurgy method, *Wear.* 266 (2009) 37-45.
<https://doi.org/10.1016/j.wear.2008.05.013>

[153] M. Sameezadeh, M. Emamy, H. Farhangi, Effects of particulate reinforcement and heat treatment on the hardness and wear properties of AA 2024-MoSi₂ nanocomposites, *Mater. Des.* 32 (2011) 2157-2164.
<https://doi.org/10.1016/j.matdes.2010.11.037>

[154] A. Saravanakumar, P. Sasikumar, Dry sliding wear behaviour of Al6063/Al₂O₃P/GrP hybrid metal matrix composites, *J. Balk. Tribol. Assoc.* 22 (2016) 1253-1264.
<https://doi.org/10.1108/00368791211262499>

[155] A. Vencl, I. Bobic, S. Arostegui, B. Bobic, A. Marinković, M. Babić, Structural, mechanical and tribological properties of A356 aluminium alloy reinforced with Al₂O₃, SiC and SiC+ graphite particles, *J. Alloys Compd.* 506 (2010) 631-639.
<https://doi.org/10.1016/j.jallcom.2010.07.028>

[156] J. Larsen-Badse, Influence of grit size on the groove formation during sliding abrasion, *Wear.* 11 (1968) 213-222. [https://doi.org/10.1016/0043-1648\(68\)90559-0](https://doi.org/10.1016/0043-1648(68)90559-0)

[157] R.W. Johnson, A study of the pickup of abrasive particles during abrasion of annealed aluminium on silicon carbide abrasive papers, *Wear.* 16 (1970) 351-358.
[https://doi.org/10.1016/0043-1648\(70\)90101-8](https://doi.org/10.1016/0043-1648(70)90101-8)

[158] S. Sawla, S. Das, Combined effect of reinforcement and heat treatment on the two body abrasive wear of aluminum alloy and aluminum particle composites, *Wear.* 257 (2004) 555-561. <https://doi.org/10.1016/j.wear.2004.02.001>

[159] A.. Riahi, A.. Alpas, The role of tribo-layers on the sliding wear behavior of graphitic aluminum matrix composites, *Wear.* 251 (2002) 1396-1407.
[https://doi.org/10.1016/s0043-1648\(01\)00796-7](https://doi.org/10.1016/s0043-1648(01)00796-7)

[160] M.L.T. Guo, C.Y.A. Tsao, Tribological behavior of self-lubricating aluminium/SiC/graphite hybrid composites synthesized by the semi-solid powder-densification method, *Compos. Sci. Technol.* 60 (2000) 65-74.
[https://doi.org/10.1016/S0266-3538\(99\)00106-2](https://doi.org/10.1016/S0266-3538(99)00106-2)

[161] S. Suresha, B.K. Sridhara, Wear characteristics of hybrid aluminium matrix composites reinforced with graphite and silicon carbide particulates, *Compos. Sci. Technol.* 70 (2010) 1652-1659. <https://doi.org/10.1016/j.compscitech.2010.06.013>

[162] W. Aiguo, H. J. Rack, Abrasive wear of silicon carbide particulate-and whisker-reinforced 7091 aluminum matrix composites, *Wear.* 146 (1991) 337-348.
[https://doi.org/10.1016/0043-1648\(91\)90073-4](https://doi.org/10.1016/0043-1648(91)90073-4)

[163] A.M. Glazer, The first paper by W.L. Bragg-what and when?, *Crystallogr. Rev.* 19 (2013) 117–124. <https://doi.org/10.1080/0889311X.2013.813494>

LIST OF PUBLICATIONS

The publications are based on the present research work was classified into journals and conferences attended.

Publications in International Journals

1. A Prasad Reddy, P Vamsi Krishna, R N Rao. Mechanical and wear properties of aluminium based nanocomposites fabricated through ultrasonic assisted stir casting. **Journal of Testing and Evaluation**, Vol. 48 (4), 1-22, (2018). **ASTM International Publications**. <https://doi.org/10.1520/JTE20170560> (SCI)
2. A Prasad Reddy, P Vamsi Krishna, R N Rao. Strengthening and mechanical properties of SiC and Gr reinforced Al6061 hybrid nanocomposites processed through ultrasonically assisted casting technique. **Transactions of the Indian Institute of Metals**. Vol. 72 (9) 2533-2546, (2019). **Springer Publications**. <https://doi.org/10.1007/s12666-019-01723-y> (SCI)
3. A Prasad Reddy, P Vamsi Krishna, R N Rao. Tribological behaviour of Al6061-2SiC-xGr hybrid metal matrix nanocomposites fabricated through ultrasonically assisted stir casting technique. **Silicon**. 1-19, (2019) **Springer Nature Publications**. <https://doi.org/10.1007/s12633-019-0072-9> (SCI)
4. A Prasad Reddy, P Vamsi Krishna, R N Rao. Two body abrasive wear behaviour of AA6061-2SiC-2Gr hybrid nanocomposite fabricated through ultrasonically assisted stir casting. **Journal of Composite Materials**. Vol. 53(15), 2165-2180, (2019) **Sage Publications**. <https://doi.org/10.1177/0021998318822723> (SCI)
5. A Prasad Reddy, P Vamsi Krishna, R N Rao. Dry sliding wear behavior of ultrasonically-processed AA6061/SiCp nanocomposites. **International Journal of Automotive and Mechanical Engineering**, Vol. 14 (4) (2017), 4747-4768. **UMP Publications**. <https://doi.org/10.15282/ijame.14.4.2017.12.0373> (Scopus)
6. A Prasad Reddy, P Vamsi Krishna, R N Rao. Al/SiC_{NP} and Al/ SiC_{NP}/X nanocomposites fabrication and properties-A Review. **Proceedings of the Institution for Mechanical Engineers, Part N: Journal of Nanomaterials, Nanoengineering and Nanosystems**, Vol. 231(4) (2017) 155-172. **Sage Publications**. <https://doi.org/10.1177/2397791417744706> (Scopus)

Paper presented in International Conferences

1. A Prasad Reddy, P Vamsi Krishna, R Narasimha Rao, N V Murthy. Silicon carbide reinforced aluminium metal matrix nanocomposites-A Review. **5th International Conference of Materials Processing and Characterization (ICMPC 2016)**. **Materials Today Proceedings**, Vol.4 (2017) 3959-3971. **Elsevier Publications**. <https://doi.org/10.1016/j.matpr.2017.02.296> (Scopus)

BIO-DATA

Personal Information:

Name : A Prasad Reddy
Father's name : A. Madhava Reddy
Mother's name : A. Saraswathi
Gender : Male
Date of Birth/Age : 10-05-1986/ 33 yrs



Educational Qualifications:

S. No	Degree/Course	Discipline/Area/Specialization	Name of Institute/University	Year	Division % or CGPA
1	Ph.D	Mechanical Engineering	National Institute of Technology-Warangal, Telangana, India.	June '14 to till date (Thesis submitted)	
2	M.Tech	Materials Technology	National Institute of Technology-Warangal, Telangana, India.	2012-14	(8.48/10) 1 st Class with Distinction
3	B.Tech	Mechanical Engineering	K.S.R.M.C.E, Kadapa/ S. V. University Andhra Pradesh, India	2004-08	(68.29%) 1 st Class with Distinction
4	Intermediate	Mathematics, Physics and Chemistry	S.C.S.S Junior College, Tirupati, Andhra Pradesh, India	2001-03	(89.3%) 1 st Class with Distinction
5.	S.S.C	Mathematics, Science and Social studies	Board of Secondary Education	2001	(73.2%) 1 st Class

Present position: PhD Research Scholar, Department of Mechanical Engineering, National Institute of Technology- Warangal, India-506004.

Research Interests:

- Nanotechnology, Nanomaterials, Composites, Surface coatings, Hydrogen energy storage materials and Mechanical behaviour of materials.

Publications:

- Journals: 10 (Published)
- Conference: 05 (International Conferences) + 01 (National Conference)

Correspondence Address:

A Prasad Reddy (PhD Research Scholar), C/O Dr. P. Vamsi Krishna, Associate Professor, Department of Mechanical Engineering, National Institute of Technology, Warangal, Telangana, India-506 004.

Residential Address:

S/O A Madhava Reddy, H.No: 14-16, P.K.P Thanda (Post), Nallamada (Mandal), Kadiri (T), Anantapuramu (District), Andhra Pradesh, India-515 501.